Advancing Freeze-Thaw Resistance in Concrete: from Mechanistic Investigations to Predictive Models for Salt Frost Scaling Durability

By

Yuguo Zhong

A dissertation submitted in partial fulfillment
of the requirements for the degree of
Doctor of Philosophy
(Civil Engineering)
in the University of Michigan
2023

Doctoral Committee:

Professor Will Hansen, Chair
Professor Victor C. Li
Professor Zhichao Liu, Wuhan University of Technology
Professor Jwo Pan

Yuguo Zhong

yuguoz@umich.edu

ORCID iD: 0000-0003-2398-9459

Dedication

This thesis is dedicated to my mother Mrs. Ping Jiang.

Acknowledgements

I still remember the Chinese New Year's Eve when I received the offer to the University of Michigan. It marked the start of my dream, one that would take me across oceans to Ann Arbor. In the 5.5 years, this town has become my home, and its people my family. Here, I have experienced the full spectrum of emotions - from the excitement of success to the heartbreak of setbacks. As I bid adieu to my mentor, colleagues, and friends, I cannot help but reflect on the many hands that have guided me through this journey.

First and foremost, I am indebted to my advisor, Professor Will Hansen. His unwavering support and belief in my abilities have been my guiding light throughout my academic journey. His open-mindedness and expert guidance have been invaluable in shaping my research, and his infectious sense of humor has helped me stay positive even during the most challenging times. Without him, my success in Ann Arbor would not have been possible.

I am deeply grateful to my committee members, Professors Victor C. Li, Zhichao Liu, and Jwo Pan. Their helpful feedback and insightful suggestions have been crucial in improving my research. I also appreciate Bo Meng, the former Ph.D. student in our group who provided me with lots of instructions on experiments. I would like to extend my thanks to Jan Pantolin, Steve Donajkowski and Justin Roelofs for their tireless support in the laboratory. I want to express my gratitude to the Construction Field Services Division of MDOT, especially Andy Bennett, Cameron Minney, and Thomas Ethan Bahmer for facilitating concrete making and testing.

My time in Ann Arbor would not have been complete without the love and encouragement of my friends. Silun Zhang, Tianjiao Lei, Qianying Shi, Jipu Wang, Xin Zhang, Fei Xue, Daixi Yang, Anni Wang, Xingwu Zhou, Yuning Zhang, and so many others have been there through thick and thin. Their companionship has been my anchor in turbulent times. And to my badminton buddies Xiaoxu Chen, Zhiyoong Fu, Jeren Hsu, Jizhou Huang, Kexuan Huang, Jiwei Mei, Shuteng Niu, Yizhi Tang, and Yiqi Zhang - our games together will remain some of my fondest memories.

Lastly, I would like to express my deepest gratitude to my family back in China. Though COVID-19 has kept us apart, their steadfast love has always been my driving force. To my grandparents who raised me, and to my father who always encouraged me, I owe a debt of gratitude. And to my mother, Mrs. Ping Jiang - she is my rock, my inspiration, and the compass that always guides me. Her selflessness and support have been the greatest gifts of my life.

As I leave Ann Arbor, I am reminded that time may leave its mark on my skin, but within my spirit, youth still thrives. For as long as I live, I shall hold on to the memory of the love and support that carried me through this journey. Forever love, forever young.

Table of Contents

List of Figures

List of Tables

List of Appendices

Abstract

In North America, where winter temperatures frequently dip below freezing, deicing salt is a common solution for melting snow and ice on roadways. However, this practice can result in the top layer of concrete flaking off, a phenomenon known as salt frost scaling. This problem not only leads to costly damage to infrastructure such as roads and bridges but also poses safety hazards for drivers and pedestrians. Therefore, it is crucial to understand the mechanisms underlying salt frost scaling and to develop effective strategies to mitigate its impacts. This thesis proposes a three-pronged approach to investigate this issue, including laboratory studies, mechanistic analyses, and predictive modeling. The experimental results have shown the low concentration of salt solution causes the most severe scaling. The previously established cryogenic suction mechanism combined with the micro-ice-lens pumping provides a sound explanation for the phenomenon. Pore drying and ice expansion due to freezing likely creates additional space for moisture uptake during freeze-thaw (F-T) cycles by enlarging the capillary pores and opening the channel to connect previously unconnected pores. This study also has revealed that hydrophobic impregnations fail to prevent the pumping effect associated with the F-T cycles and a marked negative effect of hydrophobic impregnation on the F-T resistance has been observed. These results shed light on the link between salt frost scaling and internal cracking, both of which depend on the degree of saturation, with the former associated with local moisture conditions and the latter with global moisture conditions. Large moisture uptake and poor air void system increase the likelihood of reaching the critical degree of saturation which leads to severe damage. These findings pave the way for modeling scaling. The polynomial regression model is proposed to quantify the scaling based on sorptivity, which is a measure of capillary suction and freezing water susceptibility, and the ability of the air void system to provide pressure relief. The results show that more permeable concrete should be equipped with a better-quality air void system. Finally, a machine learning model implemented by XGBoost algorithms was proposed to distinguish between scaling-resistant and non-scaling-resistant concrete based on previously identified

important parameters. The results demonstrate the importance of sorptivity and spacing factor in scaling. This model, combined with the Shapley value, provides valuable insights into the scaling resistance of concrete and can be used as a reliable and efficient assessment tool for concrete quality.

Chapter 1. Introduction

1.1 Background

The phenomenon of frost damage may be familiar to many who have accidentally left a full bottle of drink in the freezer. When water freezes, it undergoes volumetric expansion of about 9%, which can potentially destroy the container. The mechanisms behind frost damage may differ depending on the material, but any material containing moisture, whether it is in the cracks of rocks or the pores of the concrete, is susceptible to this type of damage, known as internal cracking or internal frost attack. Internal cracking is a common form of distress in concrete and can result in a significant decrease in the concrete's modulus of elasticity and eventual disintegration.

In addition to internal cracking, salt frost scaling is another common form of concrete deterioration in Northern America caused by F-T in combination with the deicing salt solution. Salt frost scaling is a progressive type of deterioration that gradually erodes the very thin layers of paste or mortar. The initial layer is destroyed with the increase in F-T cycles and subsequent layers are repeatedly attacked, potentially leading to the destruction of the concrete structure in some extreme cases. Spalling, for example, is one common distress associated with the salt frost attack as illustrated in Figure 1.1 which shows the joint spalling in joint plain concrete pavement (JPCP) on M-14 in Ann Arbor, Michigan. The joint core in Figure 1.2 demonstrates the erosion of the cementitious binder at the bottom. This in tandem with truck loading and trapped liquid in the joint can cause shear failure and joint spalling, which can worsen over time and eventually require full-depth repair.

Salt frost scaling is a complex issue that is not yet fully understood. However, certain common features are typically observed in association with salt frost scaling. For instance, it occurs only when surface liquid is present and when the concrete reaches a particular level of saturation. Moreover, exposure to a salt solution exacerbates the issue, making it much more severe than exposure to pure water.

Figure 1.1 Joint spalling in JPCP on M-14, Ann Arbor, Michigan (courtesy of Prof. Will Hansen)

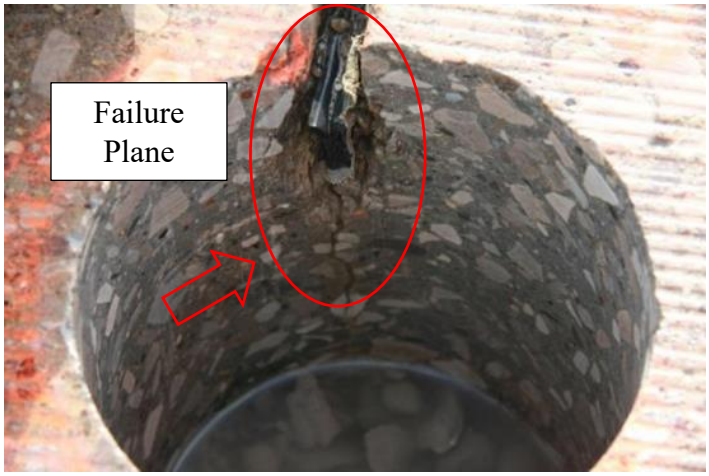

Figure 1.2 Joint core showing erosion of the cementitious binder (courtesy of Prof. Will Hansen)

Salt frost damage is caused by the uptake of liquid, and most materials-related distress (MRD) mechanisms in concrete require liquid for the distress to progress. The reduction of permeability can diminish moisture ingress and mitigate the effects of a given MRD, including salt frost scaling (Hansen et al. 2010). Hydrophobic admixtures have proven effective in non-freeze applications for controlling moisture uptake and penetration of chloride ions, thus reducing the risk of reinforcement corrosion. Although they seem to be a simple solution for preventing salt frost scaling, previous studies have been limited and have shown conflicting results. Therefore, further research is needed in this area.

To evaluate the salt scaling resistance of concrete and predict its performance in field exposure conditions, different countries and regions have established their own standard procedures. The

most common standard procedures include ASTM C 672 (2012), MTO LS 412 (2006), NQ 2621-900 (2002), SS 13 72 44 (Swedish Institute for Standards, 2019), and CDF test (Setzer et al. 1996). These standard procedures usually involve subjecting a specimen to a large number of F-T cycles and measuring its mass loss, which can be laborious and time-consuming. There is a growing interest in using durability related factors, such as water transport properties or air void system quality, to rapidly evaluate salt scaling resistance and improve concrete design and durability. Consequently, the prediction of scaling using different modeling methods has become a major research focus.

1.2 Objectives and scope of research

The primary objective of this study is to enhance the comprehension of F-T related damage in pavement applications and provide guidelines for a rapid assessment of salt frost scaling resistance.

Hydrophobic impregnation has been demonstrated to be an effective method to reduce water uptake and reduce corrosion risk at room temperature. However, there is limited research on the impact of hydrophobic treatment on salt frost durability, and the available data provide conflicting results. Consequently, this study aims to assess the effectiveness of two types of hydrophobic impregnation, applied either internally as part of the mix components or externally as a surface treatment, on the F-T and deicer scaling resistance using the RILEM TC 176-IDC Capillary suction, Internal damage, and Freeze-thaw (CIF) Test. The laboratory concretes used for pavement applications are characterized by a wide range of air content and supplementary cementitious material (SCM) types. The study aims to examine the link between surface scaling and internal cracking based on the analysis of the results.

The air void system is an important factor in the salt frost scaling resistance of concrete. Concrete exposed to a freezing environment requires a sufficient number of air voids to protect its structural integrity by providing internal shelter spots to accommodate excessive pressure build-up. Therefore, the quality of the air void system has been an important indicator for salt frost scaling resistance and many efforts are made to investigate and improve the characterization of the air void system using different parameters. This thesis conducts a comprehensive study of these parameters and the correlation between scaling and air void parameters is discussed. However, in most cases, it is challenging to characterize scaling using one single parameter due to the complex nature of the problem. A polynomial regression model is being proposed to predict scaling based

on the balance between the quality of the air void system and the isothermal water uptake property from a sorption test.

Since 2009, machine learning has been utilized for the study of cement hydration, concrete degradation mechanisms, and the discovery of concrete materials. In this study, an XGBoost algorithm is employed to implement a binary classification model aimed at determining if a concrete sample is scaling resistant or not. Shapley value, based on cooperative game theory, is employed to interpret the feature importance and feature effects on the scaling resistance. Machine learning provides a quicker and more efficient way to predict concrete behavior, reducing the need for extensive experiments while still providing accurate results.

1.3 Organization of the thesis

This doctoral thesis consists of a comprehensive investigation into salt frost scaling in concrete.

In Chapter 2, an in-depth review of the common features and mechanisms of salt frost scaling is conducted, and the key factors that affect its occurrence are summarized. This chapter also covers the theory of water transport properties, which is fundamental to understanding salt frost scaling.

Chapter 3 introduces the experimental program used in the thesis, including the raw materials and mix characteristics, as well as the detailed test procedures.

Chapter 4 delves into the laboratory F-T results of high-performance concrete, discussing moisture uptake behavior in various conditions, the pessimum effect, and an extended cryogenic suction model explaining salt frost scaling. The effect of lightweight aggregate on concrete durability is also explored.

Chapter 5 explores the influence of hydrophobic impregnation on the behavior of concrete in F-T cycles. The surface impregnation by the use of silane treatment, and the internal impregnation using a kind of permeability-reducing admixture at mixing are discussed separately. The way that they affect the F-T behavior is analyzed combined with their working mechanism. Based on the analysis, the link between salt frost scaling and internal cracking is discussed.

In Chapter 6, the relationship between scaling and key parameters is thoroughly investigated. This involves the exploration of the water transport properties as well as a comprehensive study of the characterization of the air void system. The chapter also attempts to quantify scaling using a

polynomial regression model including both the water transport property as a pressure cause and the air void system as a pressure relief.

Building upon the previous chapters, Chapter 7 proposes a binary classification model based on the XGBoost algorithm to classify concrete as scaling resistant or not using 18 predictor variables, such as water-cement ratio (w/c), curing age, sorptivity, and spacing factor. To interpret the feature importance and their effects on scaling resistance, the Shapley value based on cooperative game theory is employed.

Finally, in Chapter 8, conclusions of the thesis study are provided, along with recommendations for future research directions.

The thesis roadmap is displayed in Figure 1.3.

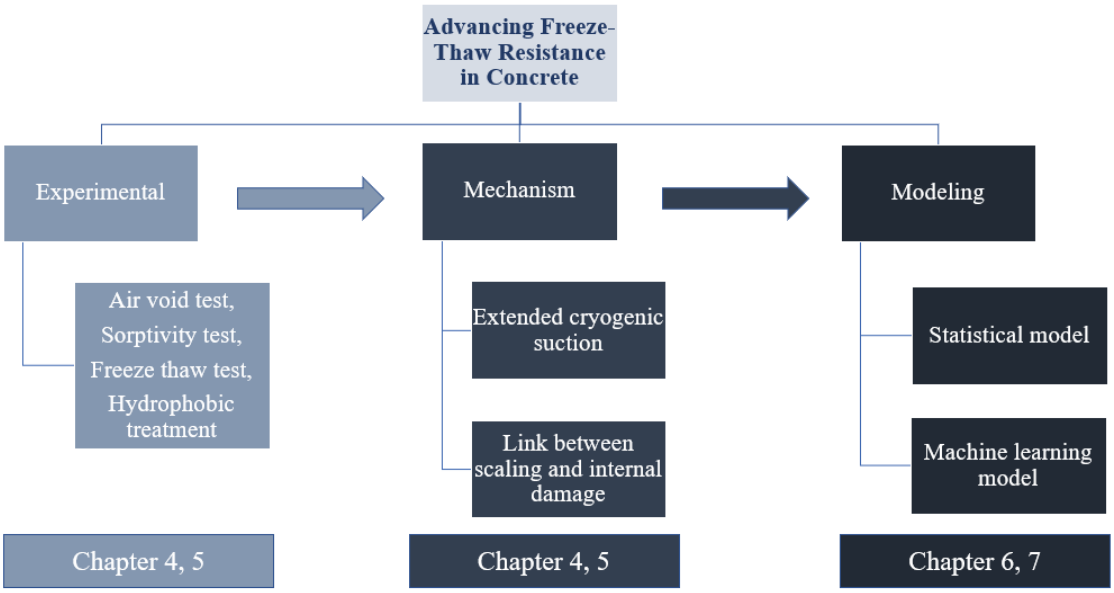

Figure 1.3 Thesis roadmap

Chapter 2. Review of Freeze-Thaw Scaling in Concrete

2.1 General

It has been well documented that the deterioration caused by F-T exposure mainly lies in two aspects: surface scaling and internal cracking. Powers first described these damages in 1945 (Powers 1945) defining surface scaling as the progressive loss of material from the surface layer of the paste or mortar, and internal cracking as large losses in strength and resilience, with little change in weight or appearance. This definition has been constantly recognized and used by laboratory and field results in recent decades. Surface scaling is a complex problem due to its strong dependence on the microstructure of the concrete surface layer (Pigeon et al. 1996). The irregular arrangement of hydrated cement paste, various hydration products, and pore spaces make it challenging to model the microstructure of concrete (Marchand et al. 1996). Furthermore, the presence of salt solutions and freeze-thaw action further complicates this issue, requiring a comprehensive understanding of the deicer salt scaling mechanism and careful consideration of important parameters to accurately characterize concrete frost durability. In the context of this study, the terms "salt frost scaling", and "surface scaling" are used interchangeably when the scaling is attributed to the repeated freeze-thaw cycles in combination with salt solutions.

In this chapter, the fundamentals of water transport properties are discussed, which is crucial in understanding the mechanism behind salt frost scaling. Additionally, a review of its common features is provided. The proposed mechanisms by various researchers are presented and key properties that impact salt frost scaling are identified.

2.2 Basic properties of water and ice

Water plays a significant role in the F-T damage of concrete. This section aims to provide an overview of the fundamental properties of water and ice, which serve as a theoretical foundation for accurately analyzing transport phenomena.

2.2.1 Water

In order to better understand the water flow in concrete, the properties of water such as density, heat capacity, as well as surface energy need clarification.

The density of the water varies with temperature and can be calculated as

$$\rho = -3479.56 + 46.301T - 0.1591T^2 + 1.8171 \cdot 10^{-4}T^3, \quad \text{Eq. 2.1}$$

where ρ is the density of the water (kg/m^3) and T is the temperature ($243.15^\circ K < T < 293.15^\circ K$) (Lindmark 1998).

The density of the deicer salt solution depends on the concentration. For the most common NaCl solution, the density at $293^\circ K$ is

$$\rho(c) = 7.2416c + 997.98, \quad \text{Eq. 2.2}$$

where c is the concentration of NaCl in % by the weight of the concentration and c should be less than 26% with an error of less than 1%.

The surface tension of water or deicing salt solution varies with the temperature and content of the solutes in the liquid. When the temperature is $293^\circ K$, the surface tension is

$$\sigma_{l-v}(c)_{293^\circ K} = \frac{72.72 + 0.325c}{1000}, \quad \text{Eq. 2.3}$$

where $\sigma_{l-v}(c)$ is in $\mathrm{J/m^2}$ and c is the concentration of NaCl in % by the weight of the concentration. c should be less than 20% with an error of less than 1%.

The surface tension of a surface liquid water vapor is also a function of temperature as

$$\sigma_{l-v}(T) = -0.1484 \cdot 10^{-3}T + 0.11623, \quad \text{Eq. 2.4}$$

where T should be between 265 and $297^\circ K$.

2.2.2 Ice

The density of ice as a function of temperature can be estimated as

$$\rho(T) = \frac{\rho(273.15)}{(1 + \alpha(T - 273.15))^3}, \quad \text{Eq. 2.5}$$

where $\rho(T)$ is the density at temperature T, $\rho(273.15)$ is the density at $T = 273.15^\circ K$, 1 atm ($916.4\ kg/m^3$) and α is a coefficient of linear expansion.

The density of the ice is known to be less than that of water. At 0°C, the density of ice is 916.4 kg/m^3 while that is 999.8 kg/m^3 for ice at the same temperature. This phase transition brings an expansion of about 9.1%.

The surface energy of ice at different temperatures can be estimated by

$$\sigma_{l-s} = \frac{0.2T - 21.63}{1000}. \quad \text{Eq. 2.6}$$

2.3 Flow in concrete

2.3.1 Moisture flow at room temperature

There are three primary mechanisms responsible for moisture transport in concrete: diffusion, permeability, and capillary suction.

Diffusion is the transfer of mass from areas of high concentration to areas of lower concentration. Fick's first law of diffusion states that the rate of diffusion is directly proportional to the concentration gradient and the diffusion coefficient, which is given by the following formula

$$F = -D\frac{\partial c}{\partial x}, \quad \text{Eq. 2.7}$$

where F is the mass flux $(g/m^2 s)$, D is the diffusion coefficient (m^2/s), c is the concentration of the solution (g/m^3) and x is the flow distance (m).

Diffusion is a complex mass transfer process that is not restricted to one-way movement. In the context of deicing salt solutions, diffusion occurs as a result of salt ions moving from areas of higher concentration to areas of lower concentration, and water molecules from areas of lower concentration to higher concentration until equilibrium is reached. It is important to note that osmosis, which is a special type of diffusion, involves only a one-way movement of the solvent across a semi-permeable membrane towards a high-concentration solution. The driving force behind osmosis is the vapor pressure difference between the solutes or solvents in the two solutions, as illustrated in Figure 2.1.

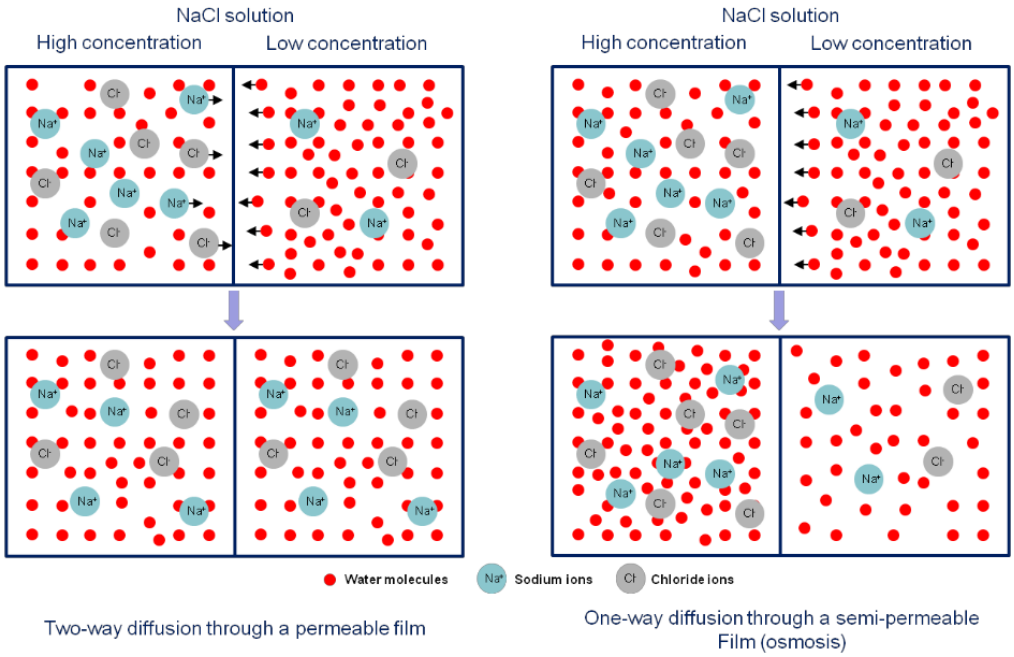

Figure 2.1 Schematic representation of diffusion and osmosis process (Liu 2014)

Permeation refers to the penetration of a liquid or gas into a solid under the influence of a pressure head. This process is typically associated with a material property known as the coefficient of permeability. In the case of an incompressible liquid flowing through concrete, the flow can be described using Darcy's Law for laminar flow through a porous medium

$$\frac{dq}{dt}\frac{1}{A} = \frac{K'\rho g}{\eta}\frac{\Delta h}{L}, \qquad \text{Eq. 2.8}$$

where $\frac{dq}{dt}$ is the flow rate (m^3/s), A is the penetrated area, K' is the permeability of the concrete (m^2) and is an intrinsic material property independent of liquid. Δh is the pressure head drop along the flow length L (m). ρ is the density of the liquid (kg/m^3), g is the acceleration due to gravity (m/s^2), η is the dynamic viscosity of the liquid $(Pa \cdot s)$.

For water, the expression can be simplified as

$$\frac{dq}{dt}\frac{1}{A} = K\frac{\Delta h}{L}, \qquad \text{Eq. 2.9}$$

where K is the coefficient of water permeability (m/s) and is equal to $9.75 \cdot 10^6 K'$ at 20°C

Permeation is a transport mechanism associated with saturated flow, whereas capillary suction is related to unsaturated flow, which is more prevalent in civil engineering materials and can more accurately describe the transport behavior of moisture in concrete.

The physics of the unsaturated flow is expressed using the extended Darcy equation (Hall 1989)

$$\boldsymbol{q} = K(\theta)\boldsymbol{F}_{\mathrm{c}}(\theta), \qquad \text{Eq. 2.10}$$

where $\boldsymbol{q}$ is the vector flow velocity, θ is the water content, K is the hydraulic conductivity and $\boldsymbol{F}_{\mathrm{c}}$ is the capillary force which can be determined as the gradient of the capillary potential $\boldsymbol{\Psi}$

$$\boldsymbol{F}_{\mathrm{c}} = -\nabla\boldsymbol{\Psi}(\theta). \qquad \text{Eq. 2.11}$$

For one-dimensional cases with isotropic conductivity,

$$\boldsymbol{q} = -K(\theta)\frac{d\boldsymbol{\Psi}}{dx}. \qquad \text{Eq. 2.12}$$

Eq. 2.12 is usually written as

$$\boldsymbol{q} = -D(\theta)\frac{d\theta}{dx}, \qquad \text{Eq. 2.13}$$

where $D(\theta)$ is the hydraulic diffusivity and equals to $K(\theta)\frac{d\boldsymbol{\Psi}}{d\theta}$. The unsaturated flow equation is mathematically transformed into a diffusion equation, while it is important to note that capillarity, rather than molecular diffusion, is the underlying process.

2.3.2 Moisture flow under freezing

The process of moisture flow under freezing can be explained through the thermodynamic properties of water which are influenced by temperature, pressure, surface tension, and the presence of salt solutions. The equilibrium phase of the water is determined by the minimum of the partial Gibbs function (chemical potential) which can be written as (Borgnakke et al. 2012)

$$g = g_0 - \int sdT + \int vdP + \int \sigma dA + RT\ln y, \qquad \text{Eq. 2.14}$$

where g_0 is the reference Gibbs function, g is the Gibbs function due to the effect of surface tension and salt with change in pressure and temperature. $-\int sdT + \int vdP$ is the Gibbs function due to changes in pressure and temperature, $\int \sigma dA$ is the effect of surface tension, and the integral is used from a cylindrical geometry. Additionally, the effect of salt is given by $RT\ln y$, where y represents the mole fraction of solvent. For ice, $y = 1$ while for salt-water, $y < 1$.

The final expression for the Gibbs function of ice in a pore of radius r is

$$g = g_{\text{sat }T} + v_{\text{sat }T}(P - P_{\text{sat }T})\left[1 - \frac{1}{2}\beta_T(P - P_{\text{sat }T})\right] + \sigma_{s-l}\frac{2v_{\text{satT}}}{r}, \qquad \text{Eq. 2.15}$$

where σ_{s-l} is the surface energy change when a liquid spreads over the matrix surface, β_T is the isothermal compressibility $= -\left(\frac{1}{v}\right)\left(\frac{\partial v}{\partial P}\right)_T = 250 \times 10^{-9}\ \text{kPa}^{-1}$, $v_{\text{sat }T}$ is the variation of the specific volume, $P_{\text{sat }T}$ is the saturated pressure, r is the pore radius. Surface tension develops as a very thin layer of liquid covers the solid phase. The surface energy of the matrix-air interface can be estimated based on that of the liquid-air interface (Lindmark 1998).

The Gibbs function for pure water is expressed as:

$$g_{liqT,P_0} = RT_R\left(c_1 + c_2\tau + c_3\tau\ln\tau + \sum_{i=1}^{3} a_i\alpha^{n_i} + \sum_{i=1}^{4} b_i\beta^{m_i}\right), \qquad \text{Eq. 2.16}$$

where $R = 461.51805\,J\cdot\ kg^{-1}\cdot K^{-1}, T_R = 10K$, dimensionless coefficients a_i, b_i, c_i, n_i, and m_i are tabulated. Dimensionless temperature coefficients are determined by

$$\tau = \frac{T}{T_R}, \alpha = \frac{T_R}{T_a - T}, \beta = \frac{T_R}{T - T_b},$$

where T_a = 593 K, T_b = 232 K, which is in the valid range of application.

For a salt solution in a pore of radius r, the Gibbs function can be calculated as

$$g = g_{liqT,P} + \sigma_{l-v}\frac{2v_{l0}}{r} + RT\ln y. \qquad \text{Eq. 2.17}$$

Figure 2.2 (a) depicts the Gibbs free energy of water and ice as a function of pore size at a temperature of $-20°C$. The results demonstrate that the Gibbs free energy of ice is considerably lower than that of water in larger pores. Notably, water in pores that are less than 10 nm does not freeze due to the high surface tension. This implies that, in a frozen state, moisture will flow from finer capillaries or gel pores to coarser pores that contain ice because of the chemical potential difference. The low vapor pressure around ice exerts an attraction on water from finer pores, promoting the growth of ice from the gel pores or finer capillaries. This phenomenon occurs because freezing cannot occur in situ, as has been observed in previous studies (Pickett 1953, Powers et al. 1953, Rønning 2001).

The decrease in temperature leads to a decrease in the Gibbs free energy of water and ice (Figure 2.2 (b)). The rate of decrease is much faster for ice than for water, which increases the driving potential for spontaneous liquid transport.

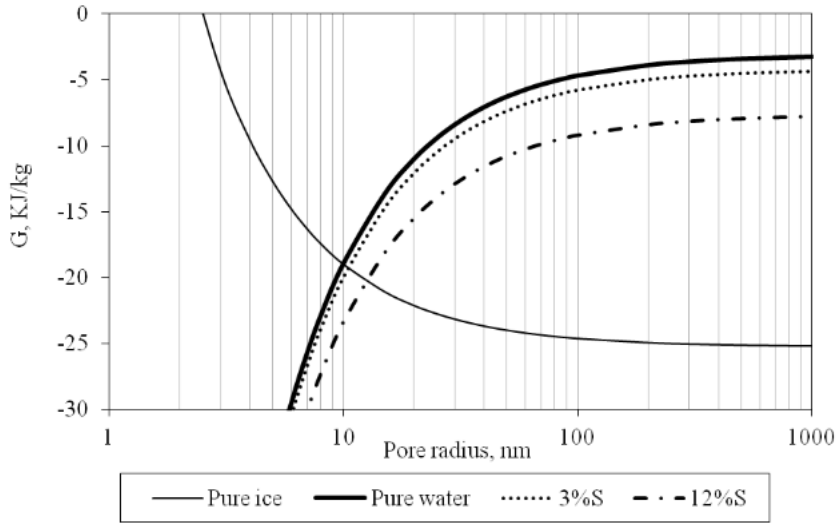

(a)

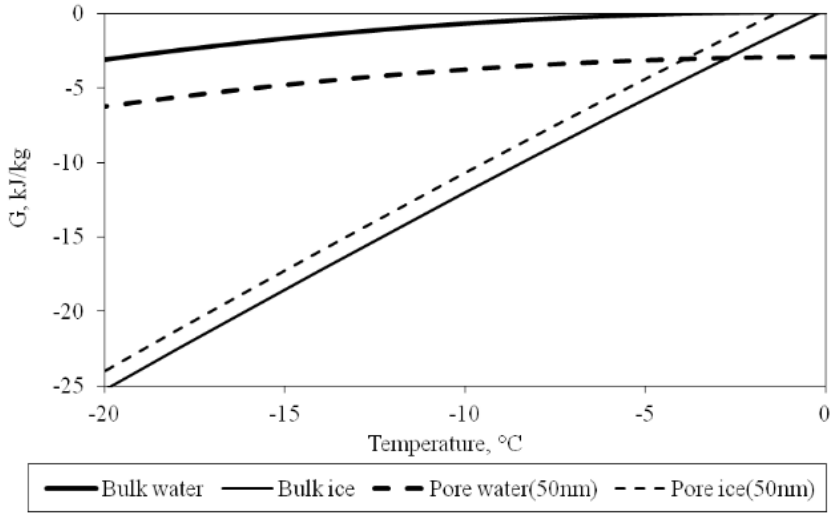

(b)

Figure 2.2 Gibbs free energy of water and ice as a function of (a) pore size at -20 °C and (b) temperature (Liu 2014) (Note: 3%S and 12%S means 3% and 12% salt solution, respectively)

2.4 Salt frost scaling features in concrete

Although the cause of salt frost scaling is still subject to debate, certain features have been consistently observed in laboratory and field results which are summarized in this section.

2.4.1 Importance of exterior solutions

One of the prerequisites for the development of salt frost scaling is the presence of outer solutions. Researchers have shown that, when concrete is frozen and no liquid is present on the surface, no scaling occurs (Verbeck et al. 1957, Studer, 1993). Moreover, Fagerlund and Lindmark reported that salt concentration outside the concrete is more important in terms of causing scaling than inner concentration which has a marginal effect as shown in Figure 2.3 (Fagerlund, 1993; Lindmark, 1993).

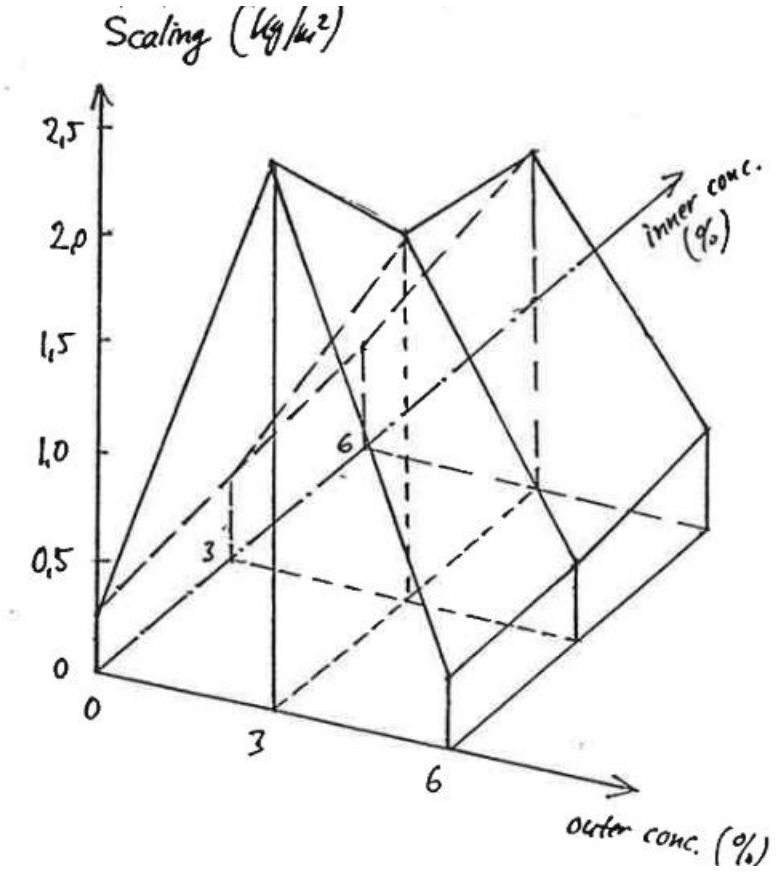

Figure 2.3 The salt scaling after 56 freeze-thaw cycles of the same concrete but with different outer and inner salt concentrations (Lindmark, 1993)

2.4.2 Paste swelling

Upon close examination of the exposed surface of concrete, a notable characteristic has been discovered that the paste region surrounding the coarse aggregate particles in concrete mixes with high w/c or insufficient air entrainment swells as shown in Figure 2.4 (Liu 2020). The scaled materials collected from such concrete mostly consist of flat flakes, with a close-up view of a flake,

revealing embedded sand particles in the cement paste. This indicates that stresses causing scaling originate from the surface in the paste phase.

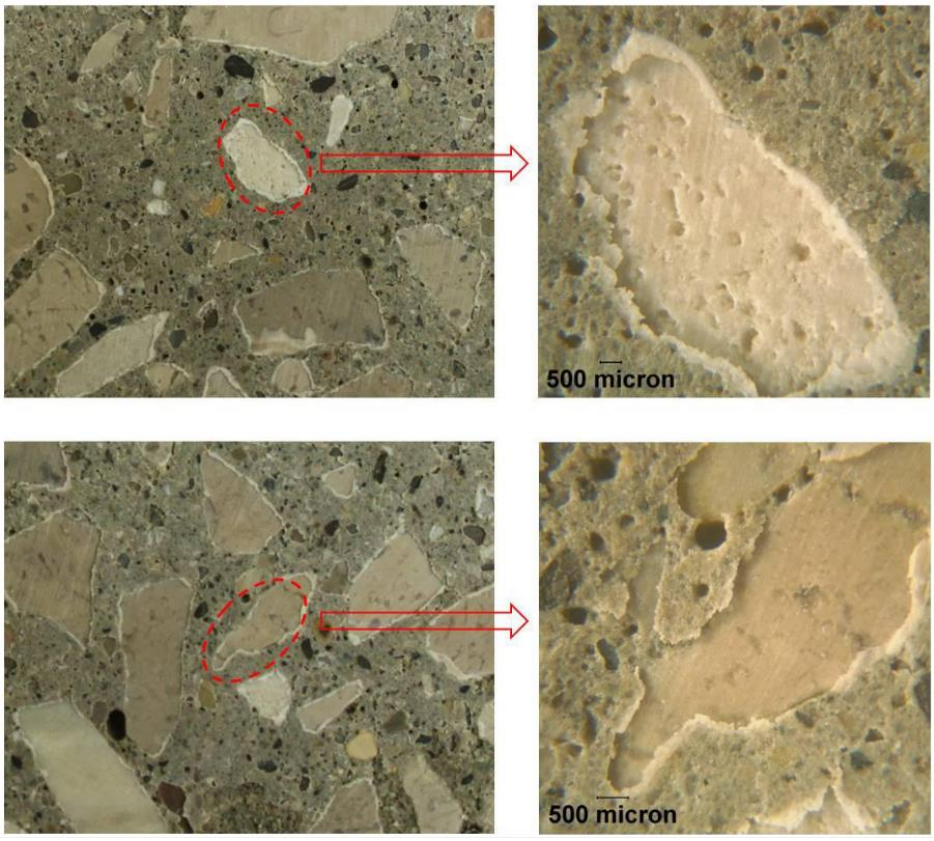

Figure 2.4 Swelling of paste around coarse aggregate particles under salt exposure

2.4.3 Pessimum effect

The pessimum effect of salt in concrete refers to a phenomenon where a low level of salt concentration in concrete can actually worsen its durability and increase the risk of damage from F-T cycles, typically occurring at around 3% salt solution (see Figure 2.5 and Figure 2.6). The presence of salt in concrete can cause an increase in the material's moisture content, which can in turn increase the likelihood of damage from freezing and thawing. However, if the salt concentration continues to increase, it can inhibit the formation of ice crystals during freezing, which can lead to decreased damage from ice expansion. This phenomenon has been observed in several studies (Verbeck et al. 1957, Fagerlund 1973, Sellevold et al 1991, Lindmark 1998, Rønning 2001).

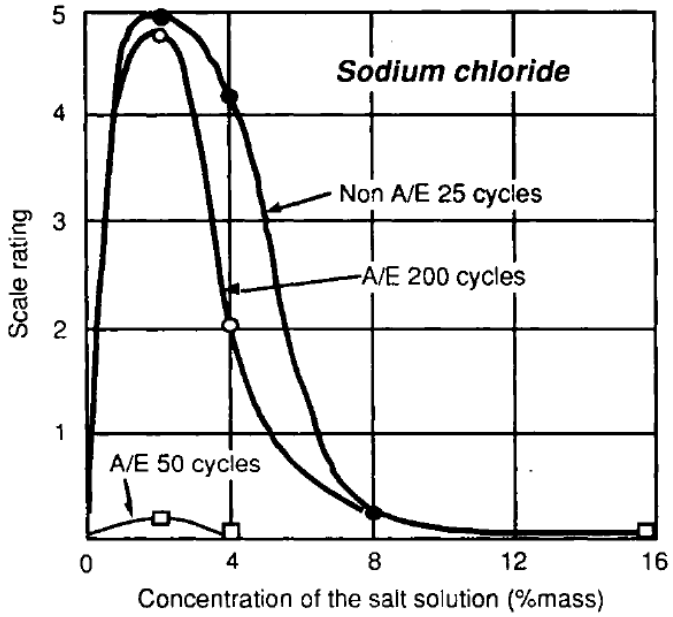

Figure 2.5 Effect of the concentration of the NaCl solution on the surface scaling (Verbeck et al. 1957)

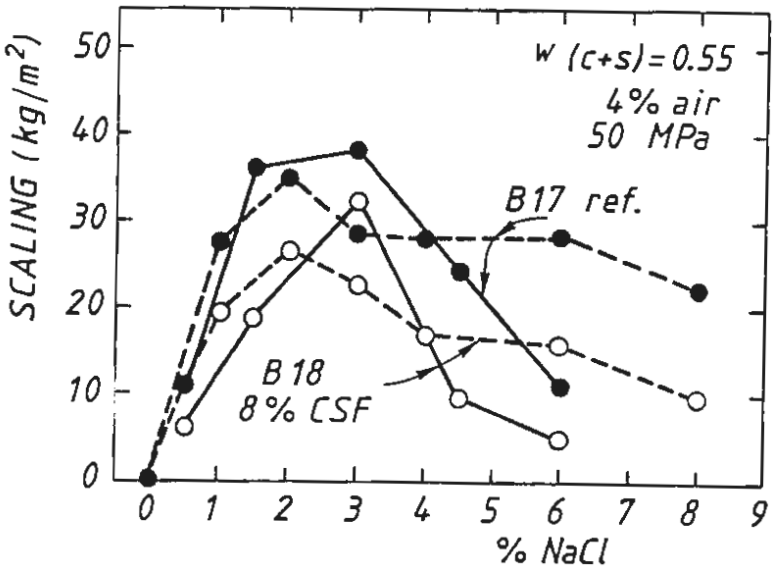

Figure 2.6 Salt frost scaling with different salt concentrations (Sellevold et al. 1991)

2.4.4 Protection from air entrainment

Air entrainment in concrete is a process of deliberately introducing tiny air bubbles into the mix during the mixing stage to improve the concrete's resistance to F-T cycles. Researchers discovered the benefits of air entrainment accidentally in the late 1930s when they observed that concrete

blended with Portland and natural cement containing "crushed oil" exhibited greater resistance to surface scaling (Jackson 1944). The air bubbles provide space for the expansion of water when it freezes, preventing the buildup of pressure that can cause cracking or scaling in the concrete. A comprehensive discussion of the air void system is presented in Chapter 6.

2.5 Salt frost attack mechanism

The mechanisms behind salt frost scaling are complex and multifaceted, involving a range of physical, chemical, and mechanical processes. In this section, some of the key mechanisms that have been proposed to explain salt frost scaling are reviewed. Understanding these mechanisms is crucial for developing effective mitigation strategies to minimize salt frost scaling and improve the durability of concrete structures in cold regions.

2.5.1 Hydraulic pressure and osmotic pressure

In the introduction, the closed container was mentioned as the most straightforward mechanism of frost deterioration. It suggests that if more than 91.7% of the container is initially filled with water, pressure will develop as the specific volume of ice is larger than that of water. However, in 1945, Powers challenged this theory by noting that even if concrete contains enough air which can accommodate the volume increase during freezing and seems less critically saturated, it would still fail (Powers 1945). He proposed an alternative theory known as the 'hydraulic pressure hypothesis' which suggests that the failure is not caused by ice expansion pressure, but rather by the hydraulic pressure resulting from the expelled water from the pore during ice formation. The hydraulic pressure in concrete is influenced by a range of factors, such as the freezing rate, cooling rate, coefficient of permeability of the gel, and the length of water passages. Fagerlund (1979) proposed a model to describe hydraulic pressure, which is illustrated in Figure 2.7. The maximum hydrostatic pressure is associated with the cooling rate, freezing rate, and the distance between air voids, and can be expressed mathematically by the following equation:

$$p_{max} = p_{x=\frac{d}{2}} = \frac{0.09}{8k} \cdot \frac{d_{wf}}{d\theta} \cdot \frac{d\theta}{dt} \cdot d^2, \qquad \text{Eq. 2.18}$$

where $\frac{d_{wf}}{d\theta}$ represents the freezing rate, which is the volume increase of frozen water for every 1 °C decrease in temperature ($m^3/(m^3 \cdot °C)$), $\frac{d\theta}{dt}$ is the cooling rate (°C/s), k is the coefficient of

permeability of the frozen material, d is the distance between two air voids and x represents the distance between the freezing point and the air void on one side.

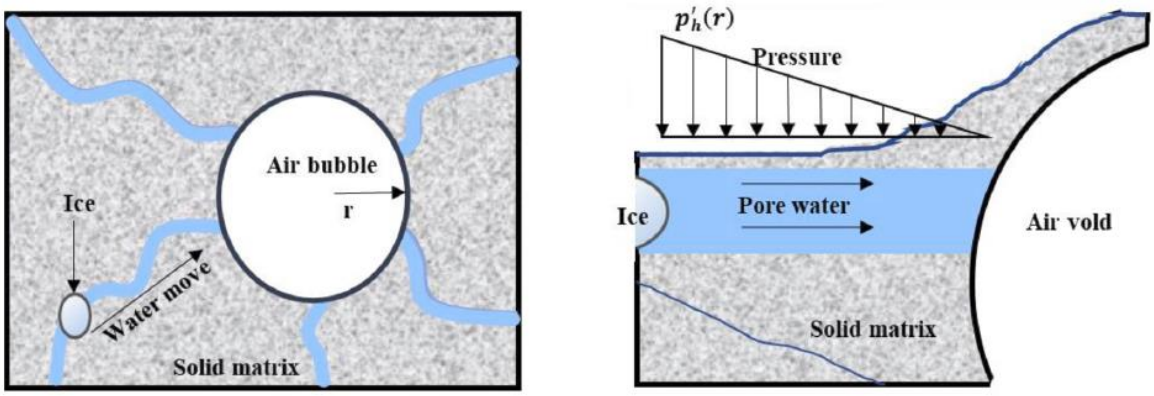

Figure 2.7 Powers hydraulic pressure model (Yu et al. 2017)

The hydraulic pressure hypothesis fails to account for the impact of salt solution. In response to this limitation, Powers and Helmuth conducted further research and observed that non-air-entrained concrete paste expands during the cooling process and at constant sub-zero temperatures, while air-entrained paste contracts (Powers et al. 1953). To explain this phenomenon, they proposed osmotic micro ice body growth as a mechanism for concrete deterioration.

In order to comprehend the theory, it is crucial to note that the freezing point of pore liquid is influenced by the size of the pore, and this correlation can be described as follows:

$$r = \frac{2\gamma_{CL}}{\sum_m (T_m - T)}, \qquad \text{Eq. 2.19}$$

where r is the radius of the pores, γ_{CL} is the crystal liquid interface energy, $\sum_m$ is the melting entropy, T_m is the melting point and T is the temperature. In concrete that has pores and air voids of different sizes, the melting/freezing points are different. This leads to the coexistence of ice, water, and vapor.

The hypothesis suggests that in the presence of a salt solution within concrete pores, the freezing process commences in the larger pores. As cooling progresses, the concentration of the salt solution within these large pores increases, leading to the migration of unfrozen water from smaller pores toward the site of ice formation. This migration is attributed to the potential difference created by the differences in free energy. Osmotic pressures generated by the presence of salts

result in the transportation of additional moisture toward the pores where both ice and salt solution coexist, thereby promoting the growth and expansion of ice lenses.

2.5.2 Critical degree of saturation

It has been demonstrated that only when the water content extends a certain value, deterioration can possibly develop. The degree of saturation at which the deterioration occurs is called the critical degree of saturation, S_{cr}. In practice, not all water in concrete freezes at 0°C and a higher degree of saturation above 91.7% is permissible, known as the effective degree of saturation S_{eff}. The effective degree of saturation is defined as

$$S_{eff} = \frac{V_f}{V_f + a}, \quad \text{Eq. 2.20}$$

where V_f is the volume of freezable water and a is the volume of air (Fagerlund 1973). However, it is usually hard to determine the freezable water amount so a simpler calculation is used as

$$S = \frac{V_w}{V_{\text{pore}}} = \frac{V_w}{V_w + a}, \quad \text{Eq. 2.21}$$

where V_w is the volume of water in 'water-saturated' specimen (Lindmark 1998). In 1977, Fagerlund conducted a study on the critical degree of saturation and the rate of moisture uptake (under isothermal conditions) to estimate the potential service life of a material (Fagerlund 1977). However, he acknowledged that the true service life can be influenced by the changes in the microstructure of the material in the exposed environment. The mechanism of water uptake beyond capillary suction remains unknown. Moreover, the critical degree of saturation is a macro description that cannot explain the micro mechanism.

2.5.3 Micro-ice-lens model

Setzer established the theory of micro-ice-lens based on the non-equilibrium thermodynamics and three-phase (unfrozen water, ice, and vapor) equilibrium in porous solids (Setzer 2001). The deterioration process is divided into two stages. During cooling, a frost shrinkage is generated because the unfrozen gel water is sucked into the ice front due to a negative pressure which is needed to reach the thermodynamic equilibrium. During heating, the water is prevented from flowing back by the micro-ice lenses. If external water is available, it will be sucked in. When it reaches critical saturation, the expansion of ice bodies exerts on the matrix (Setzer 2004). The F-T cycle is analogous to a low-temperature pump, which is powered by the change of temperature

and migration of supercooled water. The saturation of concrete increases with an increase in the number of F-T cycles, and when the critical saturation is reached, the concrete fails.

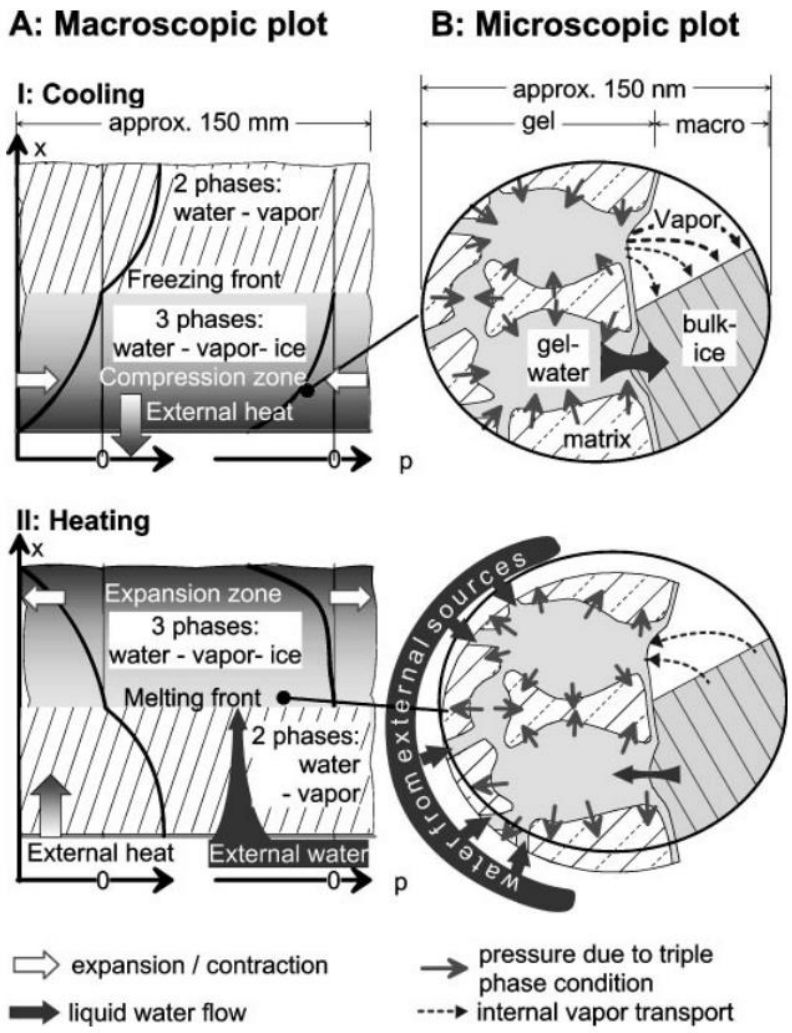

Figure 2.8 Micro-ice-lens model (Setzer 2001)

2.5.4 Glue Spalling

In the 2010s, Valenza et al. introduced the concept of "glue spall" to explain the mechanism of salt scaling (Valenza et al. 2007). The term "glue-spalling" was originally used in the manufacture of ornamental glass. The procedure is illustrated in Figure 2.9. In the first step, a type of epoxy is spread onto the glass surface, similar to an ice layer on a concrete surface. After the epoxy is cured, the composite is cooled. During cooling, high tensile stresses are generated in the glass surface due to the mismatch in the coefficient of thermal expansion between the glass and glue at the

boundary of the islands, as the epoxy shrinks relative to the substrate (Figure 2.10—σ_{gs}). Cracks develop under the tensile stress and ultimately cause the removal of a thin piece of glass.

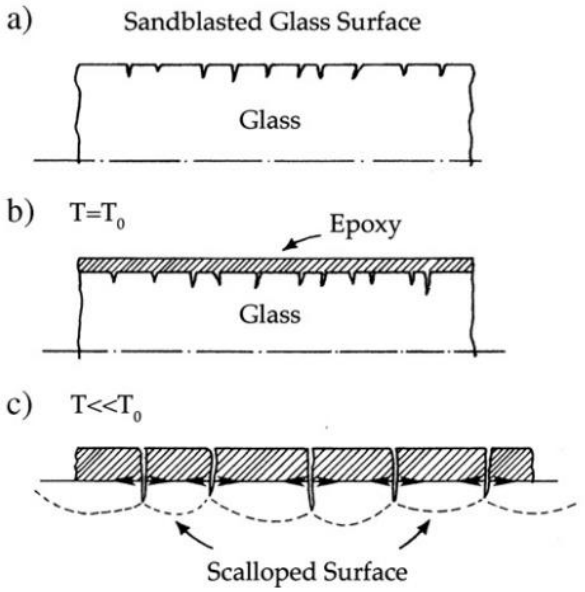

Figure 2.9 Illustration of Glue-spall mechanism by the fabrication of ornamental glass (Valenza et al. 2007)

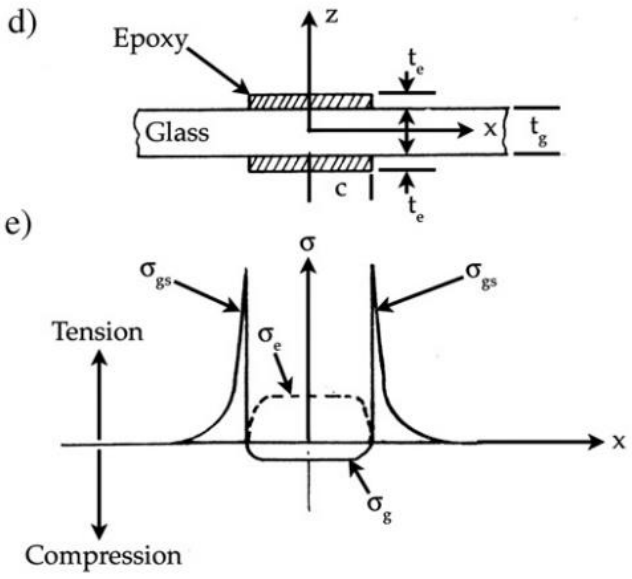

Figure 2.10 Geometrical dimensions (A) and stress profile (B) (Valenza et al. 2007)

Similarly, according to Valenza et al., cracking in the concrete surface formed in the ice layer can also lead to scaling. Glue-spalling occurs when two conditions are met: (a) a crack forms in the ice

layer, and (b) the tensile strength of the ice layer is high enough to induce stress on the concrete surface, promoting crack development in the concrete surface. The authors conclude that the tensile strength of concrete is the main factor affecting F-T scaling resistance in this case. The main deficiency of this model is that it is based on the assumption that the existence of strong bonding between the ice layer and the concrete surface. Otherwise, cracks cannot penetrate the substrate. Additionally, scaling typically consists of small flakes of paste and sand grains, whereas this theory suggests that scaling should be granular and much larger than the flakes due to the specific distance at which cracks occur in ice or brine layers.

2.5.5 Nanofluidic salt trapping

A recent study by Zhou et al. proposed a mechanism for freezing-thawing damage in concrete known as "nanofluidic salt trapping," which involves mathematical models of dissolved ions that are confined between the growing ice and charged pore surfaces (Zhou et al. 2020). In an open pore, water and ions can move freely without causing any pressure (Figure 2.11 (a)). When freezing begins, ions become excluded from the advancing ice, leading to an increase in salt concentration in the surrounding confined liquid electrolyte. The bottleneck between ice crystals and long, tortuous pore pathways results in the trapping of many ions, causing a dramatic increase in salt concentration inside the trapped freezing zone (Figure 2.11 (b)). The formation of ice in closed pores creates a large disjoining pressure that expels ions from the nucleus until surface ions are condensed or solid salt precipitates. This pressure is transmitted to the solid matrix, leading to surface cracking and spalling. However, this model is unable to explain the relationship between the concentration of the salt solution and the degree of freeze-thaw damage, as well as the benefits of the air-entraining agent.

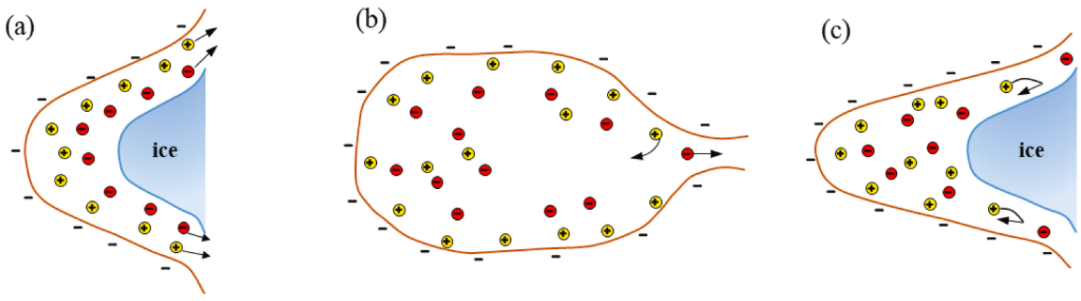

Figure 2.11 Schematic pictures of nanofluidic salt trapping. (a) open pore (b) bottleneck pore (c) confined freezing

2.6 Properties affecting the salt frost scaling resistance

To evaluate the salt scaling resistance of concrete, it is crucial to understand the principal contributing factors. Environmental conditions, such as the concentration of deicing salt solution, lowest temperature, and cooling rate, can significantly impact salt scaling. However, although the outer environmental factors are important for a better understanding of the mechanism of salt scaling, they are not in the scope of this section as they are usually unrealistic to be controlled in the field. Consequently, this section will primarily focus on concrete properties. The properties of concrete that affect salt scaling resistance can be categorized into three groups: material properties, mixture characteristics, and hardened properties.

2.6.1 Material properties

- Portland cement

The cement bears the brunt when exposed to the freeze-thaw cycles. The type of Portland cement obviously is a key factor in producing durable concrete. The use of finer cement has been shown to increase scaling resistance by reducing the average size of capillary pores (Marchand et al. 1994). It has also been hypothesized that the faster hydration rates of finer cement reduce the chance of damage due to plastic shrinkage, although this has not been systematically verified. The cement composition also plays a major role in the scaling resistance. Fagerlund suggested that the use of low alkali/low C3A cement increases scaling resistance, as high alkali/high C3A cement can interfere with air entrainment, leading to a coarser air void structure as shown in Figure 2.12 (Fagerlund 1995). Lower cement content has also been linked to better scaling resistance as long as the w/c is low enough and the workability is sufficient (Marchand et al. 1994). This is because a higher paste content typically results in higher concrete porosity.

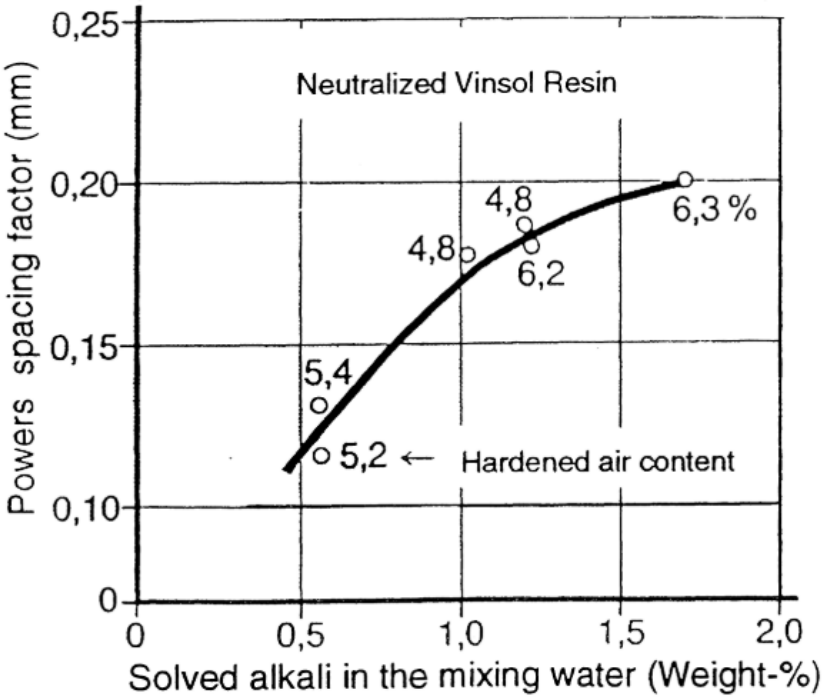

Figure 2.12 Relationship between spacing factor and alkali content in the mixing water

- Supplementary Cementitious material

Silica fume (SF) is a by-product of silicon material or ferrosilicon alloys. It is known to increase the early strength by providing nucleation sites for hydration products and leads to grain refinement which in turn reduces porosity (Scrivener et al. 2004). Additionally, it increases the fracture toughness of the interfacial transition zone (ITZ) (Detwiler et al. 1989). Despite the benefits of silica fume, its impact on salt frost scaling resistance is still controversial. Some studies have shown that silica fume can strengthen resistance by reducing the permeability of concrete, refining capillary pores, and improving concrete with a higher w/c (>0.40) and non-air-entrained concrete (Aitcin et al. 1986). However, when the w/c is less than 0.35, the benefits of silica fume are marginal (Sorensen 1983, Sellevold et al. 1991). On the other hand, some studies have suggested that the use of silica fume can undermine the scaling resistance of concrete. For example, Figure 2.13 shows that the development of scaling in concrete with SF accelerates after a few F-T cycles, possibly due to rapid water uptake in the air void structure (Fagerlund 1995). The critical degree of saturation is achieved after a shorter period. However, it should be noted that the content of SF in Figure 2.13 is unacceptably high. The replacement level of SF should not exceed 10% (usually less than 5%) due to its high silica content (Neville 1995).

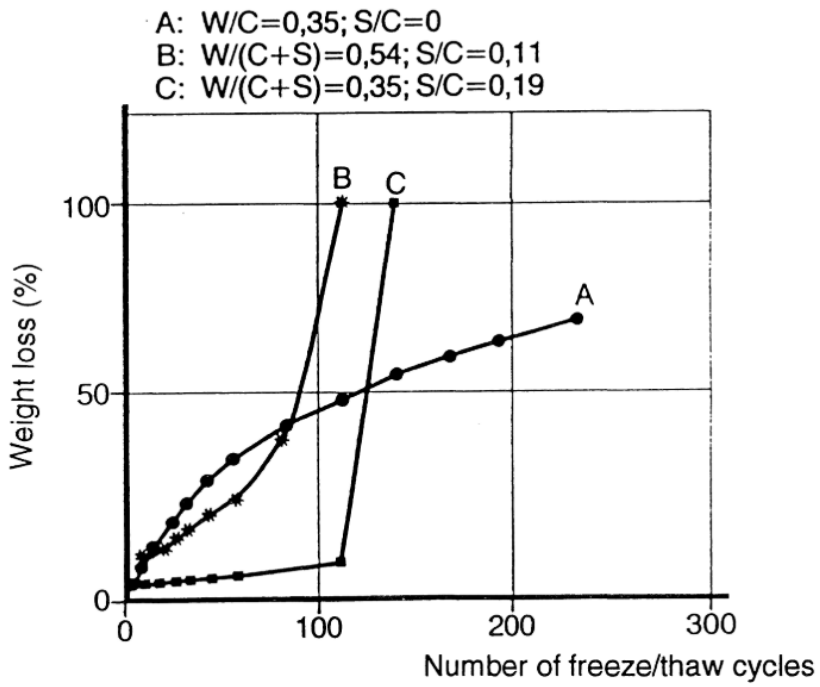

Figure 2.13 Salt scaling development of concrete with and without silica fume (S = silica fume; C = Portland cement; W = water)

Fly ash (FA) is a by-product of the coal-fired power industry and its particle size range is similar to that of Portland cement particles, which are at least two orders of magnitude larger than SF particles. This suggests that it has a slower pozzolanic reaction and requires a longer curing period to achieve its benefits. The moisture uptake of FA concrete can be reduced depending on the curing regimes and the content of FA (Gopalan 1996, Olufemi 2016). However, many studies have reported that the addition of FA diminishes the resistance to salt scaling, probably due to inadequate curing periods and increased brittleness of the cement paste resulting from reduced calcium hydroxide content (Langlois et al. 1989, Whiting 1989, Bilodeau et al. 1992, Talbot et al. 2000). On the other hand, the refinement in the capillary pore structure reduces the amount of freezable water. This is why some studies have shown that FA has improved the scaling resistance, both in the laboratory (Islam 2018) and in the field (Thomas 1997). FA is also found to make the air void content more unstable and unpredictable, which may result in a high spacing factor. This issue can be addressed by increasing the dosage of air-entraining agents (Gebler et al. 1983). Moreover, the reactive silica content in FA is only about 50% compared to 90% in SF. For these reasons, the recommended FA content is not to exceed 30% (Neville 1995).

Blast furnace slag is a waste product during the production of pig iron. When quenched and ground to a fine powder, it is referred to as ground granulated blast furnace slag (GGBFS). The hydroxyls present in the water must break down the glassy structure of GGBFS, leading to slow hydration. Compared to ordinary concrete, GGBFS concrete generally exhibits lower early strength, but longer curing periods can yield a denser microstructure and stronger concrete. An increasing percentage of GGBFS may reduce water absorption due to the blocking of capillary pores resulting from the chemical reaction between the salt solution and the cementitious material (Cheng et al. 2005, Panesar et al. 2009). Research on the effect of GGBFS on salt scaling resistance has yielded conflicting results. Some studies report reduced salt-frost resistance of concrete with increasing GGBFS content, particularly for larger additions (Panesar et al. 2007, Tavasoli et al. 2018, Correia et al. 2020). However, some field observations and laboratory tests conducted on cored specimens indicate that GGBFS concretes have better salt scaling resistance, as long as the GGBFS does not exceed 50% (Hooton, 2012; Liu et al. 2014). These conflicting results clearly highlight the need for further research to clarify the influence of GGBFS on the deicer salt scaling resistance of concrete.

- Aggregate

It has been demonstrated that aggregate does not play a significant role in determining scaling resistance. Sound aggregate particles are usually able to withstand freezing without sustaining damage. Nonetheless, low-porosity aggregate is suggested to be used concerning that water expelled from high-porosity aggregate may cause disruptive pressure at the interfacial transition zone (ITZ) (Marchand et al. 1994). However, some studies have also found that the use of low-weight, highly porous aggregate does not significantly impact the scaling resistance of low w/c ratio concrete (Jones et al. 2015). In fact, the internal water reservoirs of such aggregates may facilitate the hydration process, resulting in denser surface layers.

2.6.2 Mixture characteristics

- Water-to-cementitious ratio

The water-cementitious ratio (w/cm) is a fundamental and critical property of concrete that determines its porosity, affecting almost all mechanical properties and durability.

The relationship between permeability and capillary pore space is illustrated in Figure 2.14 (Powers et al. 1954), which demonstrates that as capillary pore space increases, permeability also increases rapidly. This means that an increase in micropore porosity promotes the growth of ice bodies. As the w/c increases, capillary porosity also increases, leading to an increase in moisture absorption, which is directly proportional to the number of ice bodies present during freezing.

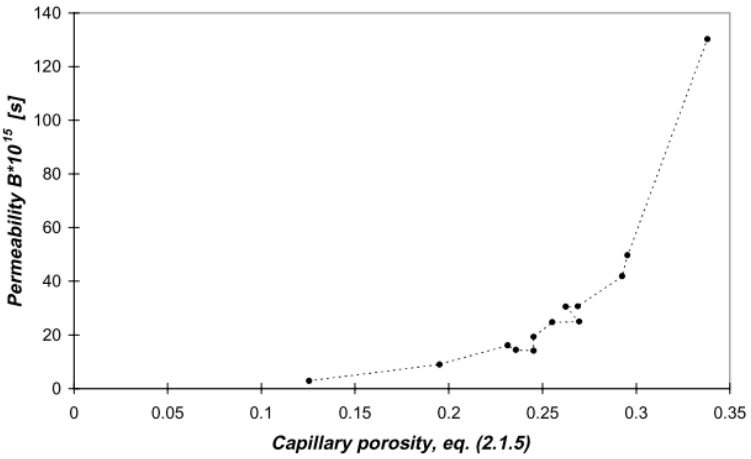

Figure 2.14 Water permeability vs. capillary porosity of cement paste. w/c ratios 0.46- 0.71, $\alpha \approx 0.93$ (Powers et al. 1954)

Most field and laboratory studies have shown that decreasing the w/cm increases the scaling resistance of concrete (Hammer et al. 1990, Rose et al. 1989, Sakai et al. 1995, Lindmark 1998). For Portland cement without SCM, some studies have proposed a critical value of 0.3 for the w/cm, below which air entrainment is unnecessary for protection against salt-frost attack (Gagné et al. 1990, Sakai et al. 1995). This is because the dense nature of the paste and aggregate-paste interfaces reduces the amount of freezable water in the concrete, preventing the degree of saturation required for damage to occur. It is recommended that a maximum w/cm of 0.45 should be used to ensure adequate scaling resistance, as permeability increases rapidly above this threshold (ACI committee 201 2016, American Concrete Pavement Association 1996).

- Curing regimes

Concrete curing is an important process that involves maintaining proper moisture levels and temperature to promote cement hydration in the early stages. Proper curing is essential for achieving adequate workability and durability of concrete, particularly in the surface layers (Fagerlund 1986, Langlois et al. 1989). The duration of curing is dependent on various factors such

as the composition and properties of the concrete mix, including the w/cm and the presence of SCMs. Longer curing periods can decrease the sorptivity of the concrete and improve its scaling resistance, as demonstrated by the decrease in permeability of the cement paste (Bai et al. 2002, Tasdemir 2003). Gagné et al found that extending the curing period from 14 to 28 days improves the scaling resistance of the reference concrete (Gagné et al. 2011). Ho et al. found an increase in the quality of concrete based on their sorptivity results after they increased the initial water curing period from 1 to 7 days (Ho et al. 1989). Hewlett et al showed that the surface absorption is decreased as the water curing period extends for concrete with different w/cm (Figure 2.15) (Dhir et al. 1987). In addition to the curing duration, the type of curing can also affect scaling resistance, with some studies indicating that membrane-forming curing compounds may be more effective than water curing (Delegrave et al. 1997, Radlinski et al. 2008), although the reasons for this are not yet fully understood.

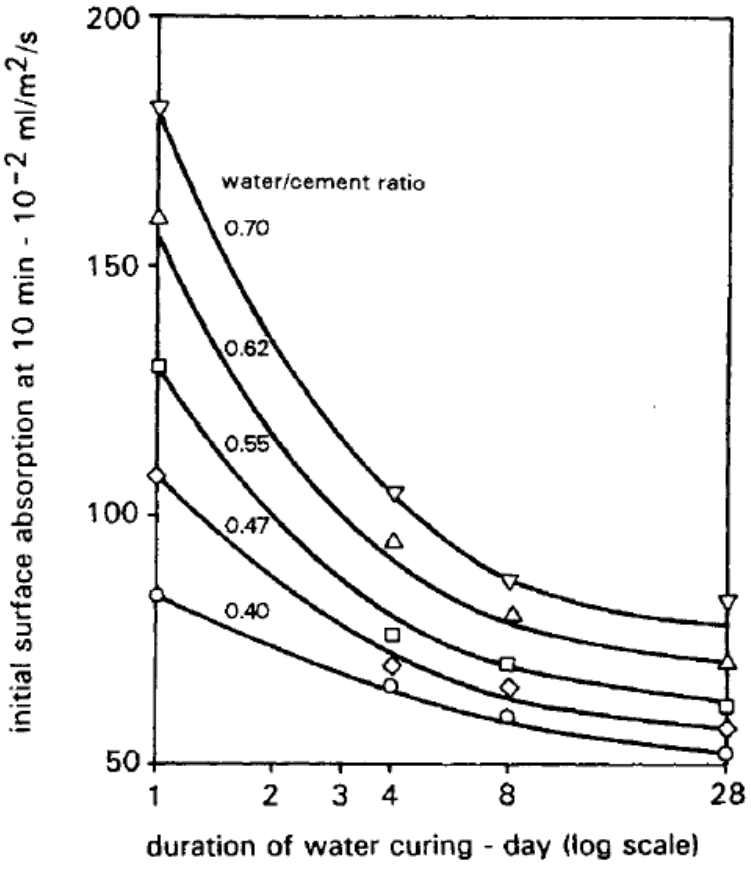

Figure 2.15 Influence of curing conditions on concrete water absorption (Dhir et al. 1987)

2.6.3 Hardened Properties

- Air void system

To prevent salt frost scaling in concrete, it is necessary to prevent the formation of internal ice and pressure buildup on the pore walls. This is where air voids come into play, serving as a protective shelter for the concrete. For durable concrete, it is essential to have uniformly distributed, fine-sized air voids that are close together throughout the paste (Whiting et al. 1983). During freezing, water can transfer to nearby air voids and have extra space to accommodate the volume change associated with icing. However, once all air voids are filled with water, they cannot provide further protection against frost damage. It is important to note that the air content should not be too high as it may compromise the compressive strength of the concrete. More details about the air void system will be discussed in Chapter 6.

- Water transport property

One prerequisite for F-T damage to develop is sufficient water uptake, as dry concrete specimens or concrete that has not reached the critical saturation level are usually free from F-T attacks, as discussed earlier in this chapter. Higher permeability and greater connectivity of the capillary network can lead to higher saturation and more severe damage, and therefore, water transport-related properties can be a good indicator of freeze-thaw scaling resistance. More details about the water transport property will be discussed in Chapter 6 as well.

2.7 Summary

This chapter presents an overview of the fundamental characteristics of the moisture transport properties in concrete. Capillary suction is the dominant property due to the nature of moisture conditions in concrete in the field. Additionally, water flow in concrete during freezing due to potential differences is discussed, followed by a discussion of common phenomena observed in scaling and hypotheses put forth in recent decades. However, no single mechanism can explain salt frost scaling due to complexity of the issue. Some key factors such as w/cm and SCMs that are related to scaling resistance are summarized.

Chapter 3. Experimental Program

3.1 General

In this Chapter, the properties of raw materials, the mix design, and the testing procedures employed in this thesis work are discussed. An extensive experimental program has been undertaken, including surface scaling test, internal cracking test, moisture uptake test, air void analysis, and rapid chloride permeability test.

3.2 Materials

Table 3.1 shows the chemical analysis of the two fly ashes used in this study, as well as the low-alkali Portland cement and grade 100 slag cement. The silica fume used in the experiment was obtained from another state, and its chemical analysis is not available.

For all mixes, 2NS sand from Martin Aggregate was selected with a fineness modulus of 2.74, an absorption capacity of 0.92%, and specific gravity (oven dry) of 2.66. For mixes with silica fume, 26A coarse aggregate (CA) from Ottawa lake with an absorption capacity of 1.98%, and a specific gravity of 2.66 was employed, while 6AA coarse aggregate from Port Inland that had an absorption capacity of 1.19%, and a specific gravity of 2.56 was used for other mixes. The lightweight fine aggregate (Haydite, LWA) was obtained from MDOT's Brighton storage yard with an absorption capacity of 21.5% with a specific gravity of 1.5.

3.3 Mix characteristics and specimen preparation

Air-entrained concrete mixes were prepared with a w/cm ranging from 0.35 to 0.45. The replacement level with GGBFS and fly ash was set at 30%, while that with silica fume ranged from 4 to 8%. One mix consisted of a 0.45 w/cm ternary blend containing 25% GGBFS and 6% silica fume. The air-entraining agent dosage rate was determined to achieve a target air content of 6.5%. The target slump was between 75 to 100 mm, with a superplasticizer dosage of 4.0 ml/kg cementitious material. Cylindrical specimens (100 mm in diameter and 200 mm in height) and concrete beams (100 mm × 100 mm × 400 mm) were cast in the laboratory following ASTM C 192 (2014). All the specimens were removed from the mold after one day and submerged in tap

water at 20℃ until testing. The mix design is listed in Table 3.2, with further information given in the corresponding chapters.

Table 3.1 Chemical analysis for cement and supplementary cementitious material

Compound	Formula	Cement	GGBFS	Class C fly ash	Class F fly ash
Silicon Dioxide	SiO_2	19.78	37.69	31.12	49.63
Aluminum Oxide	Al_2O_3	4.42	8.43	16.84	16.17
Iron Oxide	Fe_2O_3	3.06	0.53	5.37	5.85
Calcium Oxide	CaO	63.33	37.75	29.66	14.76
Magnesium Oxide	Mgo	2.26	11.94	7.86	4.77
Sodium Oxide	Na_2O	0.2	0.3	2.22	3.64
Potassium Oxide	K_2O	0.47	0.48	0.46	2.2
Titanium Oxide	TiO_2	0.29	-	1.36	0.64
Manganic Oxide	Mn_2O_3	0.11	0.43	0.02	0.04
Phosphorous Pentoxide	P_2O_5	0.13	0	1.27	0.34
Strontium Oxide	SrO	0.06	0.06	0.37	0.3
Barium Oxide	Bao	0.06	0.06	0.73	0.63
Sulfur Trioxide	SO_3	2.56	2.49	2.2	0.85
Tricalcium Silicate	C_3S	66.11	-	-	-
Dicalcium Silicate	C_2S	6.83	-	-	-
Tricalcium Aluminate	C_3A	6.53	-	-	-
Tetracalcium Aluminoferrite	C_4AF	9.33	-	-	-

3.4 Test procedures

3.4.1 Air void analysis

The air-void system in hardened concrete was evaluated using both point count procedures and the linear traverse method, as per ASTM C457 (2012). To perform this assessment, an air void analyzer (shown in Figure 3.1) was utilized. Square specimens with dimensions of 100 mm (length) × 100 mm (width) × 20 mm (thickness) were cut from the beam for this purpose (Figure 3.2 (b)).

To obtain a smooth surface, specimens were first polished using silicon carbide abrasives (Figure 3.3 (a)). The point count procedure involved determining the volume fractions of air voids, paste, and aggregate on the polished surface by recording the number of stops over each phase under the

crosshair of a microscope (as shown in Figure 3.2 (d)). The same scanned surface was used for the linear traverse test (Figure 3.2 (c)). Prior to the start of the linear traverse test, the surface was coated with barium sulfate to fill all the air voids, and the remainder of the surface was painted black to create a sharp contrast between the air voids and the concrete matrix (Figure 3.3 (b)). The automatic image analysis was used to scan this area and the air void characteristics report could be automatically generated.

Table 3.2 Mix design of concrete systems

Batch ID	Mix proportion (kg/m^3)							
	Water	CA	Sand	LWA	Cement	GGBFS	SF	FA
035-30%GGBFS	137	1068	693	0	273	117	0	0
035-30%GGBFS-10%LWA	137	1068	623	47	273	117	0	0
035-30%GGBFS-25%LWA	137	1068	519	118	273	117	0	0
035-30%GGBFS-40%LWA	137	1068	416	188	273	117	0	0
037-8%SF	156	922	820	0	391	0	31	0
039-4%SF	156	922	826	0	391	0	16	0
040-30%GGBFS	156	1068	640	0	273	117	0	0
040-30%GGBFS-25%LWA	156	1068	480	109	273	117	0	0
040-30%GGBFS-40% LWA	156	1068	384	174	273	117	0	0
040-8%SF-18%LWA	156	922	616	138	359	0	31	0
040-4%SF-18%LWA	156	922	619	138	375	0	16	0
040-Control	156	910	842	0	390	0	0	0
040-30%Fly ash Class C	134	1054	741	0	234	0	0	100
040-30%Fly ash Class F	134	1054	741	0	234	0	0	100
045-30%GGBFS	150	1112	655	0	234	100	0	0
045-6%SF-25%GGBFS	160	910	849	356	245	89	21	0

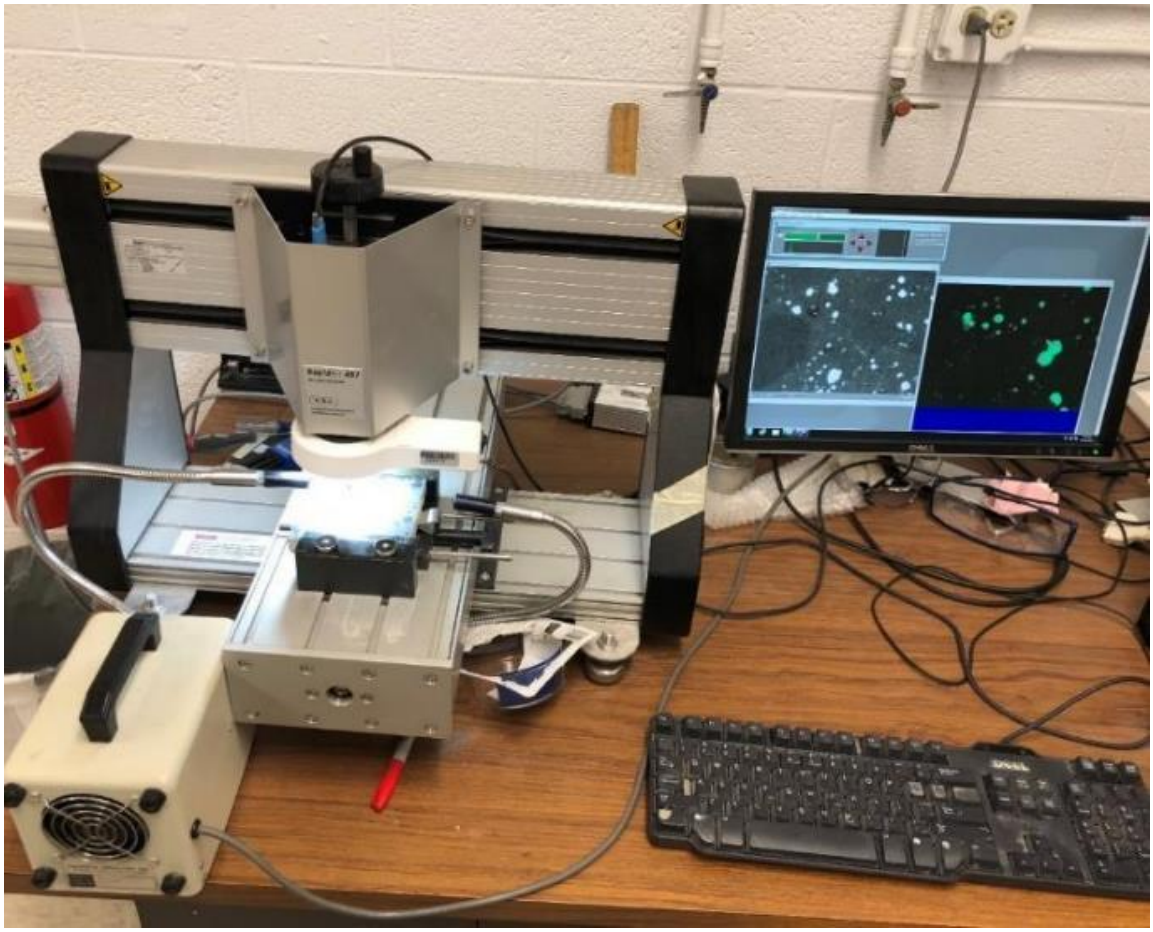

Figure 3.1 Air void analyzer

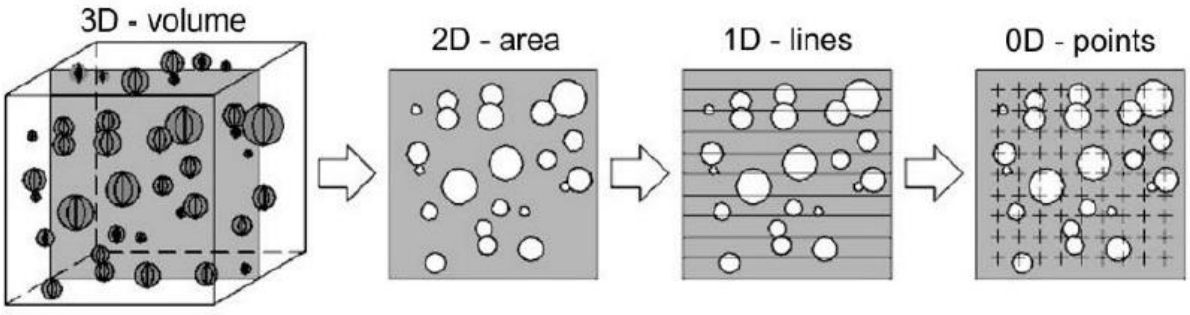

(a) (b) (c) (d)

Figure 3.2 Schematic plot for air void analysis (a) concrete cubes (b) surface for image analysis (c) ASTM C 457 linear traverse method (d) ASTM C 457 point count method

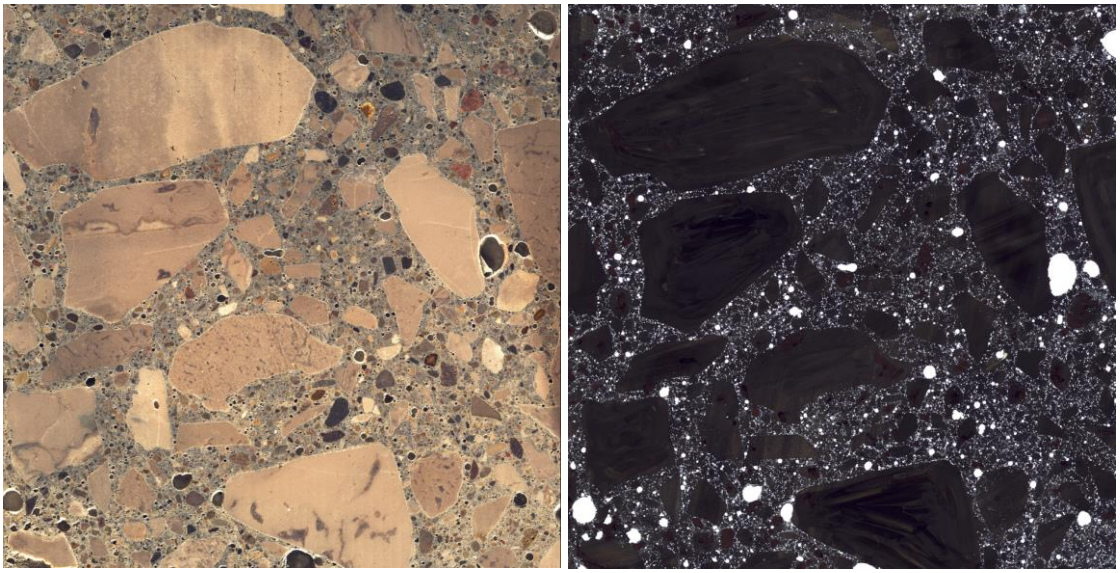

(a) (b)

Figure 3.3 Concrete samples for image analysis (a) before coating (b) after coating

3.4.2 Sorption test, surface scaling, and internal cracking test

After being water cured, 100mm (length) ×100mm (width) ×70mm (height) duplicate specimens were prepared for each batch mix cutting from casted beams using a diamond blade sawing machine. The RILEM CIF method was employed for conducting the freeze-thaw test, which involves three stages according to RILEM: drying process, capillary suction (pre-saturation), and freeze-thaw test (Setzer et al. 1995, 2004).

Specimens prepared for freeze-thaw testing were dried in an oven at 50°C for about two weeks until a constant weight was reached. The mass of specimens was monitored throughout the drying process to ensure the moisture condition of the specimens was well-defined before the F-T test. This was crucial for evaluating the salt frost scaling results in a laboratory test procedure.

After the specimens were dried, they were cooled down to room temperature and then the lateral surfaces of the specimens were wrapped in aluminum foil with butyl rubber. The mass before and after wrapping was recorded. A one-week saturation test was commenced in deionized water and the weight gain was monitored at regular intervals. This period is critical for the filling of capillary pores and the distribution of moisture into unconnected pores or entrained air voids.

Bulk moisture uptake Q in concrete was calculated from the weight measurement of the specimen

$$Q_t(mm^3/mm^2) = \frac{W_t - W_0}{\rho A_c} * 10, \quad \text{Eq. 3.1}$$

where ρ is the density of the test liquid, in g/cm^3, A_c (cm^2) is the effective area of the concrete test surface. W_t is the mass of the specimens during saturation at time t, in g. W_0 is the mass of the specimens before the start of saturation, after wrapping, in g.

Prepared specimens were transferred to a salt frost test machine as shown in Figure 3.4 (a) and placed in a steel container (Figure 3.4 (b)). The test was conducted at a rate of two cycles per day, using the temperature profile presented in Figure 3.4 (c). The specimens were placed on spacers measuring 5 mm in height (Figure 3.4 (d)) with the bottom surface in contact with test liquid (salt solution or pure water). During the one-hour isothermal period at 20°C, scaled-off materials were collected and dried to a constant weight (Figure 3.4 (e)). The mass loss per unit surface area (g/m^2) was determined by the following formula

$$m_{loss} = \frac{\mu_n}{A_c} \times 10^4, \quad \text{Eq. 3.2}$$

where μ_n (g) is the cumulative dry weight of the scaled-off materials after the nth F-T cycle.

The bulk moisture uptake of each specimen at the nth cycle was calculated as

$$Q_n = \frac{W_n - W_0 + \mu_n}{\rho A_c} * 10, \quad \text{Eq. 3.3}$$

where W_n is the weight of the specimen at the nth cycle.

Internal damage in concrete after the nth F-T cycle was evaluated by the relative dynamic modulus of elasticity (RDM) shown in Figure 3.4 (f). The transit time in the coupling medium t_c is calculated by

$$t_c = \frac{l_c}{v_c}, \quad \text{Eq. 3.4}$$

where t_c is the transit time in the coupling medium, l_c is the transit length, and v_c is the velocity of the ultrasonic signal in the coupling medium. It was usually assumed that v_c is 1490 m/s for water at about 20°C.

The change of relative transit time is determined by the following equation

$$\tau_n = \frac{t_{cs} - t_c}{t_n - t_c}, \qquad \text{Eq. 3.5}$$

where τ_n is the relative transit time of the specimen and has no unit, t_{cs} is the total transit time at the end of pre-saturation and before the F-T test, in ms, and t_n is the total transit time after the nth freeze-thaw cycle, in ms.

The internal damage is indicated by the relative change of dynamic modulus of elasticity $R_{u,n}$ which is determined as

$$R_{u,n} = \tau_n^2. \qquad \text{Eq. 3.6}$$

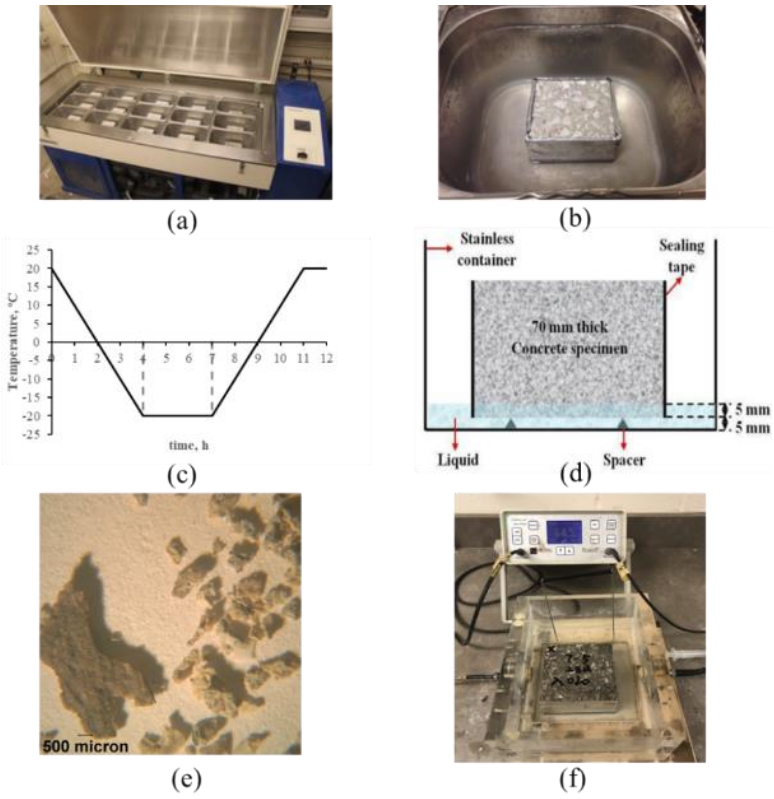

Figure 3.4 F-T test setup

3.4.3 Shrinkage test

Autogenous shrinkage beams were cast in sealed 7.5 by 10 cm steel molds, measuring 84 cm in length. Displacement measurements, accurate to within 0.1 micrometers, were taken every 10 minutes from the time of placement, with the resulting displacement values being converted to strain. A schematic of the autogenous shrinkage test setup is presented in Figure 3.5 which shows the specimen was fixed at one end while an LVDT was attached to the moveable endplate at the

other end. To minimize friction between the specimen and the mold, a flexible membrane covered the bottom and two sides. The laboratory test setup is displayed in Figure 3.6.

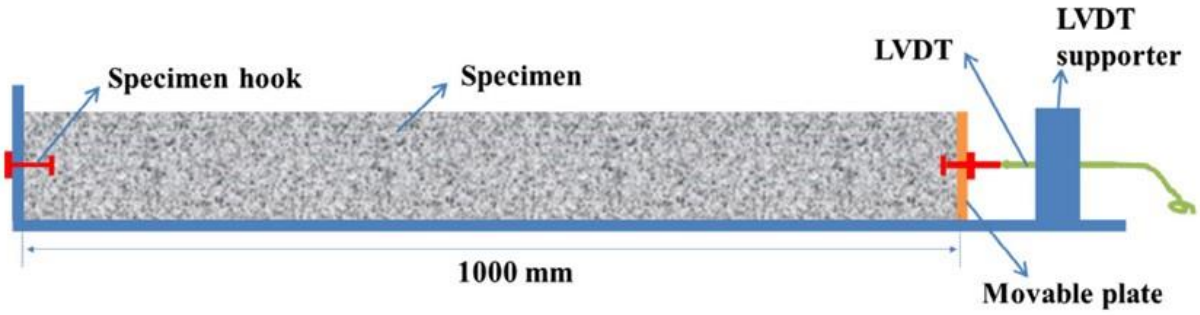

Figure 3.5 Schematic illustration of uniaxial shrinkage test.

Figure 3.6 Shrinkage test setup

3.4.4 Rapid chloride permeability test and resistivity test

The evaluation of chloride ingress resistance in concrete was tested according to ASTM C1202 (2012) and the test setup was displayed in Figure 3.7.

The specimens of 100mm in diameter and 50mm long were positioned in the measuring cell, containing a fluid reservoir at each face of the specimen. One reservoir was filled with sodium chloride (3.0% NaCl) solution, while the other was filled with sodium hydroxide (0.3 N NaOH) solution. The reservoir containing the NaCl was connected to the negative terminal, and the NaOH reservoir was connected to the positive terminal of the device's unit. Once started, the test automatically measured the total electrical current passing through a concrete specimen for a

period of 6 hours at a standard voltage of 60 VDC. The chloride permeability is divided into five categories based on the value of the total charge as shown in Table 3.3.

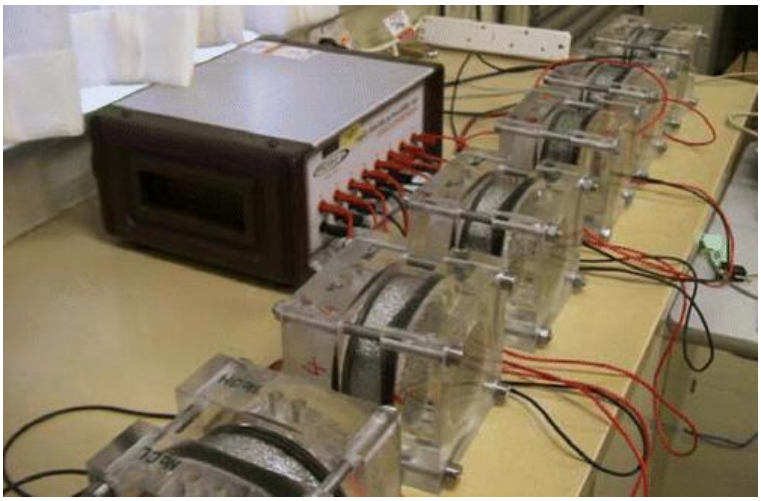

Figure 3.7 RCPT setup

Table 3.3 Chloride permeability rating of concrete

Chloride permeability	Charge (Coulomb)
High	>4000
Moderate	2000-4000
Low	1000-2000
Very low	100-1000
Negligible	<100

It can be seen that the addition of SCM can greatly reduce the chloride permeability of the concrete, especially after 28 days (Figure 3.8). Extending the curing period can also reduce the permeability as all concrete have a low to very low permeability after 90 days.

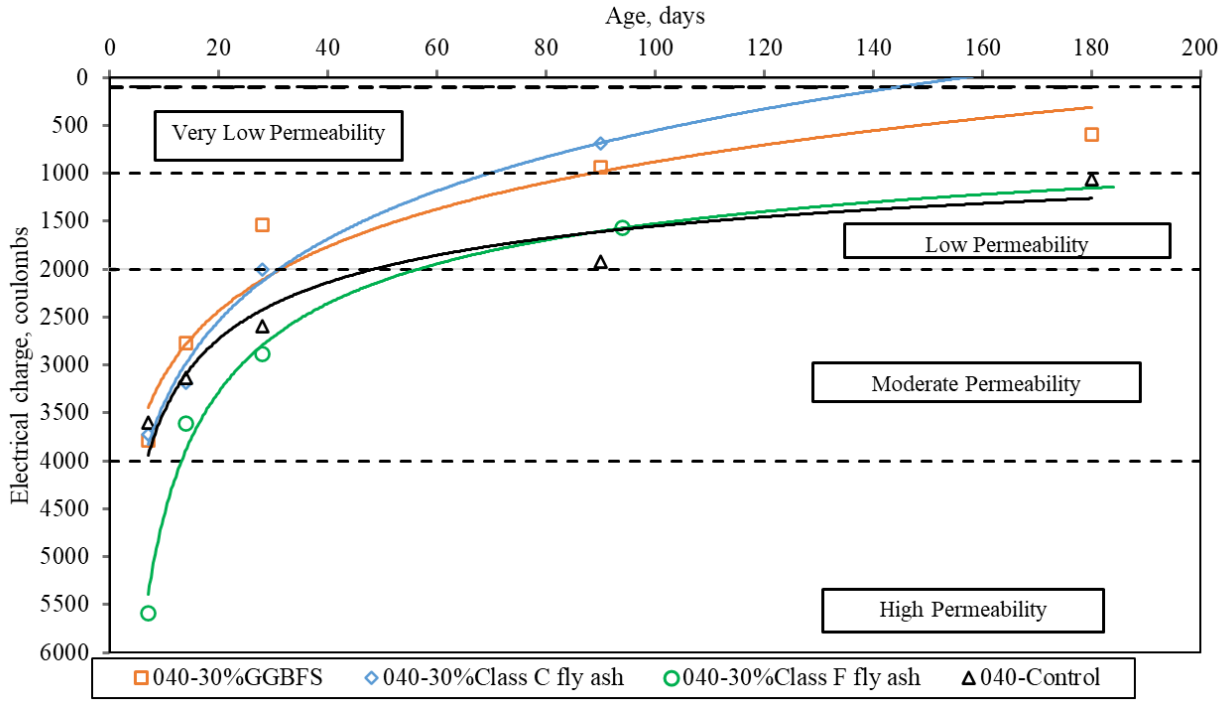

Figure 3.8 Age-related changes in concrete's chloride permeability

Chapter 4. Preliminary Laboratory Studies on High-Performance Concrete

4.1 General

High-Performance Concrete (HPC) in this context is defined as being resistant to freeze-thaw exposure in the presence of deicer salt, while also possessing low shrinkage and low permeability characteristics. HPC is characterized by a low w/c and the use of SCM (Aïtcin 1998). Its superior durability and sustainability have made it increasingly popular for use in infrastructure such as pavements, bridge decks, and off-shore platforms. This chapter focuses on evaluating the behavior of HPC, particularly its F-T performance.

Moisture conditions are critical to the durability of HPC under F-T exposure. Concrete has been found to exhibit additional moisture uptake during F-T cycling beyond capillary suction due to the pumping effect, which can result in an increase in saturation levels and F-T damage. This chapter investigates the behavior of control concrete and HPC with respect to moisture uptake during pre-saturation and F-T cycling. Additionally, an extended cryogenic suction model is discussed that can explain the cause of scaling during F-T cycles as well as the pessimum effect previously mentioned in Chapter 2.

Shrinkage-related cracking is a common issue for HPC. To address this problem, this study investigates the potential benefits of adding pre-soaked lightweight fine aggregate to HPC to improve its crack resistance. The effectiveness of internal curing (IC) is explored, which is based on maintaining high internal pore humidity (>90%) to mitigate self-desiccation and consequent autogenous shrinkage (Wei 2008). Another potential benefit is that the additional water can promote long-term cement hydration (>28 days), resulting in the densification of the pore space and reduced permeability. However, there are some drawbacks to consider, such as an increase in internal pore saturation levels, which may impact frost durability resistance. Laboratory testing is necessary to demonstrate that key durability properties, including long-term low shrinkage (>28 days), low permeability to unsaturated liquid uptake, and frost durability, can be achieved through internal curing.

4.2 Moisture uptake in isothermal conditions and during the F-T stage

This study measures the bulk moisture uptake in both isotherm room temperature conditions and during the F-T cycles. During the pre-saturation stage, all the concrete samples are exposed to deionized water. The moisture uptake of concrete during this stage can be caused by two mechanisms: quick capillary suction and slow diffusion process (Sandström et al., 2012). Figure 4.1 provides a summary of the moisture uptake process, which is divided into three stages. In Stage I, capillary suction is the primary mechanism in moisture uptake which depends on the capillary porosity and pore structure of the hydration products within the cement paste. This process continues for the first several hours. Stage II is a transition process from capillary suction to diffusion, which occurs after most of the connected capillaries are filled with water. After about one day, moisture uptake mainly depends on diffusion into the unconnected pores or entrained air voids and is relatively slow (stage III).

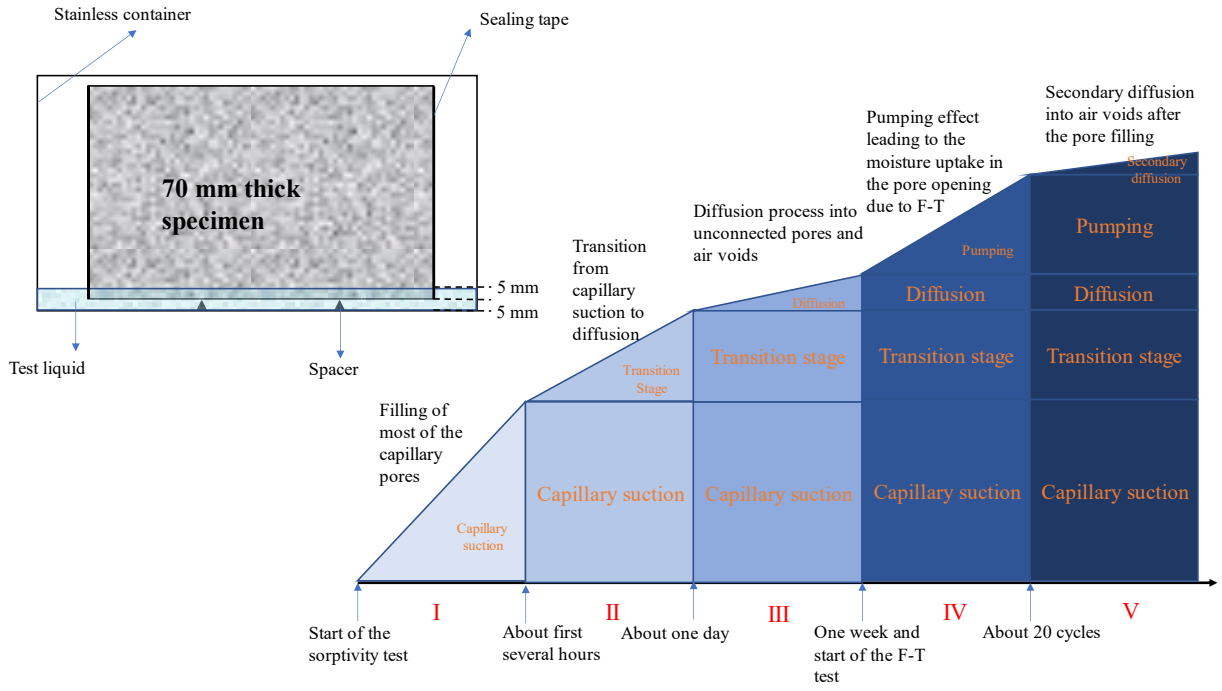

Figure 4.1 Summary of moisture uptake in the entire process

After one week, the specimens with the container are transferred to the F-T test chamber. A prolonged F-T test is adopted in order to observe the complete behavior of concrete with the change in the degree of saturation. Concrete samples have notably accelerated moisture uptake in stage IV. This is caused by the 'pumping effect' and has also been reported by many other researchers

(Jacobsen et al. 1994, Fagerlund 1995, Auberg et al. 1997, Rønning 2001, Setzer 2009, Liu et al. 2018). Jacobsen conducted a thorough review of the pumping effect mechanism (Jacobsen 2002). Previous studies by Powers and our group suggested that during freezing, the external ice surrounding the exposed surface forms first and generates hydraulic pressure that forces the liquid into the unsaturated concrete pores. Upon thawing, the melting of internal ice results in a volumetric contraction and creates suction that draws liquid inside the concrete as shown in Figure 4.2 (Powers et al. 1953, Liu et al. 2018). After most of the pores are filled with water, there is an even slower moisture uptake due to the secondary diffusion into the air voids or other unconnected pores in stage V.

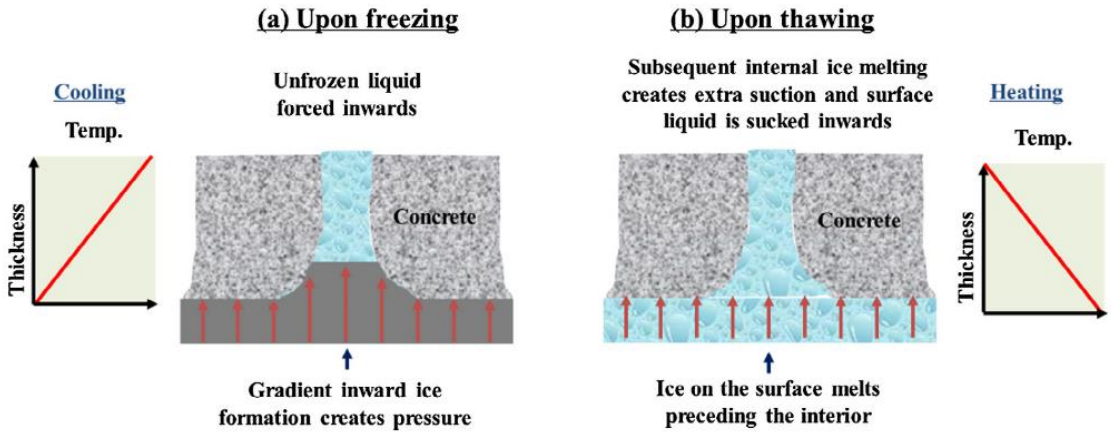

Figure 4.2 A conceptual model for the pumping mechanism associated with the external pressure and internal suction upon freezing and thawing, respectively.

During the F-T stages (IV and V), different test liquids are used to investigate the effect of salt concentration on F-T damage in the concrete systems. Specifically, deionized water, 3%, and 12% salt solutions are selected for this study. Figure 4.3 shows that the salt solution causes additional moisture uptake in the five different systems compared to water exposure, which is consistent with findings from previous studies (Jacobsen et al. 1994, Lindmark 1996, Rønning 1999, Liu et al. 2015a). The concrete samples exposed to the 12% salt solution exhibit the greatest moisture uptake during the F-T cycles, as shown in Figure 4.4. However, the difference in moisture uptake between different test liquid exposure is not significant, with only a 1 to 2 mm variation.

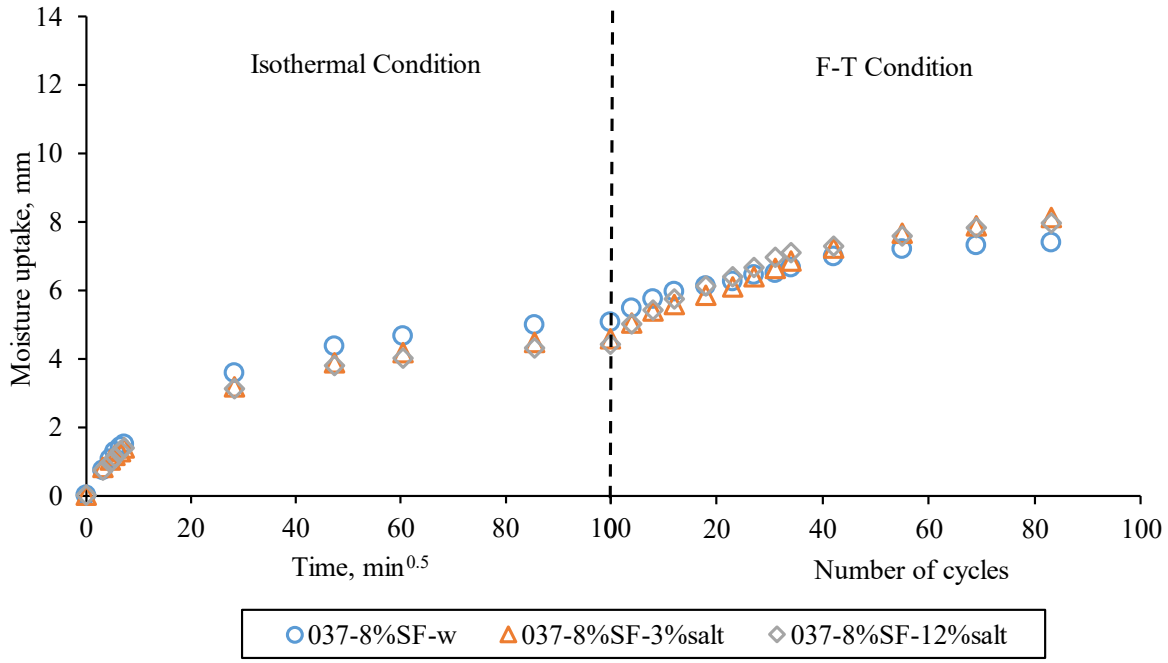
Isothermal Condition
F-T Condition
Moisture uptake, mm
Time, min0.5
Number of cycles
037-8%SF-w
037-8%SF-3%salt
037-8%SF-12%salt

(a)

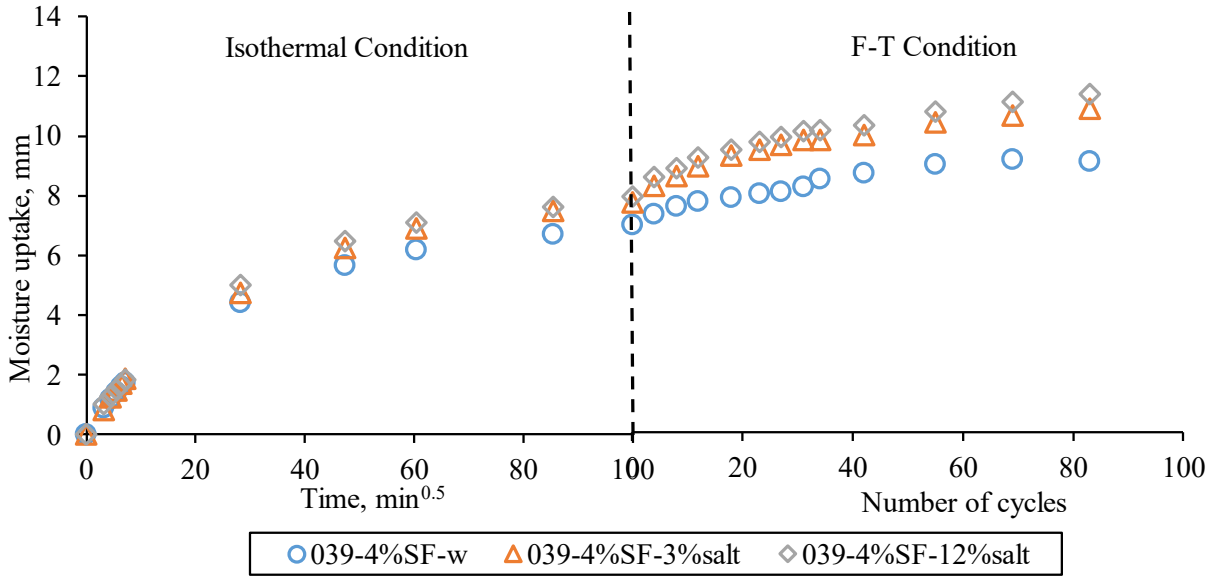
Isothermal Condition
F-T Condition
Moisture uptake, mm
Time, min0.5
Number of cycles
039-4%SF-w
039-4%SF-3%salt
039-4%SF-12%salt

(b)

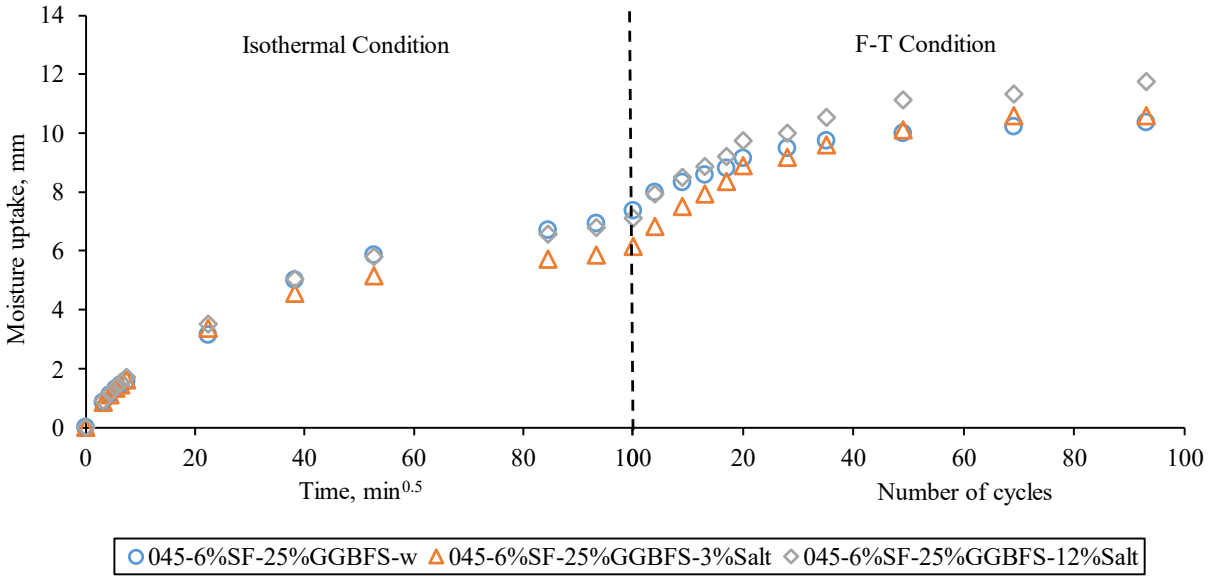
Isothermal Condition
F-T Condition
Moisture uptake, mm
Time, min0.5
Number of cycles
045-6%SF-25%GGBFS-w
045-6%SF-25%GGBFS-3%Salt
045-6%SF-25%GGBFS-12%Salt

(c)

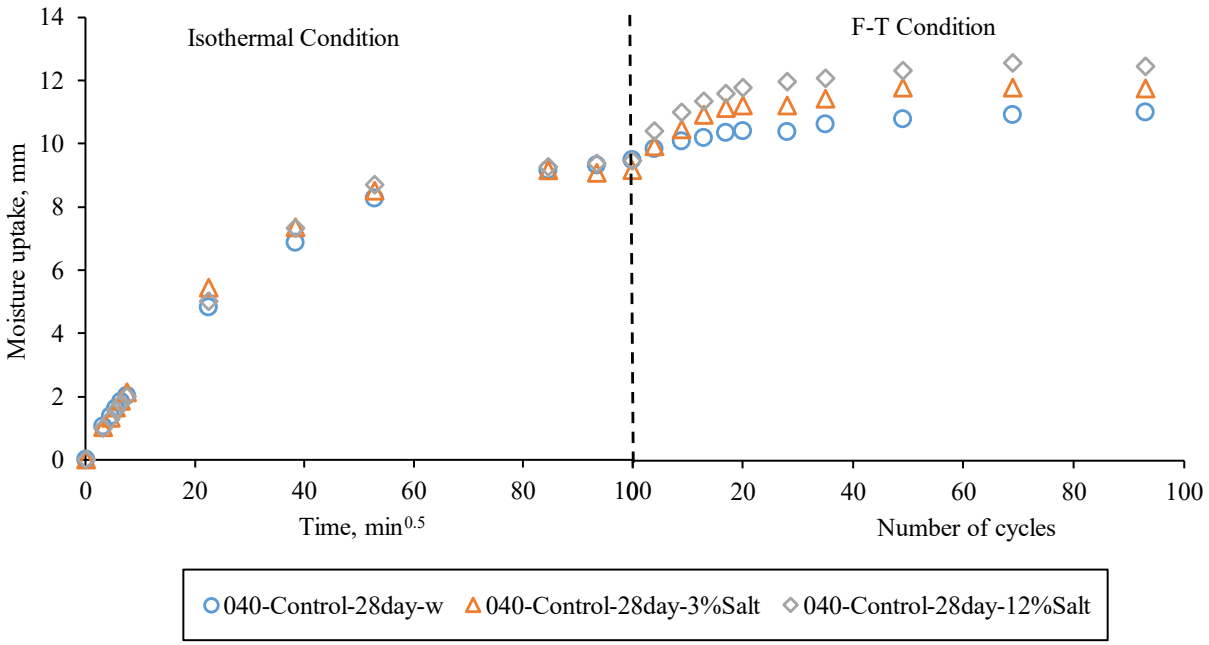
Isothermal Condition
F-T Condition
Moisture uptake, mm
Time, min0.5
Number of cycles
040-Control-28day-w
040-Control-28day-3%Salt
040-Control-28day-12%Salt

(d)

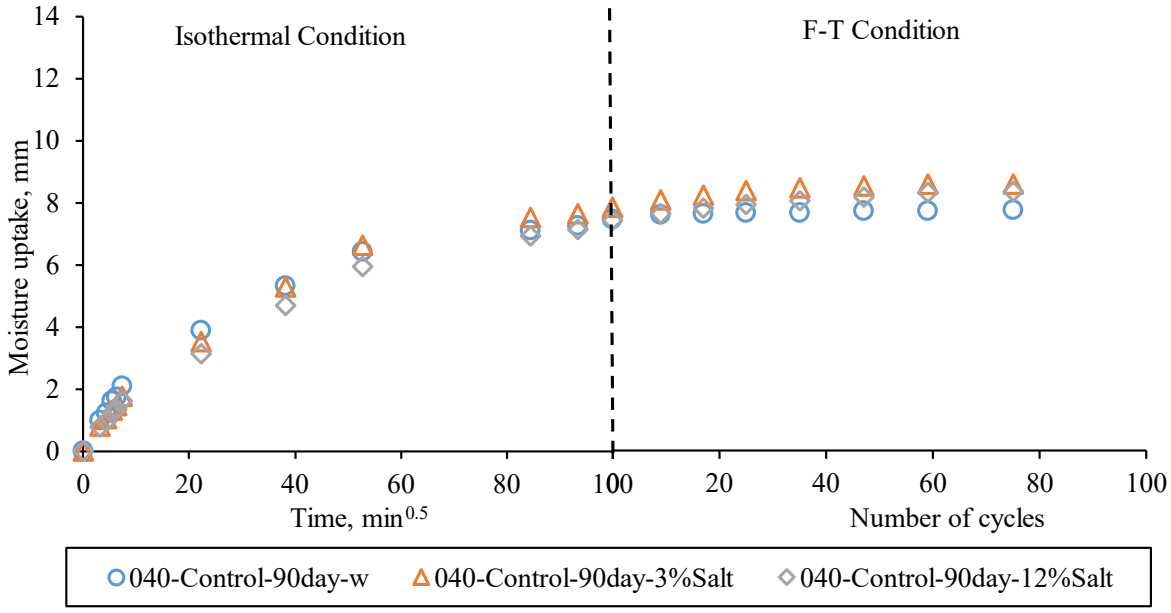

(e)

Figure 4.3 Moisture uptake in isothermal room-temperature conditions exposed to deionized water and during F-T cycles exposed to different test liquids (0, 3%, and 12% salt solution) for systems of (a) 037-8%SF, (b) 039-4%SF, (c) 045-6%SF-25%GGBFS, (d) 040-Control-28day, (e) 040-Control-90day.

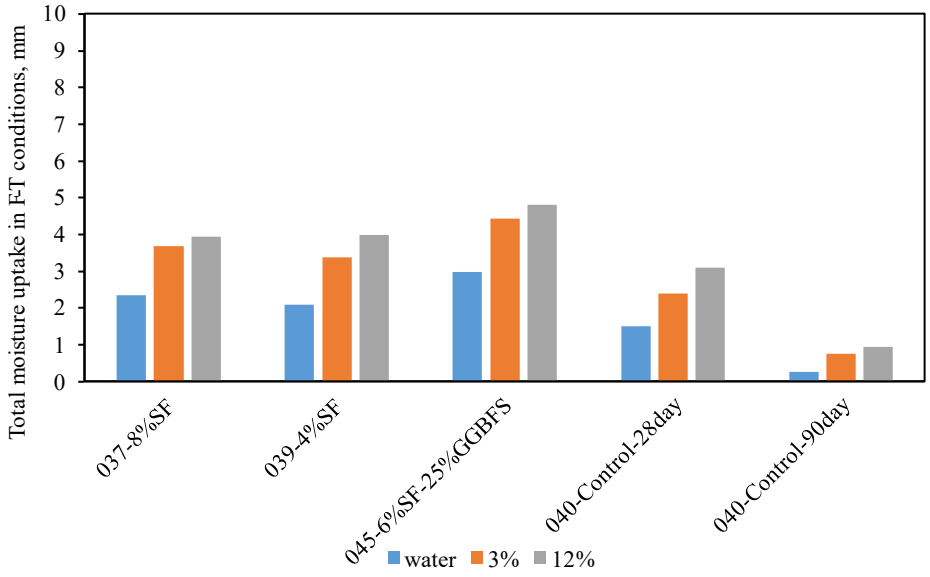

Figure 4.4 Comparison of total moisture uptake during F-T cycles exposed to different test liquids

4.3 Pessimum effect on salt frost scaling

The surface of concrete exposed to 3% develops a severe scaling after about 56 cycles. The scaling of concrete with water exposure is negligible (all below 0.5 kg/m^2) (Figure 4.5). Most of the concrete exposed to 12% has a scaling of less than half of the concrete exposed to 3% which develops the highest scaling. This is in agreement with the other researchers' findings (Verbeck et al. 1957, Sellevold et al. 1991, Lindmark 1998, Marchand et al. 1999, Setzer 2009, Liu 2014), known as the 'pessimum effect'.

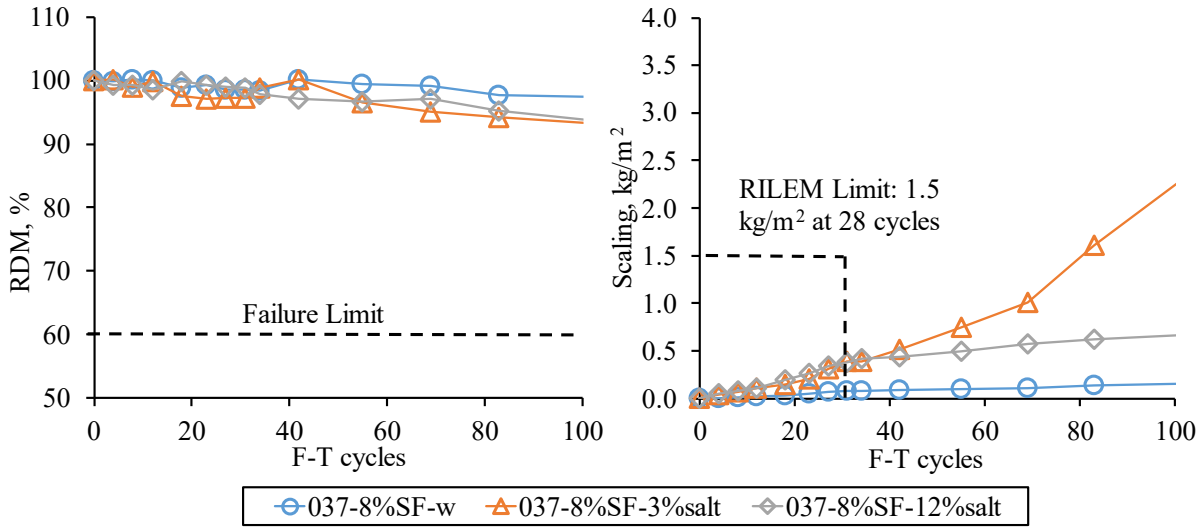

(a)

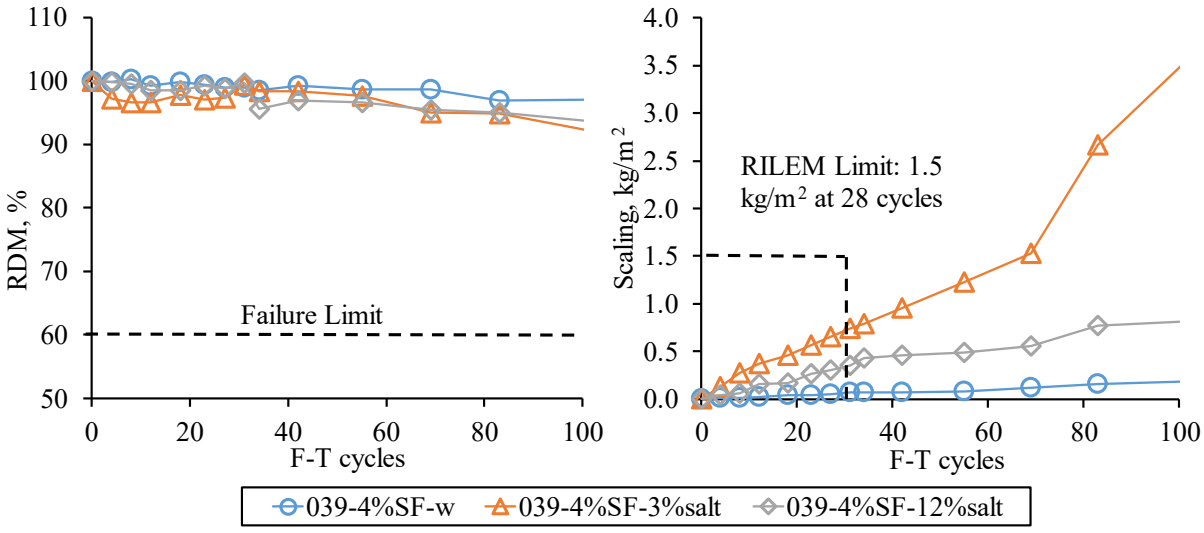

(b)

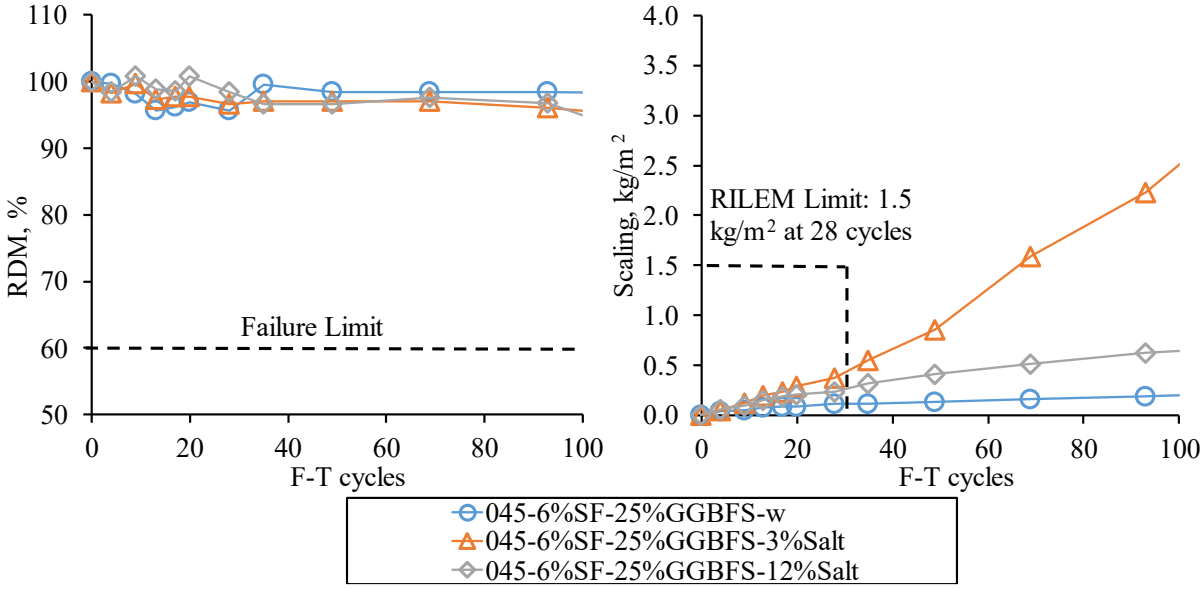
RDM, %
F-T cycles
Failure Limit
Scaling, kg/m 2
RILEM Limit: 1.5
kg/m2 at 28 cycles
045-6%SF-25%GGBFS-w
045-6%SF-25%GGBFS-3%Salt
045-6%SF-25%GGBFS-12%Salt

(c)

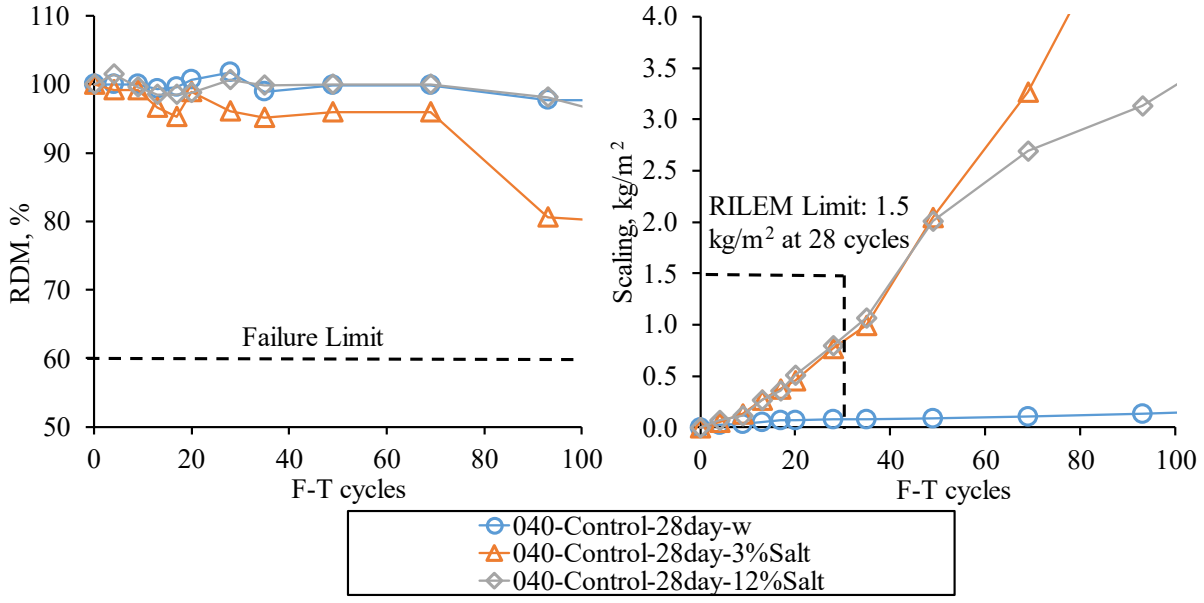
RDM, %
F-T cycles
Failure Limit
Scaling, kg/m 2
RILEM Limit: 1.5
kg/m2 at 28 cycles
040-Control-28day-w
040-Control-28day-3%Salt
040-Control-28day-12%Salt

(d)

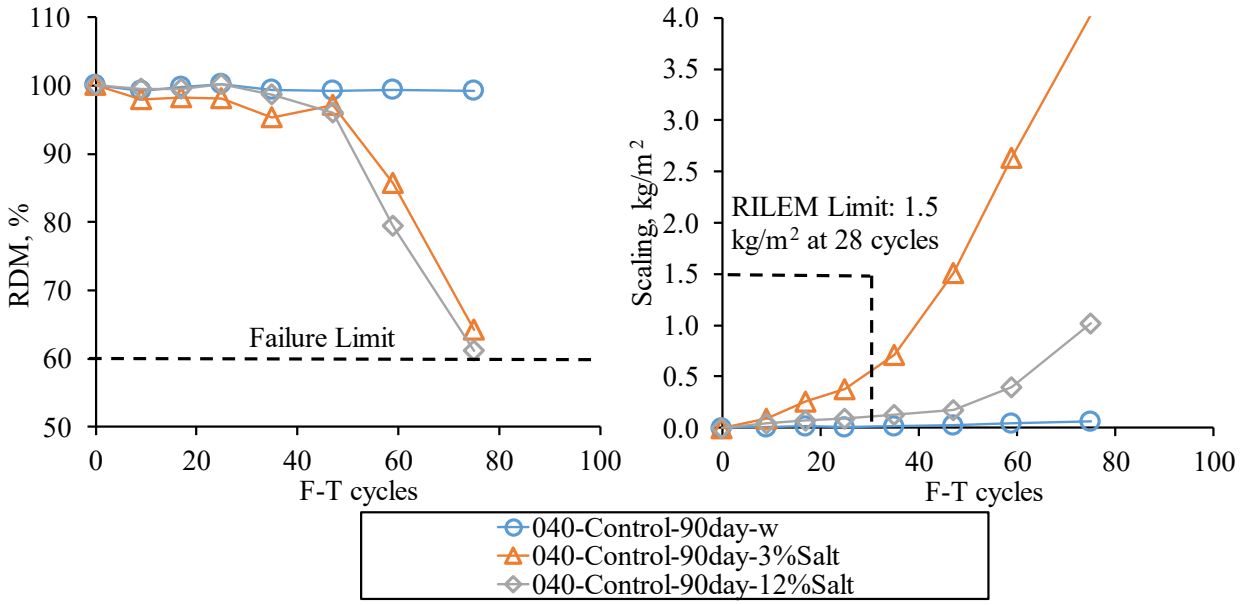

(e)

Figure 4.5 RDM and scaling development for systems of (a) 037-8%SF, (b) 039-4%SF, (c) 045-6%SF-25%GGBFS, (d) 040-Control-28day, (e) 040-Control-90day with exposure to different test liquids (0, 3%, and 12% salt solution)

Photos presented in Figure 4.6 illustrate that the 039-4%SF system with 3% salt solution exposure has much more severe surface damage compared to the water and 12% salt solution exposure. According to the literature review as shown in Figure 4.7 (a), the pessimum salt solution lies in the range between 0.5% and 6%. The salt solution concentration above the range causes much less damage. This is consistent with our laboratory findings in Figure 4.7 (b). The only exception is the 040-Control-28day exposure to 12% salt solution which develops a comparable scaling with 3% salt solution exposure. This may be associated with the poor quality of the air void system which is discussed in Chapter 6.

Figure 4.6 Surface of 039-4%SF exposed to pure water (left), 3% salt solution(middle), and 12% salt solution (right)

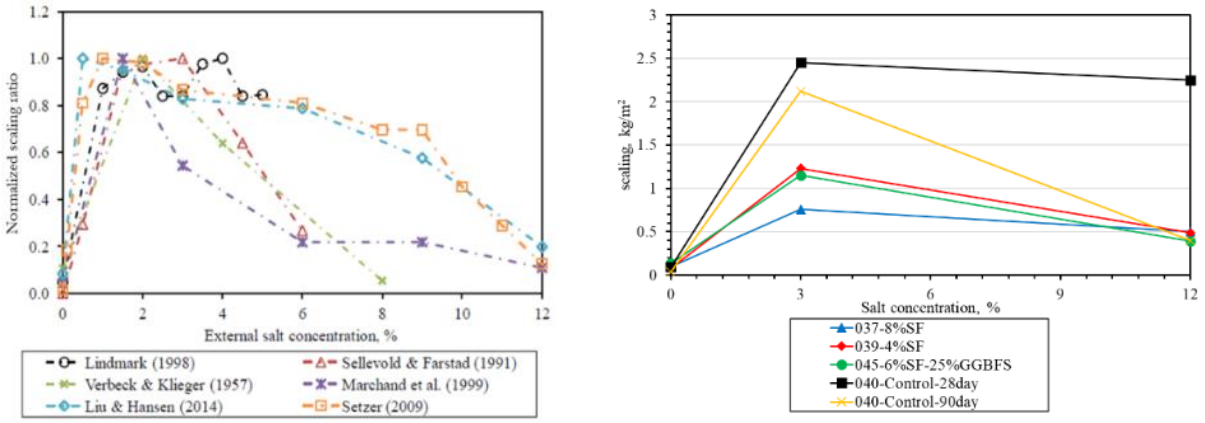

(a) (b)

Figure 4.7 Pessimum effect (a) from literature review (Liu 2014) (b) from this study

4.4 New insights regarding the cryogenic suction mechanism

In a pre-wetted cementitious material subjected to freezing conditions, the growth of ice bodies occurs in the pores or voids of the cementitious matrix once nucleation begins. This phenomenon is associated with the spontaneous movement of unfrozen water in gel pores or very fine capillary pores toward the micro ice bodies until a thermodynamic equilibrium is established between the ice body and the surrounding pore solution (Powers et al. 1953). The driving force behind this moisture flow has been extensively explained in terms of the Gibbs function difference between ice and unfrozen water, which is facilitated by the wide distribution of pore size and the presence of dissolved alkalis (Borgnakke et al. 2012, Liu et al. 2015a).

Concrete may also have access to external liquids, and when the liquid is pure water that freezes completely at temperatures below 0 °C, there is little ice growth in the concrete (Conde et al. 2018) as shown in Figure 4.8 (a). However, when the test liquid is a salt solution, and the temperature is

below freezing point but above the eutectic temperature of the solution, the solution does not freeze completely. Rather, it exists as a mixture of ice and brine channels as shown in Figure 4.8 (b). A microscopic image of brine channels is presented in Figure 4.9.

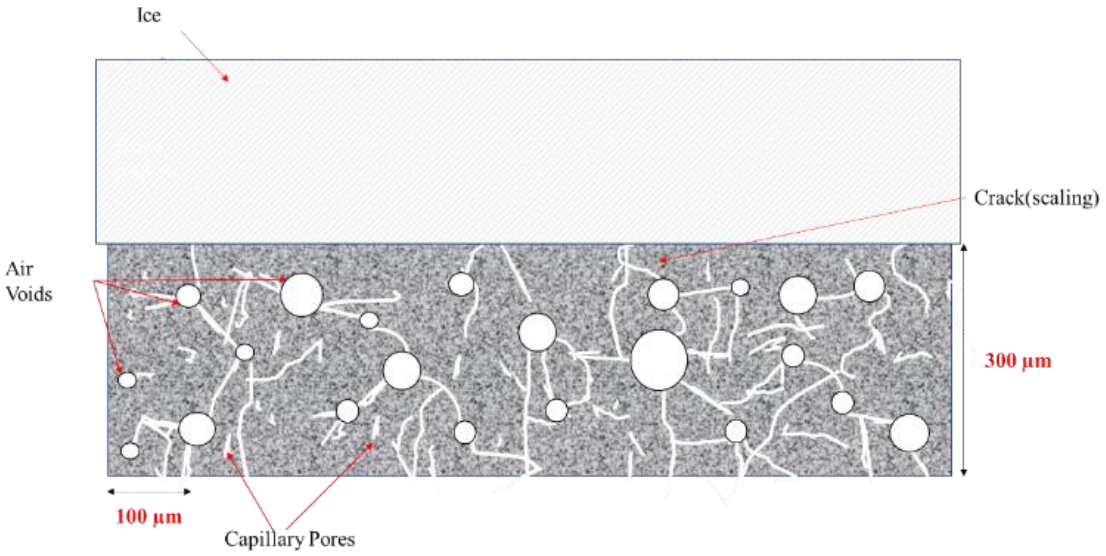

(a)

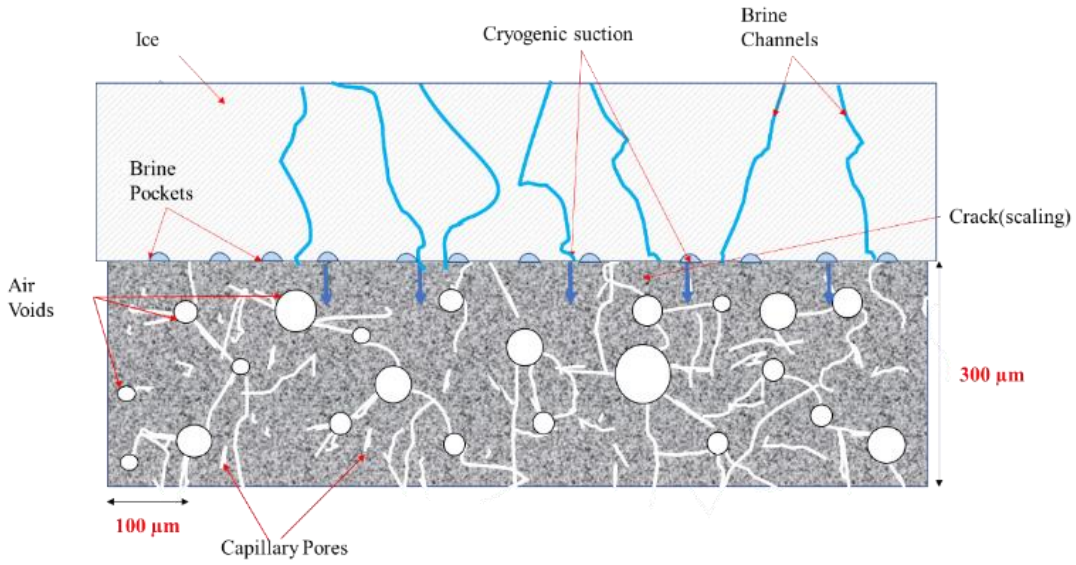

(b)

Figure 4.8 Schematic illustration of cryogenic suction when concrete is exposed to (a) pure water (b) deicing salt solution

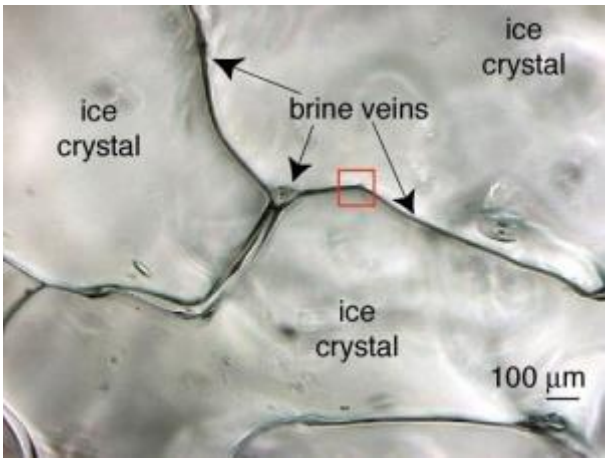

Figure 4.9 In situ microscopic image of ice crystals and brine pockets (Junge et al. 2001)

Cryogenic suction mechanism attributes the salt frost scaling to the continuous growth of ice body under sub-freezing temperature. The formation of ice depletes the nearby pore solution, causing the concrete to take in the outer solution. The ice bodies grow continuously, exerting pressure on the pore walls to a depth that allows moisture to flow with ease (Figure 4.10). This process continues until the concentration in the pore liquid surrounding the ice body reaches equilibrium and becomes sufficiently high (Lindmark 1998). The cryogenic suction theory emphasizes the absorption of concentrated brine that is not frozen at the core. As deicer concentrations increase, scaling should be intensified. However, the reduced impact of high salt concentrations in salt frost scaling tests cannot be completely accounted for by this theory. This suggests that there are additional mechanisms involved in liquid absorption that must be taken into account (Mueller 2022). During thawing, the outer test solution melts before the ice in the concrete can melt, causing the hardened cement paste to expand and the gel pores to strive to regain their pore solution. However, the internal redistribution of moisture is inhibited as the pore solution is still trapped in the frozen capillaries. Instead, the concrete takes up the melted test solution, leading to an intensive saturation that exceeds the uptake by cryogenic suction of brine. The major part of liquid uptake occurs during thawing, and suction by the micro ice lens pump (Setzer 2009) can balance the deicing salt concentration and should account for reduced scaling intensity when test solutions exceed a certain salt concentration. Consequently, the extended cryogenic mechanism provides strong evidence for the pessimum effect.

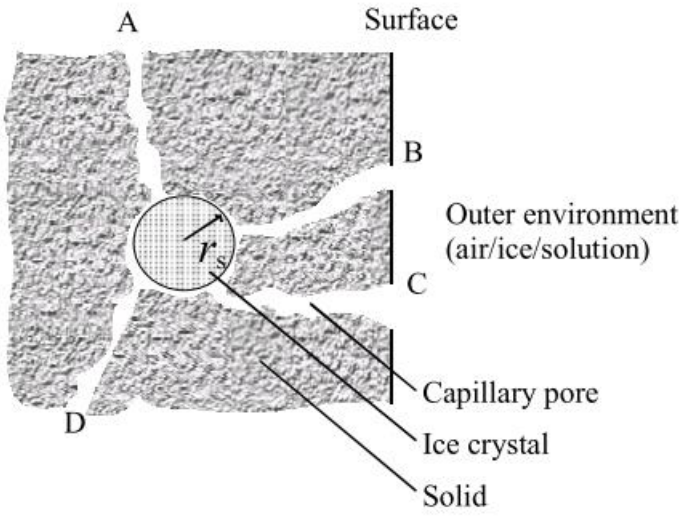

Figure 4.10 Ice body growing close to the surface of a micro-porous material (Lindmark 1998)

This study presents a hypothesis that the pore drying process, which involves the migration of water in gel pores and small capillary pores to the ice front, and ice expansion during freezing, may contribute to an enlargement of capillary size. This enlargement creates channels that link previously unconnected pores, resulting in an increase in pore connectivity as shown in Figure 4.11 (Pigeon et al. 1995). This increased connectivity is expected to allow for more moisture uptake during freeze-thaw cycles and increase the amount of freezable water.

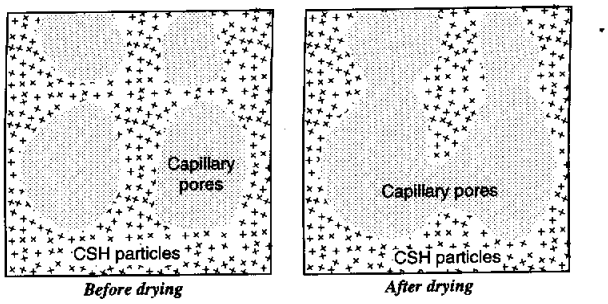

Figure 4.11 Schematic illustration of the influence of drying on the continuity of the capillary pores in hardened cement paste (Pigeon et al. 1995)

To model this phenomenon, three components are considered: a) the initial amount of ice formation in the capillary pores, b) the presence of unfrozen brine transported through the capillary network, and c) the capillary pore system that controls both the rate of capillary suction and the amount of freezable water (Liu et al. 2015a). The unfrozen brine serves as the source of the

cryogenic suction, while ice formation and nucleation act as the initiator. Furthermore, the expansion of capillary pores also provides additional space for moisture uptake and contributes to the continuation of cryogenic suction. This process repeats and leads to the expansion of the surface region and generation of scaling.

4.5 F-T behavior of control concrete and HPC

To simulate the worst-case scenario for HPC, the test in this study uses a 3% salt solution. The performance of control concrete and HPC are compared in this section.

4.5.1 Control concrete

The control concrete with a 0.40 w/cm is not immune to F-T damage even with an extended curing age as illustrated in Figure 4.12. The scaling of concrete accelerates after a certain number of cycles, followed by a reduction in RDM, which is related to the critical saturation of concrete (Fagerlund 1975). Figure 4.12 (a) shows that the longer curing age, from 28 days to 90 days, reduces the moisture uptake of concrete. This decrease is due to longer hydration leading to a denser paste and a decrease in concrete permeability (Gagné et al., 2011). However, as discovered by Gopalan (1996), longer curing seems to have a marginal effect on the scaling development of control concrete (Figure 4.12 (b)). Both control systems experience significant surface damage as shown in Figure 4.13. While the control concrete meets the RILEM limit of 1.5 kg/m^2, it does not guarantee good long-term F-T performance. As a result, this study imposes a more stringent requirement of 1 kg/m^2 after 56 cycles for HPC.

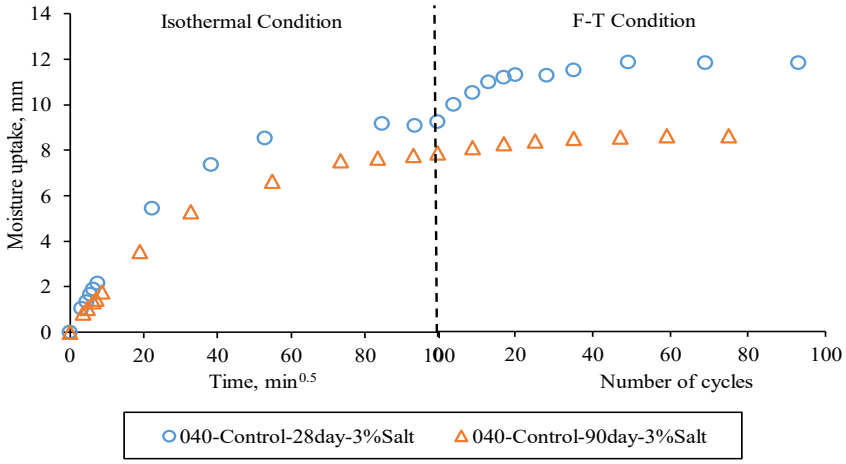

(a)

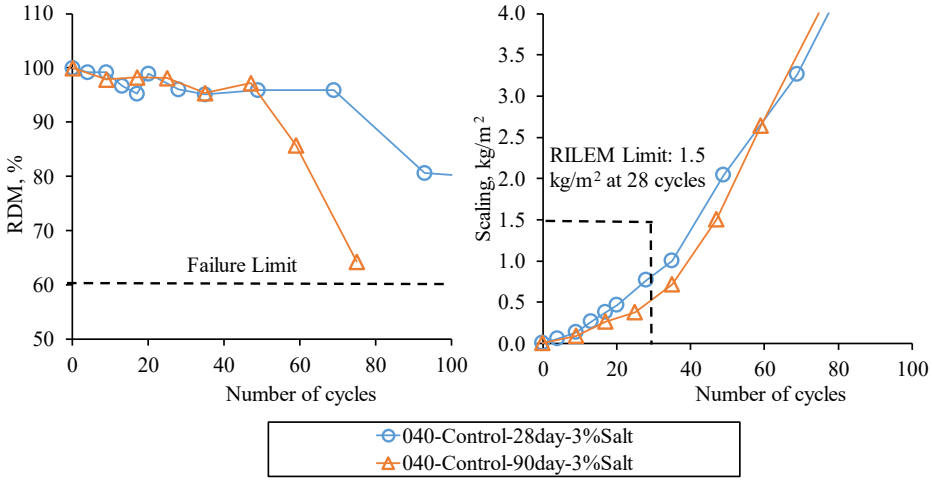

(b)

Figure 4.12 Moisture uptake and F-T test results of control systems with (a) 28-day water curing (b) 90-day water curing

(a) 040-Control-28day (b) 040-Control-28day

(a) 040-Control-90day (b) 040-Control-90day

Figure 4.13 Comparison of 040-Control-28day and 040-Control-90day systems (a) before and (b) after the F-T test

4.5.2 High-performance concrete

In this study, the strength and durability of HPC are improved through the addition of SCM and/or by lowering the w/cm. To achieve the desired HPC properties, a 30% replacement level of Portland cement with GGBFS and fly ash is adopted, which is supported by previous studies (Marchand 1994, Thomas 1997, Neville 2005). The GGBFS concrete is wet-cured for 28 days, while the fly ash concrete is wet-cured for 90 days due to the slower pozzolanic reaction and compressive strength development, as shown in Figure 4.14.

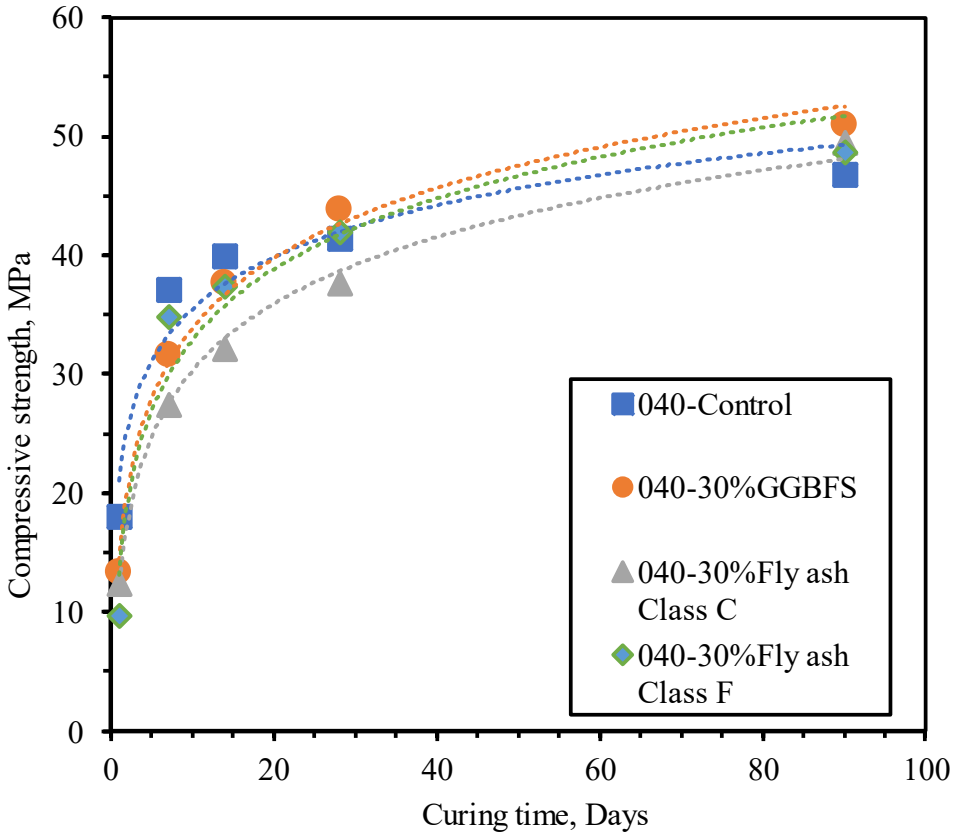

Figure 4.14 Compressive strength development for control concrete and HPC with a w/c of 0.40

- Discussion about the calculation of moisture uptake

The conventional method for calculating moisture uptake, as per ASTM C 1585, considers the entire exposed surface area, including the aggregates that have low water absorption capacity and limited connectivity. To make this study more comparable to others, we have adopted the conventional moisture uptake calculation method throughout, except for this particular section.

The capillary pores are primarily responsible for moisture uptake, particularly during Stage I in Figure 4.1. Consequently, this section proposes a modified calculation method that takes into account the capillary volume or capillary surface area to assess the impact of SCM and w/c on capillary porosity and moisture uptake.

The capillary porosity of concrete can be estimated by (Nielsen 1993)

$$\frac{V_{cap}}{V_{cem}} = \frac{w/c - 0.38\alpha}{0.32 + w/c}, \qquad (\frac{w}{c} > 0.38) \qquad \text{Eq. 4.1}$$

$$\frac{V_{cap}}{V_{cem}} = \frac{w/c(1-\alpha)}{0.32 + w/c}, \qquad (\frac{w}{c} \leq 0.38) \qquad \text{Eq. 4.2}$$

where V_{cap} is the volume of capillary pores, in cm^3, V_{cem} is the volume of cement paste, in cm^3, w/c is the water-to-cement ratio, α is the relative maturity. For simplicity, it can be estimated as

$$\alpha \approx 1 - 0.5\left(\frac{t_R}{t}\right)^{0.2}. \qquad \text{Eq. 4.3}$$

For non-drying ordinary Portland cement hydrated at normal room temperature, an average relaxation time of $t_R \approx 3$ days is suggested.

The height of moisture uptake can then be calculated as

$$H_{cap} = \frac{m_{liquid}}{\frac{V_{cap}}{H_{specimen}} \times \rho_{liquid}}, \qquad \text{Eq. 4.4}$$

where m_{liquid} is the weight of the moisture uptake, $H_{specimen}$ is the height of the specimen, ρ_{liquid} is the density of the liquid.

The capillary pore saturation level can be calculated from

$$P = \frac{m_{liquid}}{V_{cap} \times \rho_{liquid}} \times 100\%. \qquad \text{Eq. 4.5}$$

Using Eq. 4.4 and Eq. 4.5, H_{cap} and P can be plotted as a function of time or F-T cycles.

As the concrete samples approach a capillary moisture uptake of 70 mm (which corresponds to the height of the specimens, Figure 4.15 and Figure 4.16 (a)) or a capillary suction of approximately 100% (Figure 4.15 and Figure 4.16 (b)), they begin to undergo a transition from capillary suction to diffusion into unconnected pores or entrained air voids. This marks the end of capillary suction

in isothermal conditions. The control concrete reaches 100% capillary saturation quickly. The addition of SCM in HPC reduces the rate of moisture uptake (i.e., sorptivity) and total water absorption under isothermal conditions. Compared to the control concrete, the SCM concrete has a shorter stage I and II and lower moisture uptake (see Figure 4.15 (a) and Figure 4.16 (a)). This is mainly because the pozzolanic reaction of SCM will densify the microstructure of the concrete, reduce the average size of the pores and increase the pore discontinuity.

After a certain number of F-T cycles, the average pore size and porosity increase (Pogorelov et al. 2016). This increase together with the moisture accommodating function of air voids, explains why the saturation level can go much higher than 100%. The total moisture uptake of GGBFS concrete is well below that of the 28-day control concrete in the entire process. Fly ash concrete develops a comparable moisture uptake in the long term compared to the 90-day control concrete under pumping effect. Nevertheless, all concrete with SCM is found to reduce salt frost scaling. The scaling in HPC linearly increases with F-T cycles and remains less than about 0.5 kg/m^2 during the test period. This observation suggests that the phenomenon of scaling cannot be entirely explained by the overall moisture uptake of the bulk material, as scaling primarily occurs on the surface of the material, while the bulk moisture uptake represents a universal status. This is consistent with the cryogenic suction model.

The w/c, as one of the most important properties of concrete, also plays a critical role in the F-T resistance. Many studies have suggested that the lower the w/c, the lower the capillary suction (Fagerlund 1982, Pinto et al. 2018, Yang et al. 2021). A low w/c might densify the microstructure of the concrete surface causing the reduction of its permeability and the amount of freezable water in pores. This can be seen from the fact that the 035-30%GGBFS concrete has an even smaller moisture uptake compared to 040-30%GGBFS concrete during room temperature. However, lowering the w/c of 040-30%GGBFS does not further improve the scaling resistance as it already has a very low scaling. More details will be discussed in Chapter 6.

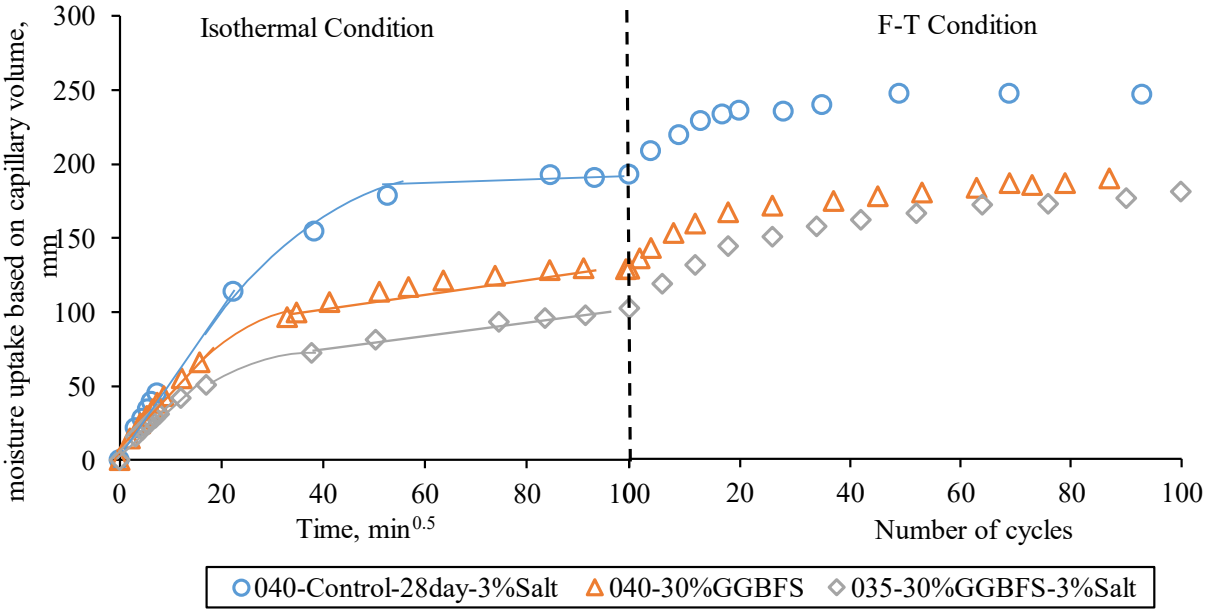
Isothermal Condition
F-T Condition
moisture uptake based on capillary volume, mm
300
250
200
150
100
50
0
0
20
40
60
80
100
20
40
60
80
100
Time, min0.5
Number of cycles
040-Control-28day-3%Salt
040-30%GGBFS
035-30%GGBFS-3%Salt

(a)

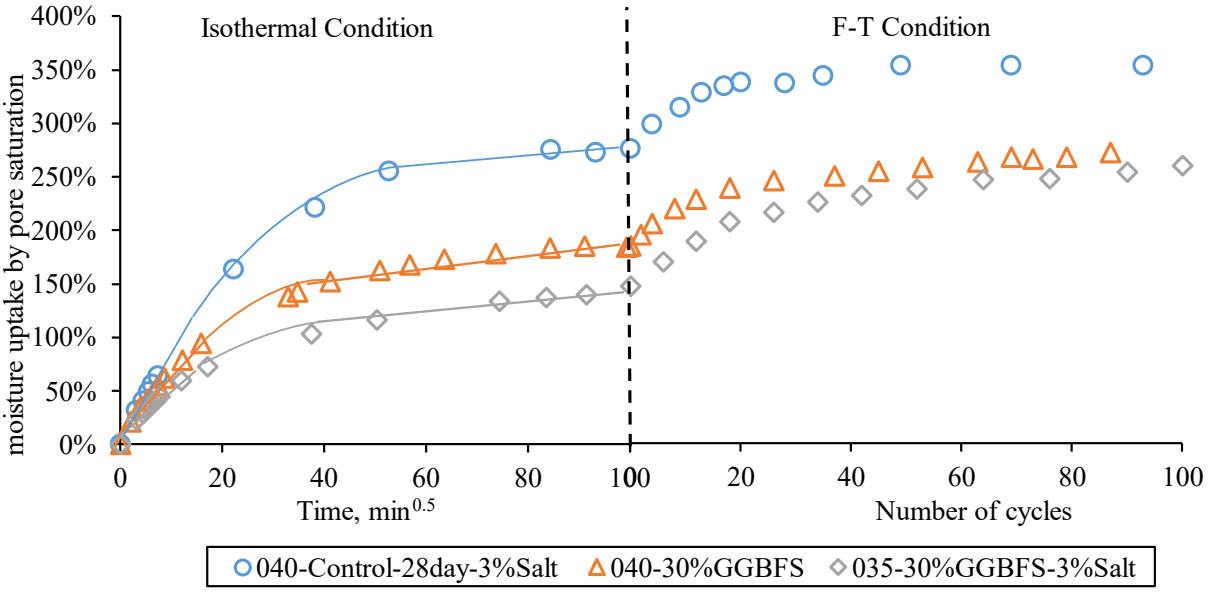
Isothermal Condition
F-T Condition
moisture uptake by pore saturation
400%
350%
300%
250%
200%
150%
100%
50%
0%
0
20
40
60
80
100
20
40
60
80
100
Time, min0.5
Number of cycles
040-Control-28day-3%Salt
040-30%GGBFS
035-30%GGBFS-3%Salt

(b)

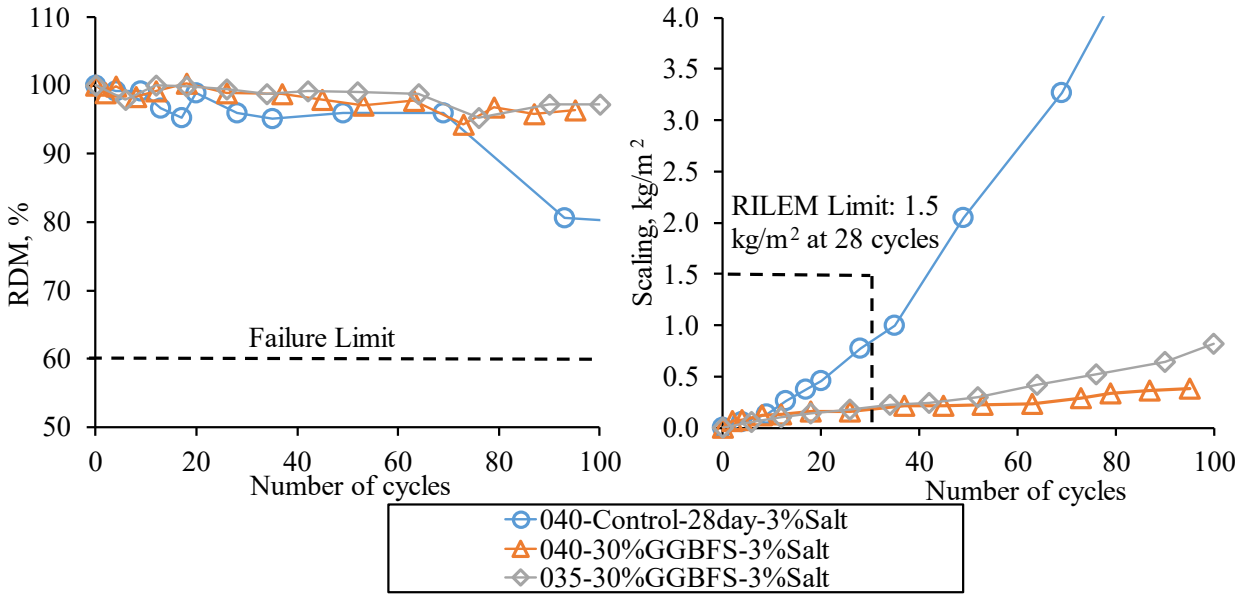

(c)

Figure 4.15 (a) moisture uptake based on capillary pore volume and (b) saturation level and (c) F-T test results of control systems and GGBFS concrete with 28-day water curing

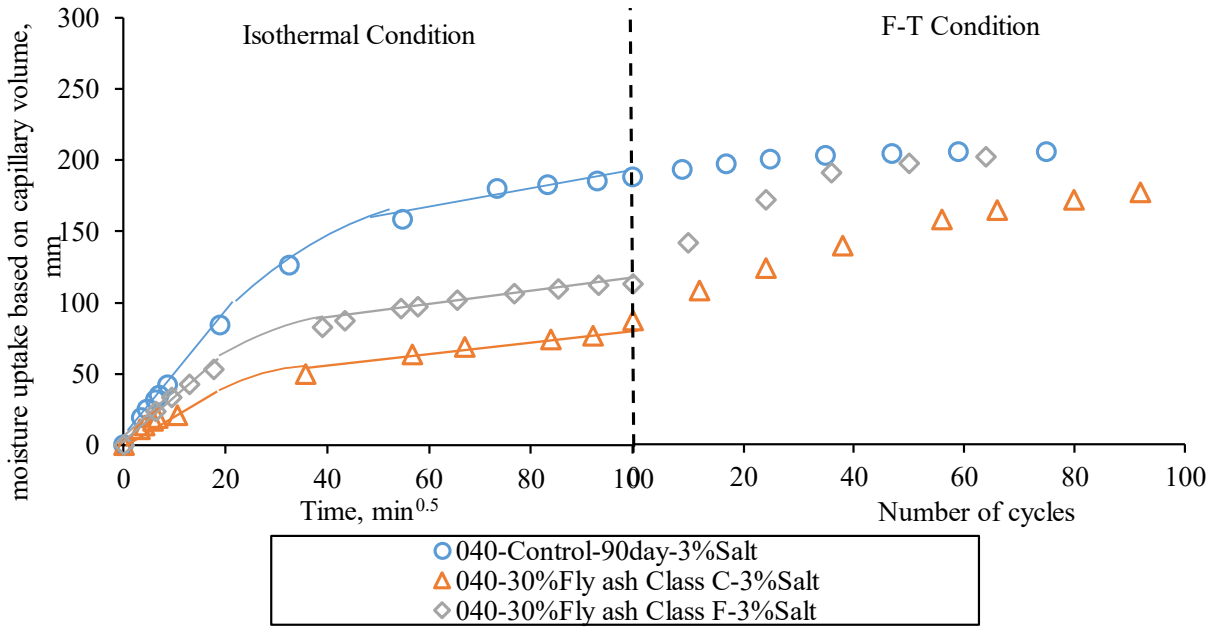

(a)

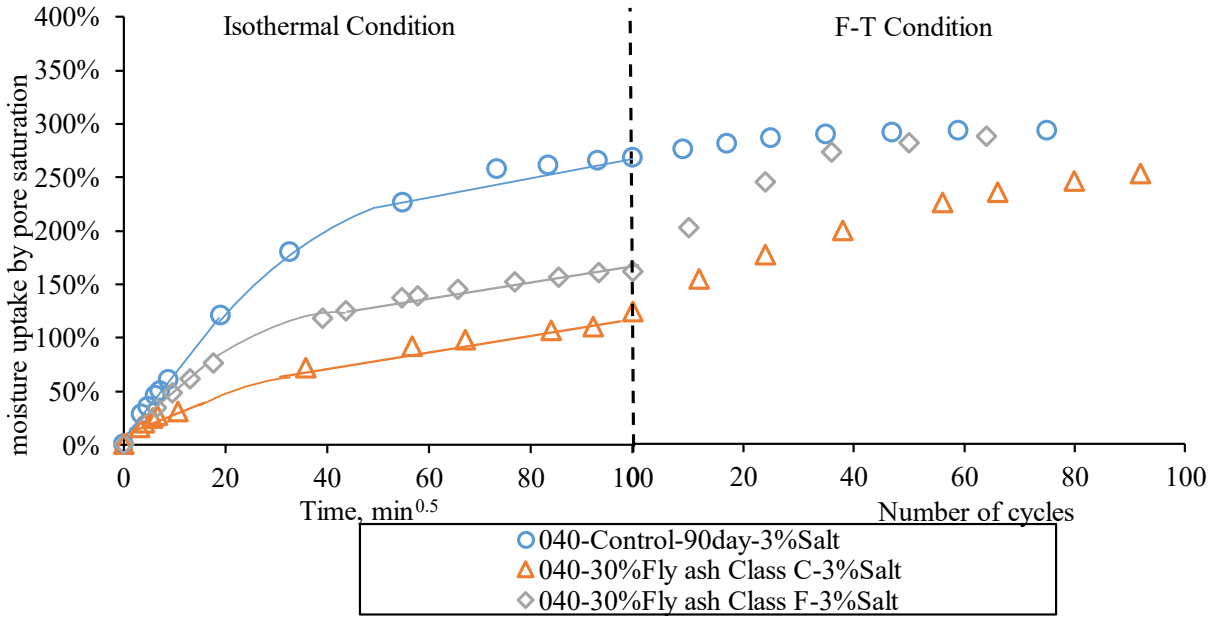

(b)

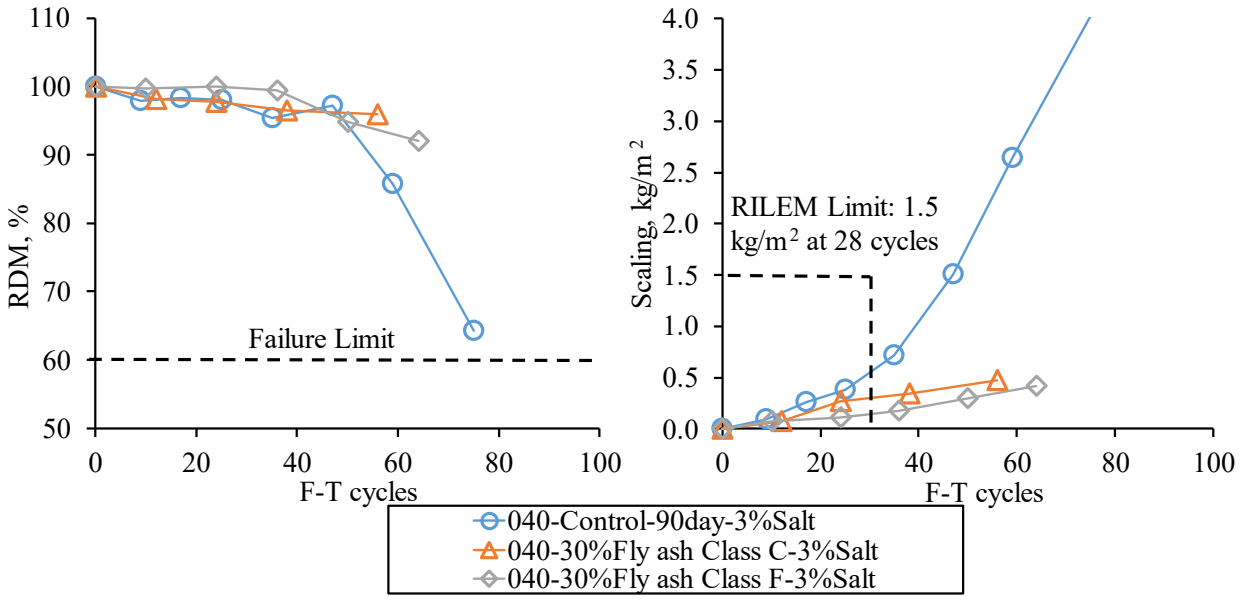

(c)

Figure 4.16 (a) moisture uptake based on capillary pore volume and (b) saturation level and (c) F-T test results of control systems and fly ash concrete with 90-day water curing

4.6 Effect of lightweight aggregate on HPC

One concern for HPC is the shrinkage-induced cracking associated with the low w/c, exacerbated by the replacement of Portland cement with GGBFS (Wei 2008). This can be addressed by internal curing. Internal curing has emerged as a new curing methodology with great promise for producing HPC with increased resistance to early-age shrinkage-related cracking and enhanced durability associated with increased hydration of the Portland cement. Internal curing in this project is accomplished by using pre-wetted LWA. This type of material is currently included in an established practice in the U.S. (ACI Committees 308, 213 2022, Bentz et al. 2011). The major benefits of internal curing are to maximize the hydration of cement and minimize self-desiccation (i.e. pore-drying) and associated early-age shrinkage (autogenous) cracking. Figure 4.17 illustrates the differences between internal and external curing (Castro et al., 2010). External curing can only penetrate a few cm into the concrete due to capillary pore discontinuity while a partial replacement of fine aggregate with pre-wetted LWA offers more effective curing as it enables water to be distributed more equally across a cross-section. Internal curing is especially preferred in low w/cm concretes (<0.42) where capillary water is insufficient for maximizing the hydration of cement (Bentz 2008). Moreover, due to pore-drying from curing to between 80% and 90% internal RH, these mixes undergo autogenous shrinkage, which in turn increases cracking potential.

The objectives of this project are to determine from a laboratory testing program the efficacy of using presoaked LWA shown in Figure 4.18 for internal curing on compressive strength, shrinkage, water permeability, and frost durability. This is accomplished by investigating these properties for two w/cm (0.35 and 0.40) and different LWA to sand replacement levels for concrete mixes consisting of 30% GGBFS. A total of seven concrete batches were produced in the concrete laboratory at MDOT.

4.6.1 Compressive strength

One of the factors that designers, contractors, and owners are most concerned with is the mechanical properties of the mixture, especially compressive strength. Based on the experimental results, the addition of LWA does not affect the compressive strength for both w/cm systems (Figure 4.19). In general, two opposite factors affecting LWA's effect on the strength are a) the strength and water-entrained porosity of LWA, and b) the contribution of internal curing to the

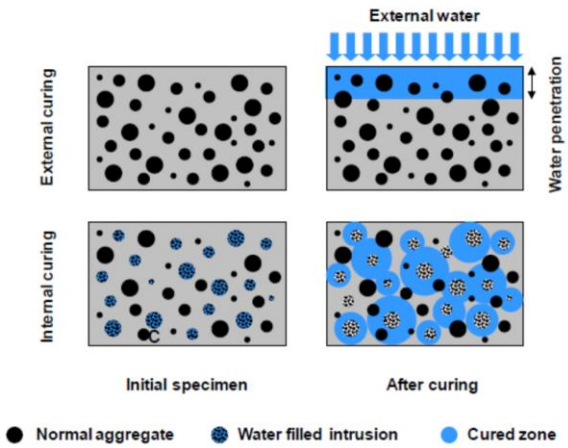

Figure 4.17 Illustration of the difference between external and internal curing (Castro et al. 2010).

Figure 4.18 Lightweight fine aggregate used in this study

hydration. It is known that LWA usually has lower strength compared to normal aggregate but at the same time, considering the IC effect, the hydration degree of concrete with LWA is increased resulting in a higher strength of concrete. Although some researchers found LWA has reduced the strength of concrete and the negative effect is more obvious if the percentage of LWA is increased (Costa et al. 2012), many would argue that LWA has not undermined or even enhanced the concrete strength (Jozwiak-Niedzwiedzka 2005, Cusson et al. 2008, Byard et al. 2010, Streeter 2012). This may depend on the LWA type, moisture content, strength and concrete properties such as mixture proportions, curing conditions, and testing age (Bentz et al. 2011).

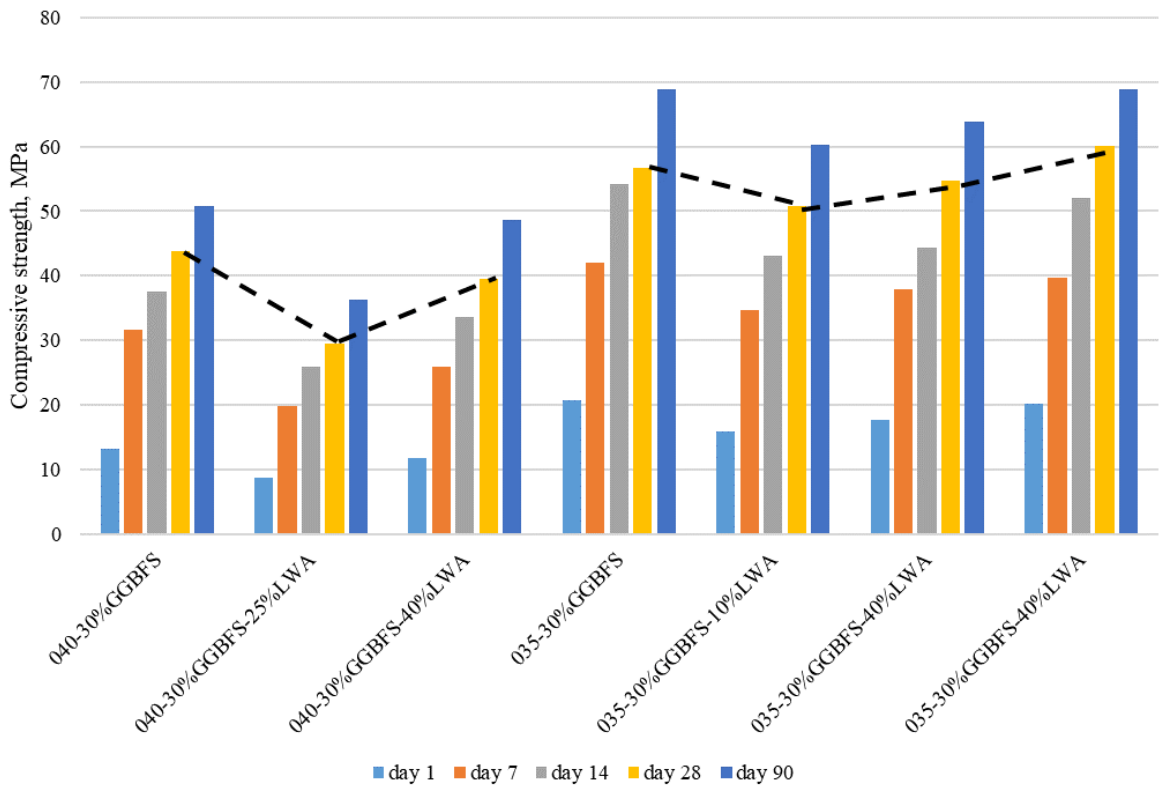

Figure 4.19 Effect of LWA on the compressive strength of concrete

4.6.2 Autogenous shrinkage

Consistent with results from the literature review (Bentur et al. 2001, Geiker et al. 2004, Henkensiefken et al. 2009), the addition of 25% to 40% LWA is effective in mitigating hydration-related shrinkage (e.g. autogenous) for both w/cm studied.

The autogenous shrinkage development results are presented in Figure 4.20 and Figure 4.21. Positive values mean expansion while negative values mean shrinkage. The results clearly show that for both w/cm, after several days' expansion, the control SCM mix begins to shrink significantly during the research period and probably keeps shrinking because of the continuous pozzolanic reaction. A mix containing 25% and 40% LWA, after the expansion stage, remains stable during the research period despite some minute fluctuations due to temperature change. Consequently, LWA has efficiently mitigated autogenous shrinkage.

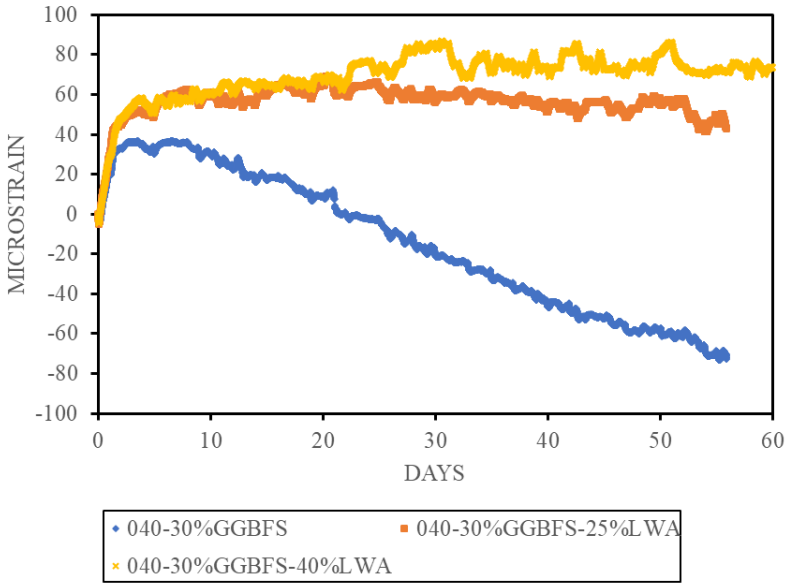

Figure 4.20 Effect of LWA replacement level on autogenous shrinkage for 0.40 w/cm

Moreover, as the LWA replacement volume increases, autogenous shrinkage decreases. The concrete containing 10% LWA by total fine aggregate volume is effective in mitigating shrinkage for a shorter sealed curing period (about 28 days) (Figure 4.21), while a 25% to 40% LWA content is effective for much longer periods. This is consistent with other researchers' conclusions (Henkensiefken et al. 2009).

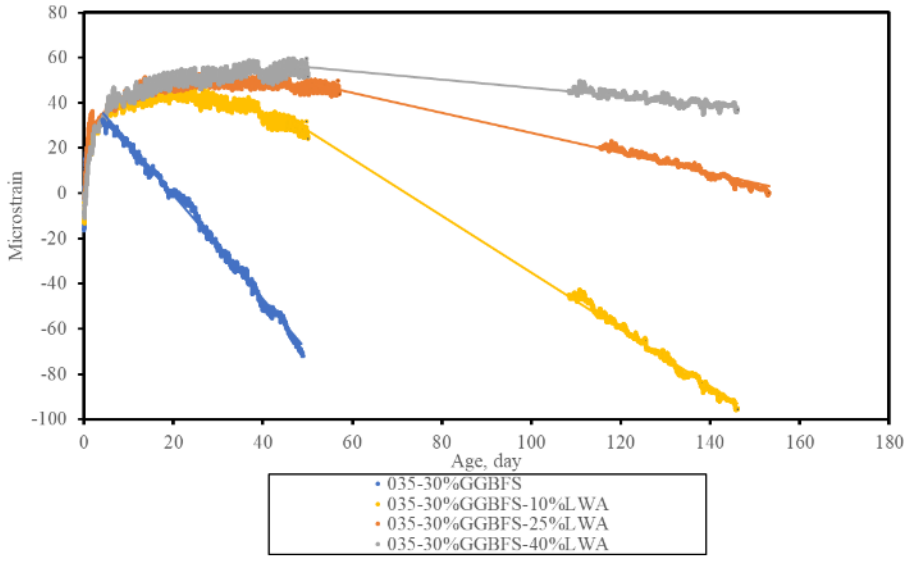

Figure 4.21 Effect of LWA replacement level on autogenous shrinkage for 0.35 w/cm

4.6.3 F-T behavior

The concrete with LWA shows a similar moisture uptake profile as the concrete without LWA during both stages. The reason may be that like normal aggregate, the aggregate is isolated and has a much lower level of connectivity compared to capillary pores. It can only take water through slow diffusion which makes the moisture uptake through LWA limited and no appreciate difference to that of the normal concrete (Figure 4.22 (a) and Figure 4.23 (a)).

One of the reasons why LWA is not widely used in the cold climate is the concern that it may adversely affect the F-T resistance (Mao 2004, Jones et al. 2014). However, scaling for all specimens in both systems is quite low and far below the 1.0 kg/m^2 mass loss limit after 56 cycles (Figure 4.22 (b) and Figure 4.23 (b)). The scaling for specimens containing LWA was slightly less than the control mix. The good scaling resistance of concrete with LWA could be attributed to the remaining porous structure (Figure 4.24) after water provided for internal curing leaves the LWA and is used for hydration which may function like the air void system and provide pressure relief (Gong et al. 2019). Another explanation could be that the surface layers of concrete with LWA should be denser than traditional concrete, and therefore more resistant to scaling. Samples for all batches do not show any internal cracking as RDM stays above 90% for the research period.

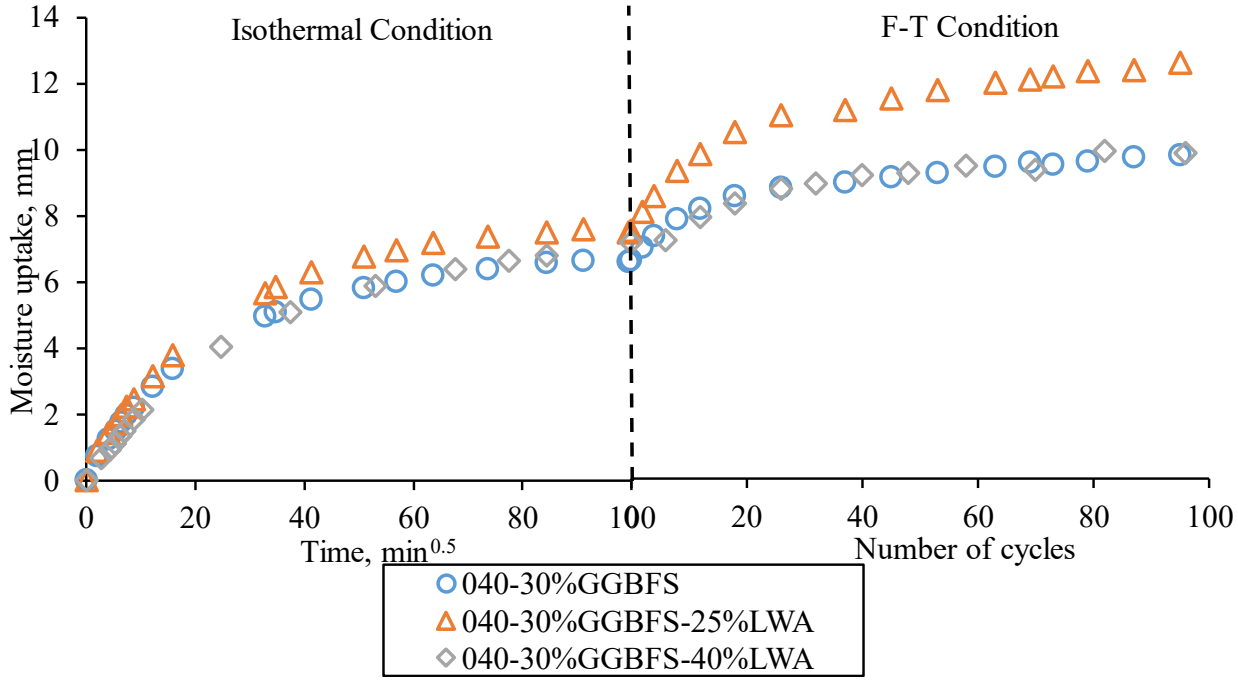

(a)

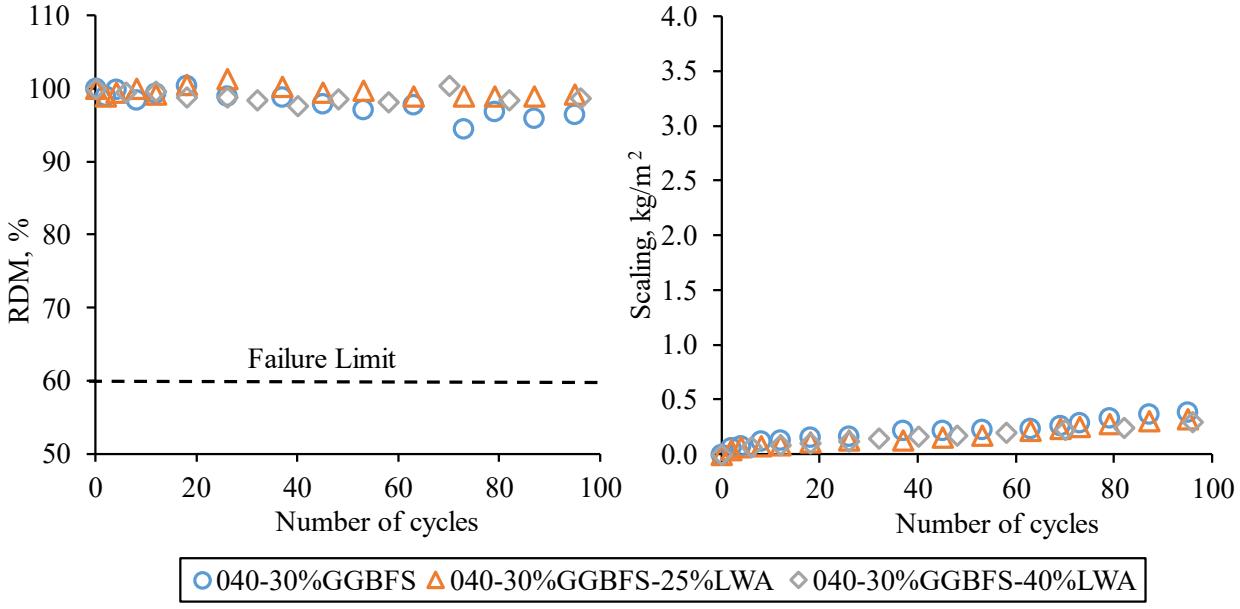

(b)

Figure 4.22 (a) moisture uptake and (b) F-T test results of 040-30%GGBFS concrete systems with 0, 25%, 40% LWA.

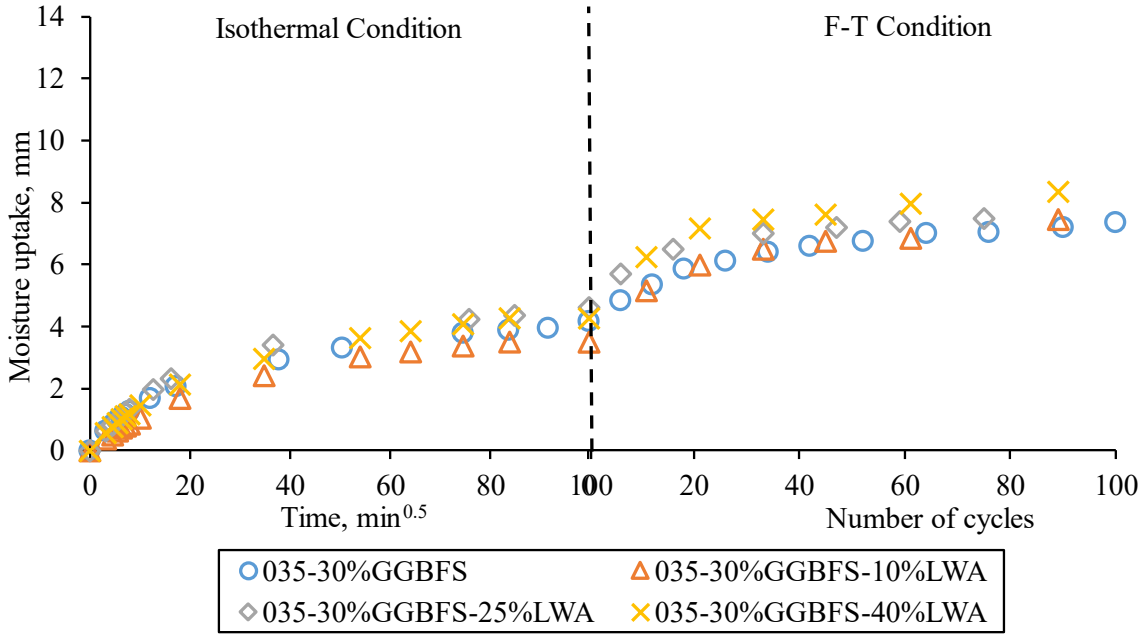

(a)

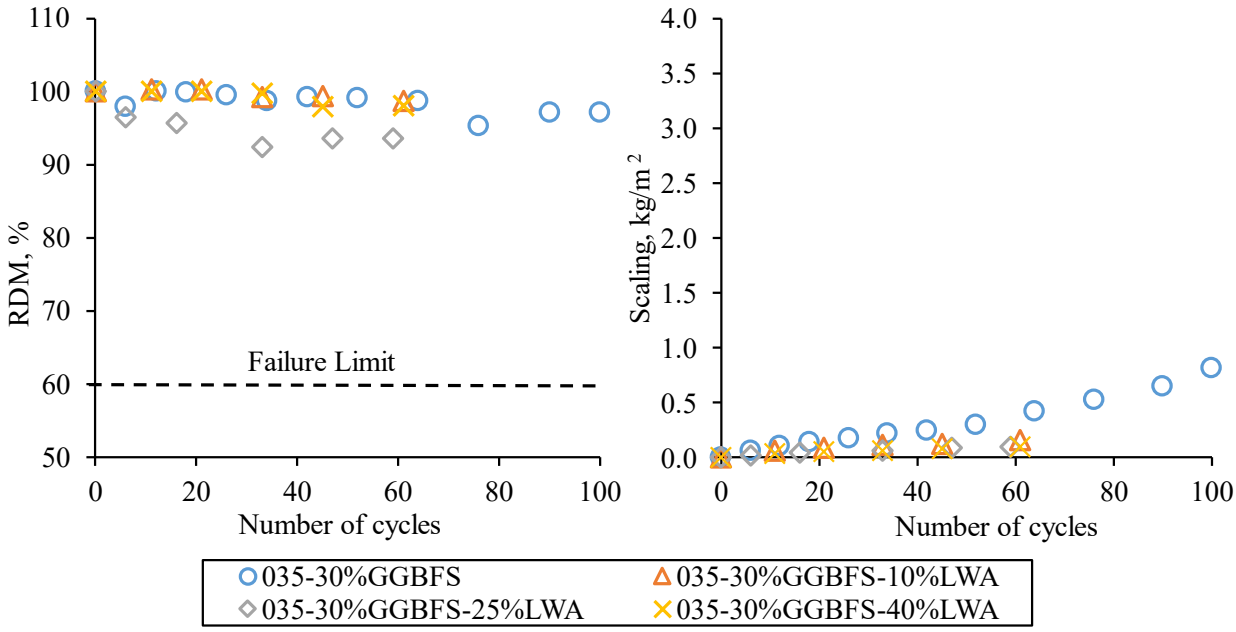

(b)

Figure 4.23 (a) moisture uptake and (b) F-T test results of 035-30%GGBFS concrete systems with 0, 10% 25%, 40% LWA.

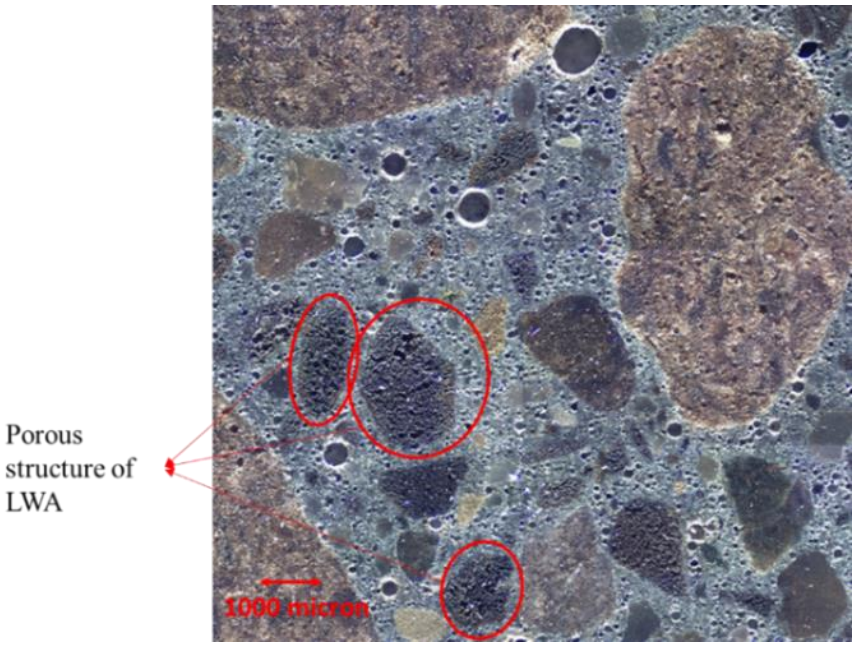

Figure 4.24 Microscopic picture of LWA

4.7 Summary

This chapter discussed the moisture uptake behavior of concrete in isothermal conditions with deionized water exposure and during F-T cycles with water/salt solution exposure followed by the study of the internal cracking and salt frost scaling resistance. The test variables include salt solution concentration (0, 3%, and 12%), w/cm (0.35-0.45), SCMs (GGBFS, fly ash, and silica fume), curing length (28 and 90 days) and LWA content (0 – 40%). The major findings are summarized as follows:

- The extended cryogenic suction model provides a reasonable explanation for salt frost scaling and the pessimum effect. Pore drying and ice expansion due to freezing likely creates additional space for moisture uptake by enlarging the capillary pores and opening the channel to connect previously unconnected pores.
- The aggregate constitutes the majority of the concrete but remains largely unconnected, resulting in low water absorption. To account for this, a modified method for measuring moisture uptake in concrete that takes into account the capillary pore volume or area is proposed. The modified method sheds more light on the moisture uptake behavior of the concrete.
- The addition of SCM, a low w/cm, and lengthening of curing periods can reduce the capillary suction due to the decrease in the connectivity of the pores and fining pore size. The GGBFS concrete with 28-day curing and fly ash concrete with 90-day curing at a 30% replacement level can improve the F-T performance.
- Long-term autogenous shrinkage can be mitigated by adding pre-wetted LWA at a 25% to 40% volume content of total fine aggregate. Excellent F-T resistance are found for all LWA mixes. LWA contents of 25% or 40% do not compromise F-T resistance or compressive strength.

Chapter 5. Study of Hydrophobic Impregnation on the Freeze-Thaw Resistance

5.1 General

The superhydrophobic properties of plant leaves, such as lotus, have garnered significant interest among scientists, as illustrated in Figure 5.1 (Shirtcliffe et al. 2009). The unique hierarchical structures of convex or papillar epidermal cells, combined with three-dimensional wax structures on top, make it difficult for these surfaces to become wet. As a result, water droplets on such surfaces have low energy through adsorption and tend to form spherical droplets.

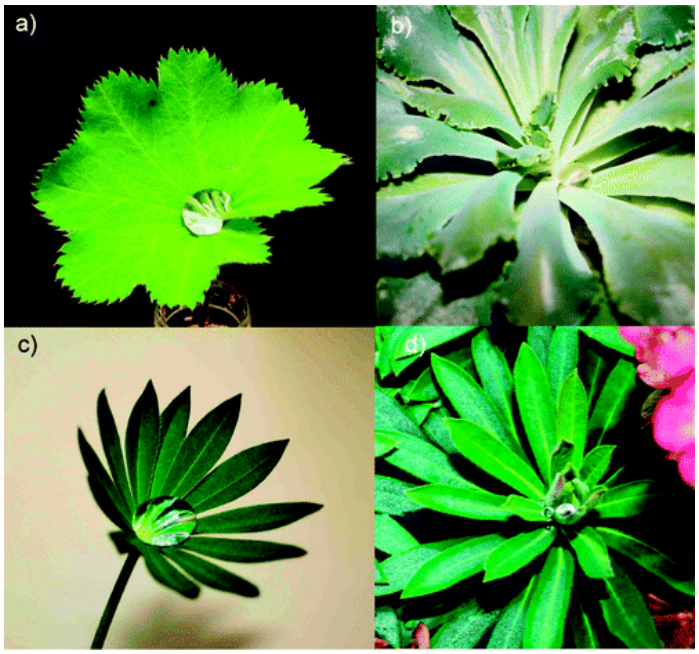

Figure 5.1 Plants showing retained water droplets. (a) Lady's Mantle, (b) Echeveria, (c) Lupin, (d) Euphorbia. (Shirtcliffe et al. 2009)

Hydrophobic impregnation is a well-known method to reduce water absorption and improve the corrosion resistance of reinforced concrete. However, its effectiveness in enhancing the F-T resistance of concrete remains unclear. This study aims to evaluate the impact of two hydrophobic impregnation methods, namely internal impregnation (IIP) using a pore blocking admixture during mixing and surface impregnation (SIP) with a penetrating pore liner applied to the surface of pre-

dried hardened concrete after extended curing, on F-T and deicer scaling resistance using the RILEM TC 176-IDC CIF test. The results demonstrate that only the control concretes without hydrophobic impregnation remain F-T resistant. The surface impregnated concrete shows severe scaling in the long term, while the internally impregnated concrete is damaged both externally and internally soon after reaching critical saturation. The study clearly demonstrates that hydrophobic impregnation does not benefit concrete with good F-T resistance, and maintaining a hydrophilic pore structure is crucial to ensure the free flow of water and the normal functioning of the air void system. The results also suggest that salt frost scaling shares a similar mechanism with regular F-T attacks both of which depend on the pore structure and the quality of the air void system.

5.2 Effect of surface impregnation on F-T durability

5.2.1 Mechanism of surface impregnation

Silane, a common type of pore liner, consists of small molecules (1.0×10^{-6} – 1.5×10^{-6} mm in diameter) and can effectively penetrate into the concrete. Silane molecules can combine with the hydrated cement paste in the near-surface region of the concrete and form a pore liner on the walls of pores, which act as water repellents (see Figure 5.2). This pore lining blocks the penetration of water and water ions while still allowing air and water vapor to move in and out of the concrete, enabling it to breathe.

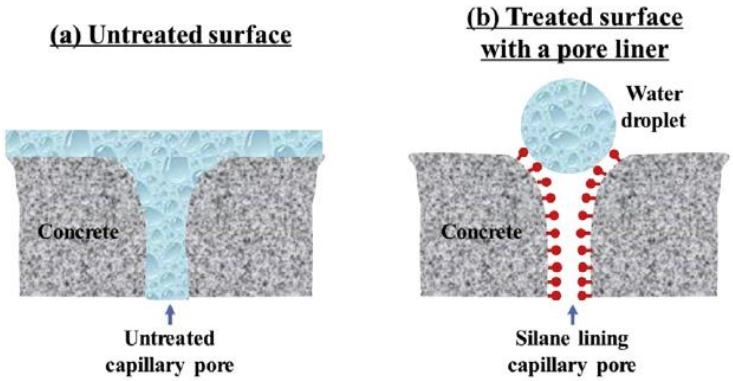

Figure 5.2 Illustration of hydrophobic effect on water-repelling (Liu et al. 2016b)

The wettability of a solid surface by a liquid can be quantified using the water contact angle. Geometrically, the contact angle is defined as the angle formed by the three-phase boundary between the liquid (*l*), vapor (*v*), and solid (*s*), as shown in Figure 5.3. The relationship between the surface tension and contact angle can be explained by the well-known Young equation.

$$\gamma^{sv} = \gamma^{sl} + \gamma^{lv} \cos\theta, \qquad \text{Eq. 5.1}$$

where θ is the contact angle, γ^{sl} is the solid/liquid surface tension, γ^{sv} is the solid/vapor surface free energy, and γ^{lv} is the liquid/vapor surface tension.

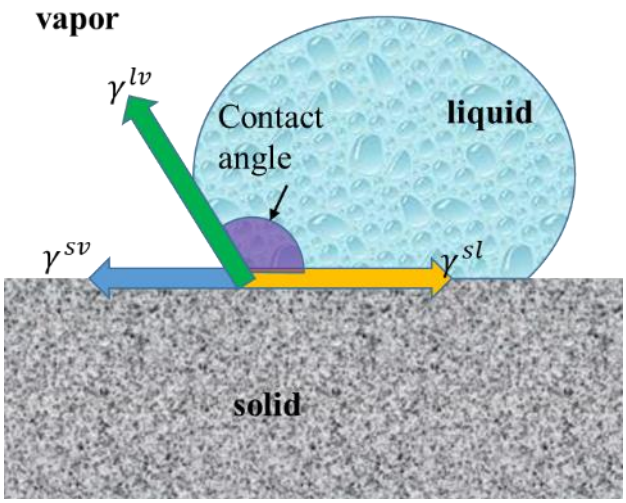

Figure 5.3 Schematic representation of the relationship between surface tensions and contact angle

From Eq. 5.1,

$$\cos\theta = \frac{\gamma^{sv} - \gamma^{sl}}{\gamma^{lv}}. \qquad \text{Eq. 5.2}$$

The solid/vapor surface free energy γ^{sv} of the concrete surface with hydrophobic treatment is smaller than solid/liquid surface tension γ^{sl}, and $\cos\theta$ will be negative (i.e., contact angle $\theta > 90°$) which suggests that the surface has low wettability.

Washburn's equation shows that increasing the contact angle can limit water penetration under considerable pressure. The pressure head (p) required to force water with surface tension (σ) into a pore of radius (r) is given by (Washburn 1921)

$$p = \frac{-2\sigma\cos\theta}{r}. \qquad \text{Eq. 5.3}$$

For example, if a contact angle of 120° for surfaces coated with fatty acids and a maximum capillary size of 5000 Å, the pressure head that is required for water to enter the concrete is 14 m.

5.2.2 Mix design and specimen preparation

The mix design of the systems studied in this section is presented in Table 5.1. The raw material properties are previously explained in Chapter 3. Both the concrete with and without SIP have the same mix design. The hardened air properties are displayed in Table 5.2. It can be seen that all concrete systems meet the recommendations of ACI 201 (2021) with a spacing factor of smaller than 200 microns and a specific surface greater than 25 mm^{-1}.

Table 5.1 Mix design and fresh air content of concrete

Batch ID	Mix Design (kg/m^3)						air content (%)
	Water	C.A.	Sand	LWA	Cement	SCM	
035-S-(SIP)	136	1062	620	0	272	116	3.7
040-S-(SIP)	156	1068	640	0	273	117	7.1
040-S-25L-(SIP)	156	1068	480	109	273	117	10.0
040-S-40L-(SIP)	156	1068	384	174	273	117	7.7

Note: S means GGBFS; 25L means addition of 25% LWA;

Table 5.2 Hardened air properties of concrete

Batch ID	air content, %	spacing factor, µm	specific surface, 1/mm
035-S-(SIP)	2.9	170	37
040-S-(SIP)	6.1	108	43
040-S-25L-(SIP)	8.8	73	46
040-S-40L-(SIP)	5.8	110	42

After 28 days of water curing and drying, the surface of the concrete is treated with a silane water repellent layer before conducting the sorptivity test. The application process of the silane is shown in Figure 5.4.

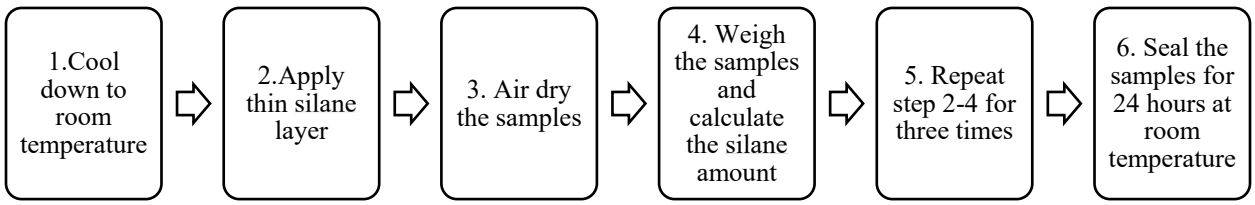

Figure 5.4 Surface impregnation procedure

5.2.3 Moisture uptake and F-T test results

Previous studies have established that a SIP is effective in reducing water sorption and penetration of chloride ions, thereby reducing the risk of reinforcement corrosion at temperatures above freezing (Nolan et al. 1995, de Vries et al. 1997, Basheer 2006, Tittarelli et al. 2008, Medeiros et al. 2009, Dao et al. 2010, Gong et al. 2012, Christodoulou et al. 2013, Zhu et al. 2013, Christodoulou et al. 2014, Franzoni et al. 2014, Güneyisi et al. 2014, Hassani et al. 2017, Matar et al. 2020. Zhang et al. 2022). Figure 5.5 - Figure 5.8 display the moisture uptake under isotherm and F-T conditions for both surface impregnated and control concrete, along with their respective F-T test results. The results of moisture uptake at isothermal room temperature, as shown in Figure 5.5 - Figure 5.8 (a) indicate that SIP is highly effective in resisting water penetration, resulting in a reduction of around 75% in the total moisture uptake at ambient temperature due to the hydrophobic liner on the pore walls of capillaries. The capillaries of concrete with SIP remain unsaturated when the F-T test began.

During the F-T test, all concrete systems exhibit an accelerating moisture uptake beyond isothermal conditions, with the system with SIP showing an even more pronounced water uptake (Figure 5.5 - Figure 5.8 (b)). The reference concrete has a lower moisture uptake as the connected pores are near-saturated in isothermal conditions. The concrete with SIP rapidly absorbs water until it reaches the same total moisture uptake as the reference concrete under capillary suction and diffusion process in isothermal conditions indicated by the black dashed line, after which the curve tapers off. This indicates that the hydrophobic effect is incapable of resisting the pumping effect linked with the F-T cycles, which is consistent with the findings of other researchers (Perenchio 1988, Cleland 2002, FrentzelSchirmacher 2005, Liu et al. 2018).

The effectiveness of surface impregnation in reducing salt frost scaling over the long term is questionable. Prior to critical saturation, SIP concrete exhibits minimal scaling as illustrated in Figure 5.5 - Figure 5.8 (d). However, once the concrete is critically saturated, scaling significantly worsens, as seen in the steeper slope of the scaling curve. Conversely, the scaling rate of the reference concrete appears unaffected, remaining nearly linear with F-T cycles. In fact, the scaling rate of 035-S is higher than that of its 040-S counterpart due to a weaker air void system. The 035-S has a spacing factor of 170 microns while the reference concrete with 0.40 w/cm all have a spacing factor lower than 110 microns as listed in Table 5.2. Nevertheless, all the reference

concrete has a scaling of less than 1.0 kg/m^2 before 100 cycles which is much less than that of the SIP concrete in the long term. These results suggest that SIP does not provide any advantages to high-performance concrete and may actually cause potential problems. However, the problem seems limited to the surface, as most concrete samples do not develop internal cracking during testing. RDM of 040-S-SIP drops slightly below 90% after approximately 120 cycles due to the oversaturation in the concrete's interior after the development of severe scaling on the surface as shown in Figure 5.5 (e).

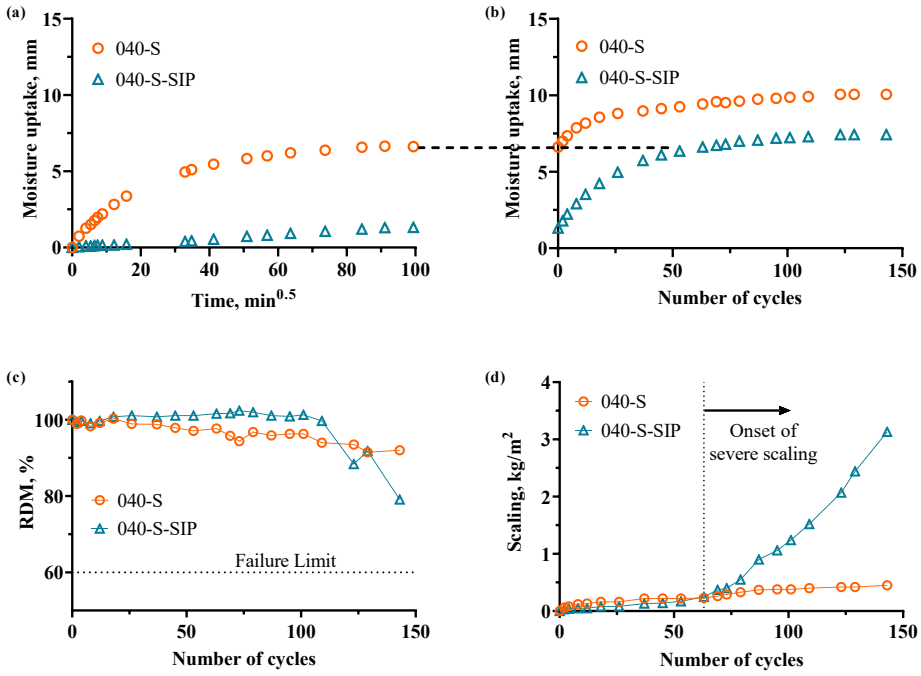

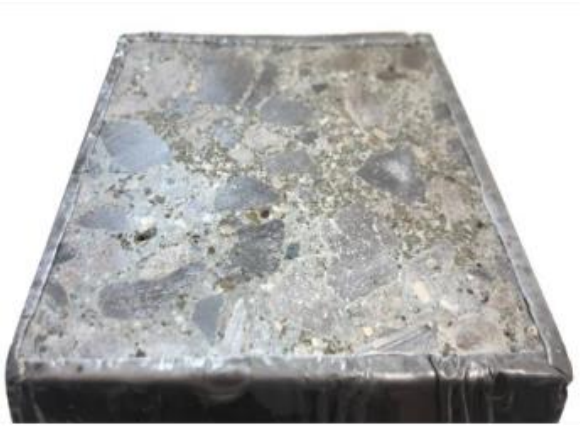

040-S at start

040-S after test

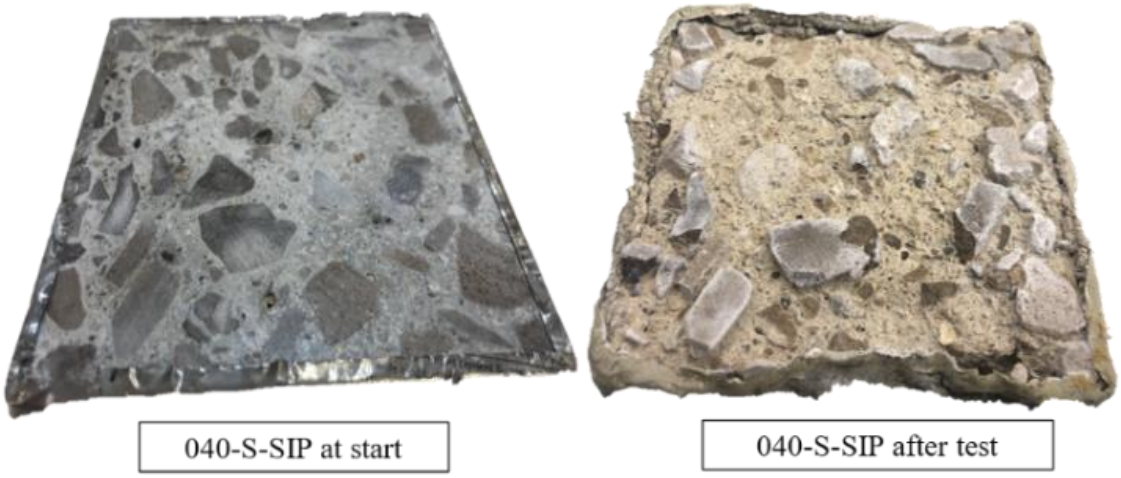

(e)

Figure 5.5 040-S-(SIP) system: moisture uptake (a) at room temperature and (b) in F-T conditions, (c) RDM, (d) scaling and (e) photos of exposure surface

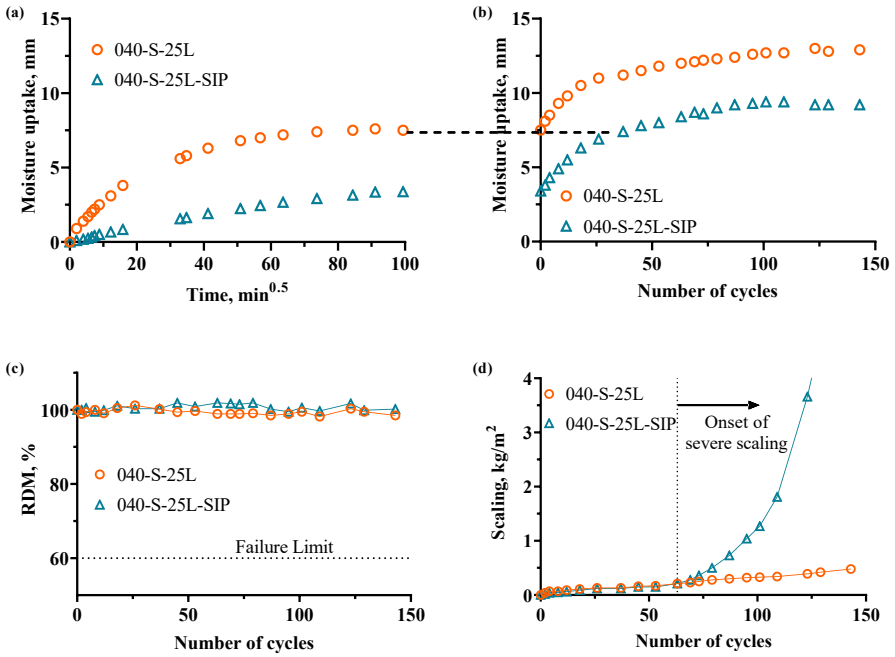

Figure 5.6 040-S-25L-(SIP) system: moisture uptake (a) at room temperature and (b) in F-T conditions, (c) RDM, and (d) scaling

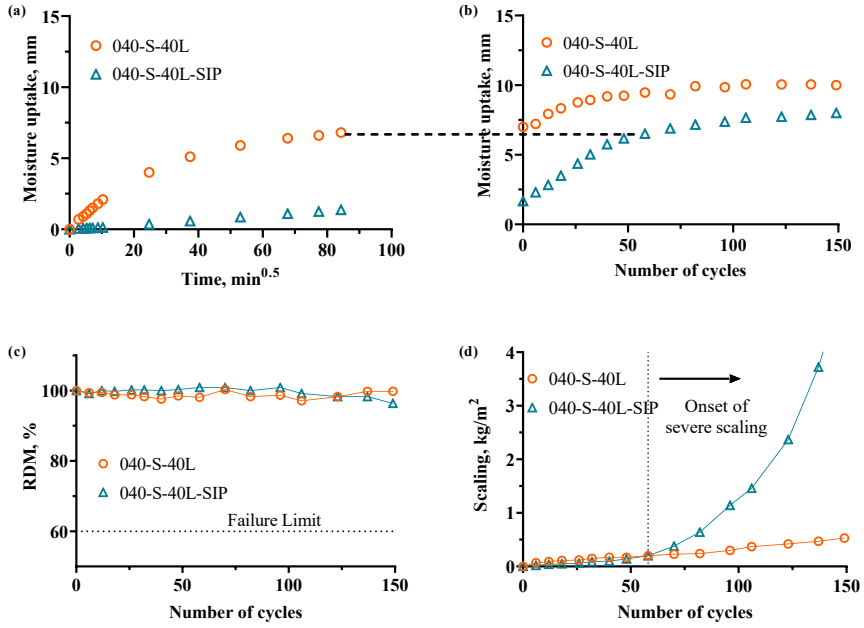

Figure 5.7 040-S-40L-(SIP) system: moisture uptake (a) at room temperature and (b) in F-T conditions, (c) RDM, and (d) scaling

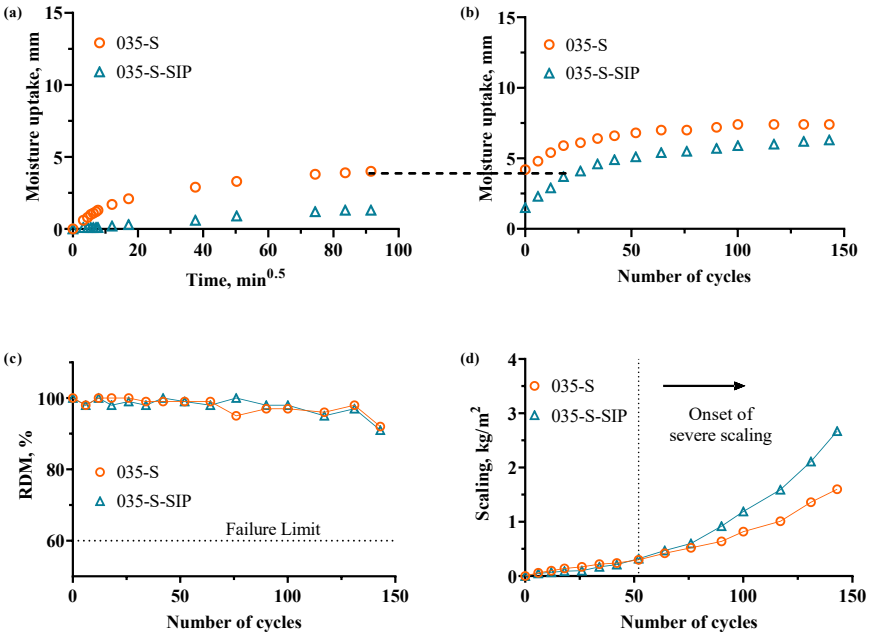

Figure 5.8 035-S-(SIP) system: moisture uptake (a) at room temperature and (b) in F-T conditions, (c) RDM, and (d) scaling

5.3 Effect of internal impregnation on F-T durability

5.3.1 Mechanism of internal impregnation

Hydrophobic impregnation can also be achieved through the use of permeability-reducing admixtures (PRA) during mix proportioning, noted as internal impregnation (IIP). PRAs comprise a variety of mineral and chemical admixtures that differ in mechanism, performance, and acceptance by the concrete industry (ACI Committee 212 2016). ACI Committee 212 on Chemical Admixtures divides PRAs into five main categories a) hydrophobic water repellents, b) polymer products, c) finely divided solids, d) hydrophobic pore blockers, and e) crystalline products. Among these, hydrophobic pore blockers are less studied and are the focus of this thesis.

Hydrophobic pore blockers can react with metallic ions supplied by cement, resulting in water-insoluble polymers that can block capillary pores in the concrete (Figure 5.9), thus increasing the disconnectivity of the pores (ACI Committee 212 2016, Tibbetts 2021). Additionally, the reactions between hydrophobic compounds and hydrating cement phases can modify the cement paste matrix and alter the surface tension of the solid/vapor interface, thereby reducing the capillary movement of water, although this effect is less dominant. In other words, the pore blocker admixture relies more on the physical effect rather than the chemical effect.

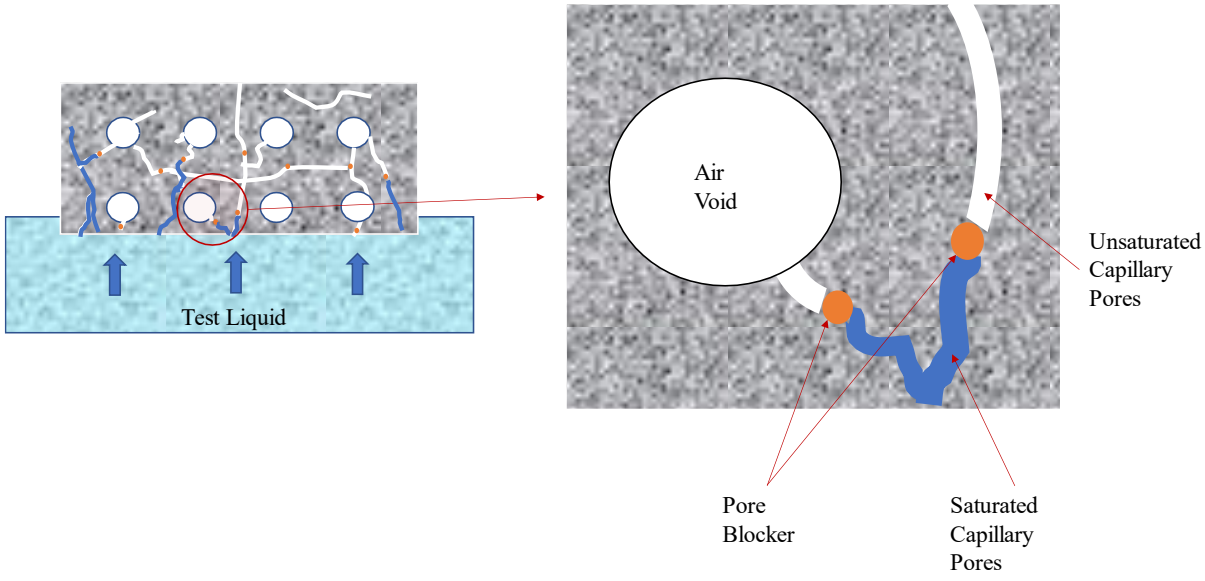

Figure 5.9 Hydrophobic pore blocker working mechanism

In a study conducted by Civjan et al, the freeze-thaw durability of concrete mixtures containing hydrophobic pore blockers was investigated, and the results indicated reduced resistance to F-T

cycles compared to the control mixes. The authors attributed this to a decrease in strength (Civjan 2008). Sharp et al found similar results in both durability factor and surface rating when comparing concrete with pore blockers to the control concrete (Sharp 2007). These conflicting results and the limited data available highlight the need for further studies to better understand the performance of pore blockers under F-T conditions.

5.3.2 Mix design

The properties of the raw materials are the same as those mentioned in Chapter 4. One type of commercial liquid PRA based on a water-soluble molecule with a dosage of 10 L/m^3 is added during concrete mixing. The concrete samples are cured for 90 days, taking into account the slower pozzolanic reaction of the fly ash concrete. The concrete mix design is displayed in Table 5.3. All concrete systems except for 040-S-IIP exhibit a favorable air void system, as listed in Table 5.4.

Table 5.3 Mix design and air content of concrete

Batch ID	Mix Design (kg/m^3)						air content (%)
	Water	C.A.	Sand	LWA	Cement	SCM	
040-S-IIP	134	1054	741	0	234	100	4.6
040-C-IIP	134	1054	741	0	234	100	8.9
040-F-IIP	134	1054	741	0	234	100	9.0
040-S-Ref	134	1054	741	0	234	100	6.1
040-C-Ref	134	1054	741	0	234	100	7.6
040-F-Ref	134	1054	741	0	234	100	5.0

(Note: S means GGBFS; C means Class C fly ash; F means Class F fly ash; Ref means reference concrete without IIP.)

Table 5.4 Hardened air properties of concrete

Batch ID	air content, %	spacing factor, μm	specific Surface, 1/mm
040-S-IIP	3.3	237	24
040-C-IIP	7.3	99	34
040-F-IIP	8.1	89	39
040-S-Ref	4.4	172	30
040-C-Ref	6.1	133	35
040-F-Ref	4.2	149	32

5.3.3 Moisture uptake and F-T results

Figure 5.10 - Figure 5.12 display the moisture uptake under isotherm and F-T conditions for both IIP and reference concrete, along with their respective F-T test results.

The results indicate that similar to SIP, IIP can reduce moisture uptake in isothermal conditions although the mechanisms behind these effects are different. Concrete with IIP has roughly half the moisture uptake of its reference counterparts (Figure 5.10 - Figure 5.12 (a)). It should be noted that the systems examined in this section were 90 days cured with the addition of 30% SCM (slag or fly ash). As discussed in Chapter 4, the reference concrete has low moisture uptake. Therefore, IIP appears to be less effective than SIP in isothermal conditions. Once the F-T cycle starts, the IIP concrete has a rapid moisture uptake as shown in Figure 5.10 - Figure 5.12 (b). It takes even fewer cycles for the capillary pores in IIP concrete to become saturated. Within 40 cycles, the total moisture uptake of IIP concrete reaches the same level as or exceeds that of the reference concrete.

The rapid moisture uptake in IIP concrete is accompanied by accelerated scaling and internal cracking development, as illustrated in Figure 5.10 - Figure 5.12 (c) and (d). Unlike SIP concrete, which exhibits a long period of low scaling before the start of non-linear scaling, IIP concrete experiences significant scaling within 20 cycles, irrespective of the type of SCM. Meanwhile, the reference concrete does not show any signs of surface scaling or internal cracking. There is a great scaling intrusion on the surface of IIP concrete with the removal of coarse aggregate. Instead, the reference concrete has an almost intact surface. The comparison of the specimens before and after the F-T test can be seen from the photos in Figure 5.10 - Figure 5.12 (e).

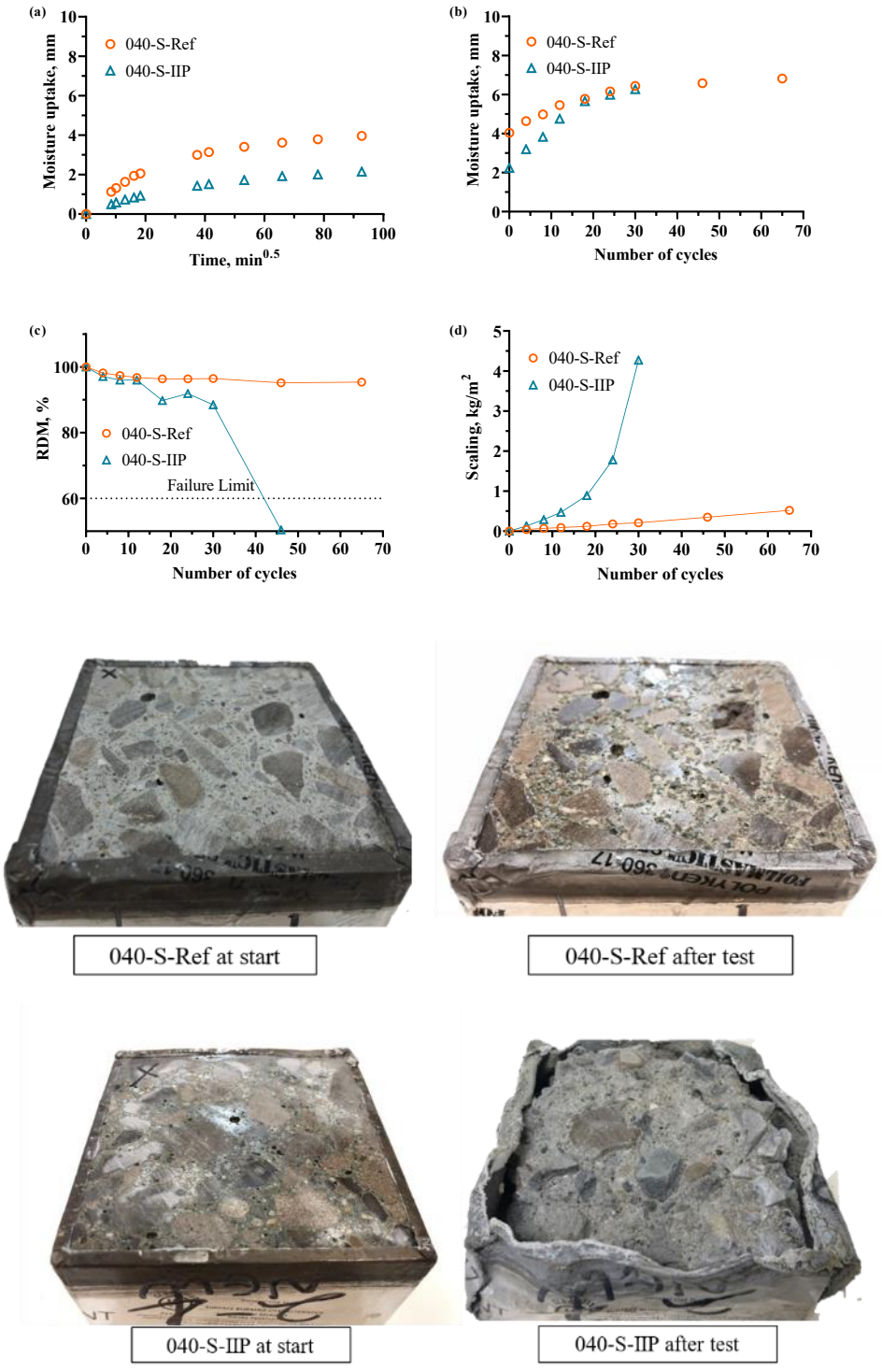

(e)

Figure 5.10 040-S-Ref and 040-S-IIP systems: moisture uptake (a) at room temperature and (b) in F-T conditions, (c) RDM, (d) scaling and (e) photos of exposure surface

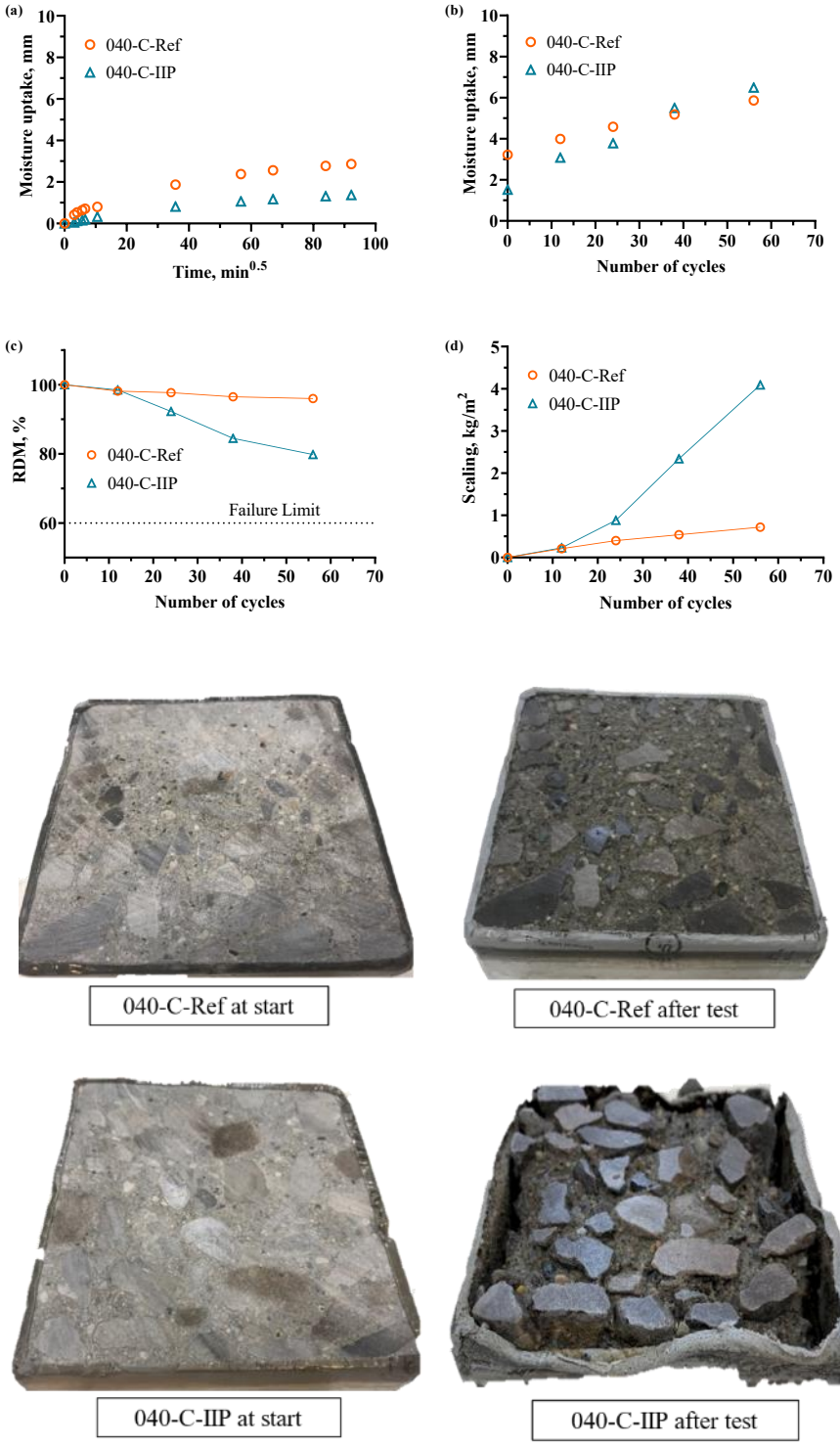

(c)

Figure 5.11 040-C-Ref and 040-C-IIP systems: moisture uptake (a) at room temperature and (b) in F-T conditions, (c) RDM, (d) scaling and (e) photos of exposure surface

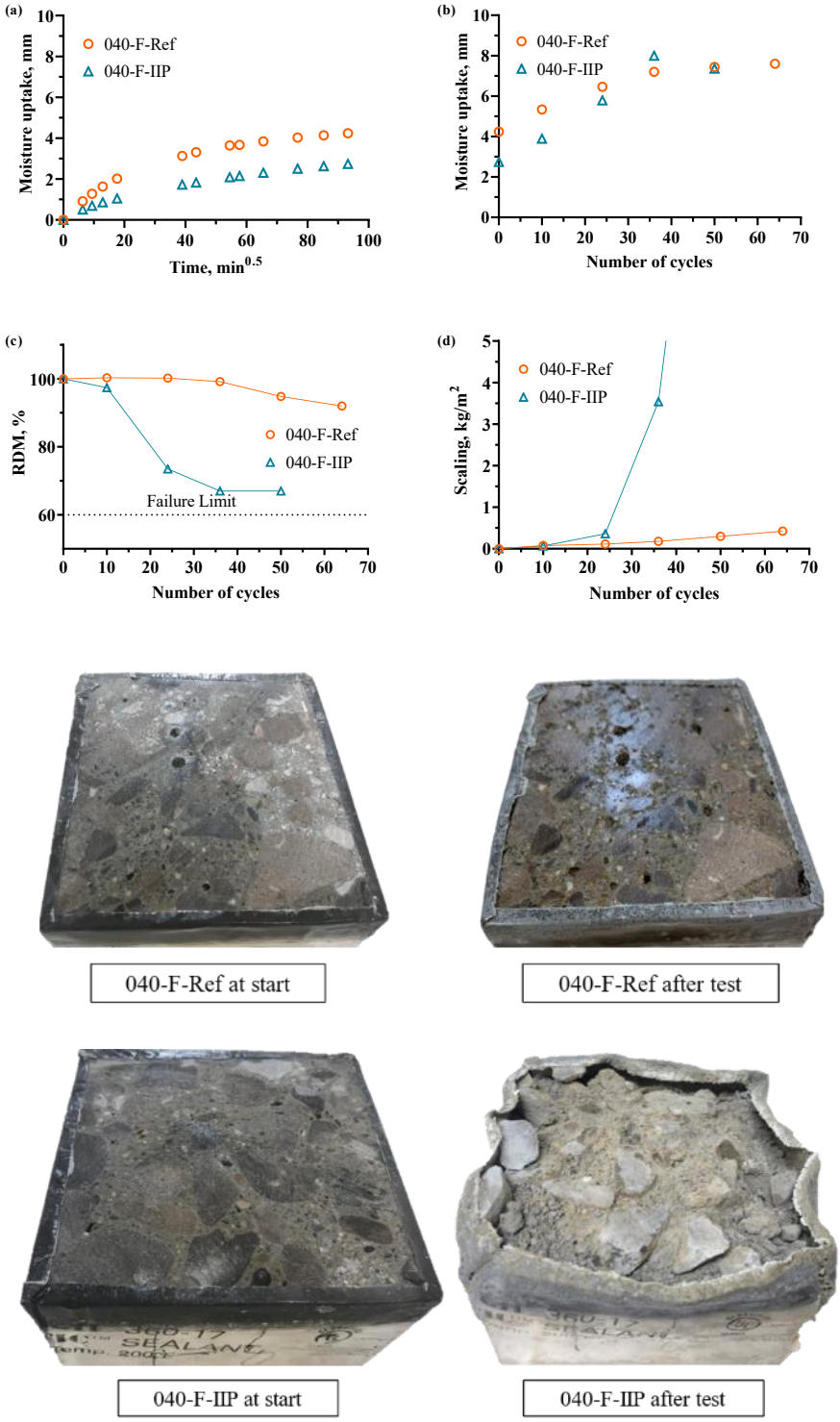

(e)

Figure 5.12 040-F-Ref and 040-F-IIP systems: moisture uptake (a) at room temperature and (b) in F-T conditions, (c) RDM, (d) scaling and (e) photos of exposure surface

5.4 F-T Deterioration with the presence of hydrophobic impregnation

The laboratory results indicate that both SIP and IIP are effective in preventing water ingress into concrete under isothermal room-temperature conditions, which can be utilized to protect reinforcement steel from corrosion. However, the use of hydrophobic impregnation has a significant impact on salt frost resistance. Neither surface impregnation nor internal impregnation is advantageous in concrete under investigation.

Figure 5.13 (a) and (b) shows the effect of air content and spacing factor on scaling under the presence of hydrophobic impregnation. Regardless of the air void system quality, the IIP concrete demonstrates a huge scaling development at about 56 cycles. Although concrete with SIP has low scaling initially, it exhibits high scaling in the long term. All the reference concrete systems have a spacing factor of less than 200 microns and insignificant scaling, below 1 kg/m^2 at 56 cycles.

As shown in Figure 5.13 (c) and (d), the reference concrete systems have an RDM of over 90%, suggesting no internal cracking. The concrete with SIP mostly experiences damage beneath the layer penetrated by impregnation. However, the concrete with IIP exhibits internal cracking for all three systems at different extents besides severe surface damage. The plots suggest that the air void system in IIP concrete does not function similarly to regular concrete and cannot provide any pressure relief.

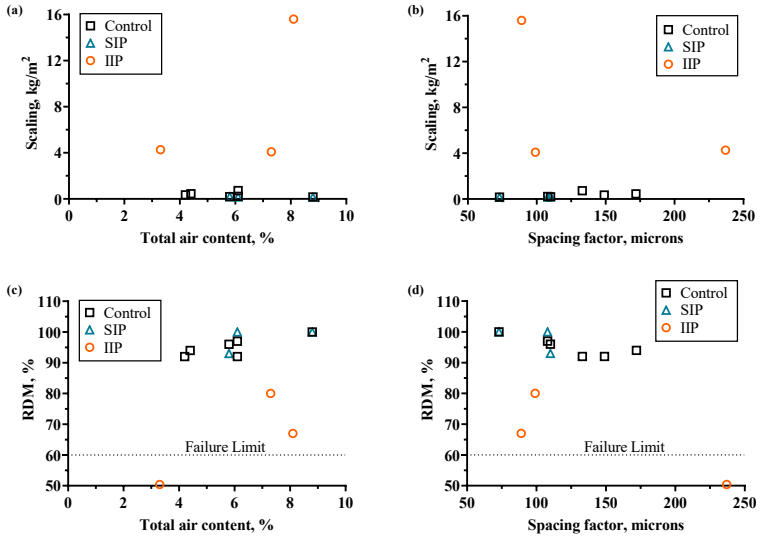

Figure 5.13 Effect of air content and spacing factor on RDM and scaling at about 56 cycles with the presence of hydrophobic impregnation.

One hypothesis proposed for the deterioration of concrete quality resulting from the use of SIP involves water entrapping and accumulation in the surface layer, as illustrated in Figure 5.14. During freezing, ice first forms on the surface of the concrete and gradually moves inward. The ice formation gradient generates external pressure overcoming the water-repelling effect and forcing water to penetrate the concrete. Once the nucleation begins, the growth of ice bodies in surface pores or voids occurs accompanied by the spontaneous movement of unfrozen pore water toward the micro ice bodies until a thermodynamic equilibrium is reached between the ice body and the surrounding pore solution (Powers et al. 1953). The underlying driving force of this moisture flow has been extensively explained in terms of the Gibbs free energy difference between ice and unfrozen water (Borgnakke et al. 2012). During the thawing process, the ice in the container and near the surface of the specimen melts first, making liquid available to be drawn towards the surface ice front. Enhanced suction due to volume relaxation of middle and top portions of concrete can overcome the hydrophobic effect and draw in unfrozen liquid (Liu et al. 2018, Gong et al. 2019). However, water is prevented from flowing back due to the presence of an impermeable layer that can restrict the free movement of water, called the water entrapping effect. This can cause less water to leave the surface-treated layer of concrete than to enter it during an F-T cycle (Perenchio 1988). As the F-T cycle continues, water accumulates in this layer, and the surface layer of the concrete becomes critically saturated, which can result in damage due to pressure build-up. The surface layer may rapidly become debonded from the rest of the concrete, leading to the deterioration (Marchand et al. 1994). However, once the surface layer is eliminated, the rest of the concrete should be similar to untreated concrete (Hazrati et al. 1997), and the internal part of the concrete will generally not be affected.

Based on the analysis, the development of damage can be divided into three stages (Figure 5.15):

- The first stage involves gradual saturation under the impregnated layer, up to a critical saturation point. This stage occurs from the first freezing and thawing cycle until the onset of nonlinear scaling. The use of SIP may effectively delay the surface layer from reaching a state of critical saturation. The length of this stage may vary, depending on the category of SIP and treatment depth. This could also account for the fact that in field conditions, silane is typically more effective than in laboratory settings, which are often harsher, such as those involving continuous water contact.

- The second stage occurs when the use of silane has a negative effect. In this stage, water movements are impeded by the presence of an impervious concrete layer, trapping much of the moisture inside the concrete, unable to be released. As water pressure builds up under the hydrophobic layer, the concrete surface, which is several millimeters deep, is mostly damaged when water expands upon freezing.
- In the third stage, after the impregnated layer is completely eliminated, the scaling behavior is similar to that of untreated concrete. However, this stage requires an extended number of freeze-thaw cycles to be observed.

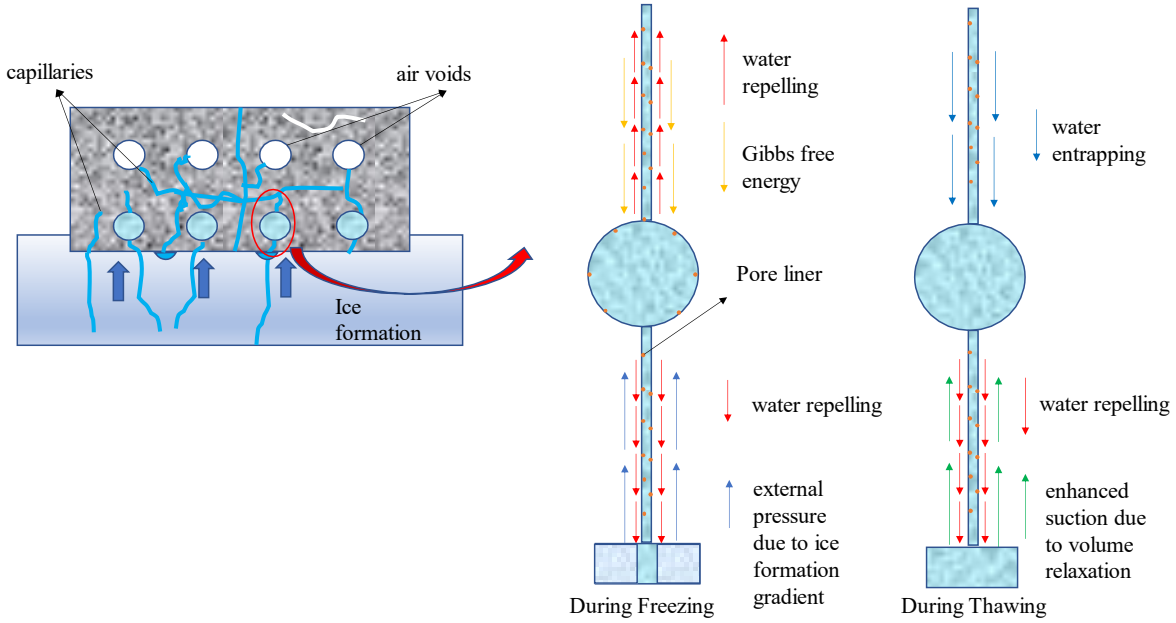

Figure 5.14 Water accumulation of silane-treated surface layer

Concrete with IIP behaves differently from that with SIP because of the presence of pore blockers dispersed throughout the matrix, which obstructs access to air voids. As a result, the pressure relief function of the air void system in the entire specimen is ineffective, as shown in Figure 5.16. This is demonstrated by the fact that, regardless of the air void system's quality, concrete with IIP tends to experience severe damage, either internally or externally in Figure 5.13**.** The absorbed water cannot be expelled into the air voids under the hydraulic pressure induced by ice expansion, instead accumulating in the capillary pores. When the moisture saturation reaches a critical point, the hydraulic or ice expansion pressure (crystallization pressure) causes significant damage, ultimately

leading to concrete failure. In this aspect, concrete with IIP behaves similarly to non-air-entrained concrete.

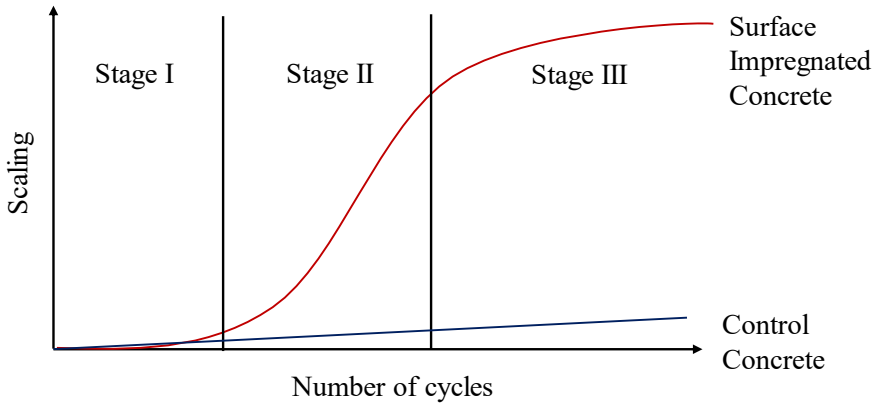

Figure 5.15 Schematic illustration of scaling development in concrete with SIP

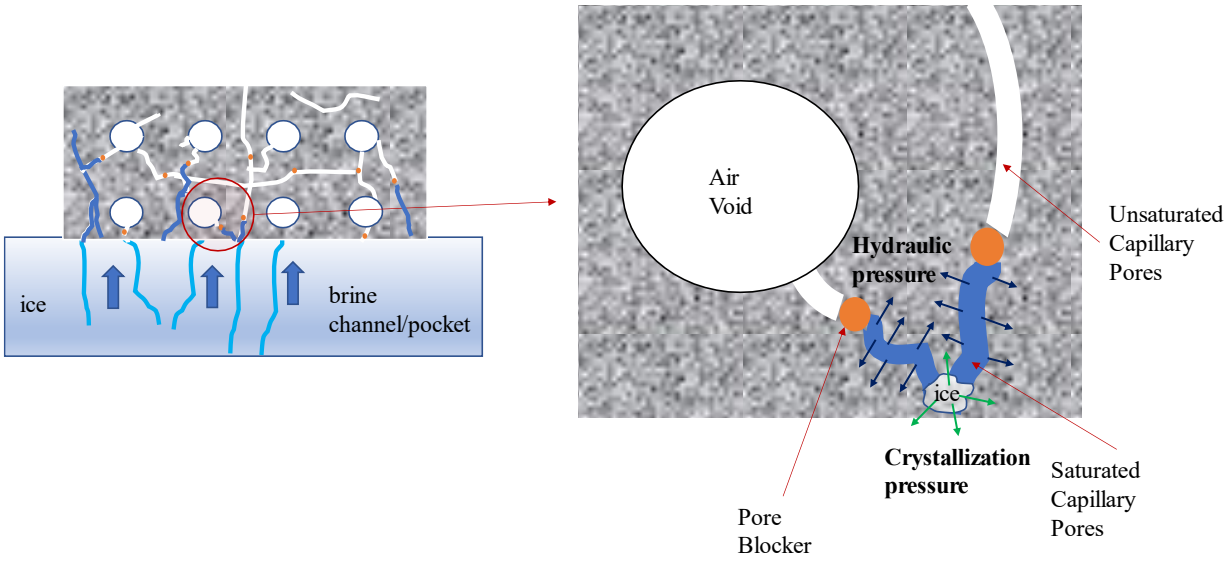

Figure 5.16 Illustration of the blocking effect during F-T cycles

5.5 The link between internal damage and surface scaling

The critical degree of saturation theory proposed by G. Fagerlund suggests that F-T damage occurs only when the moisture content in concrete reaches a certain condition. When it exceeds the critical saturation level, concrete deteriorates rapidly (Fagerlund 2004). The relationship between critical flow distance and the critical water content is illustrated in Figure 5.17. According to this theory, as the degree of saturation increases, some air voids become filled with water, causing the flow

distance to become longer and leading to an increase in pore pressure. This suggests that both flow distance and moisture content are important in determining pore pressure.

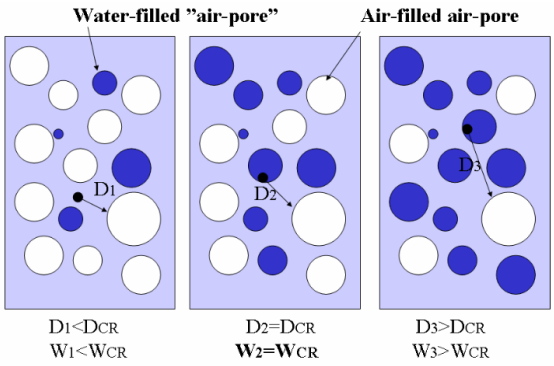

Figure 5.17 At a given, critical water content in a unit cell, the actual flow distance equals the critical value (Fagerlund 2004).

Based on Fagerlund's theory, it is proposed that the surface scaling mechanism shares similarities with internal cracking as noted in other studies (Eriksson et al. 2021). Both types of damage are influenced by moisture uptake and air void system quality.

A qualitative model has been proposed in Figure 5.18. The level of saturation during F-T cycles becomes higher in both hydrophobic impregnated and reference concrete. In Figure 5.18 (a), when the moisture uptake condition does not reach the critical saturation point during the testing period, for instance in less porous or less interconnected microstructures, the damage to the concrete develops slowly and the surface scaling occurs linearly with respect to F-T cycles as seen from the reference concrete systems in this study. Internal cracking is also less likely to occur in these cases. The air void system's quality also affects the likelihood of concrete reaching the critical degree of saturation: when air voids have a low spacing factor, water flow distance is small, and pore pressure is low, preventing severe damage. As the air voids gradually fill with water (Fagerlund 1993, Liu et al. 2016) or if the concrete has a large spacing factor with a more connected and porous pore system as shown in Figure 5.18 (b), the flow distance may increase, and the pore pressure may rise. Once the critical degree of saturation is reached, the concrete deteriorates rapidly, leading to an accelerated scaling development or a drop in RDM.

However, there is a fundamental difference between surface scaling and internal cracking. Surface scaling is influenced by local conditions of moisture uptake and air void system in the surface layer, while internal cracking depends on the overall moisture conditions and quality of the entire

air void system. Bulk moisture conditions measured in experiments do not accurately represent the moisture conditions of the surface layer. Consequently, the time for concrete to reach local and global critical saturation may not be synchronous, which is why the start of accelerated scaling and drop in RDM may not occur at the same time for many concrete samples. The quantification of scaling based on moisture uptake properties and air void system quality will be discussed further in Chapter 6.

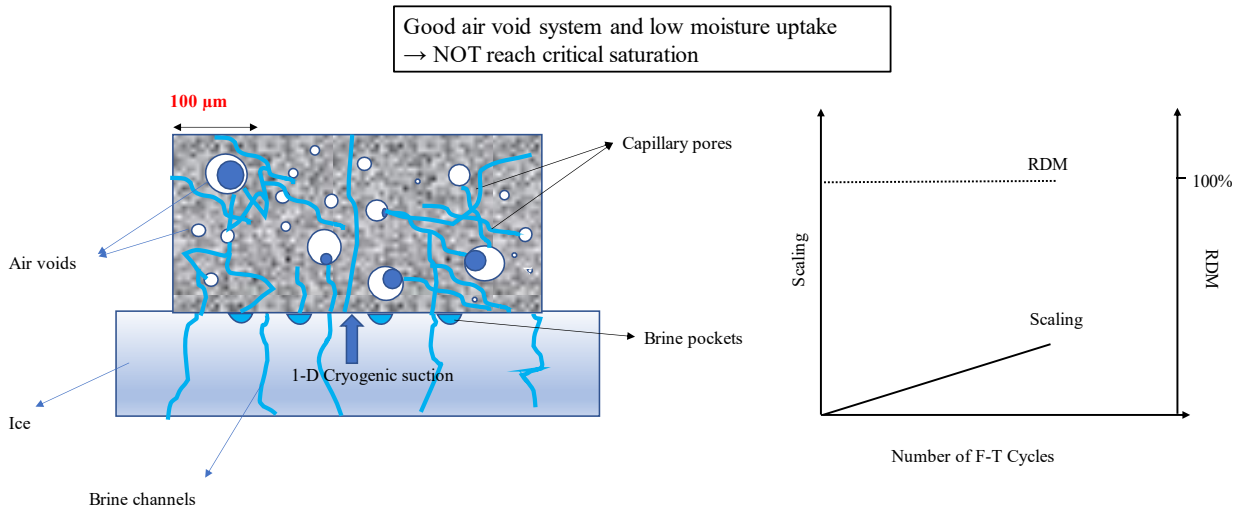

(a)

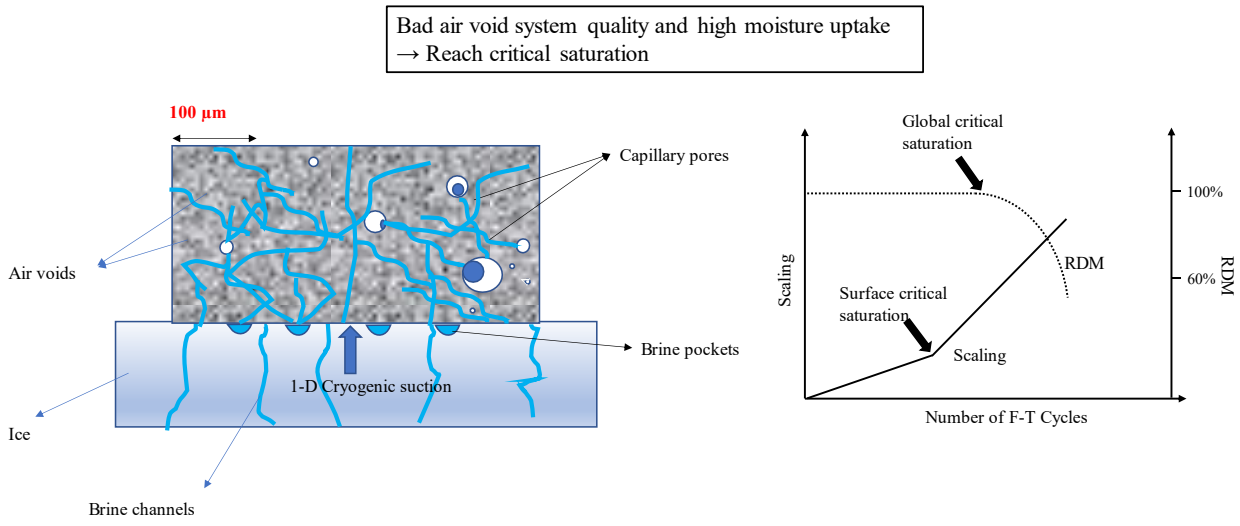

(b)

Figure 5.18 Effect of air void system and moisture uptake on the development of surface scaling and internal cracking

This finding may also explain why exposure to water and salt can produce different results in terms of scaling, while internal cracking is less sensitive to changes in salt concentration. Salt exposure causes the added degree of saturation to reach the critical degree of saturation on the surface, based on the cryogenic suction model discussed in Chapter 4. However, this increase in moisture content may be too small to cause a significant difference in the bulk degree of saturation that is associated with internal cracking. The internal cracking can occur even with pure water called regular F-T attack.

The reference concrete used in this chapter had a low scaling rate and no internal cracking, which can be attributed to the addition of SCMs and a low spacing factor. These factors prevented the concrete from reaching the critical saturation condition, either locally or globally. The surface-impregnated concrete reached critical saturation only on the surface layer, so severe scaling occurred without any internal cracking. Conversely, the internally impregnated concrete nullified the entire air void system, making the concrete quickly reach the critical degree of saturation and resulting in the most severe damage.

5.6 Summary

Hydrophobic impregnation is commonly employed to control moisture uptake, limit chloride ion penetration, and reduce the risk of steel corrosion. It has shown the potential to improve the F-T resistance of pavement concrete. In this regard, a laboratory study was conducted to evaluate the efficacy of hydrophobic impregnation, both internal and external, on the F-T durability of air-entrained concrete pavement mixes with a 0.40 w/cm ratio.

The study aimed to achieve three major objectives. Firstly, it sought to investigate the effects of two different impregnation methods on the F-T resistance of pavement mixes, one involving the addition of a pore blocking admixture during the mixing process and the other involving surface treatment with a hydrophobic silane on a pre-dried surface. The second objective focused on assessing the effectiveness of hydrophobic impregnation in preventing moisture uptake during F-T pumping. Finally, the third objective aimed to determine whether the air void system remained effective in the presence of hydrophobic impregnation. The study yielded several major findings.

- The hydrophobic impregnation involved in this study is ineffective in preventing pumping during an F-T cycle and eventually leading to oversaturation.

- The hydrophobic impregnation in this study does not produce supplementary protection for concretes with good F-T resistance. Internal pore-blocker application results in the most severe F-T deterioration, characterized by a decrease in modulus and accelerated surface scaling, irrespective of SCM type and air void parameters. In contrast, surface-treated specimens develop severe damage only in the superficial treated layer after saturation.
- The surface impregnation turns the pore structures from a hydrophilic to a hydrophobic state and causes the entrapping effect in the surface treated layer while the internal impregnation nullifies the air void system in providing pressure relief. The importance of maintaining a hydrophilic pore surface under F-T conditions can be concluded based on the negative effect of a hydrophobic treatment.
- The mechanisms of surface scaling and internal cracking both rely on moisture uptake conditions and air void quality. However, surface scaling is more related to local moisture uptake conditions, while internal cracking is associated with the overall degree of saturation. This explains why accelerated scaling and internal cracking may not occur simultaneously, with the former being more sensitive to changes in salt concentration, while the latter is not. .

Chapter 6. Quantification and Modeling of Salt Frost Scaling Resistance in Concrete

6.1 General

Conventional laboratory evaluation of salt frost scaling is known to be extremely time-consuming and labor-intensive. As a result, researchers have been exploring alternative methods to efficiently assess and predict the F-T performance of concrete in the field. In particular, they have been investigating properties such as sorptivity and air void parameters, with the aim of correlating concrete scaling resistance with these hardened properties. This approach has generated significant interest within the research community, as it has the potential to improve both quality control and service life design of the concrete by allowing for a quicker assessment of concrete performance.

This chapter is organized into three main sections. The first section provides a detailed discussion of the primary moisture transport method in concrete and introduces the theory of sorptivity. Through analysis, the relationship between scaling and critical moisture uptake properties is explored. The second section examines various air void parameters. The correlations among them and their impact on scaling are discussed. Finally, a polynomial regression model is proposed, which quantifies scaling using selected parameters, such as sorptivity and spacing factor. These topics collectively shed light on the intricate mechanisms governing scaling and offer valuable insights for designing and assessing durable concrete structures.

6.2 Water uptake properties as a predictor of salt frost scaling resistance in concrete

An understanding of moisture transport in concrete and mortar is crucial for estimating their service life as building materials and improving their quality. Concrete structures absorb water through diffusion, permeation, and capillary suction. Diffusion is a mass transfer process from high to low concentration areas (Dullien 2012) which is a very slow process. Permeation is a kind of saturated flow that occurs when a liquid or gas penetrates a solid under pressure and is related to the material's permeability (Yong et al. 1992). However, saturated flow is uncommon in

concrete structures due to alternating moisture and dryness exposure. On unsaturated concretesurfaces, capillary suction is a significant mode of transport and better characterizes the transport behavior (Hall 1989, Wilson et al. 1999).

6.2.1 Discussion on the unsaturated flow and sorptivity theory

When a tube of a small diameter such as a capillary pore comes into contact with free water, a meniscus can form within the tube as a result of the contact angle between water and the tube walls. This meniscus is formed to meet the minimum surface energy requirements. A pressure drop ΔP will be produced by the surface tension force at the interface which can be captured by Laplace's law

$$\Delta P = \gamma k, \qquad \text{Eq. 6.1}$$

where γ is the surface tension of the liquid and k is the average curvature of the interface (Adamson et al. 1967) and k can be calculated as

$$k = \frac{2\cos\theta}{r}, \qquad \text{Eq. 6.2}$$

where r is the average radius of the pore tube and θ is the contact angle. As a result,

$$\Delta P = \frac{2\gamma\cos\theta}{r}. \qquad \text{Eq. 6.3}$$

According to Darcy's Law (Whitaker 1986), the average flow velocity V can be obtained from the following equation

$$V = -\frac{K\Delta P}{l\mu}, \qquad \text{Eq. 6.4}$$

where K is the permeability, μ is the viscosity of the liquid and l is the length along which the pressure drop is obtained. Assuming a capillary cube where $K = r^2/8$

$$V = \frac{r}{4\mu l}\gamma\cos\theta. \qquad \text{Eq. 6.5}$$

This equation does not take the effect of gravity and effects due to the details of the contact line motion into consideration. As V changes according to the radius of the tube, porous materials that have smaller pores will have slower liquid uptake. Take $V = \frac{dl}{dt}$, the following equation can be obtained (Martys 1997)

$$l = \sqrt{\frac{r\gamma \cos\theta t}{2\mu}} = St^{\frac{1}{2}}. \qquad \text{Eq. 6.6}$$

Sellevold developed a model for the computation of sorptivity based on the total porosity and average radius of the pores shown in Figure 6.1 (Sellevold 1990). Here, the permeability of the tubes assumed can be replaced by the permeability of the porous medium. Sorptivity can be calculated as

$$S = \left(\frac{\gamma r}{2\mu}\right)^{0.5} \varepsilon_0, \qquad \text{Eq. 6.7}$$

where ε_0 is the total porosity (cc/cc concrete) in the surface region and r is the average radius of the pores. This model gave a theoretical basis that sorptivity is dependent upon the total porosity, and the average size of pores.

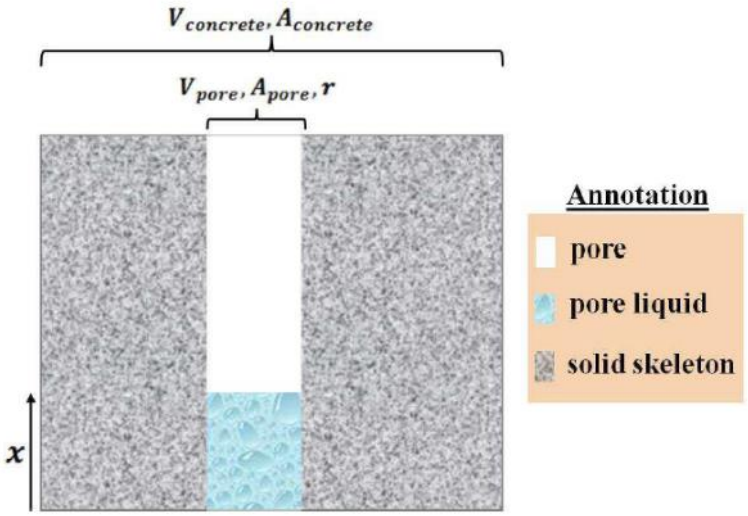

Figure 6.1 A simplified schematic model for estimating the sorptivity of concrete (Sellevold 1990)

The total porosity can be estimated

$$\varepsilon_0 = \frac{\frac{W}{C} - 0.18\alpha}{\frac{W}{C} + 0.32}, \frac{w}{c} > 0.38, \qquad \text{Eq. 6.8}$$

or

$$\varepsilon_0 = \frac{\frac{W}{C}(1 - 0.47\alpha)}{\frac{W}{C} + 0.32}, \frac{w}{c} > 0.38. \qquad \text{Eq. 6.9}$$

A deficiency of this equation is that it only applies to the Portland cement concrete. SCM has a great impact on the average size of the pores, connectivity of the concrete, and thus the porosity of the concrete. To account for this, sorptivity is plotted against capillary porosity for concrete containing 30% GGBFS, as shown in Figure 6.2. Other concrete systems are also included. The plot demonstrates that sorptivity is linearly proportional to the total porosity of the concrete, which is consistent with Eq. 6.7.

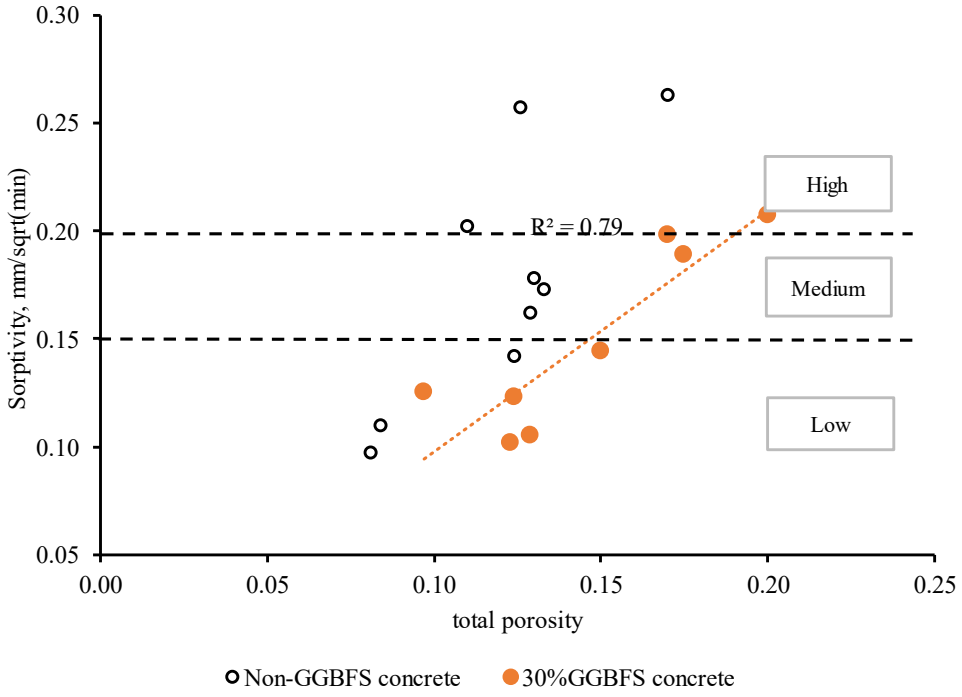

Figure 6.2 Relationship between the sorptivity and capillary porosity

It is inconvenient to obtain the pore size distribution and porosity to calculate the sorptivity. Instead, sorptivity is typically determined by analyzing the initial slope of the moisture uptake curve plotted against the square root of time, as illustrated in Figure 6.3. The moisture uptake can be described by

$$l = \frac{V}{A} = St^{\frac{1}{2}} + S_0, \qquad \text{Eq. 6.10}$$

where l is the cumulative moisture uptake per inflow concrete area, V is the volume of water uptake, and A is the surface area exposed to water, S_0 is usually found which is attributed to the filling of open surface pores.

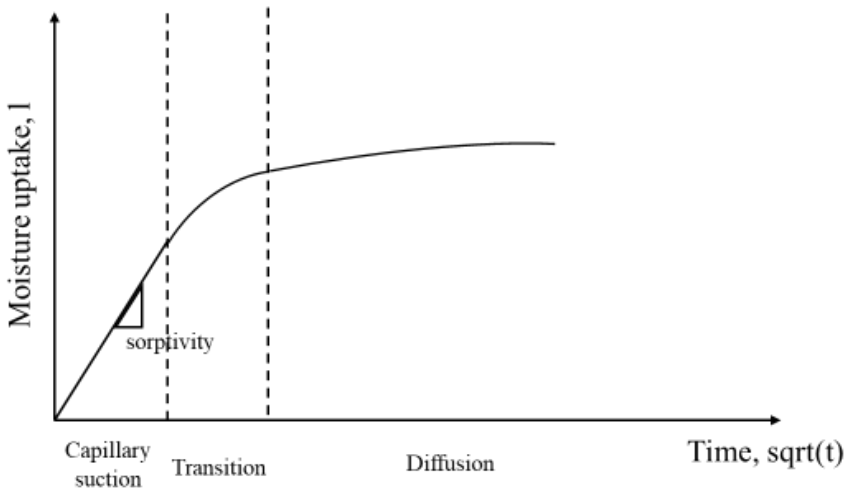

Figure 6.3 A typical moisture uptake curve in concrete

6.2.2 Relationship between F-T resistance and water transport properties

It is challenging to measure the moisture conditions in the surface layer, which is directly related to scaling. As a result, parameters such as sorptivity and total moisture uptake, which can indicate such a moisture uptake level should be considered.

The studies regarding the relationship between scaling and sorptivity are quite limited. Gagné et al. (2011) found a strong correlation between scaling resistance and sorptivity as shown in Figure 6.4. A higher sorptivity value is typically associated with larger scaling, and concrete with a low sorptivity (<0.1 mm/min$^{0.5}$) is considered durable while they admitted other parameters may influence the scaling resistance of concrete. Similar results were obtained in our research group. Liu and Hansen proposed that concretes with a high sorptivity exhibit poor scaling resistance as illustrated in Figure 6.5 (Liu et al. 2014).

This study examined 17 different air-entrained concrete systems, which varied in w/cm (ranging from 0.35 to 0.45), SCM addition (30% GGBFS, 30% fly ash, and 4-8% silica fume), and lightweight aggregate content (at 10%, 25%, and 40% levels). Table 6.1 presents the results of the sorption test and F-T test. Among the tested samples, 035-30%GGBFS-10%LWA exhibited the lowest sorptivity value of 0.09 mm/min$^{0.5}$, while the 040-Control-28day sample demonstrated the highest sorptivity value. This finding is consistent with the discussion in Chapter 4, which highlights the impact of w/cm, and SCMs on moisture uptake.

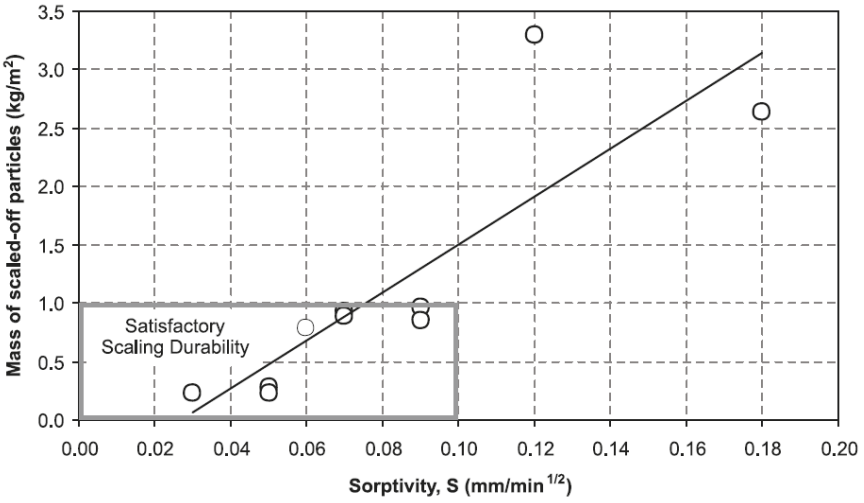

Figure 6.4 Relationship between the mass of scaled-off particles and sorptivity

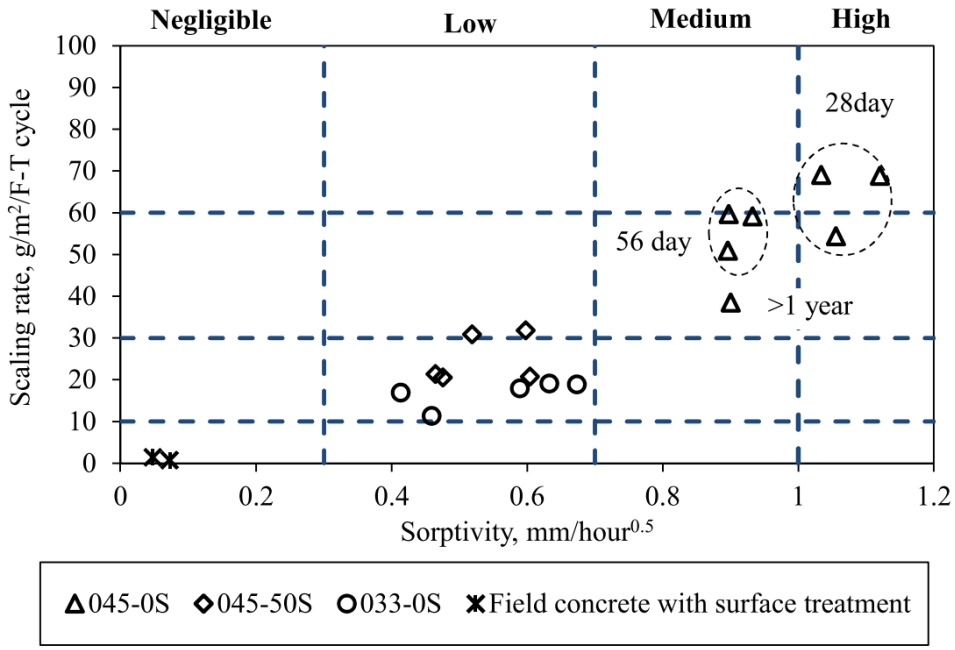

Figure 6.5 An empirical correlation between scaling rate and sorptivity in air-entrained concretes

As illustrated in Figure 6.6 (a), scaling generally increases as sorptivity increases, as a lower sorptivity suggests a denser cement paste matrix and better resistance to water penetration, which reduces the pressure source on the concrete. The most durable concrete has a sorptivity value of less than 0.15 mm/min$^{0.5}$ and a scaling of less than 1 kg/m^2. However, some data points within the black oval in Figure 6.6 (a) do not conform to this trend. The systems that are in the black oval have a much smaller spacing factor compared to those with a similar sorptivity but higher scaling.

Table 6.1 Sorption test and F-T test results

Batch ID	Curing age, day	Sorption Test		F-T performance at 56 cycles	
		sorptivity $mm/min^{0.5}$	Water absorption, mm	Scaling, kg/m^2	RDM, %
035-30%GGBFS	28	0.123	4.3	0.37	98.9
035-30%GGBFS-10%LWA	28	0.102	3.5	0.28	99
035-30%GGBFS-25%LWA	28	0.144	4.6	0.09	93.5
035-30%GGBFS-40%LWA	28	0.105	4.3	0.08	98
037-8%SF	28	0.142	4.6	0.76	96.6
039-4%SF	28	0.257	7.7	1.23	97.6
040-30%GGBFS	28	0.189	6.6	0.23	97.4
040-30%GGBFS-25%LWA	28	0.207	7.5	0.20	99.3
040-30%GGBFS-40% LWA	28	0.198	7.2	0.18	98
040-8%SF-18%LWA	28	0.162	4.5	0.44	94.4
040-4%SF-18%LWA	28	0.173	5.2	0.18	100
040-Control-28day	28	0.263	9.2	2.45	95.9
040-Control-90day	90	0.202	7.8	2.12	86
040-30% Flyash Class C	90	0.110	3.3	0.47	96
040-30% Flyash Class F	90	0.097	4.2	0.35	92
045-30%GGBFS	90	0.125	6.9	0.50	99.1
045-6%SF-25%GGBFS	28	0.178	6.1	1.15	97

This indicates that other factors may also play a role in scaling resistance (Gagné et al. 2011). The relationship between scaling and total moisture uptake exhibits a similar trend as shown in Figure 6.6 (b), with concrete having a total moisture uptake of less than 5.5 mm and being more resistant to salt frost scaling. Similarly, there are also concrete systems in the black oval that do not adhere to this trend.

The relationship between sorptivity and total moisture uptake is shown in Figure 6.7. Although there is a strong linear correlation between sorptivity and total moisture uptake, sorptivity should be a superior indicator of scaling resistance compared to total moisture uptake. The distinction between these two parameters stems from the fact that total moisture uptake is linked to the total connected pore volume and provides an overall indication of moisture levels throughout the specimen, whereas sorptivity is related to the total porosity, pore connectivity, and capillary size (Liu et al. 2015b). Sorptivity reflects the ease with which water can saturate the pores and can be useful for predicting how easily critical saturation is reached (Martys et a. 1997). Therefore, sorptivity is a more effective indicator than total moisture uptake for determining scaling resistance. Most of the concrete systems did not exhibit internal cracking after 56 cycles with only one system, 040-Control-90day, having a slightly below 90% RDM after 56 cycles, possibly due to over-saturation.

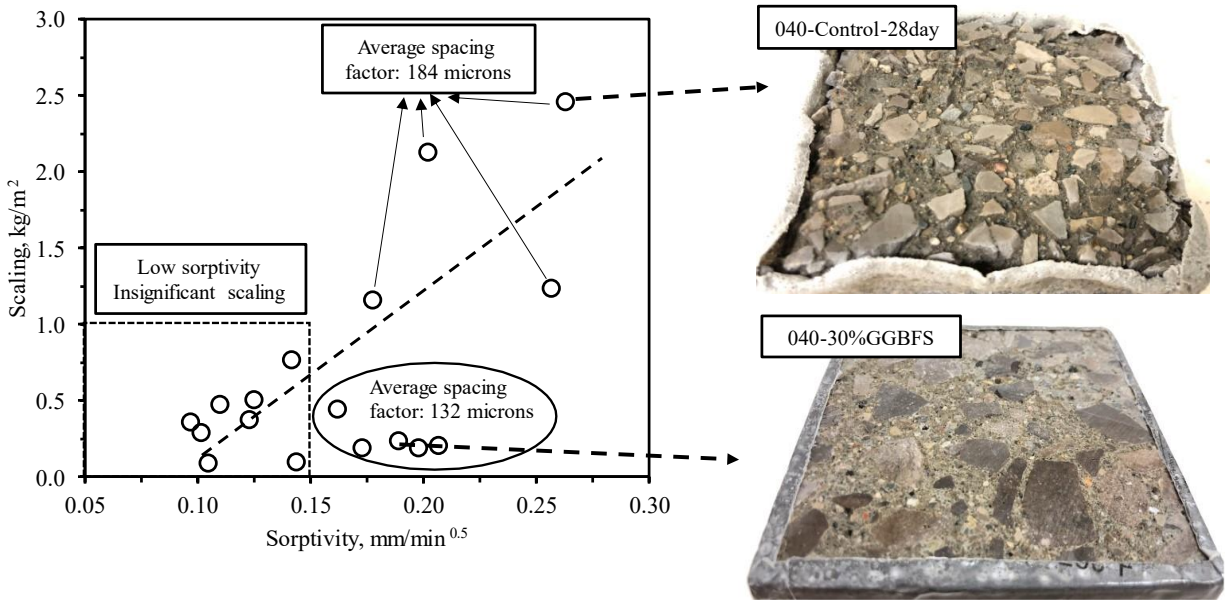

(a)

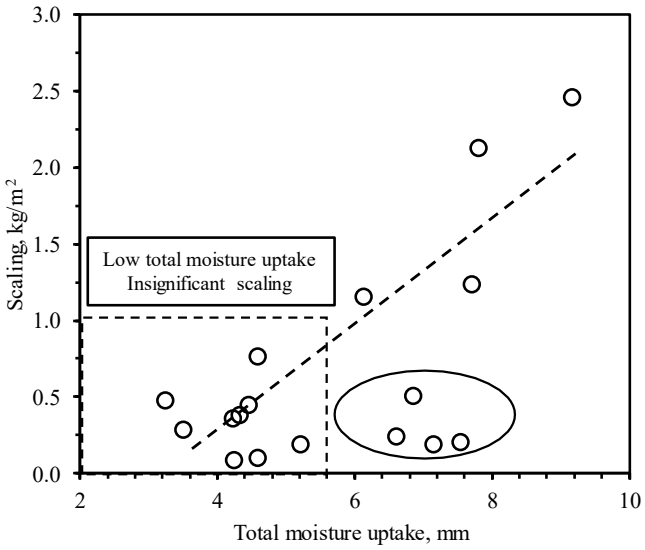

(b)

Figure 6.6 Scaling at 56 cycles with respect to (a) sorptivity (b) 7-day water absorption

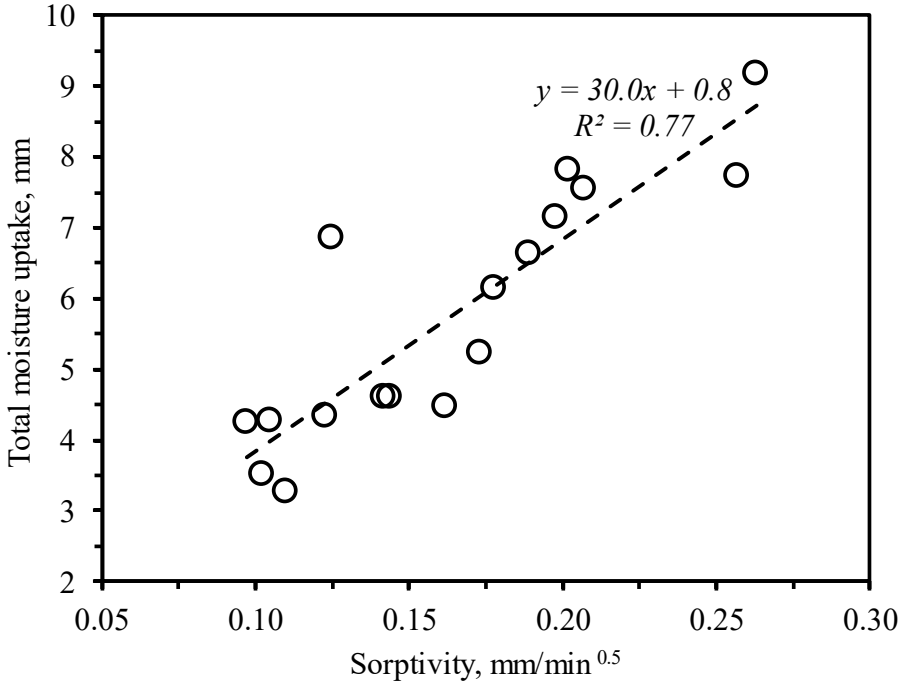

Figure 6.7 Relationship between sorptivity and 7-day total moisture uptake

6.3 A comprehensive study on the characterization of air void system

6.3.1 Introduction to air void system

The importance of an air void system in salt frost scaling resistance has been widely recognized based on laboratory and field results. While the specific physical mechanism of F-T deterioration is still debatable, it is indisputable that a sufficient number of entrained air voids in the cement paste can greatly enhance F-T durability (Snyder 1998). As a consequence, extensive efforts have been devoted to characterizing the air void system for several decades. The key characteristics pertaining to the air void system include the amount, spacing, and size distribution of the air bubbles. The specific surface which relates to the size distribution of the air voids and the air void content (with respect to paste content) are the most basic properties of the air void system. A more comprehensive parameter that represents the quality of the air void system should include both of these aspects. A summary plot of the relationship between air void content, specific surface, and other parameters is shown in Figure 6.8.

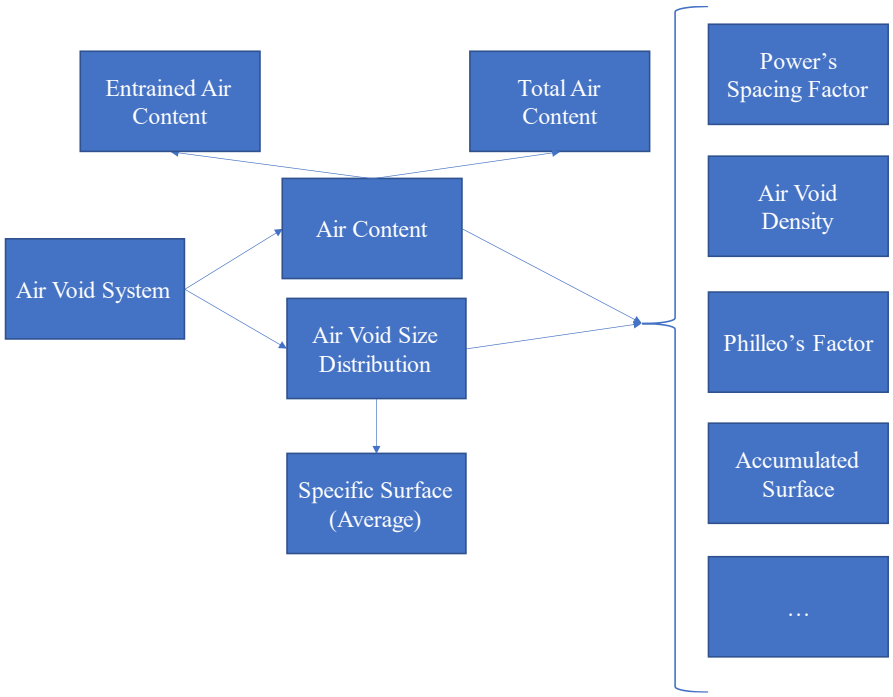

Figure 6.8 A summary of the air void parameters

ASTM C125 (2013) provides a categorization of air voids based on their size and shape. The first category is known as entrained air voids, which are spherical or nearly spherical and typically have diameters between 0.001 and 1 mm. These voids are intentionally introduced into the concrete

through the use of air-entraining agents. The second category is called entrapped air voids, which are irregular in shape and have diameters of 1 mm or more. These voids are unintentionally created during the mixing or placing of the concrete and may have a negative impact on the concrete's strength and freeze-thaw durability. It should be noted that large entrapped air voids while increasing the air content of the concrete, do not significantly affect the spacing between air voids. Figure 6.9 shows examples of these two types of air voids under a microscope. The air content of the concrete can be calculated as either total air content or entrained air content, with or without the entrapped air voids, respectively.

The air content is a critical parameter in evaluating the quality of concrete and is commonly expressed as a percentage of the cumulative air volume to the concrete volume. Specific air content requirements are recommended by standards and provisions such as ACI 201 (2016), ACI 301 (2016), and ACI 318 (2019) depending on the severity of the exposure. However, it is essential to note that meeting the recommended air content does not always guarantee optimal freeze-thaw performance. For instance, some concrete mixes with acceptable air content may have large portions of entrapped air, which offers minimal protection to the concrete, leading to an overestimation of the freeze-thaw resistance. Consequently, air content may not be a reliable indicator.

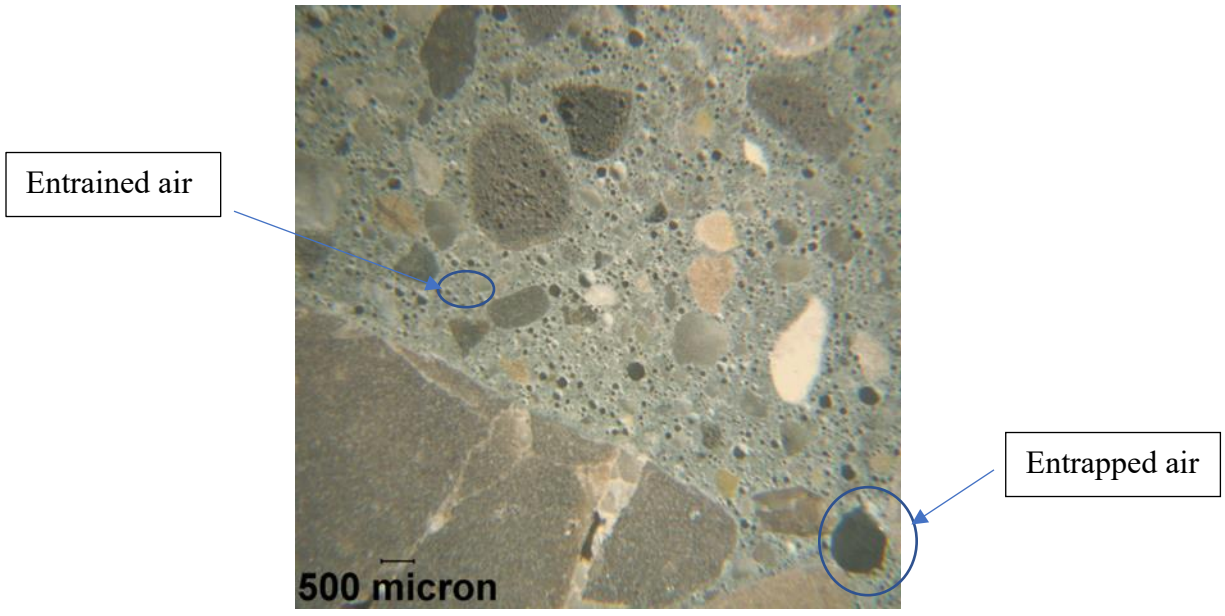

Figure 6.9 Microscopic image of concrete containing entrained and entrapped air

Specific surface α is defined as the surface area of the air voids divided by their volume. The unit of specific surface is a reciprocal length as it is associated with the average chord length of the air voids. Specific surface can be calculated using the following equation,

$$\alpha = \frac{4}{\bar{l}}, \qquad \text{Eq. 6.11}$$

where $\bar{l}$ is the average chord length. As the equation suggests, larger values of α correspond to lower $\bar{l}$ value, i.e., finer air voids on average.

It is widely acknowledged that the spacing of the voids, rather than their total volume, is what determines the susceptibility of concrete to frost damage. To obtain a more accurate diagnosis of concrete performance, the spacing can be measured using polished sections of hardened concrete. Numerous spacing equations have been proposed by researchers (Powers 1945, Philleo 1983, Lu et al. 1992, Attiogbe 1993, Pleau et al. 1996, Lindmark 1998, Lindmark 2010, Liu et al. 2019). These equations can be broadly divided into two categories: void-void proximity and paste-void proximity. Void-void proximity measures the surface-to-surface distance between two air voids and can be classified into nearest air voids or the average length of paste between two air voids intersected by a random line (i.e., Attiogbe's spacing factor or mean free path). Paste-void proximity estimates the volume fraction of paste within some distance from the surface of the air voids and is more frequently used. This study focuses on the well-known paste-void spacing factors from Powers, Philleo, Lu and Torquato.

6.3.2 Powers spacing factor

Powers spacing factor (PSF) is the most used paste-void spacing factor. It was originally proposed by Powers who suggested that hydraulic pressure is the cause of damage during frost action (Powers 1949). When water freezes, its volume increases and expels unfrozen water from the site of ice formation. This expelled water generates hydraulic pressure in the pores and can cause damage to the concrete. The pressure buildup depends on the flow length to a free surface, which is provided by the air voids. Although the validity of this hypothesis has been questioned, PSF is the earliest attempt to quantify the air void system's spacing. It has been proved effective in many experimental and field results.

Powers considered two scenarios to calculate the spacing factor. In the first scenario, where there is little paste around each air void, Powers used the 'frosting' approach by assuming that all the

paste was uniformly distributed in a layer over each air void. The mean thickness of the cement paste around the air voids can be obtained using the volume of the cement paste divided by the total surface area of the air voids. This approach was used when the paste-to-air ratio (p/A) was not greater than 4.342. In this case, the spacing factor can be calculated as

$$\bar{L} = \frac{p}{\alpha A}, \qquad \text{Eq. 6.12}$$

where $\bar{L}$ was the spacing factor, p was the paste content, α was the specific surface and A was the air content.

In the second scenario, when the paste-to-air ratio is large, the model divides the total cement paste volume into equal-sized unit cubic cells that contain a spherical air void of constant size in the center, as depicted in Figure 6.10. In this case, Powers' spacing factor is defined as half the mean distance between the periphery of the air voids and provides an estimate of the longest distance to an air void surface. It can be calculated using the following equation when p/A exceeds 4.342:

$$\bar{L} = \frac{3}{\alpha}\left[1.4\left(1 + \frac{p}{A}\right)^{\frac{1}{3}} - 1\right]. \qquad \text{Eq. 6.13}$$

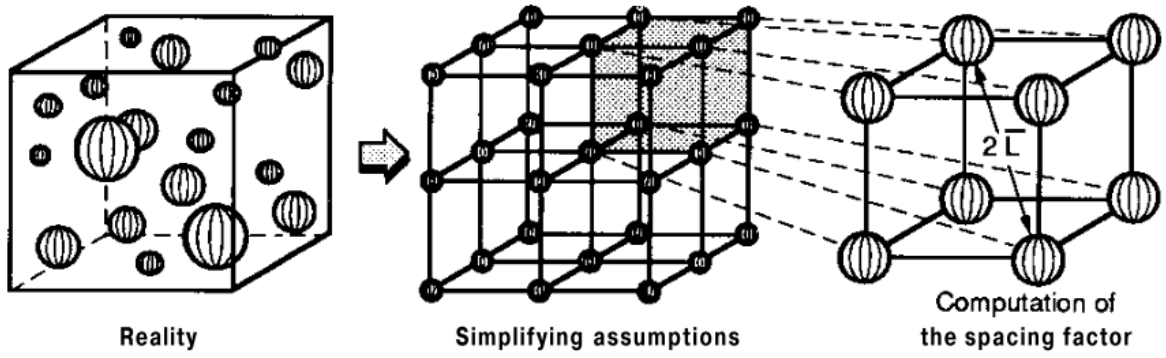

Figure 6.10 Assumption of cubic arrangement of the air voids in cement paste for spacing factor computation

It is acknowledged that the calculated spacing factor according to Powers' method tends to overestimate the actual spacing factor. Therefore, the smaller value between the two equations is generally used. Powers' equation estimates the distance from the surface of all the air voids that would include a significant portion of the paste, but the percentile of the paste included in the estimate is not specified.

Many regulating bodies and agencies adopt a spacing factor of 200 μm for concrete to achieve good salt scaling resistance. In general, scaling decreases with the decrease in the spacing factor. However, the relationship between scaling and spacing factor is not straightforward, and experimental results do not always show a strong correlation (Tanesi el al. 2007, Lindmark 2010, Hasholt 2014, Amini et al. 2019).

6.3.3 Effect of entrained air voids and entrapped air voids on spacing factor and specific surface

Powers spacing factor provides only a rough estimate of the real spacing in hardened concrete (Pigeon et al. 1996). This is due to the hypothetical system of equal-sized spherical voids uniformly distributed throughout the paste. The actual air voids in concrete are randomly distributed in space. Moreover, the entrapped air voids, which account for a significant proportion of the total air content, contribute little to the actual spacing of the air void system. The calculation of the spacing factor is based on the average specific surface of all the air voids in ASTM C 457 and thus the original value of a spacing factor is greatly affected by the large air voids.

Figure 6.11 shows cumulative air content percentage and cumulative number of air voids percentage plots based on the air void size of typical concrete. It is important to note that chords smaller than 30 microns are not included in the analysis as they are not easily detectable during analysis and may cause an overestimation of the number of air voids (Taylor et al. 2021). This exclusion has been applied by many researchers in previous studies (Jakobsen et al. 2006, Ley 2007, Peterson et al. 2009, Ramezanianpour et al. 2010, Taylor et al. 2021). Figure 6.11 demonstrates that although the number of air voids larger than 500 microns (mostly entrapped air voids) only accounts for 2% of the total number of air voids in the concrete, this portion contributes about 20% of the total air content. Consequently, it is a good practice to exclude this part of entrapped air voids when calculating the spacing factor (Pleau et al. 1990, Kang 2010, Liu 2014). The concrete presented in Figure 6.11 has a total air content of 6.1% and an entrained air (up to 500 microns) content is 4.9%. The specific surface of all air voids is 42.5 mm^{-1} compared to 51.7 mm^{-1} of the entrained air voids. The original spacing factor based on all air voids changes from 108 microns to 98 microns based on entrained air voids only.

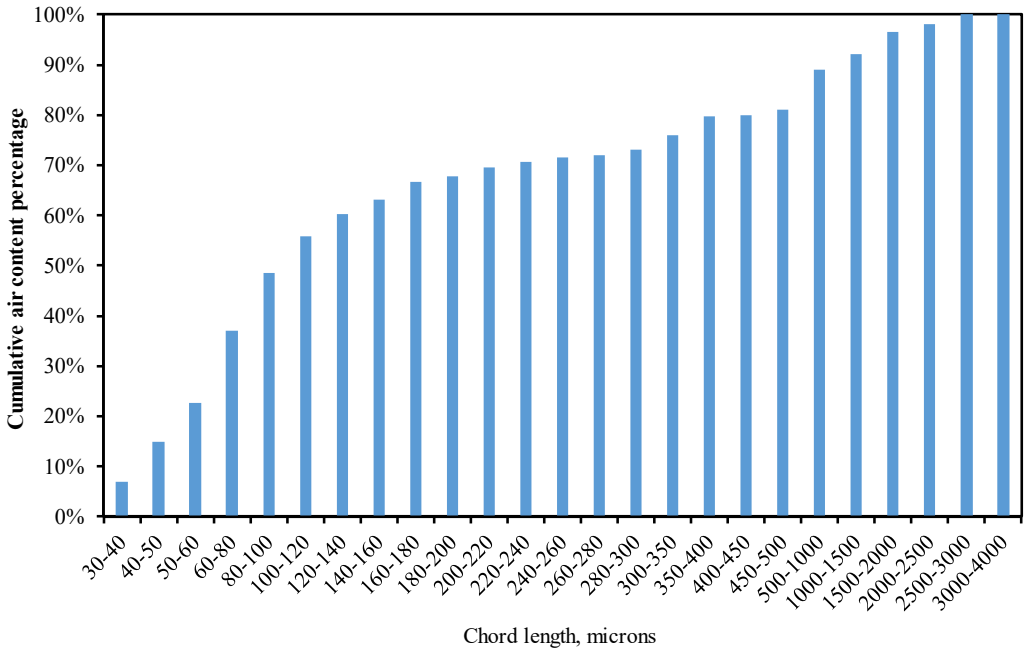

(a)

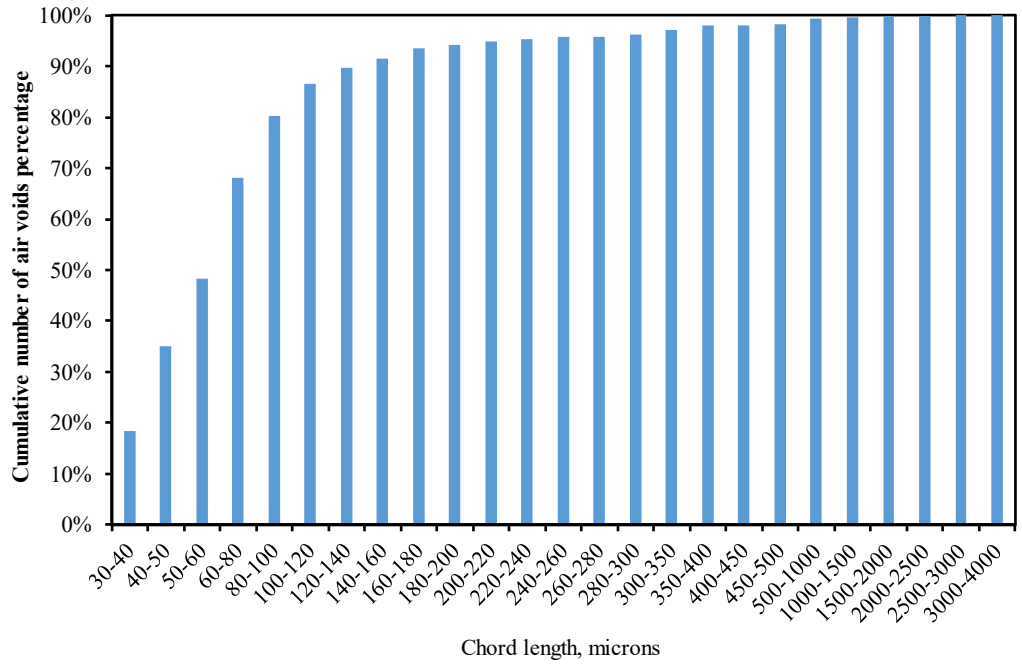

(b)

Figure 6.11 Cumulative percentage of air content and number of air voids for 040-30%GGBFS system (Powers spacing factor = 108, total air content = 6.1%)

The entrained air voids can provide a more accurate estimate of the 'real' spacing factor. The theoretical line in Figure 6.12 is drawn based on the average paste content, air content, and specific surface of all concrete samples. Depending on the paste-to-air content, the appropriate equation is used to calculate the theoretical value. The experimental data points in Figure 6.12 (b) are more closely clustered around the theoretical line than those in Figure 6.12 (a). The coefficient of determination between the spacing factor and entrained air content increases from 0.47 to 0.58.

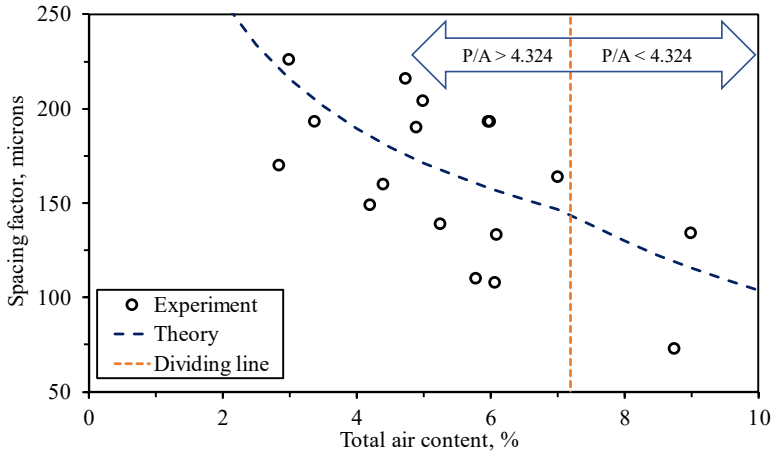

(a)

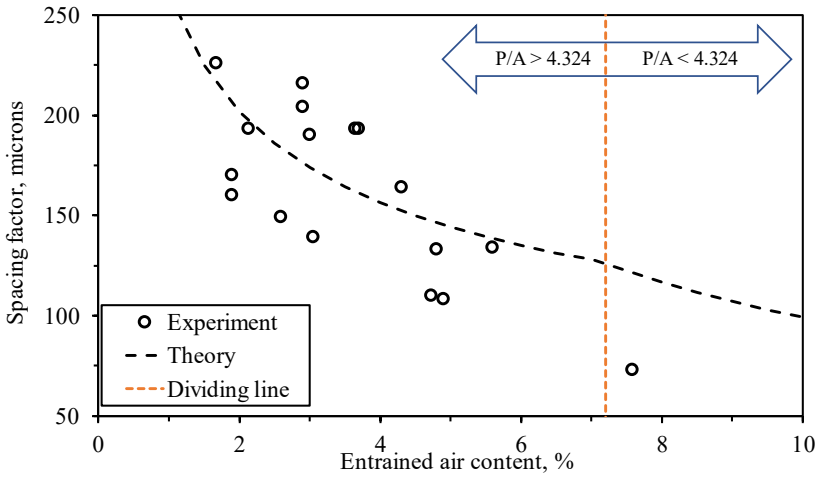

(b)

Figure 6.12 Relationship between spacing factor and (a) total air content (b) entrained air content

The relationship between the Powers spacing factor and the spacing factor based on entrained air voids was investigated, and a strong linear correlation was found (see Figure 6.13). The spacing factor based on entrained air voids accurately represents the original spacing factor, indicating that entrained air has a dominant effect in determining the spacing of the air void system. The exclusion of a few large air voids results in a smaller value of the spacing factor due to a decrease in the mean diameter of the air voids and a larger value of the specific surface. This finding is consistent with the results of previous studies (Sommer 1979, Walker 1980, Langan et al. 1986, Pleau et al. 1990).

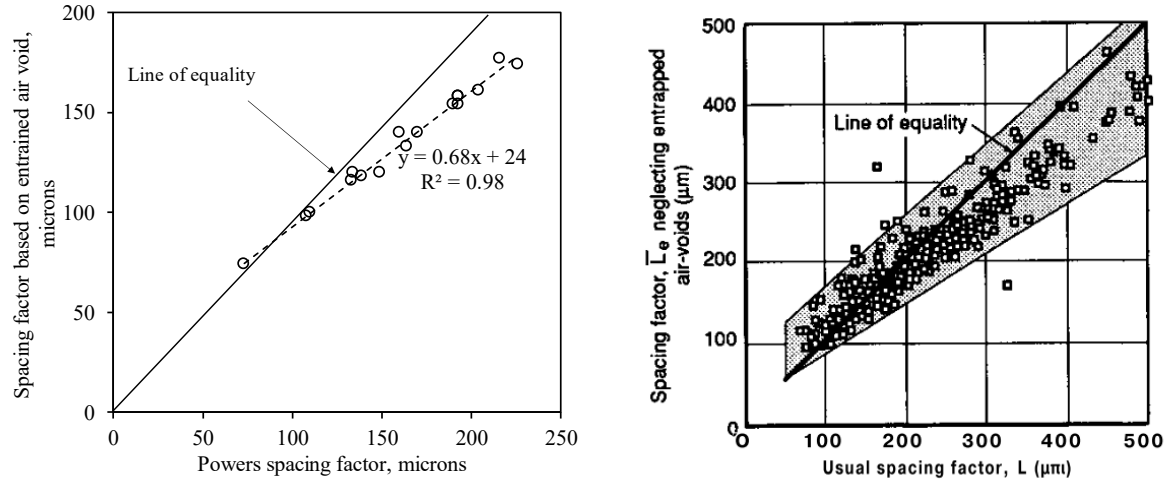

(a) (b)

Figure 6.13 Comparison between Powers spacing factor and spacing factor based on entrained air voids (a) from this study (b) from literature review (Pleau et al. 1990)

The specific surface of air voids is independent of the air void content and instead depends on the distribution of air voids, as illustrated in Figure 6.14. The entrained air void system has an average specific surface of 45.6 mm^{-1}, which is much larger than the specific surface of the entire air void system. Notably, the variation in specific surface is greater for the total air content than for the entrained air content. The standard deviation of specific surface for entrained air void system is 6.4 mm^{-1} compared to 7.6 mm^{-1} for the entire air void system. This is due to the fact that the entrained air void system has a smaller size range and specific surface is less influenced by extremely large air voids. Consequently, this may explain why the data points in Figure 6.12 (a) appear more scattered.

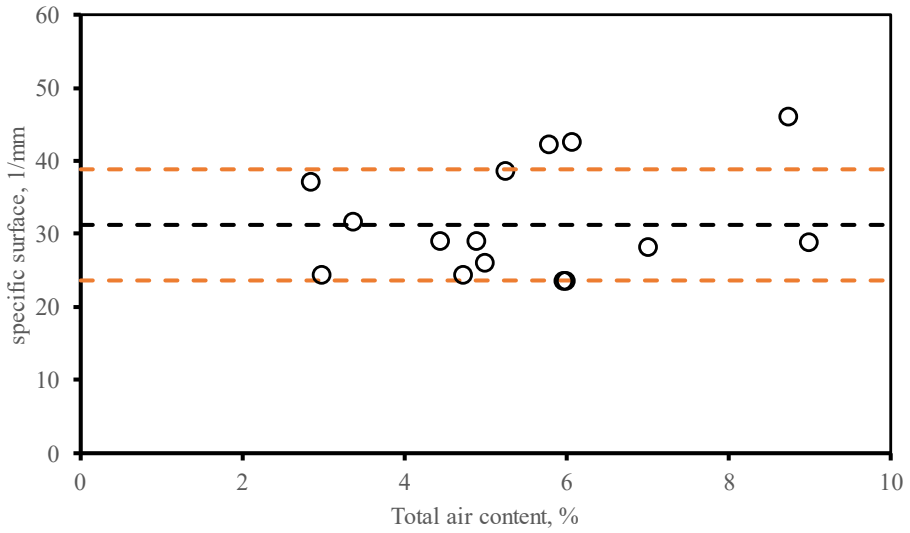

(a)

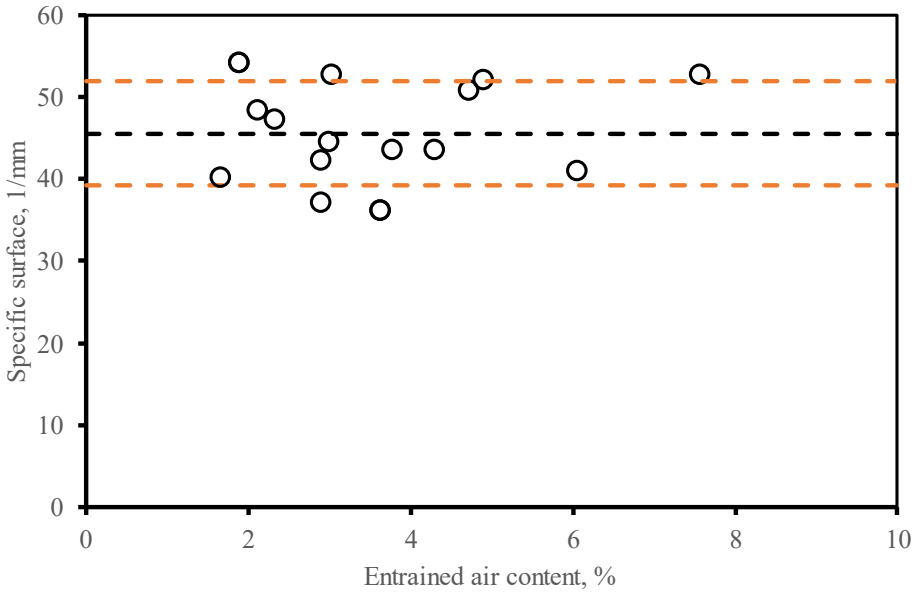

(b)

Figure 6.14 Relationship between specific surface and (a) total air content (b) entrained air content

The impact of specific surface on the spacing factor issignificant, as illustrated by the simulation in Figure 6.16. Concrete with a larger specific surface, which indicates finer air voids, will result in a smaller spacing factor for the same air content.

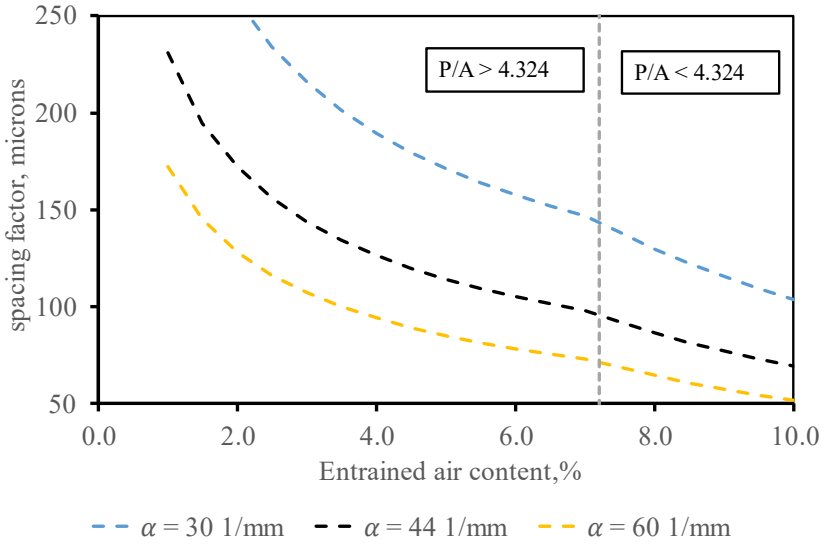

Figure 6.15 Relationship between spacing factor and entrained air content and specific surface

6.3.4 Air void density

Calculations involving paste-void proximity often include determining the number of air voids in a given volume of paste (*N*) or the air void density (*AVD*). Its calculation and applications to other parameters such as the Philleo factor are of considerable interest.

The chord size distribution can be obtained through the linear traverse test prescribed by ASTM C457, with the help of image analysis software. To represent the distribution accurately, the zeroth-order logarithmic radius distribution proposed by Roberts et al. (1981) is utilized (Roberts et al. 1981) and can be characterized by

$$\phi(r) = \frac{\exp\left[-\frac{1}{2}\left(\frac{\ln\left(\frac{r}{r_o}\right)}{\sigma_o}\right)^2\right]}{\sqrt{2\pi}\sigma_o r_o \exp\left(\frac{\sigma_o^2}{2}\right)}, \qquad \text{Eq. 6.14}$$

where r_o is the modal chord length and σ_o is the zeroth-order log standard deviation. Although the chord size usually does not represent the real radius of the air voids and the relationship between the radius and chord size can be found in other's work (Reid 1955, Snyder et al. 2001,

Fonseca et al. 2015), it is assumed that the chord size distribution can approximate the air void radius distribution in this study for simplicity. According to a general formula (Dirac 1943, Sjöstrand 2002), the average chord length can be approximately 4/3 of the average air void radius

$$\bar{l} = \frac{4}{3}R, \qquad \text{Eq. 6.15}$$

where $\bar{l}$ is the average chord length, microns, R is the average radius of air void.

The number of air voids N in the scaling (paste) volume V_S can be calculated as the total volume of air voids divided by the volume of a single air volume

$$N = \frac{\gamma V_S}{\frac{4}{3}\pi R^3}, \qquad \text{Eq. 6.16}$$

where γ is the ratio of air void in the paste, calculated as $\frac{A}{p+A}$. If the V_S is 1 mm^3, then N represents the air void density and the unit is 1/mm^3.

Combine these two equations, the following is obtained

$$N = \frac{V_S}{k\left(\frac{p}{A}+1\right)\bar{l}^3}, \qquad \text{Eq. 6.17}$$

where k is a constant that equals 1.767.

As mentioned above, the entrapped air has a great impact on the average chord length and thus on the calculation of N. Two methods can be taken to mitigate the effects of entrapped air. Firstly, the entrained air which has a narrower size range (< 500 microns) can be used instead of the total air to calculate the average size. Alternatively, the real air void size distribution can be employed to calculate the number of air voids in each class and get the total number of air voids from each size group. The percentage of the air voids of class i in paste is

$$\gamma_i = \frac{A_i}{p + A_t}, \qquad \text{Eq. 6.18}$$

where A_i is the air content of the specific class i, p is the cement paste content, A_t is the total air content.

Consequently, the number of air voids based on the air void distribution is

$$N = \sum_{i=1}^{n} \frac{V_{NS}}{k\left(\frac{p + A_t}{A_i}\right)\overline{l_i}^3}, \qquad \text{Eq. 6.19}$$

where n is the number of air void classes, $\overline{l_i}$ is the chord size length of the specific class i, the $\overline{l_i}$ takes the middle value of the class range. For example, $\overline{l_i}$ is 35 microns for chord size ranging between 30 and 40 microns size group. An example of concrete with 0.40 w/c from ASTM C 457 is given in Appendix A.

A comparison of AVD in 17 concrete systems calculated by entrained air voids, total air voids, and air void size distribution is displayed in Figure 6.16. It is obvious that the real number of voids should be much greater than that based on all air voids. This finding supports other researchers' discoveries that the actual number of air voids is significantly greater than the number utilized in calculating Powers spacing factor (Lord et al. 1951).

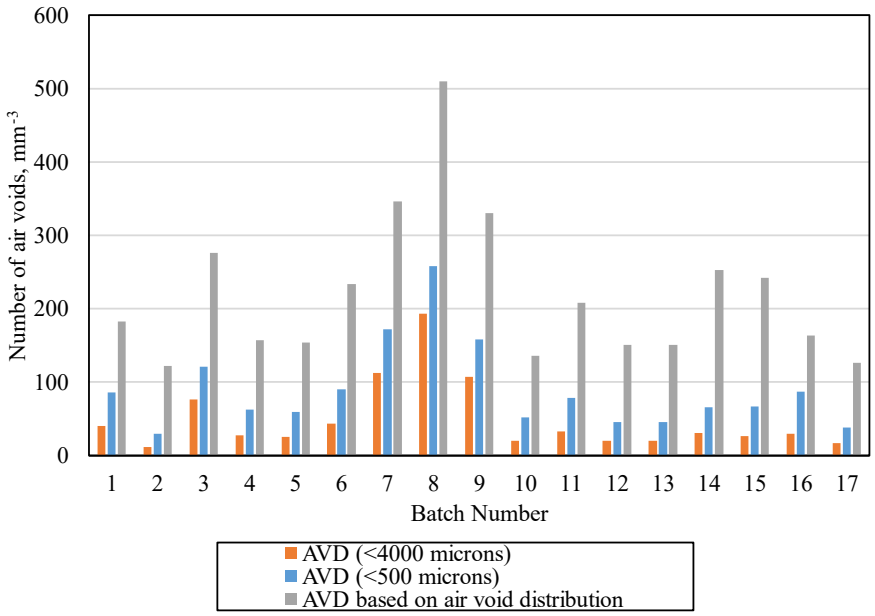

Figure 6.16 Number of air voids per volume calculated by average chord length of all air voids, entrained air voids, and chord size distribution

According to Eq. 6.17, if the specific surface is similar, the AVD increases with the air content. This is suggested in Figure 6.17 and Figure 6.18 where these three systems have a close specific surface but quite different air content. The air void density is also highly correlated with the spacing factor demonstrated in Figure 6.19. This is due to the similarity in the calculation of these

two parameters in essence. They are both associated with air content, paste content, and chord size distribution.

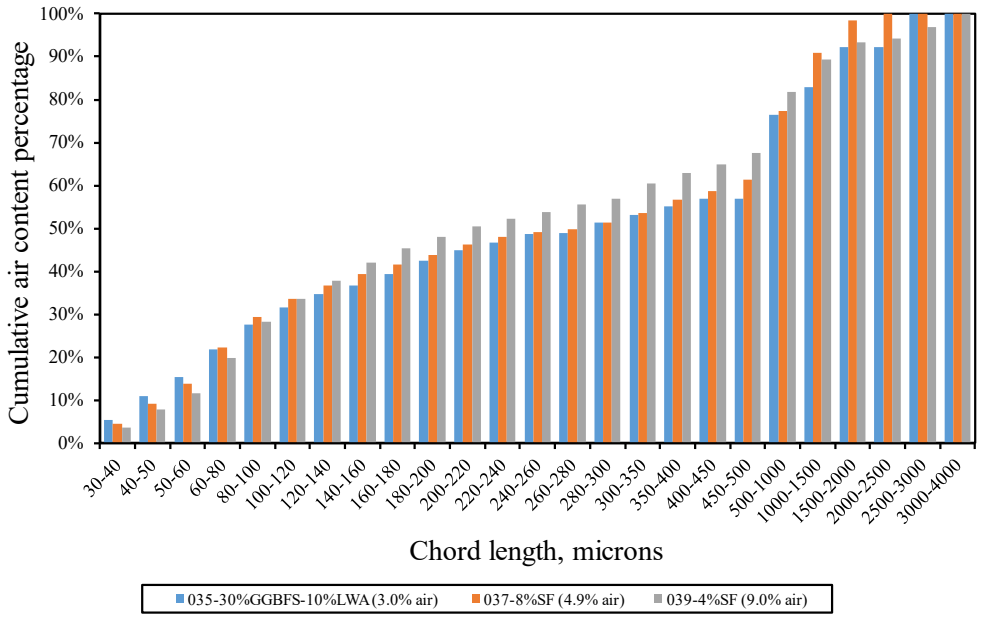

Figure 6.17 Cumulative air void content for concrete systems with low, medium, and high air content

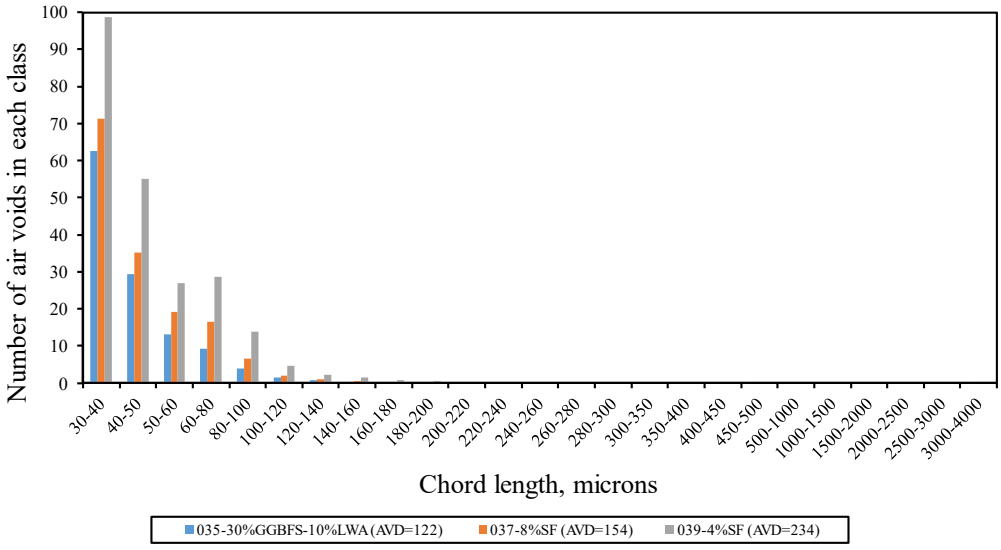

Figure 6.18 Histogram of air voids in each chord length class for concrete systems with low, medium, and high air content

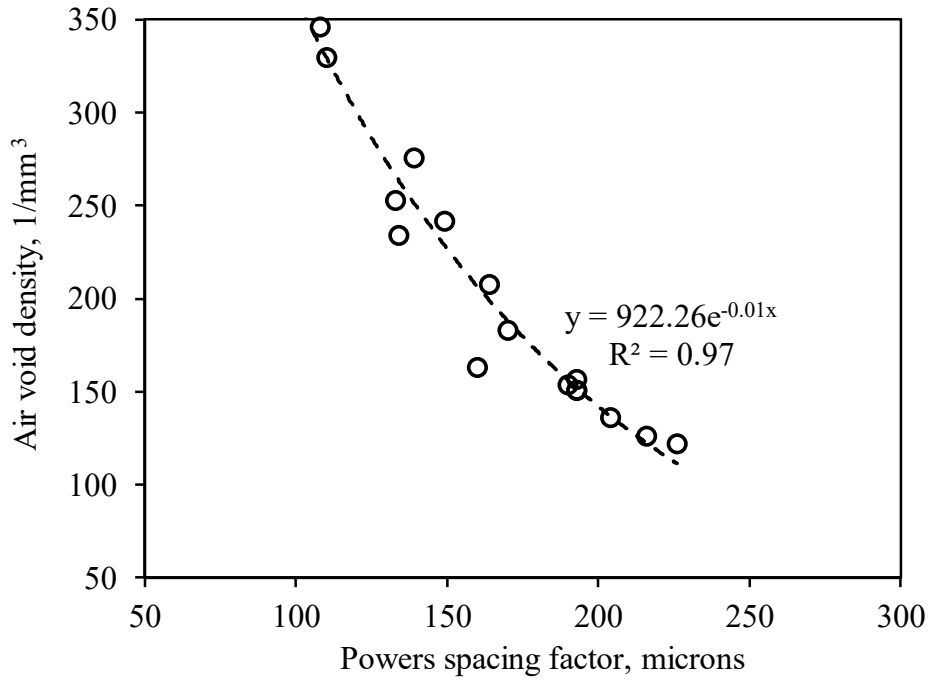

Figure 6.19 Relationship between Powers spacing factor and the air void density

6.3.5 Modified Philleo factor

The Philleo model, based on the Powers spacing factor, introduced the concept of a protected volume (Philleo 1983). The Philleo factor is defined by the ACI Concrete Terminology (2021) as:

a distance, used as an index of the extent to which hardened cement paste is protected from the effects of freezing, so selected that only a small portion of the cement paste (usually 10%) lies farther than that distance from the perimeter of the nearest air void.

The model involves generating points in the cement paste to represent the air void system, where the air void has no volume. The paste-void proximity distribution is then described by the Hertz distribution, which is improved to account for finite-sized spheres. A point can be protected if it falls within a critical distance *S* from the closest air void, as illustrated in Figure 6.20. The Philleo factor is regarded as a more realistic approach than the spacing factor to estimate the spacing of air voids in concrete for evaluating its frost durability (Pigeon et al. 1995). Moreover, the Philleo model assumes that the air voids are randomly distributed, which is a closer approximation to reality (Fagerlund 2017).

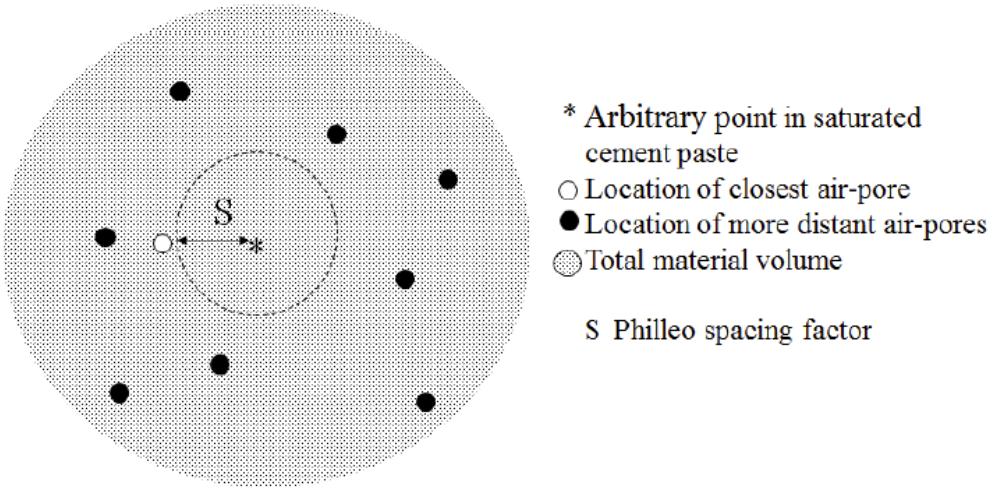

Figure 6.20 Illustration of Philleo factor

The percentage of paste (F) located within a distance of S can be calculated by

$$F = 1 - e^{-4.19\left(SN^{\frac{1}{3}}\right)^3 - 7.80\left(SN^{\frac{1}{3}}\right)^2 [\ell n 1/(1-A)]^{\frac{1}{3}} - 4.84\left(SN^{\frac{1}{3}}\right)[\ell n 1/(1-A)]^{\frac{2}{3}}}, \quad \text{Eq. 6.20}$$

where A is the air content by volume in the paste including the air voids, N is the number of air voids per unit volume.

The Philleo factor accounting for 90th percent (i.e., F=0.9) of the paste within a distance S of the nearest air voids is usually adopted and can be determined by

$$S = \frac{0.62}{N^{\frac{1}{3}}}\left[\left(\ln\left(\frac{1}{1-A}\right) + 2.303\right)^{\frac{1}{3}} - \left(\ln\left(\frac{1}{1-A}\right)\right)^{\frac{1}{3}}\right]. \quad \text{Eq. 6.21}$$

It was found that Powers' spacing factor is almost equivalent to the original Philleo factor as shown in Figure 6.21 (a) which is consistent with previous studies (Dewey 1991). However, Philleo only utilized an estimated average value of N and neglected the size distribution of the air voids when computing S. As revealed in section 6.3.4, the Philleo factor can be improved by taking into account the actual air void size distribution. Although Philleo did not consider the air void radius distribution in the equation's development, incorporating this distribution results in a much smaller Philleo factor as shown in Figure 6.21 (b) which is more realistic (Snyder 1998).

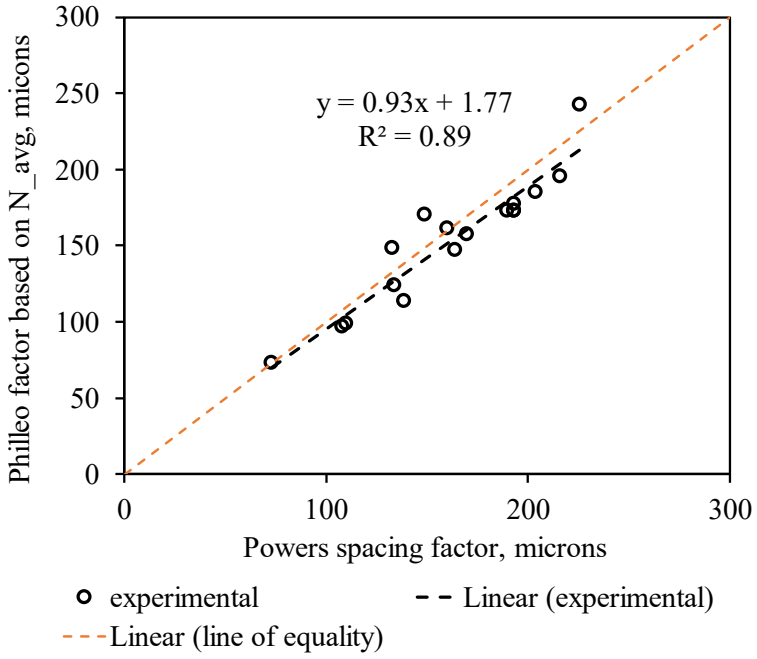

(a)

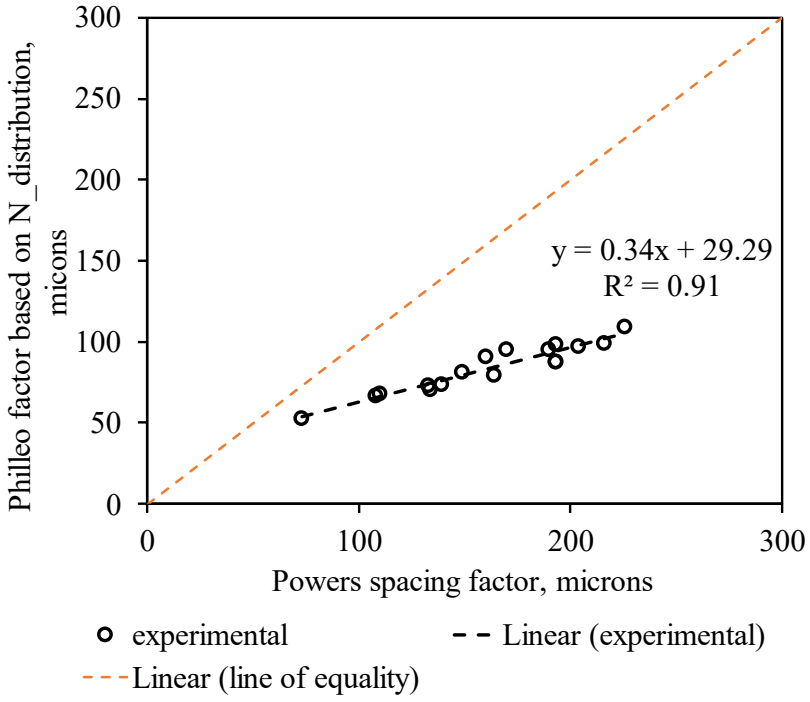

(b)

Figure 6.21 Relationship between Powers spacing factor and Philleo factor based on (a) average chord length (b) air void size distribution

6.3.6 Lu and Torquato Equations

Prior to Lu and Torquato's study, the problem of paste-void spacing distributions had mainly been solved for systems consisting of monosized spheres, using various approximation techniques that were verified by Monte Carlo simulations. However, Lu and Torquato extended these approximations to include polydispersed sphere radii, which can be used both for paste-void and void-void spacing distribution. In order to calculate paste-void and void-void proximity, they defined specific quantities as follows:

$$\sigma_k = \frac{\pi}{3} N 2^{k-1} \langle R^k \rangle, \quad \text{Eq. 6.22}$$

$$c = \frac{4\langle R^2 \rangle}{1 - A}, \quad \text{Eq. 6.23}$$

$$d = \frac{4\langle R \rangle}{1 - A} + \frac{12\sigma_2}{(1 - \sigma_3)^2} \langle R^2 \rangle, \quad \text{Eq. 6.24}$$

$$g = \frac{4}{3(1 - A)} + \frac{8\sigma_2}{(1 - A)^2} \langle R \rangle + \frac{16}{3} \frac{B\sigma_2^2}{(1 - A)^3} \langle R^3 \rangle, \quad \text{Eq. 6.25}$$

where $\langle R^k \rangle$ is the expected value of R^k for the radius distribution. The value of B depends on the exact way how the system is built and for the calculations here $B = 0$ is selected (Lu et al. 1992).

One approach used in the study was to estimate the probability of a randomly selected point in the system lying within a distance s from an air-void surface (paste-void proximity). The probability of finding the nearest air void surface at a distance s from a random point within the paste portion can be expressed by the following equation:

$$E_v(s) = 1 - \exp[-\pi N(cs + ds^2 + gs^3)]. \quad \text{Eq. 6.26}$$

As the equation suggests, the probability is only a function of s for a given concrete system. By plugging in different s the probability can be calculated. The s value represents the 90% probability that was adopted in order to compare with the Philleo factor (90%). As shown in Figure 6.22, the Lu and Torquato Factor was about 20% larger than the Philleo factor but there was a strong linear relationship between them ($R^2 = 0.96$). Lu and Torquato factor is found to be the most accurate among all the parameters in a study by Snyder (1998).

Other parameters such as Pleau and Pigeon factor which only performs well when the air content is low and Attiogbe's factor which is for void-void spacing are not included in this study.

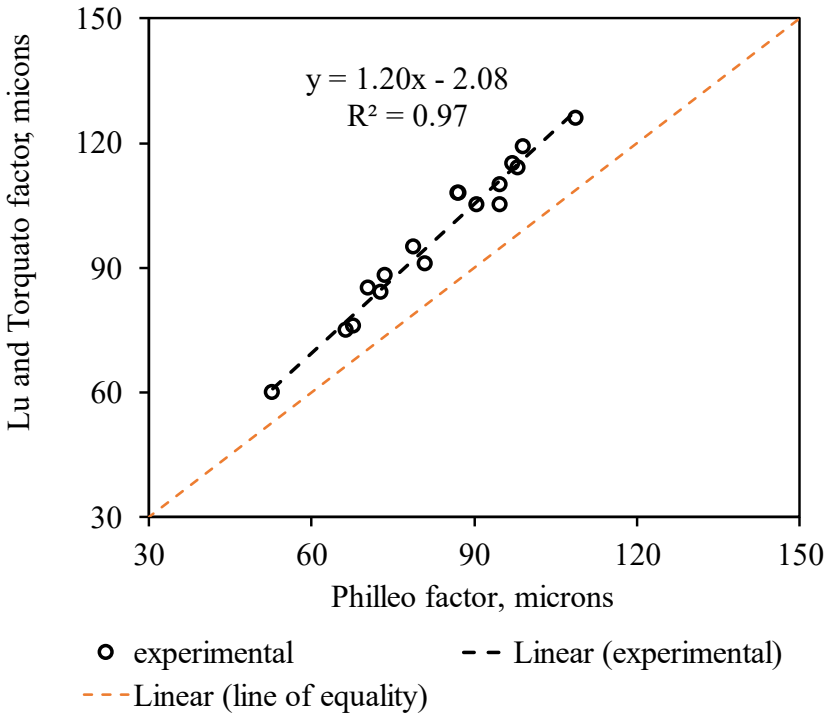

Figure 6.22 Relationship between the Lu and Torquato factor and Philleo factor

6.3.7 Accumulated surface area

More investigations are conducted in a recent couple of decades by including the surface area of air voids. For example, Lindmark came up with the accumulated surface area (ASA) of all air voids to evaluate the quality of an air void system (Lindmark 2010) which can be calculated as

$$T = \sum_{d} n_d A(d), \qquad \text{Eq. 6.27}$$

where T is the accumulated surface area, d is the average size of a certain class of air voids, n_d is the number of air voids in that size and $A(d)$ is the surface area of the air voids.

The accumulated surface area is not related to either paste-void or void-void proximity. They argued that in order for the air void system to protect the concrete, two conditions must be met. On the one hand, the total air volume should be large enough to provide space for ice formation. On the other hand, the distance between the air voids should not be too long. Small air voids have a high surface-area-to-volume ratio. However, if there are few small air voids, the total air volume will be low. In contrast, large air voids provide a large volume for ice formation but if there are too few of them the flow distance will be too large. Based on this reasoning, one can hypothesize that the accumulated surface area of all air voids in a reasonably normal air void system might be

a useful parameter for assessing the quality of the system. This is because a sufficient accumulated surface area would ensure that the total volume of air is adequate and the flow distances are kept short enough. A good correlation between scaling and accumulated surface area is observed by Lindmark in Figure 6.23 when w/c= 0.4 but not when w/c = 0.5. Moreover, the author admits that the evaluation is based on a purely qualitative analysis, as no theory predicts the shape of the curve.

One notable limitation of this parameter is its inability to account for the distance between air voids. For instance, if two systems have the same total surface area but one system contains more air voids of larger size and the other has more smaller air voids, the flow distance will differ. Therefore, this formula is only applicable when air void distributions are similar. Additionally, the author partitioned the samples into two categories based on w/c for the plot, implying that other factors should be taken into account when assessing salt frost scaling beyond the air void system.

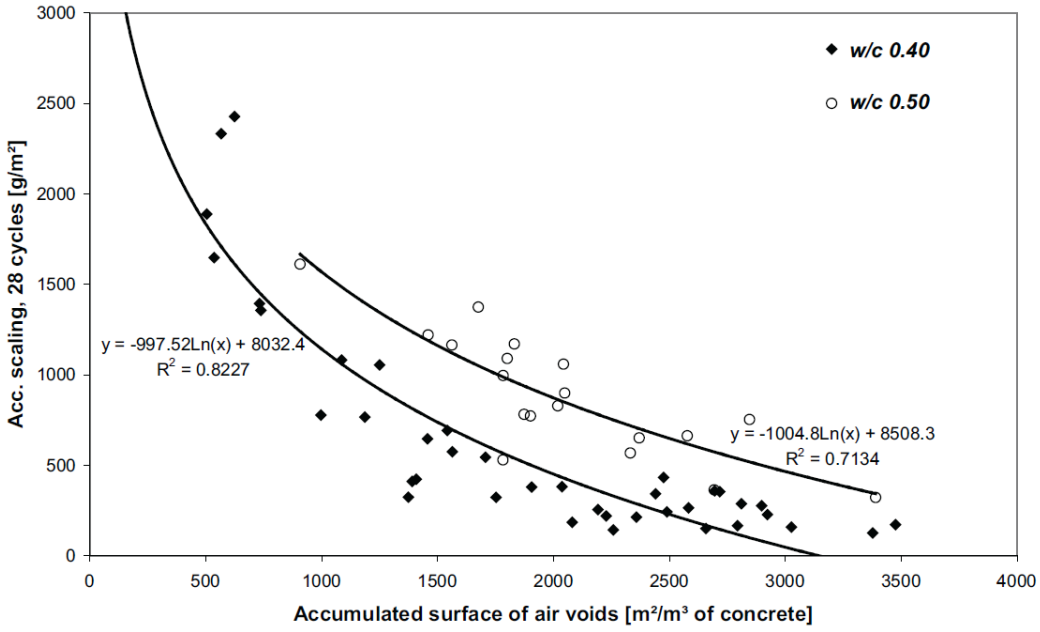

Figure 6.23 Scaling vs accumulated surface of air voids

The study again demonstrated a strong linear correlation between the spacing factor and the accumulated surface area, as illustrated in Figure 6.24, using the 17 concrete systems analyzed. Although all the recently proposed parameters including the Philleo factor, air void density, and accumulated surface area have different ways to characterize the air void system and are different from the spacing factor in values, they are in essence associated with air content and air void size distribution. As a result, these parameters exhibit a strong correlation with the Powers spacing

factor, whether linearly or non-linearly. This is consistent with findings by other researchers, as shown in Figure 6.25 (Snyder 1998). Although the spacing factor may not precisely represent the actual spacing between air voids, it is a useful indicator of the air void system's quality.

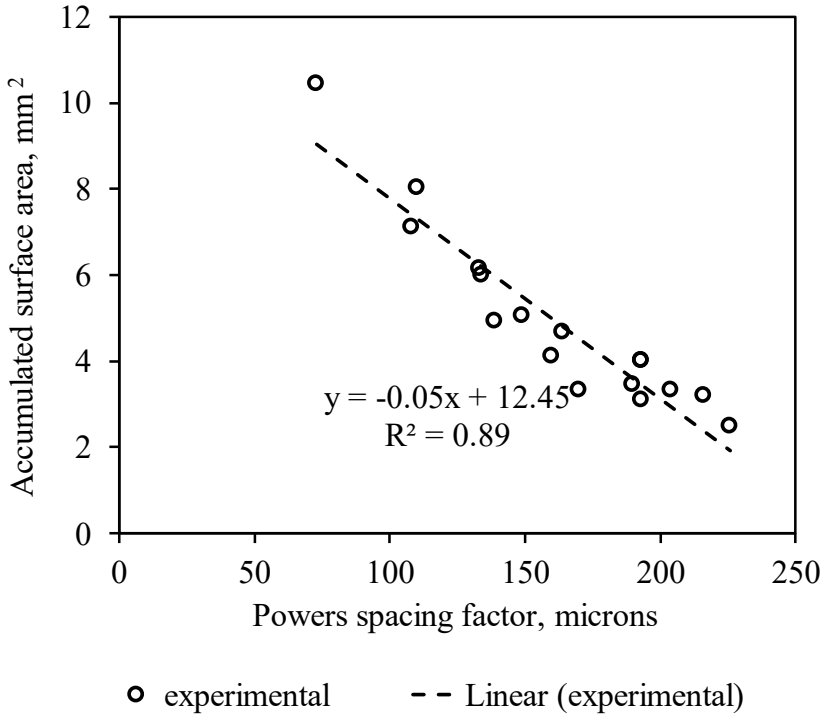

Figure 6.24 Relationship between accumulated surface area and Powers spacing factor

6.3.8 Relationship between scaling and air void parameters

Although the paste-void proximity parameters such as the Philleo factor are well-established, limited data exist on the relationship between scaling and these air void parameters. In light of the findings from earlier sections, the scaling is plotted in relation to these parameters and the results are summarized in Table 6.2. All concrete samples examined were air-entrained, with total air content ranging from 2.9% to 8.8%. The entrained air (<500 microns) content was between 1.7% and 7.6%. The spacing factor varied from 73 to 226 microns, and the specific surface area ranged from 24 to 46 mm^{-1}. Fourteen out of 17 concrete systems met the ACI 201 recommendation that the spacing factor should not exceed 200 microns and the specific surface should be at least 25 mm^{-1} (Powers et al. 1949, Powers 1954, ACI Committee 201 2016).

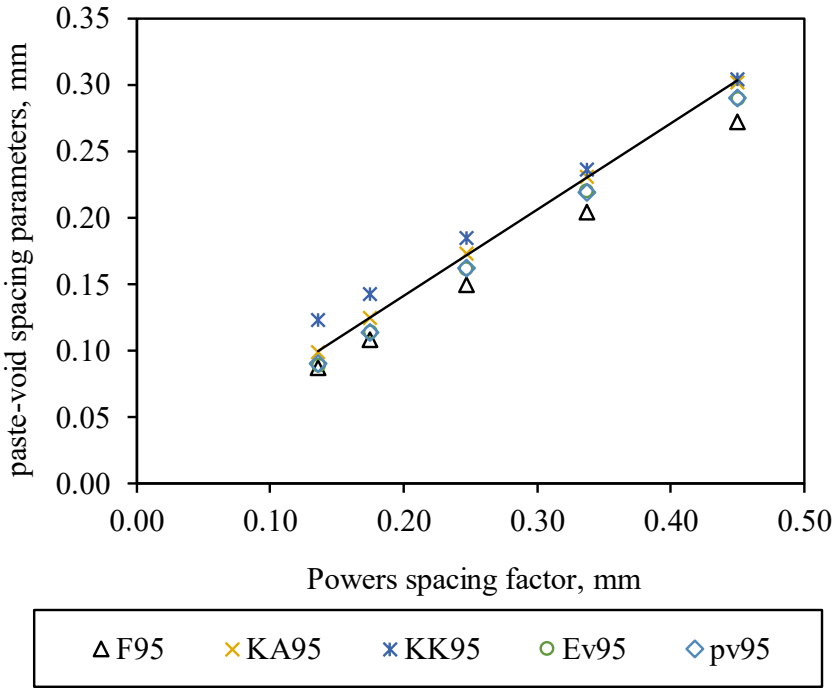

Figure 6.25 Relationship between Powers spacing factor and other paste-void spacing factors (Snyder 1998) (Note: The estimates include results from Philleo (F); Pleau and Pigeon (KA) and (KK) using the normalization factors of 1 - A and 1 – K′(0), respectively; Lu and Torquato (Ev); and Powers. 95 indicates the percentile.)

As discussed in section 6.2.2, sorptivity is important in considering salt scaling resistance. As a result, in Figure 6.26, the impact of air void parameters on salt frost scaling is demonstrated for concrete categorized by their sorptivity. Concrete with low (<0.15 mm/sqrt(min)), medium (0.15 – 0.20 mm/sqrt(min)), and high sorptivity (> 0.20 mm/sqrt(min)) are represented by blue, orange, and grey dots respectively.

Total air content is being widely used in the field as it can be quickly and easily measured. Despite total air content being a commonly used parameter, there is generally no correlation between scaling and air content. Concrete with at least 6% total air content, typically considered adequate, can still develop very high scaling, as shown in Figure 6.26 (a). Conversely, concrete with air content less than 4% had a scaling of less than 0.5 kg/m^2. This indicates that air content alone is not a reliable indicator of freeze-thaw scaling resistance. For concrete with high sorptivity, air content greater than 6% is typically recommended to reduce the scaling, while concrete with medium sorptivity should have air content greater than 5%. Low sorptivity concrete is freeze-thaw

resistant even with very low air content, which aligns with the plot in Figure 6.26 (b). A minimum entrained air content of 4% and 3% is recommended for concrete with high and medium sorptivity, respectively.

Table 6.2 Summary of air void parameters and scaling

	AC	SS	PSF	ESF	AVD	PhF	LT	ASA	Scaling
	%	mm^{-1}	microns	microns	mm^{-3}	microns	microns	mm^{-1}	kg/m^2
035-30%GGBFS	2.9	37	170	140	183	95	105	3.32	0.37
035-30%GGBFS-10%LWA	3.0	28	226	174	122	109	126	2.47	0.28
035-30%GGBFS-25%LWA	5.3	38	139	118	276	74	88	4.92	0.09
035-30%GGBFS-40%LWA	3.4	31	193	154	157	98	114	3.08	0.08
037-8%SF	4.9	29	190	154	154	95	110	3.45	0.76
039-4%SF	9.0	29	134	120	234	71	85	5.99	1.23
040-30%GGBFS	6.1	43	108	98	346	66	75	7.12	0.23
040-30%GGBFS-25%LWA	8.8	46	73	74	510	53	60	10.43	0.20
040-30%GGBFS-40% LWA	5.8	42	110	100	330	68	76	8.02	0.18
040-8%SF-18%LWA	5.0	26	204	161	136	97	115	3.33	0.44
040-4%SF-18%LWA	7.0	28	164	133	208	79	95	4.67	0.18
040-Control-28day	6.0	24	193	158	151	87	108	4.00	2.45
040-Control-90day	6.0	24	193	158	151	87	108	4.00	2.12
040-30% Fly ash Class C	6.1	35	133	116	253	73	84	6.14	0.47
040-30% Fly ash Class F	4.2	32	149	120	242	81	91	5.06	0.35
045-30%GGBFS	4.4	29	160	140	163	91	105	4.11	0.50
045-6%SF-25%GGBFS	4.7	24	216	177	126	99	119	3.19	1.15

(Note: AC = air content, SS = specific surface, PSF = Powers spacing factor, ESF = spacing factor by entrained air, AVD = air void density based on air void distribution, PhF = Philleo Factor 90% percentile, LT = Lu and Torquato equation 90% percentile, ASA = Accumulated Surface Area; scaling is the mass loss at 56 F-T cycles)

The scaling generally decreases as specific surface increases (Figure 6.26 (c)). For concrete with high sorptivity, a finer system (i.e., a larger specific surface) can significantly reduce the scaling. However, the specific surface has less impact on the concrete with medium to low sorptivity. As long as the specific surface is greater than 25 mm^{-1}, which is in line with the requirement in ACI 201 (2016), these concrete samples develop a scaling of less than 1 kg/m^2. The specific surface itself simply represents the fineness of the air void system. If the total volume of air void is low,

the concrete still cannot provide sufficient protection to the concrete. A more comprehensive parameter should also take the air content into account. Consequently, specific surface is not the best choice when determining the salt scaling resistance.

The data presented in Figure 6.26 (d) shows that scaling tends to increase with an increase in the spacing factor. The larger spacing factor indicates that water flow must travel a greater distance to prevent pressure buildup, which can lead to paste destruction before it can be released. The impact of the spacing factor is greatest in concrete with high sorptivity. For example, the 040-30%GGBFS-25%LWA concrete system has a high sorptivity (0.207 mm/sqrt(min)) but low scaling (<0.5 kg/m^2) due to a high-quality air void system with a spacing factor of 73 microns. On the other hand, the scaling of the 040-Control-90day system, which has similar sorptivity, is over 2 kg/m^2 due to a spacing factor close to 200 microns, the limit specified in ACI 201. The trend lines for concrete with high and medium sorptivity indicate that as sorptivity increases, the spacing factor must be reduced to achieve the same level of scaling resistance. Meanwhile, the F-T scaling resistance for concrete with low sorptivity is not sensitive to changes in the spacing factor.

As mentioned in previous sections, the spacing factor has a strong correlation with all other synthetic air void parameters such as Philleo Factor, air void density, etc. It is expected that a similar trend also applies to these parameters. As seen from Figure 6.26 (e) to (i), these parameters have the greatest impact in concrete with high sorptivity, as scaling increases with Philleo Factor and Lu and Torquato Factor and decreases with air void density and accumulated surface area. However, concrete systems with low sorptivity are still unaffected by changes in these air void parameters.

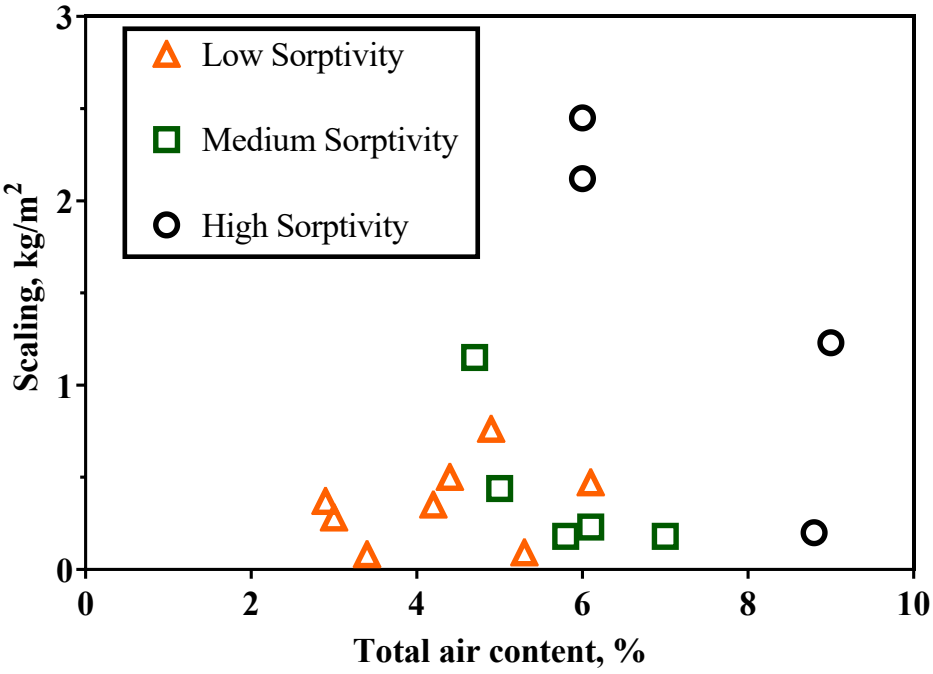
Low Sorptivity
Medium Sorptivity
High Sorptivity
Scaling, kg/m2
Total air content, %
0
1
2
3
0
2
4
6
8
10

(a)

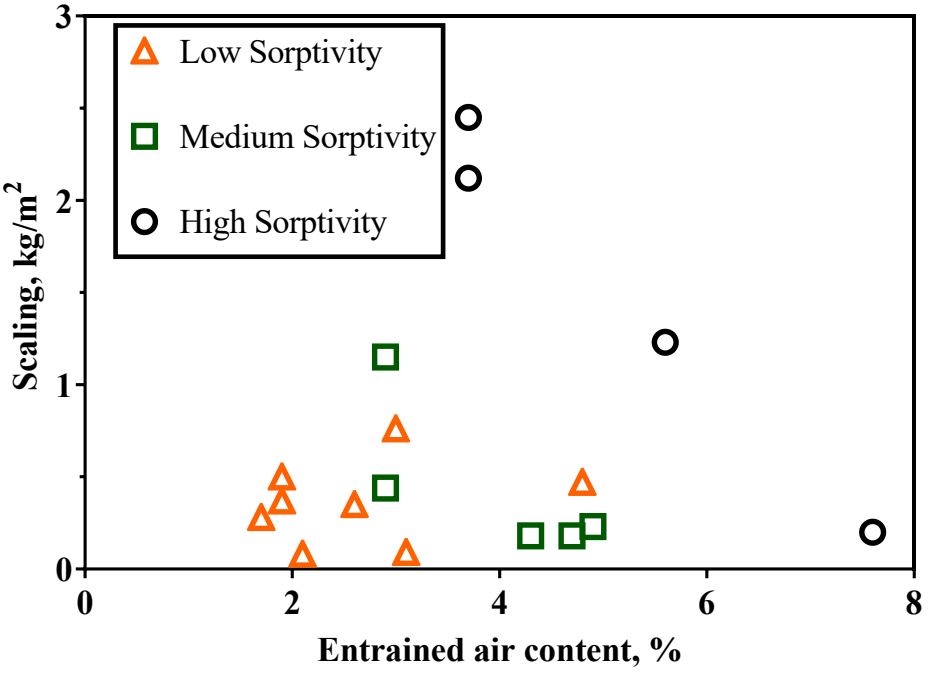
Low Sorptivity
Medium Sorptivity
High Sorptivity
Scaling, kg/m2
Entrained air content, %
0
1
2
3
0
2
4
6
8

(b)

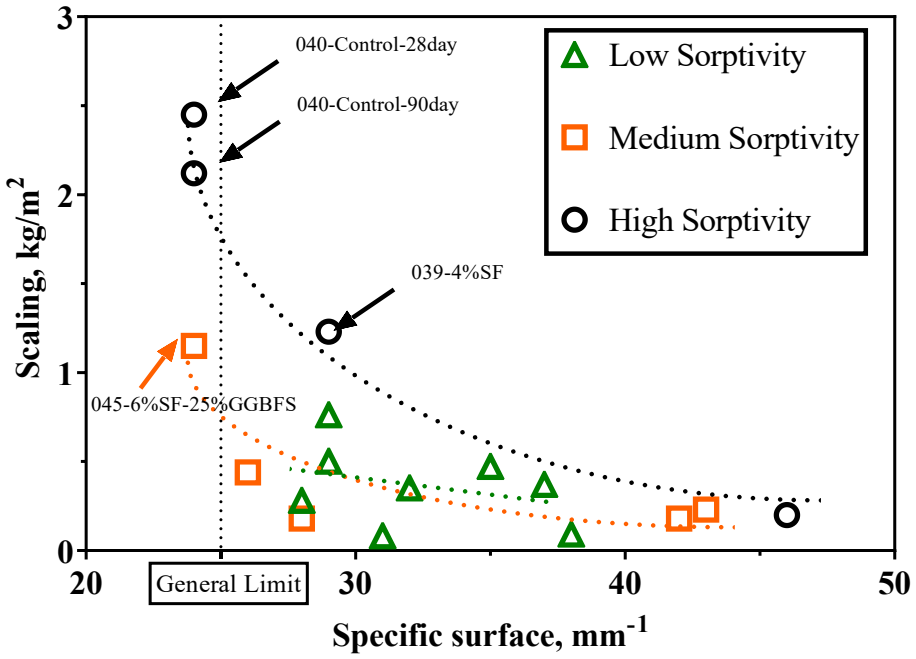
Low Sorptivity
Medium Sorptivity
High Sorptivity
040-Control-28day
040-Control-90day
039-4%SF
045-6%SF-25%GGBFS
General Limit
Scaling, kg/m2
Specific surface, mm-1
0
1
2
3
20
30
40
50

(c)

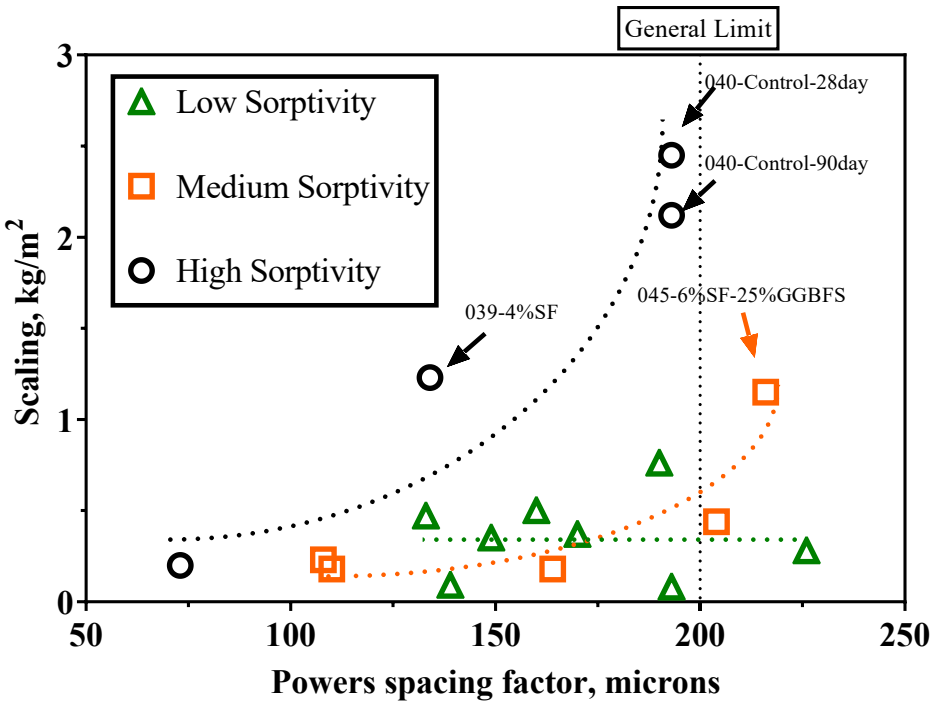
General Limit
Low Sorptivity
Medium Sorptivity
High Sorptivity
040-Control-28day
040-Control-90day
039-4%SF
045-6%SF-25%GGBFS
Scaling, kg/m2
Powers spacing factor, microns
0
1
2
3
50
100
150
200
250

(d)

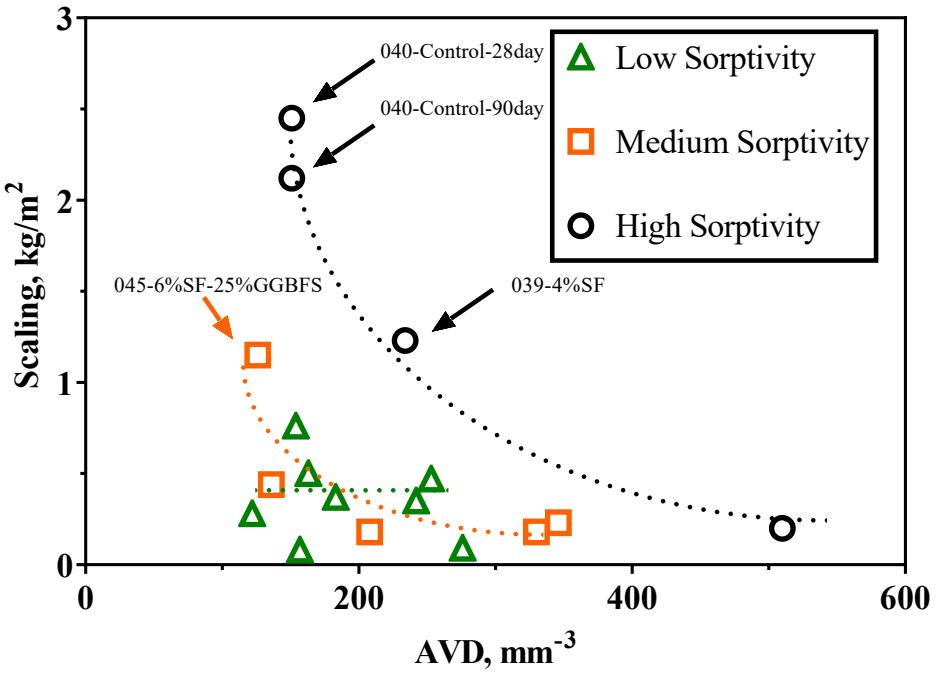
Low Sorptivity
Medium Sorptivity
High Sorptivity
040-Control-28day
040-Control-90day
045-6%SF-25%GGBFS
039-4%SF
Scaling, kg/m2
AVD, mm-3
0
1
2
3
0
200
400
600

(e)

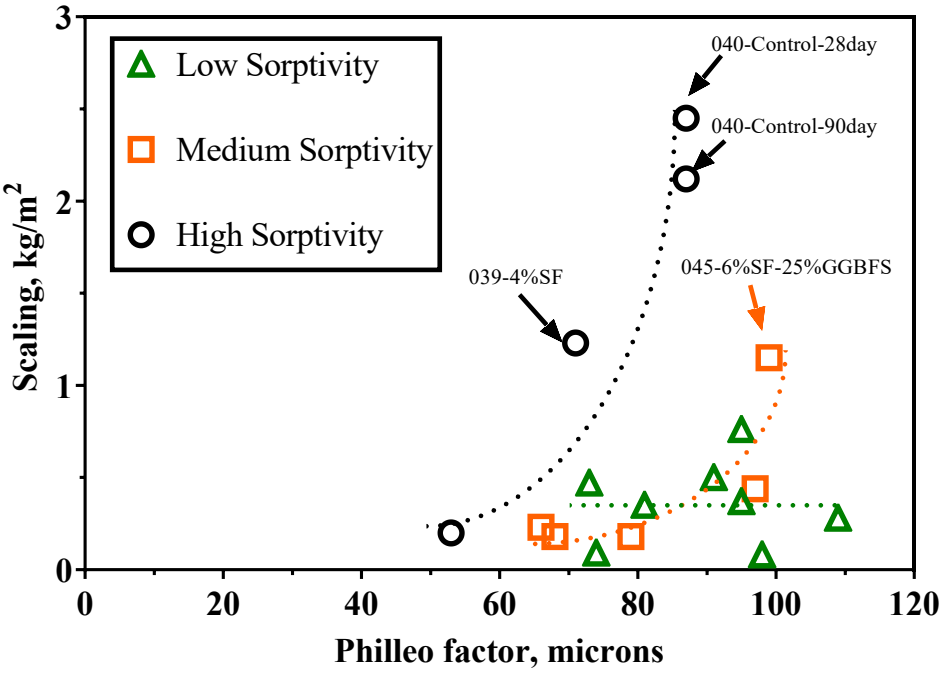
Low Sorptivity
Medium Sorptivity
High Sorptivity
040-Control-28day
040-Control-90day
039-4%SF
045-6%SF-25%GGBFS
Scaling, kg/m2
Phillleo factor, microns
0
1
2
3
0
20
40
60
80
100
120

(f)

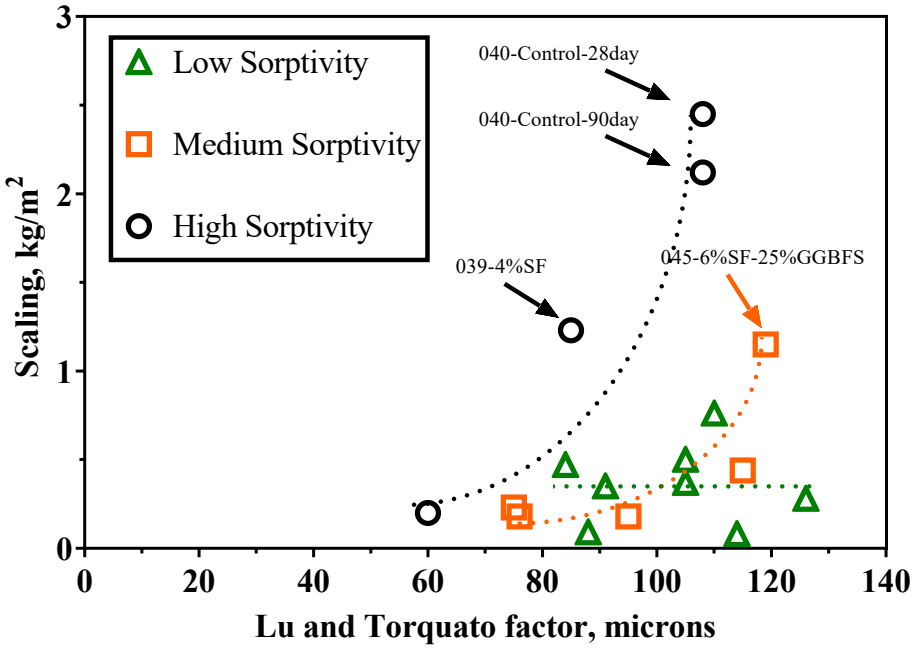

(g)

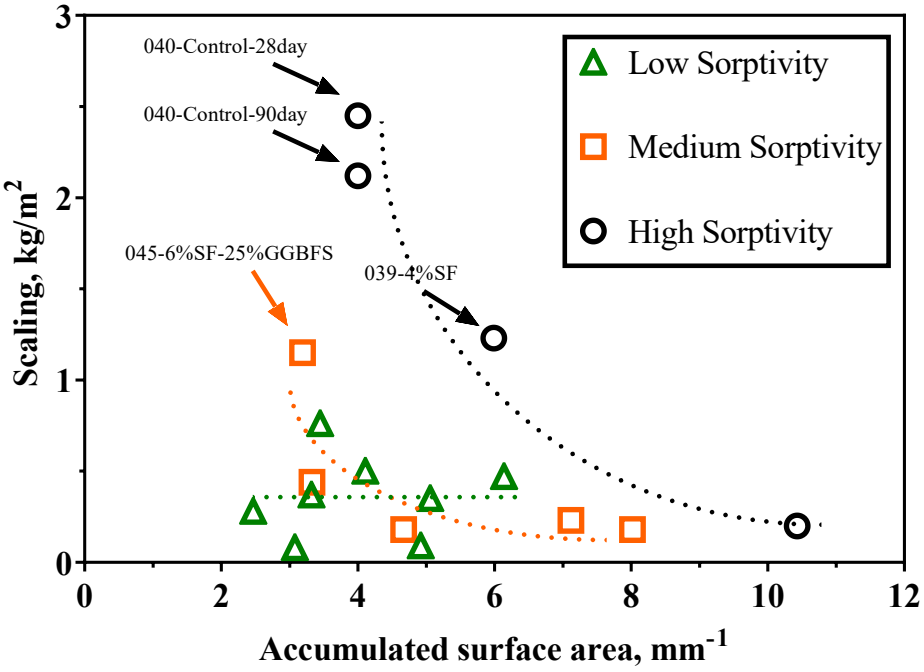

(h)

Figure 6.26 Relationship between the scaling and air void parameters

From the results, the sorptivity combined with the spacing factor can be used to predict the scaling resistance of the concrete. Sorptivity measures how easily the surface layer of concrete can absorb water and is a key factor in moisture uptake, which can be seen as the pressure cause in salt frost scaling. Meanwhile, the air void system acts as a buffer, providing pressure relief to the moisture absorbed. Therefore, salt frost scaling is determined by the balance between water uptake and the quality of the air void system in the concrete.

6.4 Quantifying salt frost scaling using two parameters

Based on the analysis, a polynomial regression model can be constructed to establish the correlation between salt scaling, sorptivity, and Powers spacing factor.

6.4.1 Modeling

Based on the analysis, a polynomial regression model can be constructed to establish the correlation between salt scaling, sorptivity, and Powers spacing factor.

Denote the dataset of n experimental points by $(x_i, y_i, z_i)_{i=1}^n$, where x_i is the sorptivity, y_i is the spacing factor and z_i is the scaling in the i-th experiment. Then, the polynomial regression model is given by

$$z_i = \sum_{\substack{k+l \le p \\ k,l \in \mathbb{N}}} \left(a_{kl} x_i^k y_i^l\right), \qquad \text{Eq. 6.28}$$

where $\mathbb{N} = \mathbb{Z} \cup \{0\}$ is the set of natural numbers, p is the order of this polynomial model, and a_{kl} is some coefficients. Note that for a given p, the number of elements in set $\{(k,l) \in \mathbb{N}^2 : k + l \le p\}$ is

$$\frac{(p+1)(p+2)}{2}.$$

Hereafter, the polynomial models are restricted with the order of not greater than 2, i.e., in the rest of this study, let $p \le 2$. In such cases, it is recommended to use a regularization method to suppress coefficients in nonlinear functions, whereas linear functions do not require such terms (Wan 2019).

Then for a given dataset $(x_i, y_i, z_i)_{i=1}^n$, the appropriate coefficients $\{a_{kl}\}$ in a polynomial regression model in Eq. 6.28 can be solved by the optimization

$$\min_{\{a_{\mathrm{kl}}\}} J(\boldsymbol{a}) = \min_{\{a_{\mathrm{kl}}\}} \sum_{i=1}^{n} \left(z_i - \sum_{\substack{k+l\leq 2 \\ k,l\in N}} \left(a_{kl} x_i^k y_i^l \right) \right)^2 + \lambda \parallel \boldsymbol{a} \parallel_*, \qquad \text{Eq. 6.29}$$

where vector $\boldsymbol{a} = (a_{00}, a_{10}, a_{01}, a_{20}, a_{02}, a_{11})^T \in \mathbb{R}^6$ consisting of all the coefficients, $\|\cdot\|_*$ is the vector norm, and λ is the regularization constant. In Eq. 6.29, the sum in the first term includes all the squared residuals, and the second term serves as a regularization. Without loss of generality, $\ell 1$ and $\ell 2$ norm can be utilized in the regularization, which are defined as follows, respectively.

$$\parallel \boldsymbol{a} \parallel_1 = \sum_{\substack{k+l\leq p \\ k,l\in\mathbb{N}}} |a_{kl}| \qquad \text{Eq. 6.30}$$

$$\parallel \boldsymbol{a} \parallel_2 = \sqrt{\sum_{\substack{k+l\leq p \\ k,l\in\mathbb{N}}} a_{kl}^2} \qquad \text{Eq. 6.31}$$

Furthermore, the optimization problem can be written in the matrix form, i.e.,

$$\min_{\boldsymbol{a}} \parallel \boldsymbol{z} - G\boldsymbol{a} \parallel_2^2 + \lambda \parallel \boldsymbol{a} \parallel_* \qquad \text{Eq. 6.32}$$

where

$$\boldsymbol{z} = (z_1, z_2, \cdots, z_n)^{\mathsf{T}},$$

$$\boldsymbol{a} = (a_{00}, a_{10}, a_{01}, a_{20}, a_{02}, a_{11})^{\mathsf{T}}$$

$$G = \begin{pmatrix} 1 & x_1^1 & y_1^1 & x_1^2 & y_1^2 & x_1 y_1 \\ 1 & x_2^1 & y_2^1 & x_2^2 & y_2^2 & x_2 y_2 \\ \vdots & \vdots & \vdots & \vdots & \vdots & \vdots \\ 1 & x_n^1 & y_n^1 & x_n^2 & y_n^2 & x_n y_n \end{pmatrix}$$

The optimization of Eq. 6.32 is a convex optimization problem.

When there is no regularization term in the optimization (Eq. 6.32), i.e., when $\lambda = 0$, the problem has an analytical solution that is given by

$$\boldsymbol{a} = (G^T G)^{-1} G\boldsymbol{z}. \qquad \text{Eq. 6.33}$$

For the problem with regularization term, i.e., when $\lambda > 0$, in this work, the CVX toolbox is employed to solve this convex optimization (Grant et al. 2014).

- Linear function

To investigate the interpretive capacity of linear models, we begin by setting the order of the polynomial to $p = 1$. This results in having only a_{00}, a_{10} and a_{01} coefficients and the problem is then given by

$$\min_{a_{00},a_{10},a_{01}} \sum_{i=1}^{n} (z_i - a_{10}x_i - a_{01}y_i - a_{00})^2.$$

To facilitate the comparison of the contribution of each variable to the output, it is necessary to normalize the original values of spacing factor and sorptivity, which can be achieved by applying the following formula:

$$x_{norm} = \frac{x_{original} - \mu}{\sigma}, \qquad \text{Eq. 6.34}$$

where μ is the average value of all samples, and σ is the standard deviation of all samples. $x_{original}$ means the original value of sorptivity/spacing factor and x_{norm} is the value after conversion which follows the standard normal distribution. The coefficients of the linear model that provide the best results are presented in Table 6.3. The modeling plots are presented in Figure 6.27. A discussion in detail is provided in section 6.4.2.

Table 6.3 Coefficients and coefficient of determination for the linear function

Type	a_{00}	a_{10}	a_{01}	R^2
Linear	-2.384	9.759	0.009	0.66
Linear Normalized	0.651	0.524	0.380	0.66

- Nonlinear polynomial function

In the nonlinear model, we use polynomials of the order of not greater than 2 and utilize a $\ell 1$ norm to minimize the number of terms in the model. Additionally, a regularization parameter of $\lambda = 0.01$ is applied, and the convex optimization in Eq. 6.32 is solved to obtain the optimal coefficients. The resulting coefficients are presented in Table 6.4.

Table 6.4 Coefficients and coefficient of determination for the nonlinear function

Term	a_{00}	a_{10}	a_{20}	a_{01}	a_{02}	a_{11}	R^2
Coefficient	0.000	-4.565	0.000	-0.005	0.000	0.091	0.77

It can be seen that even if only a small regularization parameter $\lambda = 0.01$ is used, there are only three terms appeared in the resulting polynomial model, which includes terms x_i, y_i, and $x_i y_i$. The obtained model is shown in Figure 6.28.

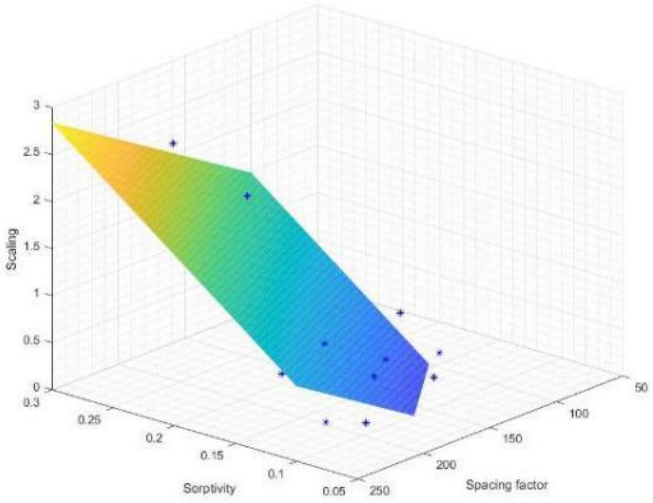

(a)

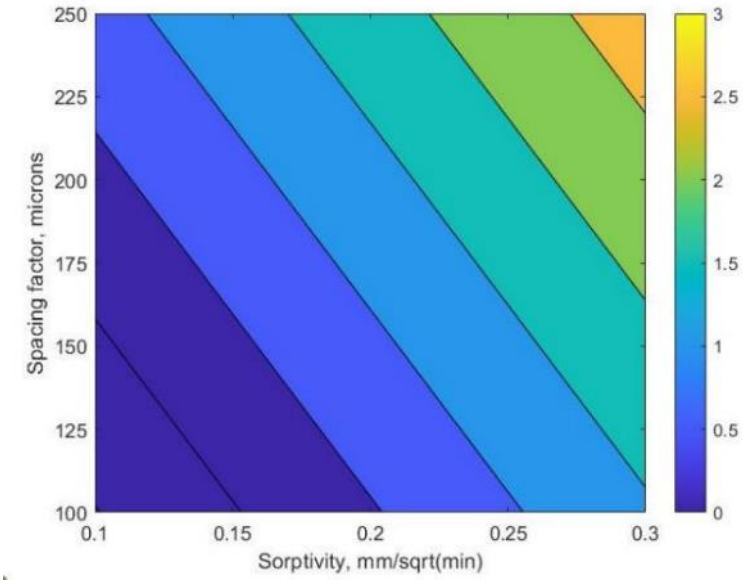

(b)

Figure 6.27 Quantification of salt scaling in concrete based on sorptivity and spacing factor: linear relationship (a) 3-D plot (b) contour plot

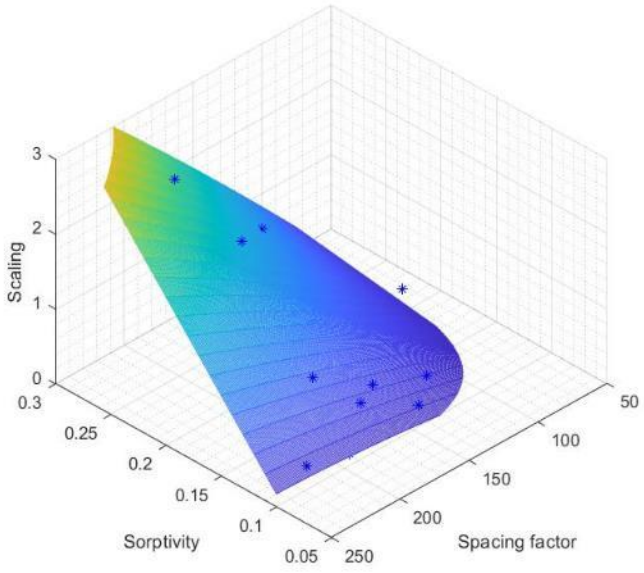

(a)

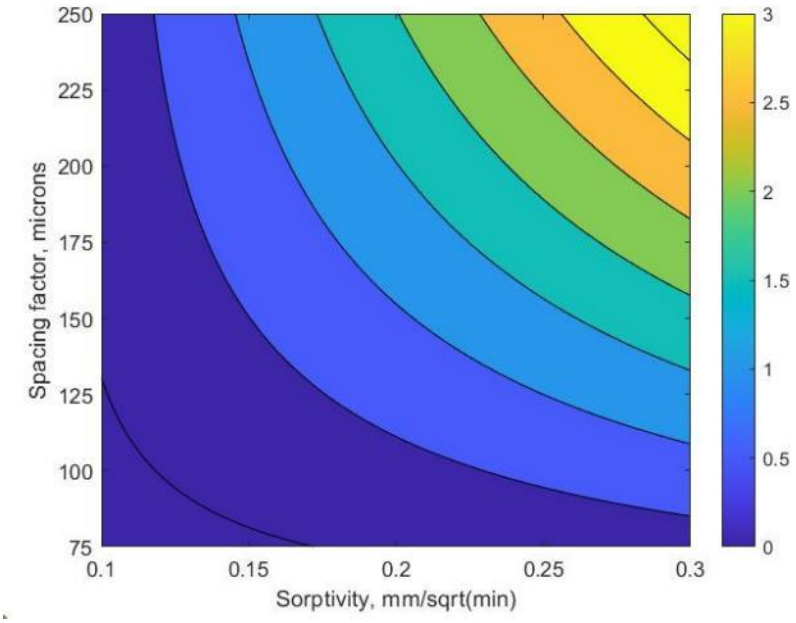

(b)

Figure 6.28 Quantification of salt scaling in concrete based on sorptivity and spacing factor: nonlinear relationship (a) 3D plot and (b) contour plot

6.4.2 Discussion regarding the modeling results

The linear model provides a simple and direct way to describe the relationship between scaling, sorptivity, and spacing factor. The modeling results show that higher sorptivity and spacing factor lead to higher scaling. A notable finding is that in the linear normalized model, the sorptivity coefficient is about 37% larger than the spacing factor coefficient, indicating that sorptivity is the dominant factor in salt frost scaling. To control scaling development, reducing pressure sources by decreasing concrete porosity or connectivity is more effective than enhancing the air void system.

The findings in section 3.2 suggest that the impact of the spacing factor on scaling is dependent on changes in sorptivity, which a linear model is unable to capture. As expected, the model's performance is less than satisfactory, as evidenced by the relatively low R^2 value.

To address these limitations, more terms are added to the nonlinear model, including a term that multiplies the spacing factor and sorptivity which can characterize the synthetic effect of these two parameters on scaling. As a result, the R^2 score has increased from 0.66 to 0.77, indicating that the nonlinear model has better interpretive capabilities. It is observed from Table 6.4 that only terms x, y and xy have nontrivial coefficients, with the rest having a coefficient of almost zero. This means that the scaling can be described by the following equation

$$z = a_{10}x + a_{01}y + a_{11}xy, \qquad \text{Eq. 6.35}$$

where z is the scaling, x is the sorptivity and y is the spacing factor.

Next, we analyze the sensitivity of the scaling with respect to the variation of the sorptivity and spacing factor. If we take the derivative of y in Eq. 6.35, it results in

$$\frac{\partial z}{\partial y} = a_{01} + a_{11}x. \qquad \text{Eq. 6.36}$$

According to the results in Table 6.4, a_{11} has a positive value, indicating that when sorptivity is high, the output is more sensitive to changes in the spacing factor, which aligns with the result in Section 6.3. Using a similar technique, it can be seen that when the spacing factor is high, variations in sorptivity can also greatly affect the output. In contrast, when either of the two values is small, changes in the other value do not significantly impact the output.

The modeling results offer an explanation for the observation that concrete with a poor air void system or high sorptivity may not develop high scaling. On the one hand, if the concrete has a high spacing factor, which indicates a poor air void system, it may not experience significant scaling if the sorptivity is low. In this case, the concrete is resistant to water penetration, and the critical degree of saturation required for severe damage may not be reached. This observation is supported by Figure 6.28 (b), which shows that concrete with low sorptivity is not impacted by changes in air void parameters. Additionally, it has been found by other researchers that in low w/c ratio concrete, which has fewer interconnected capillary pores and lower sorptivity, an air-entraining agent may not be necessary (Marchand et al. 1994). On the other hand, if the concrete has high sorptivity, which indicates higher connectivity of capillary pores and creates a favorable situation for ice formation, and also has a good quality air void system, the water can flow from the capillary pores to the nearest air voids quickly without generating high stress on the paste matrix. Specifically, when sorptivity is greater than 0.2 $mm/min^{0.5}$, the spacing factor can be maintained below 160 microns to keep the scaling under 1 kg/m^2. Conversely, when sorptivity is low, the scaling can remain low even if the spacing factor exceeds 200 microns. This situation also leads to low scaling. In short, to achieve low scaling, concrete with higher sorptivity should be equipped with an air void system of better quality.

6.5 Summary

This study examined key parameters affecting the salt frost scaling of high-performance concrete specimens. The analysis identified at least two independent variables that affect salt deicing scaling: 1) sorptivity, which measures the capillary suction property, and 2) the quality of the air void system. To visualize the impact of these variables, a polynomial regression model was proposed and a 3-D plot was created, providing an initial quantification method. The key findings of the study are:

- The ability of external water to penetrate the porosity of cementitious binder under capillary suction, measured by water sorptivity, is a crucial physical property that determines scaling resistance to deicer salt solution.
- Entrained air voids are dominating in determining spacing factor. The actual spacing between air voids should be smaller than the Powers spacing factor, and other proposed

parameters such as the Philleo factor and accumulated surface area can be highly correlated with Powers spacing factor.

- It is difficult to attribute deicer salt scaling to a single parameter. The scaling is instead a result of high sorptivity and low resistance. Moreover, scaling in concrete with higher sorptivity is more sensitive to changes in the air-void system quality.
- A polynomial regression model, which incorporates the capillary suction property causing surface ice formation and the air-void system providing resistance to pressure build-up, is proposed. The modeling results suggest that a better-quality air-void system is required for more permeable concrete. This model provides a sound explanation for why, in some cases, high scaling is not observed in concrete with a high spacing factor or high sorptivity.

Chapter 7. Concrete Salt Scaling Resistance Predictions Using XGBoost

7.1 General

Machine learning (ML) is a powerful tool that involves training a model using sample data to make predictions on unseen data, which has a wide range of applications, including e-commerce, health analytics, logistics, cybersecurity, and others. The use of ML in concrete science dates back to 1992 when Pratt and Sansalone published their research on the automated field system (Pratt et al. 1992). In recent years, advancements in ML technology have made it more accessible to users and have led to an increase in its use in concrete research. Since 2009, ML has been used to study cement hydration and concrete degradation mechanisms, and assist in concrete material design and discovery. In this context, some of the major research topics using ML for concrete science are outlined below.

1) Property prediction: Determining the properties of concrete through traditional experimental tests can be both time-consuming and labor-intensive. One of the most significant applications of ML is to predict the mechanical and durability-related performance of concrete materials based on available information, such as composition and mixture properties. For instance, ML can be used to predict the compressive strength of concrete by utilizing information such as mixture characteristics, curing age, and others. This can streamline the process of mix design and curing regime optimization (Feng et al. 2020).

2) Materials characterization: The combination of ML and non-destructive evaluation techniques, such as acoustic, electromagnetic, and optical methods, has been used to evaluate concrete properties and detect damage. For example, deep learning can be utilized in image-based characterization for the segmentation of elements such as pores, cracks, and fibers (Hilloulin et al. 2022).

In this study, a binary classification model is implemented by the XGBoost algorithm to determine if the concrete is salt frost scaling resistant or not. The dataset involves 18 predictor variables,

including w/cm, curing age, sorptivity, spacing factor, and others, which are identified as key factors impacting the salt scaling resistance of concrete based on previous discussions and analysis.

7.2 Theoretical background

The algorithm of XGBoost and the analytical tool – Shapley value are reviewed in this section.

7.2.1 XGBoost

The XGBoost algorithm (which stands for extreme gradient boosting) is an efficient implementation of the gradient boosting algorithm. XGBoost creates a sequence of decision trees to predict the output for a given input. These decision trees are constructed in a greedy manner, meaning that the algorithm chooses the splits to the tree in a way that maximizes the improvement in a certain performance metric (such as accuracy) at each step. The algorithm trains these trees in a stage-wise manner, where each tree is designed to correct the errors made by the previous tree in the sequence and their predictions are combined in a weighted manner to produce a final prediction. To find the optimal solution, XGBoost takes the Taylor expansion of the loss function to the second order and incorporates a regularization term. The schematic illustration of the XGBoost algorithm is shown in Figure 7.1 (Chen et al. 2016, Guo et al. 2020).

The XGBoost model can be characterized as

$$\hat{y}_i = \sum_{k=1}^{K} f_k(x_i), f_k \in F, \qquad \text{Eq. 7.1}$$

where K is the number of decision trees, $f_k(x_i)$ is the function of input in the kth decision tree, $\hat{y}_i$ is the predicted value, and F is the set of all possible Classification And Regression Trees (CART). The objective function of XGBoost includes training error and regularization, which is

$$X_{obj} = \sum_{i=1}^{n} l(y_i, \hat{y}_i) + \sum_{k=1}^{K} \Omega(f_k), \qquad \text{Eq. 7.2}$$

where n is the number of data points involved in training datasets, $\sum_{i=1}^{n} l(y_i, \hat{y}_i)$ is the loss function used to measure the difference between the predicted value and the real value. $\sum_{k=1}^{K} \Omega(f_k)$ is the regularization term that can be determined by

$$\Omega(f_k) = \gamma T + \frac{1}{2}\lambda \parallel w \parallel^2, \qquad \text{Eq. 7.3}$$

where T is the number of the leaf node, w is the scores of the leaf node, γ is the leaf penalty coefficient, and λ ensures that the scores of a leaf node are not too large.

In order to find the objective function which can be minimized, take the Taylor expansion of the loss function up to the second order. Then, the objective function is approximated as

$$L^{(K)} = \sum_{i=1}^{n} \left[l\left(y_i, \hat{y}_i^{(K-1)} + f_K(X_i)\right) + \frac{1}{2} h_i f_K^2(X_i) \right] + \Omega(f_k). \qquad \text{Eq. 7.4}$$

Add the loss function values of each data, and the process is as follows:

$$X_{\text{obj}} = \sum_{j=1}^{n} \left[\left(\sum_{i \in I_j} g_i \right) w_j + \frac{1}{2} \left(\sum_{i \in I_j} h_i + \lambda \right) w_j^2 \right] + \lambda T, \qquad \text{Eq. 7.5}$$

where $g_i = \partial \hat{y}^{K-1} l(y_i, \hat{y}^{K-1})$ is the first derivative, $h_i = \partial^2 \hat{y}^{K-1} l(y_i, \hat{y}^{K-1})$ is the second derivative. The optimal w and objective function values obtained by the solution are as

$$w_j = -\frac{G_j}{H_j + \lambda}, \qquad \text{Eq. 7.6}$$

$$X_{obj} = -\frac{1}{2} \sum_{j=1}^{T} \frac{G_j}{H_j + \lambda} + \lambda T, \qquad \text{Eq. 7.7}$$

where $G_j = \sum_{i \in I_i} g_i, H_j = \sum_{i \in I_j} h_i$.

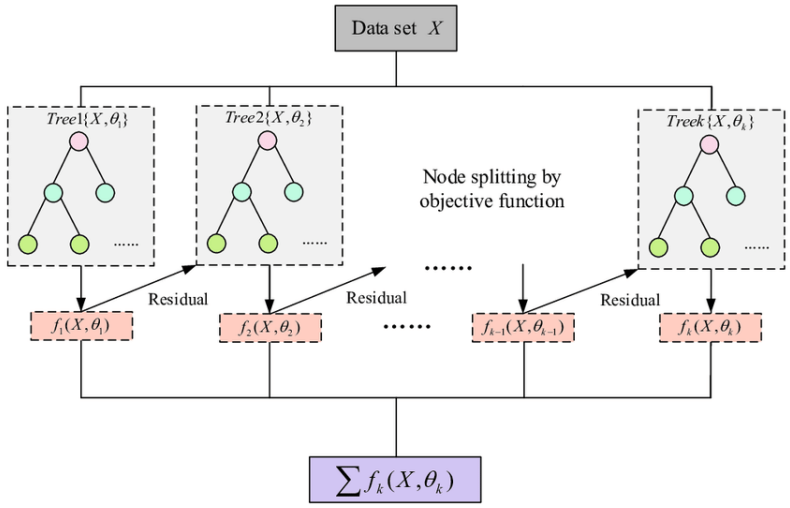

Figure 7.1 Illustration of the boosting algorithms (Guo et al. 2020)

A more detailed algorithm can be found in the work by Guo et al. (2020).

7.2.2 Shapley value

The lack of interpretability of machine learning predictions can be a hindrance to their adoption and widespread use (Molnar 2020). To overcome this challenge and build trust in the model and its outcomes, interpretability is crucial.

Shapley value is a concept in cooperative game theory that measures the contribution of each player (or player's coalition) to the overall value of the game. In the context of machine learning, the Shapley value can be used to evaluate the contribution of each feature (or set of features) to the prediction of a model (Mateo 2012). The Shapley value has the property of being both linear and fair, meaning that it assigns a value to each feature in proportion to its contribution, with the sum of all values equaling the total prediction of the model. This makes the Shapley value a useful tool for explaining the predictions of complex machine learning models, such as neural networks and ensemble models.

Denote the dataset of n data points by $(x_{ij}, y_i)^n$, where x_{ij} is the feature j value of instance i with $j \in \{1, \dots, p\}$, where p is the number of features. The feature effect (or shapely value) ϕ_{ij} of x_{ij} on the prediction $\hat{f}(x_{i\cdot})$ is its contributions to the output, weighted and summed over all possible feature value combinations and can be calculated as (Molnar 2020)

$$\phi_{ij}(v) = \sum_{S \subseteq \{x_{i1}, \dots, x_{ip}\} \setminus \{x_{ij}\}} \frac{|S|!\,(p - |S| - 1)!}{p!} \left(v\left(S \cup \{x_{ij}\}\right) - v(S)\right), \qquad \text{Eq. 7.8}$$

where S is a subset of the features used in the model called a coalition, $|S|!$ represents the number of ways features can join the coalition before feature j, $(p - |S| - 1)!$ represents the number of ways features can join a coalition after feature j, $p!$ is the number of ways to form a coalition of p features, $x_{i\cdot}$ is the vector of feature values of the instance i to be explained. $v(S)$ is the prediction for feature values in set S that are marginalized over features that are not included in set S. $v\left(S \cup \{x_{ij}\}\right) - v(S)$ is the marginal contribution of x_{ij} to coalition S and $v(S)$ can be calculated as

$$v(S) = \int \hat{f}(x_{i1}, \dots, x_{ip}) d\mathbb{P}_{X_{i:} \notin S} - E_X\left(\hat{f}(X)\right). \qquad \text{Eq. 7.9}$$

An approximate Shapley value estimation algorithm is attached in Appendix B.

The process involves assigning weights to each marginal contribution of feature *j* based on the probability that they make the contribution. These weighted contributions are then summed across all possible coalitions that feature *j* can join, resulting in an expected marginal contribution.

The author has transformed the prediction for XGBoost using the log odds ratio so the output $\hat{f}(x_i.)$ is written as

$$\hat{f}(x_{ij}) = ln\frac{p}{1-p} = \phi_0 + \sum_{j=1}^{p} \phi_{ij}, \qquad \text{Eq. 7.10}$$

where p is between 0 and 1 and can be regarded as the possibility of the instance being a positive class.

7.3 Data exploration and pre-preprocessing

7.3.1 Data source

The data used in this study is collected from a number of previous studies beyond this thesis (Pigeon et al. 1996, Panesar et al. 2009, Gagné et al. 2011, Marks et al. 2012, Liu et al. 2015, 2016c, Hilloulin et al. 2022, Nowak-Michta 2022). The study adopts binary classification (a classification problem), rather than predicting the scaling value (a regression problem), as the exact scaling value is dependent on various factors such as specific test methods, test environments, and the number of freeze-thaw cycles (F-T cycles) which are not the main focus of this study. Each F-T test method (e.g., Swedish standard, CDF/CIF, BNQ, ASTM C672) has established a scaling limit to determine the acceptability of concrete for scaling resistance after a specified number of F-T cycles (e.g., 28, 50, or 56 cycles). By using binary classification, the outcome is less subject to variation from the specific test method, compared to the scaling value.

7.3.2 Data exploration and manipulation

The dataset used in this study contains 161 data points, each with 18 predictor variables, including w/c, total cement content, water amount, cement amount, slag amount, slag content, fly ash amount, fly ash content, silica fume amount, silica fume content, air content, spacing factor, compressive strength, sorptivity, curing age, type of Portland cement, type of GGBFS, and type of fly ash. Further details regarding these features can be found in Appendix C. The response variable in this study is a binary response variable indicating whether the concrete sample exhibited salt frost scaling in excess of the limit specified by the corresponding test method. Samples with scaling

values exceeding the limit were labeled as non-resistant, while those with scaling values within the limit were labeled as resistant. The dataset included 99 samples labeled as scaling resistant (1) and 62 samples labeled as non-resistant (0). A histogram of the collected data can be found in Appendix D. A correlation heatmap of the variables has been included in Appendix E. Highly correlated features may lead to overfitting and should be carefully considered when selecting features for the model. It is recommended to eliminate features that exhibit a high degree of correlation, as they may not provide significant additional information to the model.

- Data imputation

There are four features in the dataset that have missing values (missing rate is in the parenthesis): compressive strength (6.2%), air content (6.2%), spacing factors (6.2%), and sorptivity (63.3%). To handle these missing values, the mean values are used to impute air content and spacing factor. The missing values of compressive strength are imputed using Abram's law as follows:

$$\sigma_c = \frac{A}{B^{w/c}}, \qquad \text{Eq. 7.11}$$

where σ_c is the compressive strength of concrete, w/c is the water/cement ratio, and A and B are constants for a given material, age, and test conditions (ABrAMS 1919).

Unfortunately, sorptivity has a high number of missing values due to a limited availability of data that have investigated its correlation with scaling. Typically, features with high percentages of missing values are dropped from analysis. However, since sorptivity contains valuable information regarding scaling, it was decided to impute the missing values based on domain knowledge. Sorptivity is strongly related to the pore structure of concrete and has been shown to be correlated with compressive strength at 28 days, as demonstrated in Figure 7.2. Therefore, the missing values of sorptivity were filled using the formula provided in Figure 7.2.

- Feature Encoding

The 18 predictors are a combination of continuous and categorical variables. To prepare the categorical features such as GGBFS_type for processing in the ML algorithm, they need to be transformed into numerical values. Common encoding techniques include One Hot Encoder and Label Encoder. One Hot Encoder encodes the type columns into separate columns of binary values while Label Encoder generates numerical categories in the same column. However, Label Encoder

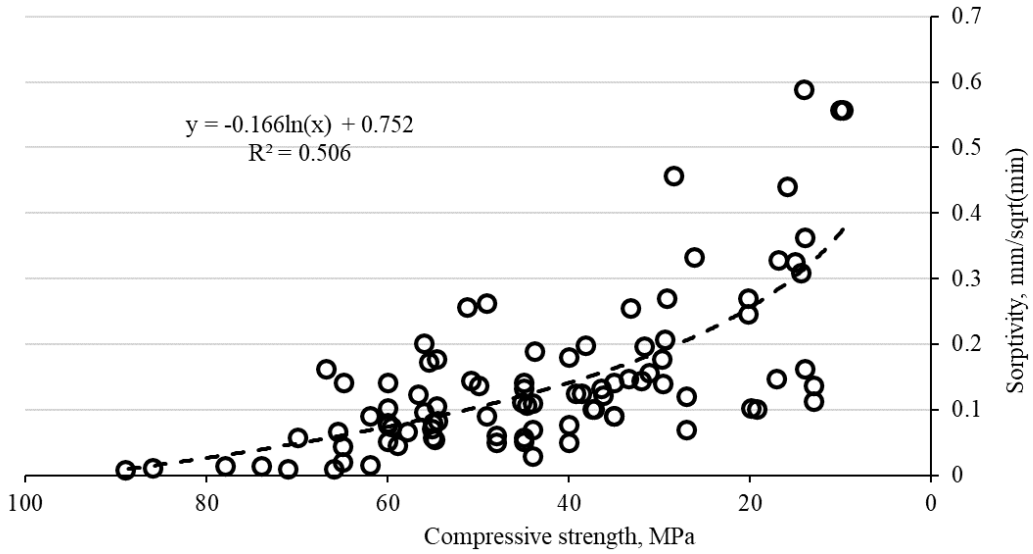

Figure 7.2 Relationship between compressive strength and sorptivity

may introduce false ordering relationships between categories, which could mislead the model. Therefore, this study employs One Hot Encoder to encode the cementitious material type columns (PC_type, GGBFS_type, and FA_type). Each generated column represents a specific cementitious material category and a '1' in a column indicates that the concrete contains the corresponding type of cementitious material as illustrated in Figure 7.3.

GGBFS_TYPE_5	GGBFS_TYPE_6	GGBFS_TYPE_7	FA_TYPE_0	FA_TYPE_1
0.0	1.0	0.0	1.0	0.0
0.0	1.0	0.0	1.0	0.0
0.0	0.0	0.0	1.0	0.0
1.0	0.0	0.0	1.0	0.0
0.0	1.0	0.0	1.0	0.0

Figure 7.3 A screenshot of part of the GGBFS type and FA type columns

- Response and features of key interest

For data exploration purposes only, the data is separated into two categories: scaling-resistant concrete and non-scaling-resistant concrete. The distribution of key features of interest is analyzed and visualized in Figure 7.4. The difference in distribution curves between the two groups for a particular feature indicates its potential importance in developing the model. The results showed

that scaling-resistant concrete typically has higher air content, lower spacing factor, w/c, and sorptivity, which aligns with previous findings.

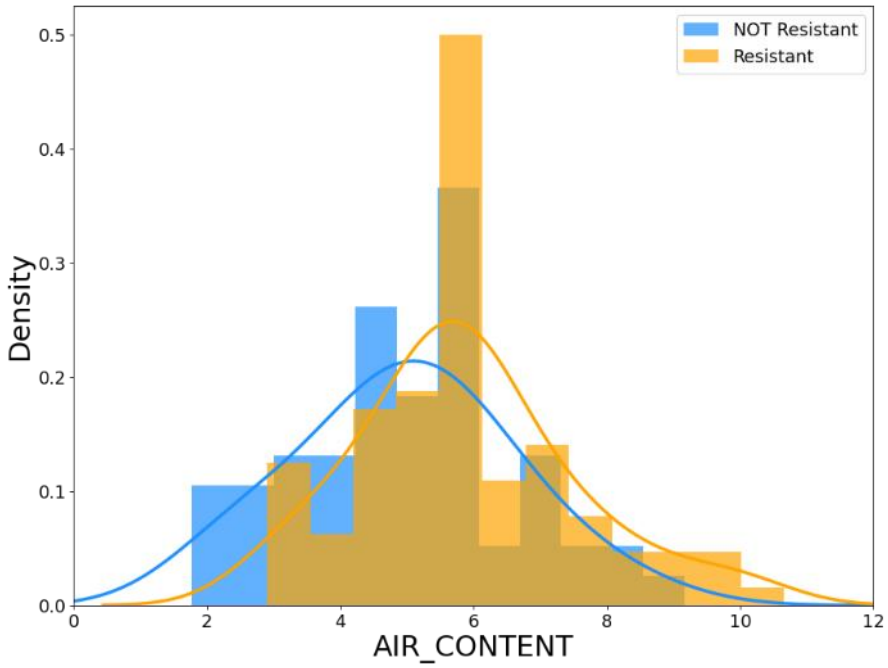

(a)

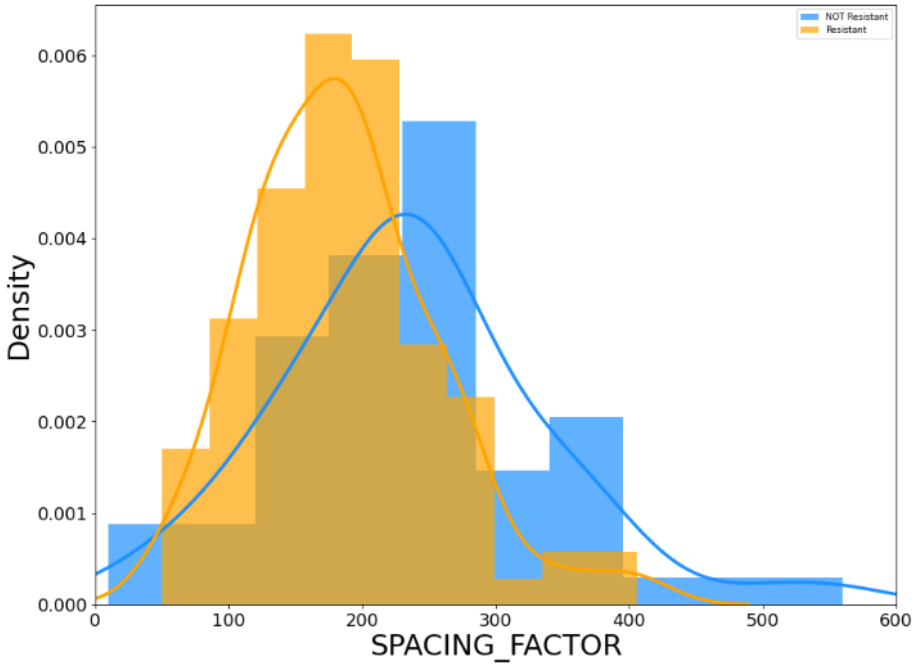

(b)

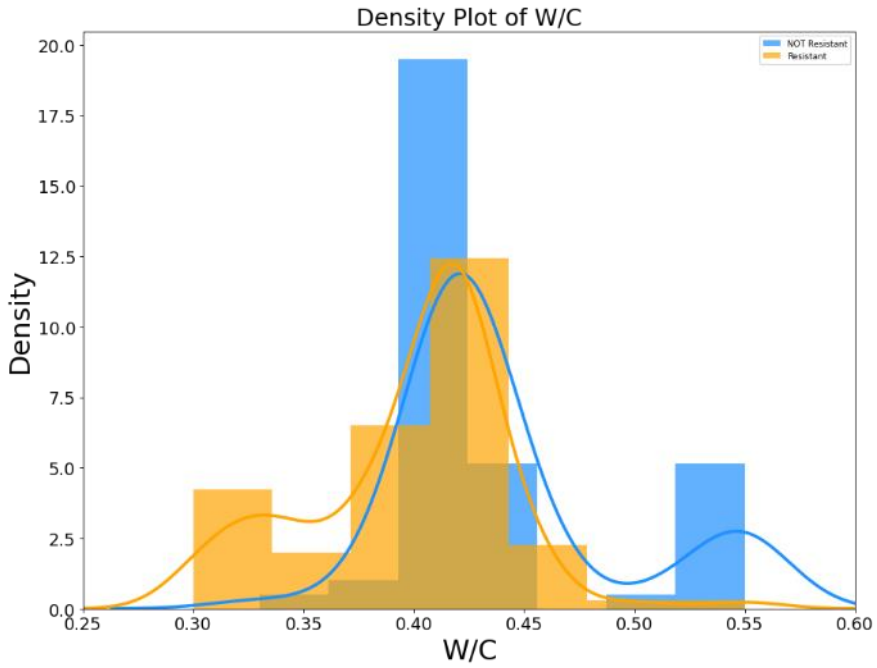

(c)

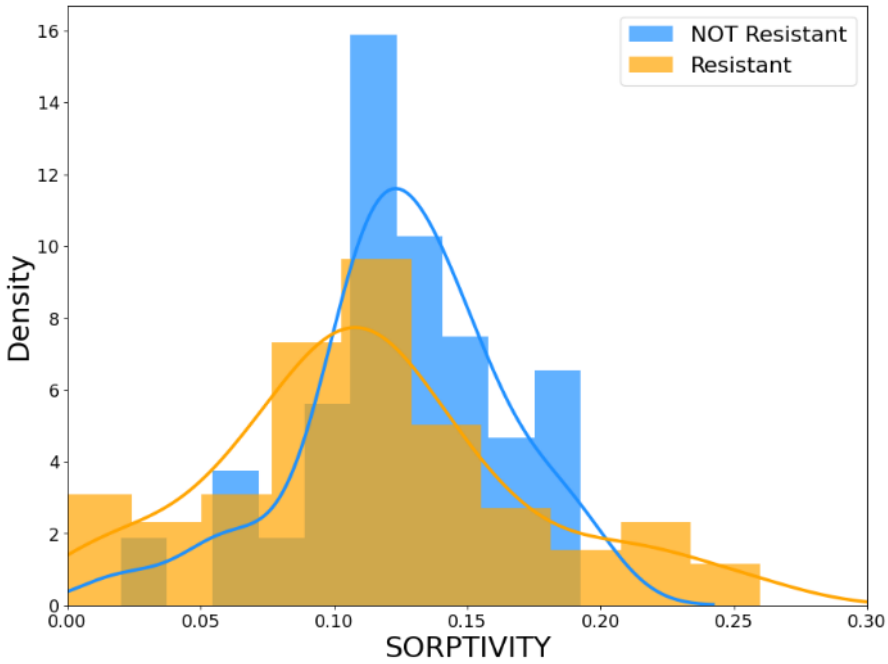

(d)

Figure 7.4 Density plot of features for scaling resistant and non-resistant concrete: (a) air content (b) spacing factor (c) w/c (d) sorptivity

7.4 Results and analysis

7.4.1 Model tuning and metrics

The XGBoost model was implemented using the standard Python library XGBoost (Chen et al. 2016). In order to optimize the model's performance, a set of hyperparameters needed to be fine-tuned. 80% of the data was used to train the model while 20% of the data was used to test the model. To determine the best combination of parameters, a grid search was performed using 5-fold cross-validation, as illustrated in Figure 7.5. The ranges used in the cross-validation and the final selected parameters can be found in Table 7.1.

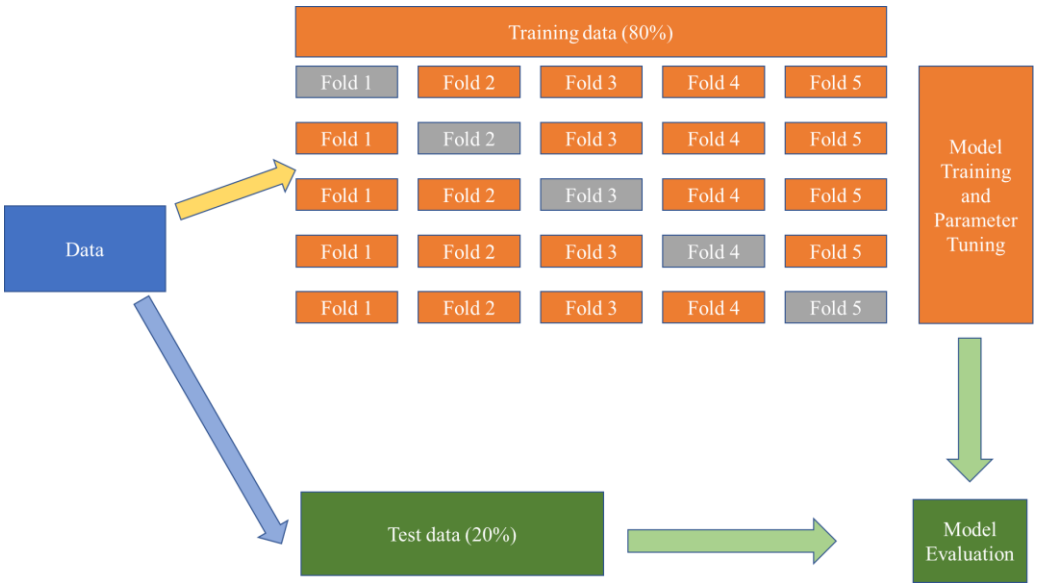

Figure 7.5 Illustration of fivefold cross-validation (the fold in gray is used to validate the model)

Table 7.1 The searching range used in cross-validation

Parameters	Explanation	Best Value (Grid Search Range)
gamma	Minimum loss reduction required to make a further partition on a leaf node.	0 (0 - 5)
max_depth	Maximum depth of a tree.	2 (1 - 4)
min_child_weight	The minimum sum of instance weight (hessian) needed in a child.	2 (1 - 4)
n_estimators	The number of trees to be produced	40 (20 - 100)
learning_rate	The step size at each iteration in optimization.	0.05 (0.001 – 0.1)

The performance metrics of the trained XGBoost model on the test dataset are presented in Table 7.2. The model achieves high values for both ROC-AUC and accuracy on both the training and test datasets. This indicates that the model has a strong capability for predicting scaling resistance.

Table 7.2 XGBoost metrics

Metrics	***Training Dataset***	***Testing Dataset***
Accuracy	0.81	0.79
ROC-AUC	0.91	0.82
F1	0.83	0.87
Precision	0.82	0.88
Recall	0.85	0.85

7.4.2 Feature importance and selection

The SHAP (Shapley Additive exPlanations) tool is employed to understand the outputs produced by an XGBoost model. This tool computes the SHAP values for each feature, which provide insights into the feature's contribution to a specific decision outcome. The magnitude of these contributions is reflected in the SHAP values, making it possible to evaluate the relative importance of each feature in the model's decision-making process.

As shown in Figure 7.6, the features are listed in order of importance, with 'spacing_factor', 'sorptivity', 'w/c', 'air_content', and 'compressive_strength' being the top five contributors. Each dot in the plot represents a single data point, and its color is indicative of the value of the feature it represents. The higher the feature value, the redder the dot will appear, providing a visual representation of the relationship between the features and the output. For example, in the case of the 'spacing_factor' feature, redder dots indicate a high spacing factor and the corresponding SHAP value is negative suggesting a greater likelihood of the concrete being non-resistant.

The compressive strength and cement, while appearing to be important, should be viewed with caution as they may have a spurious correlation with scaling resistance. This is because it is highly related to the air content and pore structure of the concrete, which is influenced by factors such as w/c, curing age, and the addition of SCMs. The cement content ranks as the sixth important factor and can be attributed to its correlation with the w/c. It may be used as an alternative feature to w/c by the model.

The SCMs do not hold a prominent position in terms of scaling resistance prediction. This is due to a combination of factors, including limited data availability for fly ash and silica fume as most concrete mixtures in this study do not incorporate these materials. Furthermore, SCMs do not directly impact scaling resistance, but rather affect it indirectly through their impact on porosity, pore continuity, and thus, sorptivity - which is considered the primary factor in scaling resistance. As a result, the relationship between scaling resistance and SCM content is more complex and implicit. Moreover, according to the modeling results, the type of cement and SCMs appear to be less significant factors compared to others.

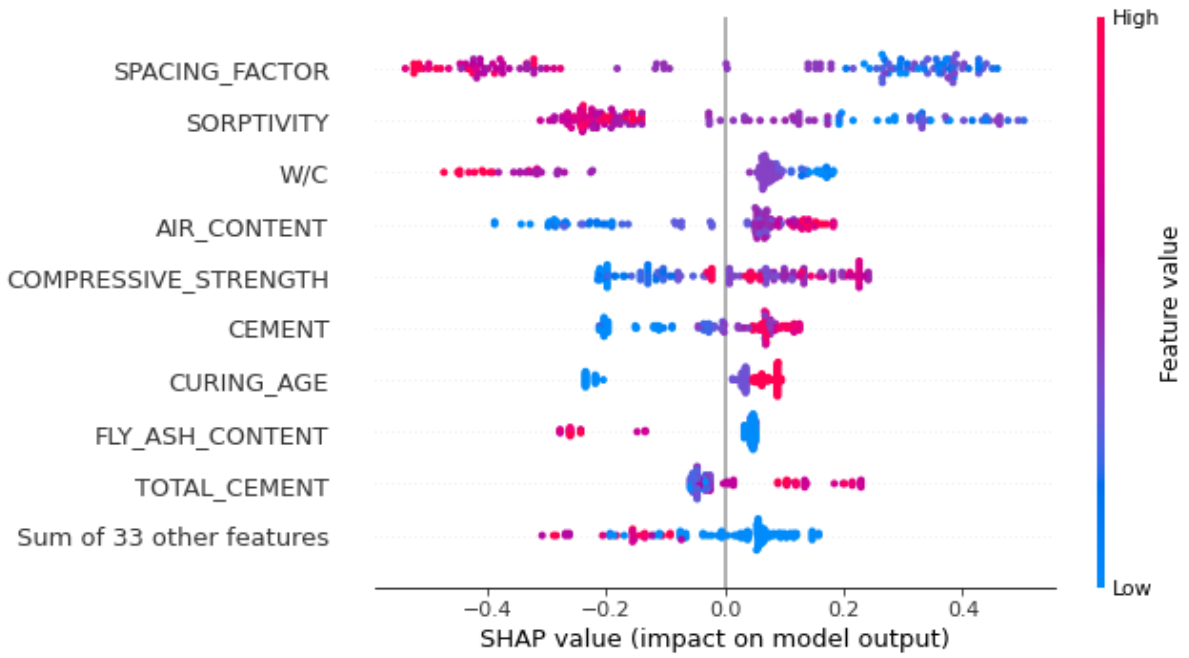

Figure 7.6 Visualizing feature importance with single data points using SHAP values

Figure 7.7 shows the importance of features based on the average absolute SHAP value of each feature for all data points. This again verifies what have been discussed above.

The following chart (Figure 7.8) summarizes the most crucial elements that affect the resistance to salt scaling. Sorptivity and spacing factor are regarded as the primary factors, while w/c, curing age, air content, and SCM are considered secondary factors. The w/c, SCM, and curing age influence the pore structure and thus the sorptivity. The air content is closely linked with the spacing factor. Despite being a vital attribute, compressive strength does not exhibit a direct cause-and-effect relationship with scaling.

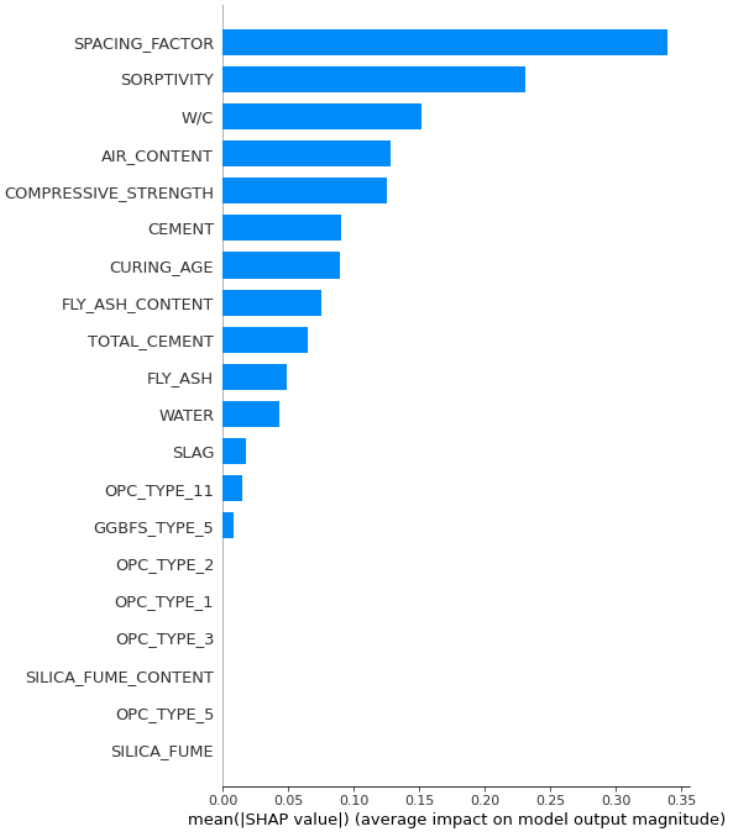

Figure 7.7 Average absolute SHAP value of features

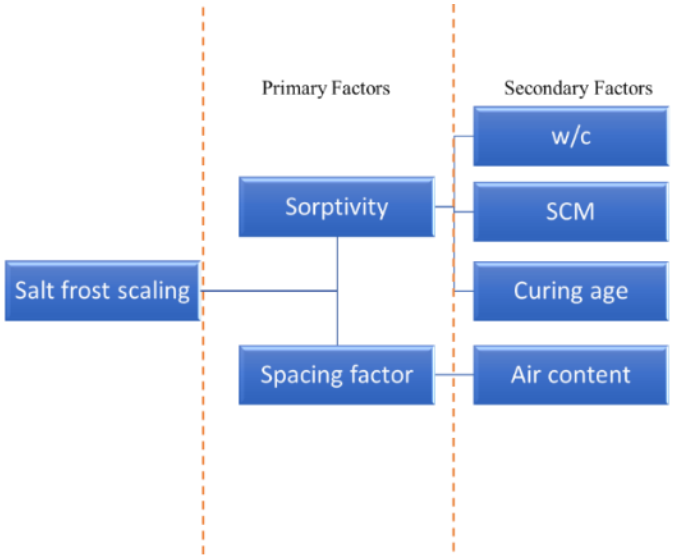

Figure 7.8 Summary of important features determining salt scaling resistance

7.4.3 Model training after feature selection

Based on the feature importance and correlation analysis, the most important features (spacing factor, sorptivity, w/c, curing age) are used to train the model again. The search range and optimal value in cross-validation are summarized in Table 7.3.

Table 7.3 Search range and optimal values in cross-validation after feature selection

Parameters	Explanation	Optimal Value (Grid Search Range)
gamma	Minimum loss reduction required to make a further partition on a leaf node.	0 (0 - 5)
max_depth	Maximum depth of a tree.	3 (1 - 4)
min_child_weight	The minimum sum of instance weight (hessian) needed in a child.	2 (1 - 4)
n_estimators	The number of trees to be produced	25 (20 - 100)
learning_rate	The step size at each iteration in optimization.	0.05 (0.001 – 0.1)

The performance of the trained XGBoost model on the training and test dataset is presented in Table 7.4. Compared to the model before feature selection, the accuracy, F1 score, prediction, and validation of the test dataset are comparable. The only metric that has changed is the ROC-AUC. Nevertheless, its impact on the model's ability to distinguish between scaling-resistant and non-resistant concrete can be effectively mitigated by selecting the appropriate threshold value.

Table 7.4 XGBoost metrics after feature selection

Metrics	***Training Dataset***	***Testing Dataset***
Accuracy	0.80	0.79
ROC-AUC	0.89	0.73
F1	0.82	0.87
Precision	0.83	0.88
Recall	0.81	0.85

The beeswarm chart and summary plot of the SHAP value for the model after feature selection (Figure 7.9 and Figure 7.10) are similar to the ones for the model before feature selection. The results have revealed that the sorptivity and spacing factor are the most important features for

scaling resistance prediction. This confirms the findings from Chapter 6 that the scaling is primarily dependent on the balance between these two properties.

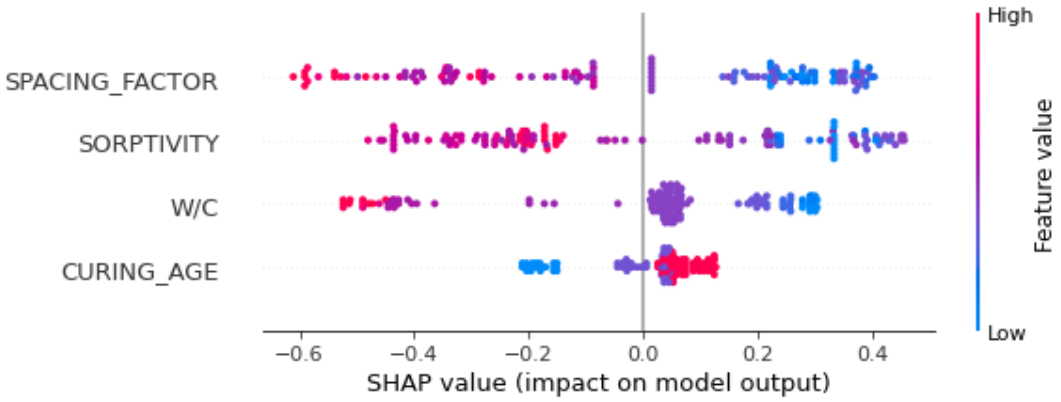

Figure 7.9 Visualizing feature importance with single data points using SHAP values after feature selection

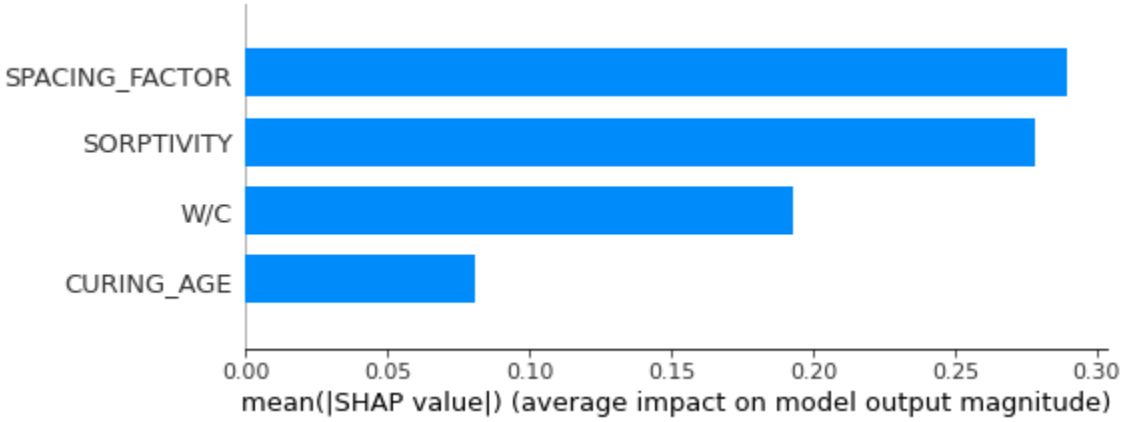

Figure 7.10 Average absolute SHAP value of features after feature selection

The dependence plot in Figure 7.11 provides a more detailed view of how each feature affects the SHAP value and salt frost scaling resistance. The spacing factor value of smaller than 200 microns has a positive impact on the output as indicated by a higher SHAP value and the concrete is more likely to be scaling resistant. This conclusion is in line with the general recommendation that suggests limiting the spacing factor to 200 microns or less for concrete. Once the spacing factor exceeds 200 microns, the SHAP value of this feature drops quickly. This indicates that the resistance of concrete to scaling decreases at an accelerated rate. Sorptivity is another important feature in determining scaling resistance. The results have shown that when sorptivity is less than approximately 0.12 mm/sqrt(min), the SHAP value of sorptivity is positive implying that the

concrete is more likely to be scaling resistant. This conclusion is consistent with the findings of Gagné et al. (2011) who found that the scaling durable concrete has a sorptivity of 0.10 mm/sqrt(min). It is important to note that for sorptivity values above 0.15 mm/sqrt(min), some of the SHAP values may appear scattered, which could be attributed to the imputation of data based on the compressive strength.

In addition to spacing factor and sorptivity, other features including w/c and curing age are also important in determining the scaling resistance of concrete. When the w/c is greater than 0.42, the scaling resistance decreases quickly as indicated by the sharp drop in the SHAP value around that point. The curing age of concrete is also a relatively important factor. As predicted by the curve, the 7-day curing period may not be sufficient to produce a positive impact on the scaling resistance. Instead, the curing length should be extended to at least 14 days and ideally to 28 days, in order to strengthen the scaling resistance.

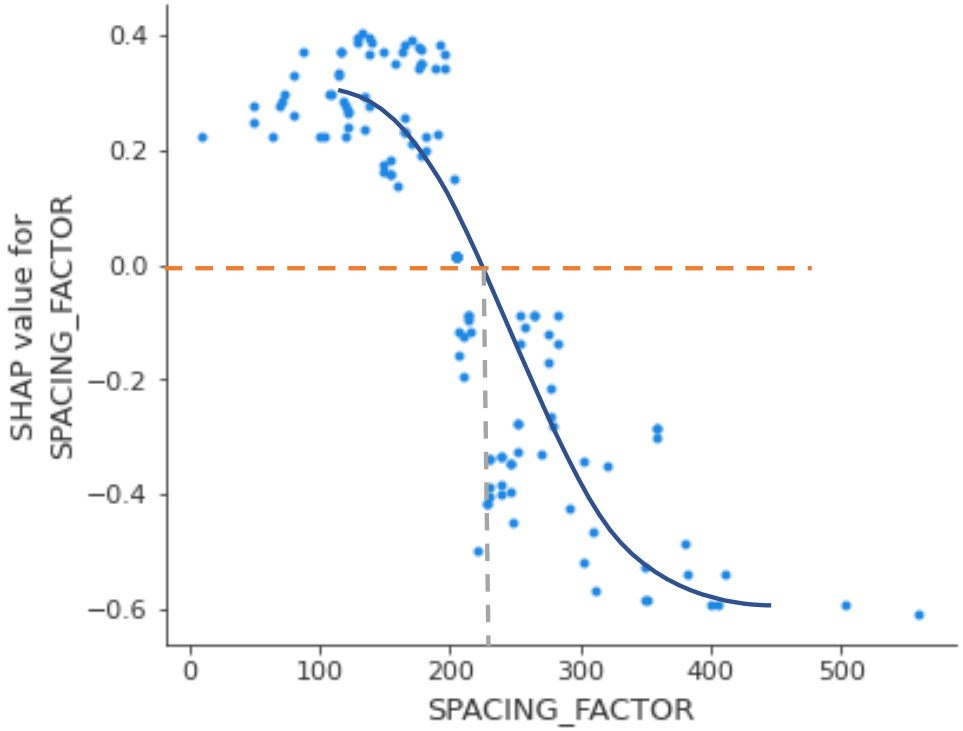

(a)

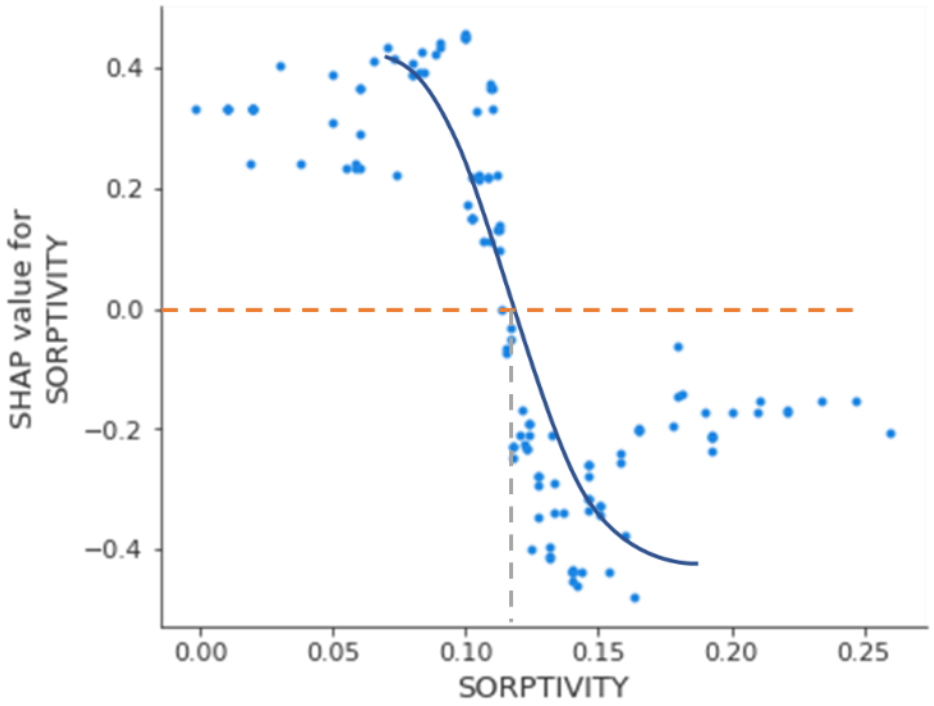
SHAP value for SORPTIVITY
0.4
0.2
0.0
−0.2
−0.4
0.00
0.05
0.10
0.15
0.20
0.25
SORPTIVITY

(b)

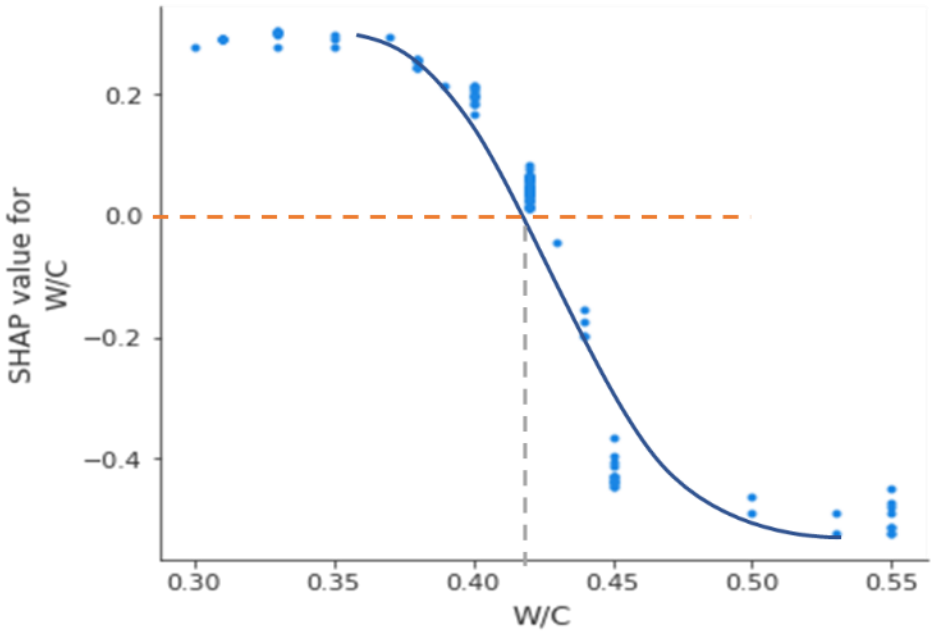
SHAP value for W/C
0.2
0.0
−0.2
−0.4
0.30
0.35
0.40
0.45
0.50
0.55
W/C

(c)

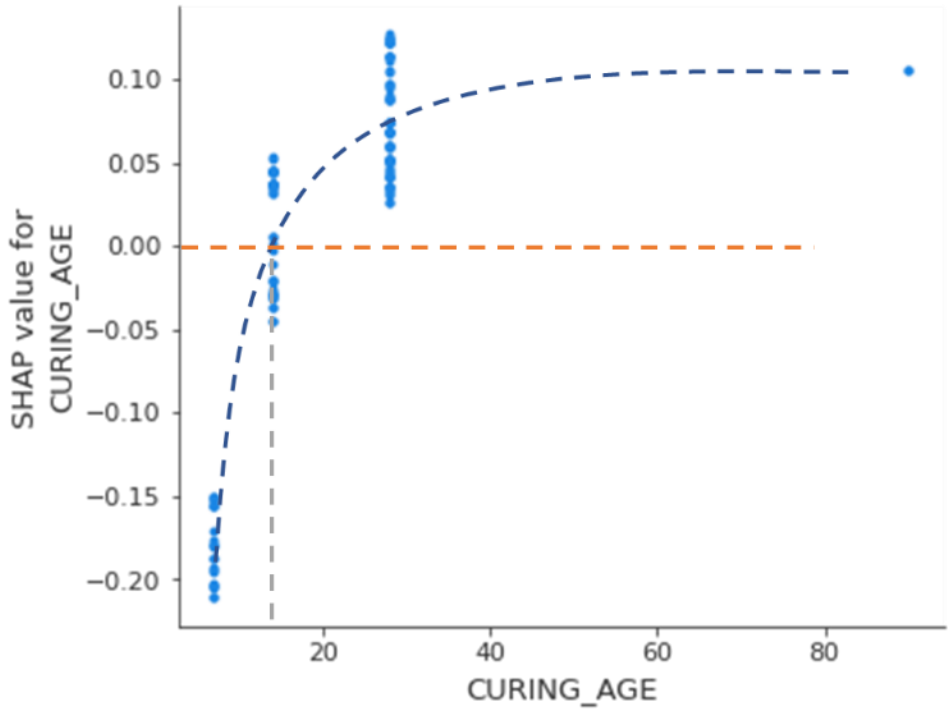

(d)

Figure 7.11 Impact of feature value on the SHAP value

The individual concrete instances can be analyzed to identify the factors contributing to their resistance or vulnerability to scaling. With the use of this analysis tool, the resistance of concrete to scaling can be predicted based on key features without the need for conducting F-T tests. This information can provide valuable guidance for concrete mix design. The mean of all predictions, also known as the expected prediction, $E[f(x)]$, is 0.185. A concrete instance with a high likelihood of being scaling resistant is analyzed in Figure 7.12 (a) using a waterfall plot. The prediction for this particular concrete is 1.367, represented as $f(x)$, with a probability of 79.7% resistance to scaling as calculated from Eq. 7.10. The selected concrete has a low sorptivity of 0.073, which accounts for an increase of 0.42 in the prediction value compared to the expected value. Furthermore, the concrete's favorable properties such as a spacing factor of 165 microns, w/c of 0.35, and 28-day curing age contribute an additional 0.38, 0.29, and 0.09 to the prediction value, respectively, further enhancing its resistance to scaling. In Figure 7.12 (b), a concrete instance with a low likelihood of scaling resistance is presented. The prediction value $f(x)$ for this concrete is -0.704 corresponding to a probability of only 33.1% that the concrete will be resistant to salt scaling. This low likelihood of resistance can be attributed to its high spacing factor of 247

microns, a sorptivity of 0.128 mm/sqrt(min), and low curing age of 7 days. These factors together negatively impact the concrete's ability to resist scaling. A challenging instance is depicted in Figure 7.12 (c) as it has feature values that are mixed in their impact on the concrete's resistance to scaling. The concrete has a very poor air void system as evidenced by a spacing factor of more than 500 microns. However, the concrete's low w/c and sorptivity indicate that it is resistant to water penetration and scaling. The prediction for this concrete is 0.15 corresponding to a 53.7% probability that the concrete is resistant. This suggests that in this case, the scaling of the concrete should be close to the limit in the specific test standard.

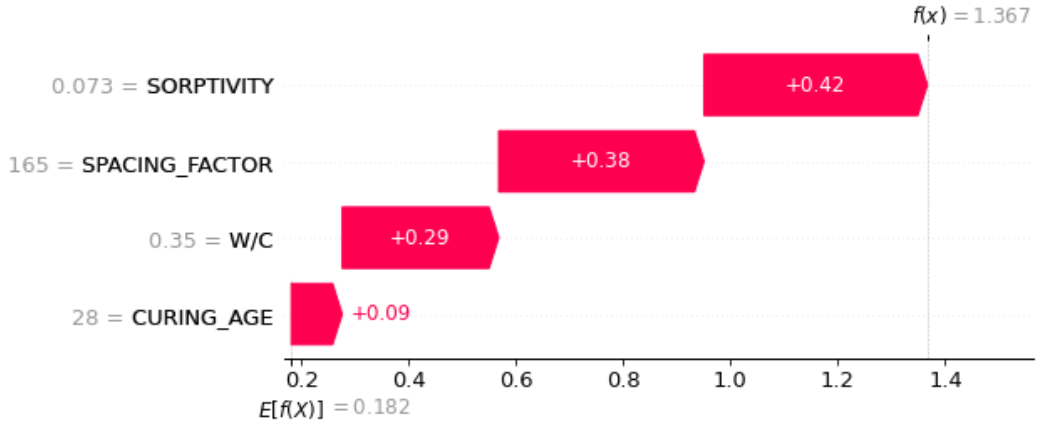

(a)

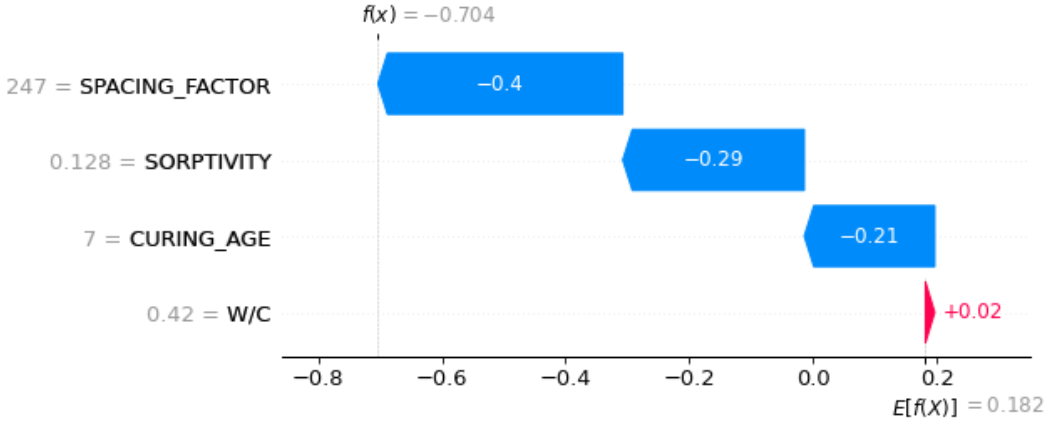

(b)

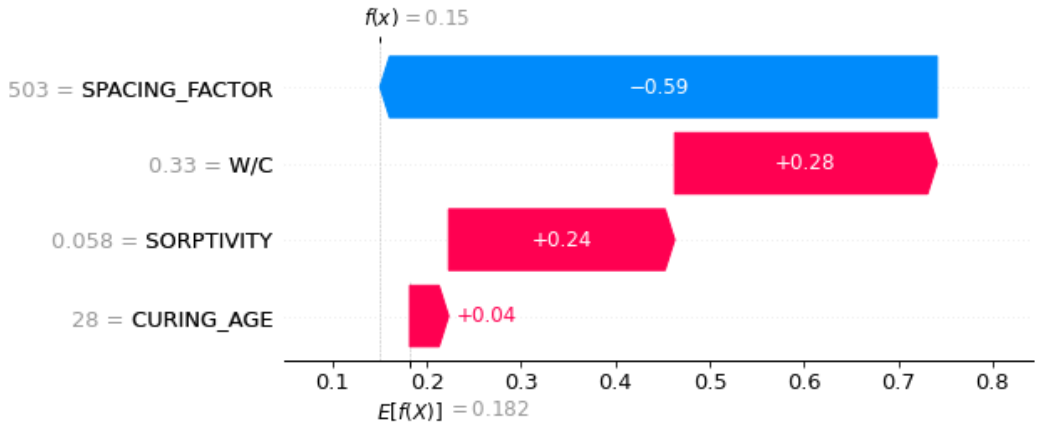

(c)

Figure 7.12 Individual concrete analysis with SHAP value: characterizing (a) Highly likely resistant, (b) Non-resistant, and (c) Challenging instances

7.5 Summary

A binary classification model is developed using the XGBoost algorithm to differentiate between scaling-resistant and non-resistant concrete. The model is trained using 18 features that are previously identified as being significant in determining the scaling resistance. The Shapley value, a method based on cooperative game theory, is utilized to analyze the relative importance of each feature. Based on the feature importance and correlation analysis, the top four features are selected to train a new model. The results are found to be comparable to those obtained from the original model. The key insights of this study are:

- The XGBoost algorithm proves its effectiveness in predicting concrete scaling resistance with an accuracy of 79% after feature selection.
- Based on the SHAP value analysis, sorptivity and spacing factor have been identified as the major factors affecting concrete scaling resistance, with secondary considerations being given to w/c, and curing age.
- The use of the Shapley waterfall plot allows for individual concrete instances to be analyzed, providing valuable insights into the concrete mix design and production process.

Chapter 8. Conclusions

8.1 Major conclusions

Freezing thawing conditions combined with deicing salt solution has led to severe deterioration of concrete in North America. Multiple previous studies have attempted to identify the underlying mechanisms responsible for scaling damage. However, no consensus has been reached on this topic. This thesis aims to shed light on the mechanism behind frost damage in concrete and provide insights into the cause of scaling, followed by quantification and predictive modeling using statistical and machine learning methods. The major conclusions are summarized based on three levels: laboratory results, mechanistic analysis, and predictive modeling.

From the laboratory results,

- Capillary suction is a primary mode of water transport in concrete. Moisture uptake based on capillary pore volume or area proposed in this study can better reflect this process. The addition of SCM, a lower w/cm, and lengthening of curing periods can reduce the capillary suction by decreasing the connectivity of the pores and fining pore size and thus improve the F-T resistance.
- Hydrophobic impregnation is found to be ineffective in preventing the pumping effect and improving the resistance of HPC to F-T cycles. Surface impregnation resulted in the conversion of pore structures from a hydrophilic to a hydrophobic state, causing the entrapping effect and severe scaling in the surface-treated layer. Internal impregnation nullified the air void system's ability to provide pressure relief and develops damages both internally and externally. Therefore, maintaining a hydrophilic pore surface and the effectiveness of air entrainment are crucial factors in ensuring concrete's resistance to frost damage.

At the mechanistic analysis level,

a) Similarities and differences between scaling and internal cracking

- The development of both deteriorations depends on the moisture uptake and air void system quality. High moisture uptake and poor air void system increase the likelihood of reaching a critical degree of saturation which suggests the onset of severe deterioration.
- Scaling is more associated with local saturation while internal cracking depends on global saturation. This explains why the development of severe scaling and internal cracking may not be synchronous. The 3% salt solution is found to promote ice growth only on the surface layer. The difference in moisture uptake between water and salt exposure is not appreciable and does not significantly impact the whole matrix. Consequently, the scaling is more sensitive to the external salt concentration change compared to internal cracking.

b) Sorptivity and air void systems are the key parameters in scaling resistance

- Sorptivity which is uniquely related to the pore structure is a better indicator of the moisture condition in the surface layer where direct measurement is challenging. Concrete with higher sorptivity can be more easily filled, reaching a critical degree of saturation and developing severe scaling.
- The quality of the air void system depends on its spacing which is a synthetic parameter of air void volume and size distribution. Air void density based on the air void size distribution is proposed to calculate the paste-void spacing parameters such as Philleo factors. Powers spacing factor is found to be strongly associated with these parameters and it is regarded as an essential indicator of the air void system quality and scaling resistance. Entrained air void system plays a dominating role in determining Powers spacing factor.

Based on the predictive modeling,

- Scaling can be quantified using a polynomial regression model involving sorptivity representing the pressure cause and spacing factor as pressure relief. The severity of scaling depends on the balance of these two parameters. Concrete that is more permeable should be equipped with a better-quality air void system.
- The machine learning model implemented by XGBoost algorithms verified the importance of these two parameters as well as other factors such as w/c and curing age in scaling. This method combined with the Shapley value based on cooperative game theory provides

valuable insights into the scaling resistance of concrete and can be used as a reliable and quicker assessment of concrete quality.

8.2 Recommendations for future work

In terms of future work, there are several recommendations that can be made.

Firstly, the measurement of pore structure and determination of the moisture uptake based on capillaries can be further investigated. While the porosity in this paper is estimated based on the w/cm and hydration degree, it does not involve the effect of SCM on the pore size and volume. The actual porosity and pore size distribution can be obtained by Mercury intrusion porosimetry (MIP) and nitrogen sorption. This would enable a more accurate characterization of moisture uptake based on capillary suction, which would in turn shed light on the relationship between capillary suction, pore structure, and frost damage and may demonstrate the hypothesis that ice expansion leads to capillary pore structure change and additional space for moisture uptake.

Secondly, air void size distribution determination can be improved. In this study, the air void size distribution was estimated using the chord size distribution. However, the use of X-ray computed tomography (XCT) can enable the determination of the real air void size distribution. This would help refine air void parameters and provide a more accurate representation of the air void system in concrete.

Thirdly, more investigations on the mechanism of the combinations of sorptivity and spacing factor are required to further improve the predictive modeling results. While the study suggests that sorptivity and spacing factor are key parameters that affect scaling, more research is needed to better understand the synergistic effect of these two parameters. Furthermore, the use of machine learning methods, such as regression models or multi-classification models, can also be explored to predict the exact value of scaling or the condition of the surface (similar to the rating class mentioned in ASTM C 672) with the availability of more data. The performance of other models such as logistic regression and neural networks can also be investigated and compared.

Finally, more studies on the effect of hydrophobic impregnation on field specimens should be conducted. While laboratory testing has shown that hydrophobic impregnation does not improve the freeze-thaw resistance of air-entrained concrete, its effects in the field need to be further investigated. For example, the use of silane treatment for non-air-entrained concrete that may be

exposed to F-T conditions can be beneficial. This is particularly relevant given that the conditions in the field are typically less severe, and the use of a surface treatment may delay the time of reaching critical saturation and improve performance.

Appendices

Appendix A Example Calculation of The Number of Air Voids In Each Class

The concrete given as an example has a total air content of 6.1% and a paste content of 29.9%. The spacing factor is 108 microns. The first three columns are obtained from the linear traverse results based on the ASTM C457. The last column is the number of air voids in each size group in a unit cube (1 mm^3). The decimal part means that some of the air voids are partially intercepting the unit cube of interest. For example, in Class No.2. with a chord size between 40 and 50 microns, the air content of that class is 0.480% and the mid-point of the chord size group is 45 microns. Consequently, the number of air voids in this class is

$$N_2 = \frac{V_{NS}}{k\left(\frac{p + A_t}{A_i}\right)\bar{l}'^3} = \frac{1}{1.767 * \left(\frac{29.9\% + 6.1\%}{0.48\%}\right) * (45 * 10^{-3})^3} = 82.80$$

AVD considering the air void distribution should be the sum of the number of air voids in each class which corresponds to the last column in the table which equals 346 mm^{-3}. This suggests that in 1 mm^3 of cementitious paste, there are approximately 346 air voids.

Table A.1 Results of number of air voids based on air void size

Class No.	Chord size (microns)	Air Content in Class	Mid-point of the chord size group	number of air voids in each class
1	30-40	0.420	35	154.19
2	40-50	0.480	45	82.80
3	50-60	0.470	55	44.46
4	60-80	0.880	70	40.38
5	80-100	0.690	90	14.90

6	100-120	0.440	110	5.20
7	120-140	0.270	130	1.93
8	140-160	0.180	150	0.84
9	160-180	0.210	170	0.67
10	180-200	0.070	190	0.16
11	200-220	0.100	210	0.17
12	220-240	0.070	230	0.09
13	240-260	0.060	250	0.06
14	260-280	0.020	270	0.02
15	280-300	0.070	290	0.05
16	300-350	0.170	325	0.08
17	350-400	0.230	375	0.07
18	400-450	0.020	425	0.00
19	450-500	0.060	475	0.01
20	500-1000	0.480	750	0.02
21	1000-1500	0.190	1250	0.00
22	1500-2000	0.270	1750	0.00
23	2000-2500	0.090	2250	0.00
24	2500-3000	0.120	2750	0.00
25	3000-4000	0.000	3500	0.00

Appendix B Shapley Value Algorithm

Approximate Shapley Estimation Algorithm (Molnar 2018):

Each feature value x_{ij}'s contribution towards the difference $\hat{f}(x_i) - \mathbb{E}(\hat{f})$ for instance $x_i \in X$.

- Require: Number of iterations M, instance of interest x, data X, and machine learning model $\hat{f}$
- For all $j \in \{1, \dots, p\}$:
  - For all $m \in \{1, \dots, M\}$:
    - draw random instance z from X
    - choose a random permutation of feature $o \in \pi(S)$
    - order instance x: $x_o = \left(x_{o_1}, \dots, x_{o_j}, \dots, x_{o_p}\right)$
    - order instance z: $z_o = \left(z_{o_1}, \dots, z_{o_j}, \dots, z_{o_p}\right)$
    - construct two new instances $-x^{*+j} = \left(x_{o_1}, \dots, x_{o_{j-1}}, x_{o_j}, z_{o_{j+1}}, \dots, z_{o_p}\right)$ $x^{*-j} = \left(x_{o_1}, \dots, x_{o_{j-1}}, z_{o_j}, z_{o_{j+1}}, \dots, z_{o_p}\right)$
    - $\phi_{ij}^{(m)} = \hat{f}\left(x^{*+j}\right) - \hat{f}\left(x^{*-j}\right)$
  - Compute the Shapley value as the average: $\phi_{ij}(x) = \frac{1}{M}\sum_{m=1}^{M}\phi_{ij}^{(m)}$

First, select an instance of interest i, a feature j and the number of samples M. For each sample, a random instance from the data is chosen and the order of the features is mixed. From this instance, two new instances are created, by combining values from the instance of interest x and the sample. The first instance x^{*+j} is the instance of interest, but where all values in order before and including feature j are replaced by feature values from the sample. The second instance x^{*-j} is similar, but has all the values in order before, but excluding feature j, replaced by features from the sample. The difference in prediction from the black box is computed:

$$\phi_{ij}^{(m)} = \hat{f}\left(x^{*+j}\right) - \hat{f}\left(x^{*-j}\right)$$

All these differences are averaged and result in

$$\phi_{ij}(x) = \frac{1}{M}\sum_{m=1}^{M} \phi_{ij}^{(m)}$$

Averaging implicitly weighs samples by the probability distribution of X.

Appendix C Explanation of Features

Table A.2 Summary of features

	Feature	Explanation
x1	w/c	Water to cementitous ratio
x2	total_cement	The total amount of cementitious material, kg/m^3
x3	water_amount	The amount of water, kg/m^3
x4	cement_amount	The amount of Portland cement, kg/m^3
x5	slag_amount	The amount of GGBFS, kg/m^3
x6	slag_content	The percentage of GGBFS, no units
x7	fly_ash_amount	The amount of fly ash, kg/m^3
x8	fly_ash_content	The percentage of fly ash, no units
x9	silica_fume_amount	The amount of silica fume, kg/m^3
x10	silica_fume_content	The percentage of silica fume, no units
x11	air_content	Air content, %
x12	spacing_factor	Powers spacing factor, microns
x13	compressive_strength	Compressive strength at 28 day, Mpa
x14	sorptivity	Sorptivity, mm/sqrt(min)
x15	curing_age	Curing age of concrete, day
x16	PC_type	Portland cement type
x17	GGBFS_type	GGBFS type
x18	FA_type	fly ash type

Appendix D Histogram of the Variables

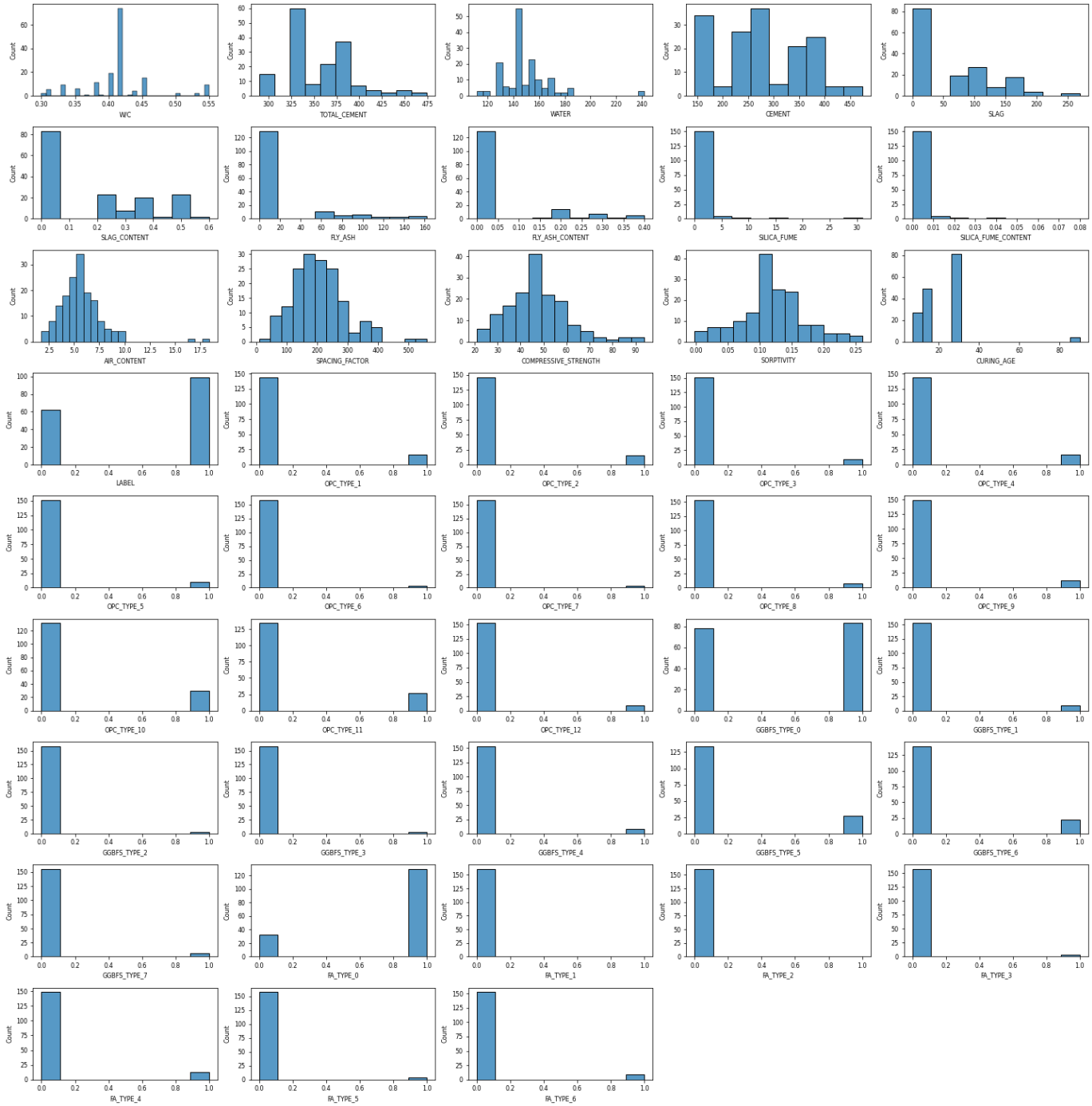

Figure A.0.1 histogram of variables

Appendix E Correlation Between Features and Response

The heatmap shows the linear correlation between the two variables ranging from -1 to 1. -1 means strongly negatively correlated while 1 means strongly positively correlated. 0 means there is no correlation.

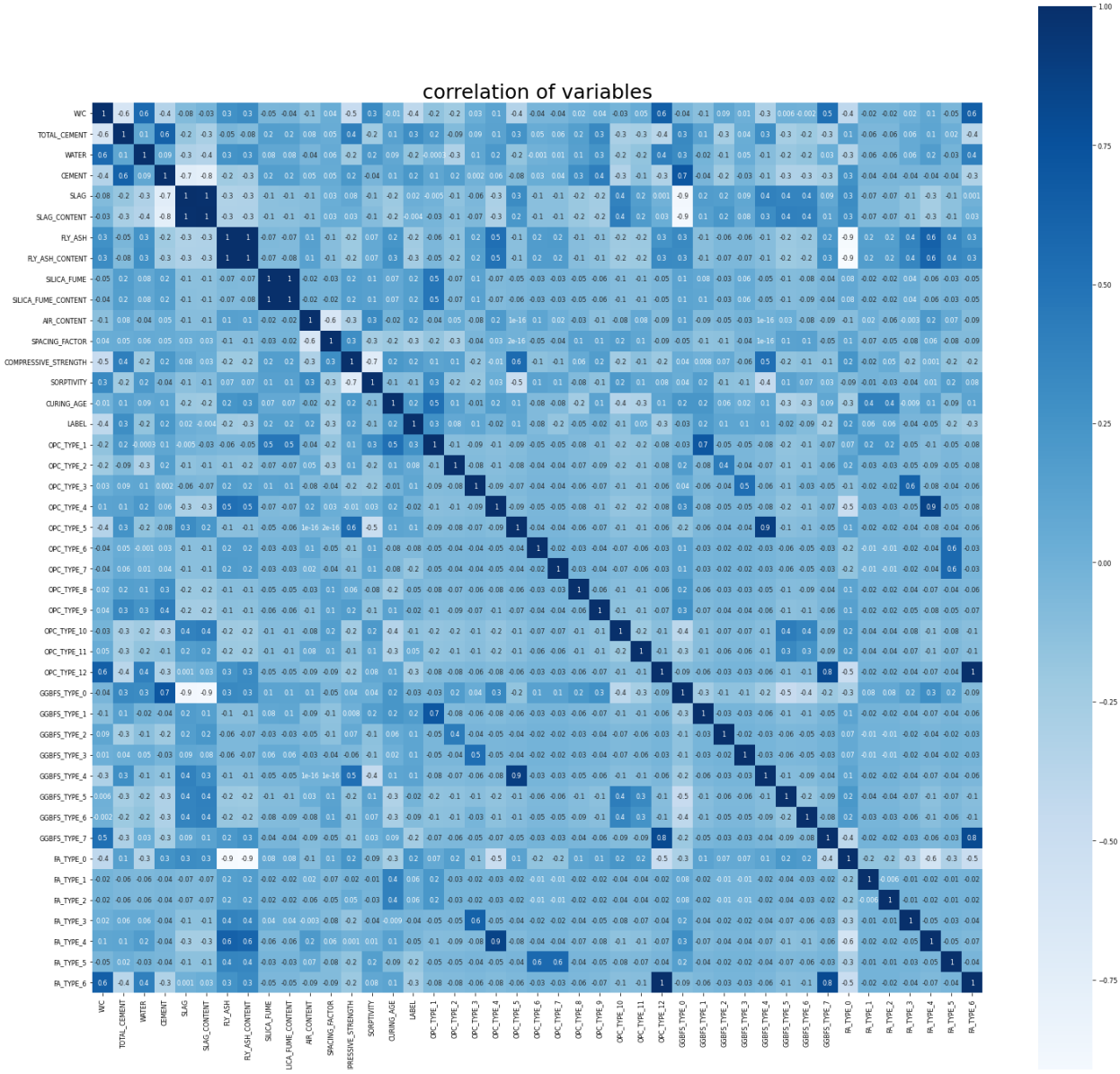

Figure A.0.2 heatmap for the variables

References

ABrAMS, D. A. (1919). *Design of concrete mixtures* (Vol. 1). Structural Materials Research Laboratory, Lewis Institute.

ACI (2021) *ACI CT-21: ACI Concrete Terminology*. Farmington Hills, MI: American Concrete Institute.

ACI Committee 201 (2016) *Guide to Durable Concrete*. Farmington Hills, MI: American Concrete Institute.

ACI Committee 212 (2016) *Report on Chemical Admixtures for Concrete*. Farmington Hills, MI: American Concrete Institute.

ACI Committee 301 (2016) *Specifications for Structural Concrete*. Farmington Hills, MI: American Concrete Institute.

ACI Committee 318 (2019) *Building Code Requirements for Structural Concrete and Commentary (Reapproved 2022)*. Farmington Hills, MI: American Concrete Institute.

ACI Committees 308, 213 (2022) *Report on Internally Cured Concrete Using Prewetted Absorptive Lightweight Aggregate (Reapproved 2022)*. Farmington Hills, MI: American Concrete Institute

Adamson, A.W. and Gast, A.P. (1967) *Physical chemistry of surfaces*. Inter-science publishers New York.

Aitcin, P. and Pigeon, M. (1986) 'Performance of condensed silica fume concrete used in pavements and sidewalks', *Durability of building materials*, 3(4), pp. 353–368.

American Concrete Pavement Association (1996) 'Scale-Resistant Concrete Pavements'.

Amini, K., Vosoughi, P., Ceylan, H. and Taylor, P. (2019) 'Linking air void system and mechanical properties to salt scaling resistance of concrete containing slag cement', *Cement and Concrete Composites*, 104, p. 103364.

ASTM C 1202 (2016) *Standard Test Method for Electrical Indication of Concrete's Ability to Resist Chloride Ion Penetration*. West Conshohocken, PA: ASTM International.

ASTM C 125 (2013) *Standard Terminology Relating to Concrete and Concrete Aggregates*. West Conshohocken, PA: ASTM International.

ASTM C 192 (2014) *Standard Practice for Making and Curing Concrete Test Specimens in the Laboratory*. West Conshohocken, PA: ASTM International.

ASTM C 457 (2012) *Standard Test Method for Microscopical Determination of Parameters of the Air-Void System in Hardened Concrete*. West Conshohocken, PA: ASTM International.

ASTM C 672 (2012) *Standard Test Method for Scaling Resistance of Concrete Surfaces Exposed to Deicing Chemicals*. West Conshohocken, PA: ASTM International.

Attiogbe, E.K. (1993) 'Mean spacing of air voids in hardened concrete', *Materials Journal*, 90(2), pp. 174–181.

Auberg, R. and Setzer, M. (1997) *Frost resistance of concrete*. CRC Press.

Aïtcin, P. (1998) *High performance concrete*. CRC press.

Bai, J., Wild, S. and Sabir, B. (2002) 'Sorptivity and strength of air-cured and water-cured PC–PFA–MK concrete and the influence of binder composition on carbonation depth', *Cement and Concrete Research*, 32(11), pp. 1813–1821.

Basheer, L. and Cleland, D. (2006) 'Freeze–thaw resistance of concretes treated with pore liners', *Construction and Building Materials*, 20(10), pp. 990–998.

Bentur, A., Igarashi, S. and Kovler, K. (2001) 'Prevention of autogenous shrinkage in high strength concrete by internal curing using wet lightweight aggregates', *Cement and concrete research*, 31(11), pp. 1587–1591.

Bentz, D.P. and Jason, W.W. (2011) *Internal curing: a 2010 state of the art review*. US Department of Commerce, National Institute of Standards and Technology.

Bentz, D.P. and Snyder, K.A. (1999) 'Protected paste volume in concrete: Extension to internal curing using saturated lightweight fine aggregate', *Cement and concrete research*, 29(11), pp. 1863–1867.

Bentz, D.P. and Stutzman, P.E. (2008) 'Internal curing and microstructure of high-performance mortars', *ACI SP256, Internal Curing of High-Performance Concretes: Laboratory and Field Experiences*, pp. 81–90.

Bilodeau, A. and MalhotraI, V. (1992) 'Concretes Incorporating High volumes of ASTM class F fly ashes: mechanical properties and resistance to deicing salt scaling and to chloride ion penetration', *ACI Symposium Publication*, 132, pp. 319–350. doi:https://doi.org/10.14359/1884.

Borgnakke, C., Hansen, W., Kang, Y., Liu, Z. and Koenders, E. (2012) 'Cryogenic suction pump mechanism for combined salt and frost exposure', in *Second International Conference on Microstructural related Durability of Cementitious Composites, RILEM Proceedings pro083,*

1113 April, 2012, Amsterdam, The Netherlands. RILEM Publications.

Byard, B.E., Schindler, A.K., Barnes, R.W. and Rao, A. (2010) 'Cracking tendency of bridge deck concrete', *Transportation Research Record*, 2164(1), pp. 122–131.

Castro, J., De, Golias, M. and Weiss, J. (2010) 'Extending internal curing concepts (using fine LWA) to mixtures containing high volumes of fly ash', in *2010 Concrete Bridge Conference: Achieving Safe, Smart & Sustainable Bridges National Concrete Bridge Council Federal Highway Administration Portland Cement Association*.

Cheng, A., Huang, R., Wu, J. and Chen, C. (2005) 'Influence of GGBS on durability and corrosion behavior of reinforced concrete', *Materials Chemistry and Physics*, 93(23), pp. 404–411.

Chen, T. and Guestrin, C. (2016) 'Xgboost: A scalable tree boosting system', in *Proceedings of the 22nd acm sigkdd international conference on knowledge discovery and data mining*, pp. 785–794.

Christodoulou, C., Goodier, C.I., Austin, S.A., Webb, J. and Glass, G.K. (2013) 'Long term performance of surface impregnation of reinforced concrete structures with silane', *Construction and Building Materials*, 48, pp. 708–716.

Christodoulou, C., Tiplady, H., Goodier, C. and Austin, S. (2014) 'Performance of silane impregnants for the protection of reinforced concrete', *Concrete Solutions*, pp. 385–392.

Civjan, S.A. and Crellin, B.J. (2008) *Field studies of concrete containing salts of an alkenyl substituted succinic acid* The New England Transportation Consortium (No. NETCR73).

Cleland, D. and Basheer, L. (2002) 'Assessing the freeze thaw durability of surface treated concrete', *Proc. of Frost Resistance of Concrete from Nano Structure and Pore Solution to Macroscopic Behavior and Testing, Essen, Germany, RILEM, Paris, France*, pp. 359–366.

Conde, M., Rovere, M. and Gallo, P. (2018) 'Molecular dynamics simulations of freezing point depression of TIP4P/2005 water in solution with NaCl', *Journal of Molecular Liquids*, 261, pp. 513–519.

Correia, V., Ferreira, G., Tang, L. and Lindvall, A. (2020) 'Effect of the addition of GGBS on the frost scaling and chloride migration resistance of concrete', *Applied Sciences*, 10(11), p. 3940.

Costa, H., Júlio, E. and Lourenço, J. (2012) 'New approach for shrinkage prediction of highstrength lightweight aggregate concrete', *Construction and Building Materials*, 35, pp. 84–91.

Cusson, D. and Hoogeveen, T. (2008) 'Internal curing of high performance concrete with presoaked fine lightweight aggregate for prevention of autogenous shrinkage cracking', *Cement and Concrete Research*, 38(6), pp. 757–765.

Dao, V.T., Dux, P.F., Morris, P.H. and Carse, A.H. (2010) 'Performance of permeability reducing admixtures in marine concrete structures', *ACI Materials Journal*, 107(3), p. 291.

Delagrave, A., Marchand, J., Pigeon, M. and Boisvert, J. (1997) 'Deicer salt scaling resistance of roller compacted concrete pavements', *ACI Materials Journal*, 94(2), pp. 164–169.

Detwiler, R.J. and Kumar, M.P. (1989) 'Chemical and physical effects of silica fume on the mechanical behavior of concrete', *ACI Materials Journal*, 86(6), pp. 609–614.

de Vries, Joop and Polder, R.B. (1997) 'Hydrophobic treatment of concrete', *Construction and Building Materials*, 11(4), pp. 259–265.

Dewey, G.R. and Darwin, D. (1991) *Image analysis of air voids in air entrained concrete*. University of Kansas Center for Research, Inc.

Dhir, R., Hewlett, P. and Chan, Y. (1987) 'Near surface characteristics of concrete: assessment and development of in situ test methods', *Magazine of Concrete Research*, 39(141), pp. 183–195.

Dirac, P. (1943) 'Approximate rate of neutron multiplication for a solid of arbitrary shape and uniform density: part I'.

Doug, H.R. and Vassilev, D. (2012) *Deicer scaling resistance of concrete mixtures containing slag cement. Phase 2: evaluation of different laboratory scaling test methods.* Iowa State University. Institute for Transportation.

Dullien, F.A. (2012) *Porous media: fluid transport and pore structure*. Academic press.

Eriksson, D., Wahlbom, D., Malm, R. and Fridh, K. (2021) 'Hygrothermomechanical modeling of partially saturated air entrained concrete containing dissolved salt and exposed to freeze thaw cycles', *Cement and Concrete Research*, 141, p. 106314.

Fagerlund, G. (1973). 'Significance of critical degrees of saturation at freezing of porous and brittle materials' (Report 40). Division of Building Materials, LTH, Lund University.

Fagerlund, G. (1977) 'The international cooperative test of the critical degree of saturation method of assessing the freeze/thaw resistance of concrete', *Matériaux et Construction*, 10, pp. 231–253.

Fagerlund, G. (1979) 'Prediction of the service life of concrete exposed to frost action', *Studies on Concrete Technology–Swedish Cement and Concrete Research Inst. Stockholm*, pp. 249–276.

Fagerlund, G. (1982) 'The capillarity of concrete', *Nordic concrete research*, (1).

Fagerlund, G. (1986) 'Effect of air-entraining and other admixtures on the salt-scaling resistance of concrete', in *J. International Seminar on "Some Aspects of Admixtures and Industrial By-Products on the Durability of Concrete"*.

Fagerlund, G. (1993). 'The critical spacing factor: preliminary version' (Report TVBM (Intern 7000-rapport); Vol.7058). Division of Building Materials, LTH, Lund University.

Fagerlund, G. (1995). 'Freeze-thaw resistance of concrete : destruction mechanisms, concrete technology, test methods, quality control : a contribution to the BRITE/EURAM project BREU-

CT92-0591 "The Residual Service Life of Concrete Structures'. (Report TVBM; Vol. 3060). Division of Building Materials, LTH, Lund University.

Fagerlund, G. (2004) *A service life model for internal frost damage in concrete*. (Report TVBM; Vol. 3119). Division of Building Materials, LTH, Lund University.

Fagerlund, G. (2017) 'The critical flow distance at freezing of concrete–theory and experiment', *Nordic Concrete Research*, (56), pp. 35–53.

Feng, D., Liu, Z., Wang, X., Chen, Y., Chang, J., Wei, D. and Jiang, Z. (2020) 'Machine learning-based compressive strength prediction for concrete: An adaptive boosting approach', *Construction and Building Materials*, 230, p. 117000.

Fonseca, P.C. and Scherer, G.W. (2015) 'An image analysis procedure to quantify the air void system of mortar and concrete', *Materials and Structures*, 48, pp. 3087–3098.

Franzoni, E., Varum, H., Natali, M.E., Bignozzi, M.C., Melo, J., Rocha, L. and Pereira, E. (2014) 'Improvement of historic reinforced concrete/mortars by impregnation and electrochemical methods', *Cement and Concrete Composites*, 49, pp. 50–58.

FrentzelSchirmacher, A. (2005) 'Water uptake and scaling of impregnated pavement concrete under freeze thaw and deicing agent attack', in *Proceedings of the 4th International Conference on Water Repellent Treatment of Building Materials; Aedificatio Publishers: Freiburg im Breisgau, Germany*, pp. 223–240.

Fuglsang, N.L. (1993) 'Strength development in hardened cement paste: examination of some empirical equations', *Materials and Structures*, 26, pp. 255–260.

Gagné, R. and Pigeon, M. (1990) 'Deicer salt scaling resistance of high-performance concrete', *ACI Symposium Publication*, 122, pp. 29–44.

Gagné, R., Houehanou, E., Jolin, M. and Escaffit, P. (2011) 'Study of the relationship between scaling resistance and sorptivity of concrete', *Canadian Journal of Civil Engineering*, 38(11), pp. 1238–1248.

Gebler, S. and Klieger, P. (1983) 'Effect of fly ash on the air-void stability of concrete', *ACI Symposium Publication*, 79, pp. 103–142.

Geiker, Metter Rica, Bentz, D.P. and Jensen, O.M. (2004) 'Mitigating autogenous shrinkage by internal curing', *ACI Special Publications*, pp. 143–154.

Gong, C., Jianzhong, L., Cuicui, C., Changfeng, L. and Liang, S. (2012) 'Study on silane impregnation for protection of high-performance concrete', *Procedia Engineering*, 27, pp. 301–307.

Gong, F. and Jacobsen, S. (2019) 'Modeling of water transport in highly saturated concrete with wet surface during freeze/thaw', *Cement and Concrete Research*, 115, pp. 294–307.

Gopalan, M. (1996) ‘Sorptivity of fly ash concretes’, *Cement and Concrete Research*, 26(8), pp. 1189–1197.

Grant, M. and Boyd, S. (2014) ‘CVX: Matlab software for disciplined convex programming, version 2.1’ [Online]. Available: http://cvxr.com/cvx

Güneyisi, E., Gesoğlu, M., Algın, Z. and Yazıcı, H. (2014) ‘Effect of surface treatment methods on the properties of self-compacting concrete with recycled aggregates’, *Construction and Building Materials*, 64, pp. 172–183.

Guo, R., Zhao, Z., Wang, T., Liu, G., Zhao, J. and Gao, D. (2020) ‘Degradation state recognition of piston pump based on ICEEMDAN and XGBoost’, *Applied Sciences*, 10(18), p. 6593.

Hall, C. (1989) ‘Water sorptivity of mortars and concretes: a review’, *Magazine of concrete research*, 41(147), pp. 51–61.

Hammer, T.A. and Sellevold, E.J. (1990) ‘Frost resistance of high strength concrete’, *ACI Symposium Publication 23*, pp. 457–487.

Hansen, W. and Kang, Y. (2010) *Durability study of the US23 aggregate test road and recent JPCP projects with premature joint deterioration.* Michigan. Dept. of Transportation. Construction and Technology Division.

Hasholt, M.T. (2014) ‘Air void structure and frost resistance: A challenge to Powers’ spacing factor’, *Materials and structures*, 47, pp. 911–923.

Hassani, M., Vessalas, K., Sirivivatnanon, V. and Baweja, D. (2017) ‘Influence of permeability reducing admixtures on water penetration in concrete’, *ACI Mater. J*, 114, pp. 911–922.

Hazrati, K., Abesque, C. and Pigeon, M. (1996) ‘Efficiency of sealers on the scaling resistance of concrete in presence of deicing salts’, *Freeze Thaw Durability of Concrete*, p. 165.

Henkensiefken, R., Bentz, D., Nantung, T. and Weiss, J. (2009) ‘Volume change and cracking in internally cured mixtures made with saturated lightweight aggregate under sealed and unsealed conditions’, *Cement and Concrete Composites*, 31(7), pp. 427–437.

Hilloulin, B., Bekrine, I., Schmitt, E. and Loukili, A. (2022) ‘Modular deep learning segmentation algorithm for concrete microscopic images’, *Construction and Building Materials*, 349, p. 128736.

Ho, D., Cui, Q. and Ritchie, D. (1989) ‘The influence of humidity and curing time on the quality of concrete’, *Cement and Concrete Research*, 19(3), pp. 457–464.

Islam, M.M., Alam, M.T. and Islam, M.S. (2018) ‘Effect of fly ash on freeze–thaw durability of concrete in marine environment’, *Australian Journal of Structural Engineering*, 19(2), pp. 146–161.

Jackson, F.H. (1944) ‘Concretes containing air entraining agents’, *Journal of the American Concrete Institute*, 40, pp. 509–515.

Jacobsen, S. (2002) 'Liquid uptake mechanisms in wet freeze/thaw: review and modelling', in *RILEM Proceedings PRO*, pp. 41–51.

Jacobsen, S. and Sellevold, E. (1994) 'Frost/salt scaling testing of concrete-importance of absorption during test', *Nordic Concrete Research*, 14(1), p. 1994.

Jakobsen, U., Pade, C., Thaulow, N., Brown, D., Sahu, S., Magnusson, O., Buck, D. and Schutter, D. (2006) 'Automated air void analysis of hardened concrete—a Round Robin study', *Cement and Concrete Research*, 36(8), pp. 1444–1452.

Jones, W.A., House, M.W. and Weiss, W.J. (2014) *Internal curing of high-performance concrete using lightweight aggregates and other techniques.* Colorado. Dept. of Transportation. Research Branch.

Jones, W.A. and Weiss, W.J. (2015) 'Freezing and Thawing Behavior of Internally Cured Concrete' Advances in Civil Engineering Materials, 4(1), pp. 144–154, doi:10.1520/ACEM20140044.

JóźwiakNiedźwiedzka, D. (2005) 'Scaling resistance of high performance concretes containing a small portion of prewetted lightweight fine aggregate', *Cement and Concrete Composites*, 27(6), pp. 709–715.

Junge, K., Krembs, C., Deming, J., Stierle, A. and Eicken, H. (2001) 'A microscopic approach to investigate bacteria under in situ conditions in sea-ice samples', *Annals of Glaciology*, 33, pp. 304–310.

Kang, Y. (2010) *Surface scaling mechanism and prediction for concrete*. University of Michigan.

Langan, B. and Ward, M. (1986) 'Determination of the Air-Void System Parameters in Hardened Concrete - An Error Analysis', in *Journal Proceedings*, pp. 943–952.

Langlois, M., Beaupre, D., Pigeon, M. and Foy, C. (1989) 'Influence of curing on the salt scaling resistance of concrete with and without silica fume', *ACI Symposium Publication*, 114, pp. 971–990.

Ley, M.T. (2007) *The effects of fly ash on the ability to entrain and stabilize air in concrete*. The University of Texas at Austin.

Ley, T., Felice, R. and Freeman, J.M. (2012) *Concrete pavement mixture design and analysis (MDA): assessment of air void system requirements for durable concrete.* Iowa State University. Institute for Transportation.

Lindmark, S. (1993) 'Influence on the salt scaling of variations in the salt concentration, the salt distribution and the freeze-thaw cycle', *Div. of Building Materials, Lund Institute of Technology, Report TVBM-7055*.

Lindmark, S. (1996). 'A hyphothesis on the mechanism of surface scaling due to combined salt and frost attack' (Report TVBM (Intern 7000-rapport); Vol. 7104). Division of Building Materials, LTH, Lund University.

Lindmark, S. (1998). 'Mechanisms of salt frost scaling on portland cement-bound materials: studies and hypothesis' [Doctoral Thesis (monograph), Division of Building Materials]. Division of Building Materials, LTH, Lund University.

Lindmark, S. (2010). 'On the Relation between Air void system parameters and Salt frost scaling' In D. Bager (Ed.), Freeze-thaw testing of concrete - input to revision of CEN test methods : workshop proceeding from a Nordic miniseminarDic (Vol. 9, pp. 41-58). Nordic Concrete Federation.

Liu, Z. (2014) 'Frost deterioration in concrete due to deicing salt exposure: Mechanism, mitigation and conceptual surface scaling model', *(Doctoral dissertation, University of Michigan).*

Liu, Z. and Hansen, W. (2014) 'Sorptivity as a measure of salt frost scaling resistance of air-entrained concrete', in *Key Engineering Materials*, 629, pp. 195–200.

Liu, Z. and Hansen, W. (2015a) 'A hypothesis for salt frost scaling in cementitious materials', *Journal of Advanced Concrete Technology*, 13(9), pp. 403–414.

Liu, Z. and Hansen, W. (2015b) 'Pore damage in cementitious binders caused by deicer salt frost exposure', *Construction and Building Materials*, 98(June), pp. 204–216. doi: 10.1016/j.conbuildmat.2015.06.066.

Liu, Z. and Hansen, W. (2016a) 'A geometrical model for void saturation in air-entrained concrete under continuous water exposure', *Construction and Building Materials*, 124, pp. 475–484.

Liu, Z. and Hansen, W. (2016b) 'Effect of hydrophobic surface treatment on freeze-thaw durability of concrete', *Cement and Concrete Composites*, 69, pp. 49–60.

Liu, Z. and Hansen, W. (2016c) 'Freeze–thaw durability of high strength concrete under deicer salt exposure', *Construction and Building Materials*, 102, pp. 478–485.

Liu, Z., Hansen, W. and Wang, F. (2018) 'Pumping effect to accelerate liquid uptake in concrete and its implications on salt frost durability', *Construction and building materials*, 158, pp. 181–188.

Liu, Z., Hansen, W., Wang, F., and Zhang, W. (2019) 'Simulation of air-void system in hardened concrete using a geometrical model', *Magazine of Concrete Research*, 71(13), pp.680-689.

Liu, Z., Ming, X., Hansen, W., and Wang, F. (2020). 'Surface Swelling Characteristics in Concrete under Salt Frost Exposure', *Journal of Materials in Civil Engineering*, 32(3), 06020002.

Lord, G. and Willis, T. (1951) 'Calculation of air bubble size distribution from results of a Rosiwal traverse of aerated concrete', *ASTM Bulletin*, 177, pp. 177–187.

Lu, B. and Torquato, S. (1992) 'Nearest-surface distribution functions for poly-dispersed particle systems', *Physical Review A*, 45(8), p. 5530.

Mao, J. and Ayuta, K. (2008) 'Freeze–thaw resistance of lightweight concrete and aggregate at

different freezing rates', *Journal of Materials in Civil Engineering*, 20(1), pp. 78–84.

Marchand, J. and Pigeon, M. (1994) 'Deicer Salt Scaling Deterioration - An Overview', *ACI Special Publication*, 145, pp. 1–46.

Marchand, J., Pigeon, M., Bager, D. and Talbot, C. (1999) 'Influence of chloride solution concentration on deicer salt scaling deterioration of concrete', *Materials Journal*, 96(4), pp. 429–435.

Marchand, J., Sellevold, E.J. and Pigeon, M. (1994) 'The deicer salt scaling deterioration of concretean overview', *American Concrete Institute, ACI Special Publication, SP-145*, pp. 1–46.

Marks, M., JóźwiakNiedźwiedzka, D., Glinicki, Michał A, Olek, J. and Marks, M. (2012) 'Assessment of scaling durability of concrete with CFBC ash by automatic classification rules', *Journal of Materials in Civil Engineering*, 24(7), pp. 860–867.

Martys, Nicos S and Ferraris, C.F. (1997) 'Capillary transport in mortars and concrete', *Cement and concrete research*, 27(5), pp. 747–760.

Matar, P. and Barhoun, J. (2020) 'Effects of waterproofing admixture on the compressive strength and permeability of recycled aggregate concrete', *Journal of Building Engineering*, 32, p. 101521.

Medeiros, M.H. and Helene, P. (2009) 'Surface treatment of reinforced concrete in marine environment: Influence on chloride diffusion coefficient and capillary water absorption', *Construction and building materials*, 23(3), pp. 1476–1484.

Molnar, C. (2018) 'A guide for making black box models explainable', *URL: https://christophm. github. io/interpretablemlbook*, p. 3.

Molnar, C. (2020) *Interpretable machine learning*. Available online: https://christophm.github.io/interpretable-ml-book/.

Mo, Y. and Lin, S. (1994) 'Investigation of framed shear-wall behaviour with neural networks', *Magazine of concrete research*, 46(169), pp. 289–299.

MTO LS412 (2006) 'Methods of Test for Scaling Resistance of Concrete Surfaces Exposed to Deicing Chemicals', *MTO Laboratory Testing Manual*.

Müller, M., Ludwig, H. and Hasholt, M.T. (2021) 'Salt frost attack on concrete: the combined effect of cryogenic suction and chloride binding on ice formation', *Materials and Structures*, 54(5), p. 189.

Neville, A.M. (1995) *Properties of concrete*. Prentice Hall. Longman London.

Nolan, E., Basheer, P. and Long, A. (1995) 'Effects of three durability enhancing products on some physical properties of near surface concrete', *Construction and Building Materials*, 9(5), pp. 267–272.

NowakMichta, A. (2022) 'Salt Scaling Resistance of Variable w/c Ratio Air Entrained Concretes Modified with Polycarboxylates as a Proper Consequence of Air Void System', *Materials*, 15(17), p. 5839.

NQ 2621-900 (2002) *Béton de masse volumique normale et constituants — Annexe B détermination de la résistance à l'écaillage du béton soumis à des cycles de gel-dégel en contact avec des sels fondants.* Bureau de normalisation du Québec, Québec.

Olufemi, Folagbade Samuel (2016) 'Absorption characteristics of cement combination concrete containing Portland cement, fly ash, and metakaolin', *Civil Engineering Dimension*, 18(1), pp. 57–64.

Panesar, D. and Chidiac, S. (2007) 'Multivariable statistical analysis for scaling resistance of concrete containing GGBFS', *Cement and Concrete Composites*, 29(1), pp. 39–48.

Panesar, D. and Chidiac, S. (2009) 'Capillary suction model for characterizing salt scaling resistance of concrete containing GGBFS', *Cement and Concrete Composites*, 31(8), pp. 570–576.

Perenchio, Williaqm F (1988) 'Durability of concrete treated with silanes', *Concrete international*, 10(11), pp. 34–40.

Peterson, K., Sutter, L. and Radlinski, M. (2009) *The practical application of a flatbed scanner for air-void characterization of hardened concrete*. ASTM International.

Philleo, R. (1983) 'A method for analyzing void distribution in air-entrained concrete', *Cement, concrete and aggregates*, 5(2), pp. 128–130.

Pickett, G. (1953) 'Flow of moisture in hardened Portland cement during freezing', in *Highway Research Board Proceedings*, pp. 276–284.

Pigeon, M. and Pleau, R. (1995) *Durability of concrete in cold climates*. CRC Press.

Pigeon, M., Marchand, J. and Pleau, R. (1996) 'Frost resistant concrete', *Construction and Building Materials*, 10(5), pp. 339–348.

Pigeon, M., Talbot, C., Marchand, J. and Hornain, H. (1996) 'Surface microstructure and scaling resistance of concrete', *Cement and Concrete Research*, 26(10), pp. 1555–1566.

Pinto, S.R., Luisa, A. and MedeirosJunior, Ronaldo A (2018) 'Effect of preconditioning temperature on the water absorption of concrete', *Journal of Building Pathology and Rehabilitation*, 3, pp. 1–10.

Pleau, R. and Pigeon, M. (1996) 'The use of the flow length concept to assess the efficiency of air entrainment with regards to frost durability: Part I-Description of the test method', *Cement, concrete and aggregates*, 18(1).

Pleau, R., Plante, P., Gagne, R. and Pigeon, M. (1990) 'Practical considerations pertaining to the microscopical determination of air void characteristics of hardened concrete (ASTM C 457

Standard)', *Cement, concrete and aggregates*, 12(1).

Pogorelov, S. and Semenyak, G. (2016) 'Frost resistance of the steel fiber reinforced concrete containing active mineral additives', *Procedia Engineering*, 150, pp. 1491–1495.

Powers, T.C. (1945) 'A working hypothesis for further studies of frost resistance of concrete', in *ACI Journal Proceedings*, pp. 245–272.

Powers, T.C. (1949) 'The air requirement of frost-resistant concrete'. in *Highway research board proceedings*, 29, pp. 184-211

Powers, T.C. (1954) 'Void space as a basis for producing air-entrained concrete', in *ACI Journal Proceedings*, pp. 741–760.

Powers, T.C. and Helmuth, R. (1953) 'Theory of volume changes in hardened Portland cement paste during freezing', in *Highway research board proceedings*, 32.

Powers, T.C., Copeland, L.E., Hayes, J.C. and Mann, H.M. (1954) 'Permeability of Portland Cement Paste', *Journal of The American Concrete Institute*, 26(51-14), pp. 285–298.

Pratt, D. and Sansalone, M. (1992) 'Impact-echo signal interpretation using artificial intelligence', *Materials journal*, 89(2), pp. 178–187.

Radlinski, M., Olek, J. and Nantung, T. (2008) 'Effect of mixture composition and initial curing conditions on scaling resistance of ternary (OPC/FA/SF) concrete', *Journal of materials in civil engineering*, 20(10), pp. 668–677.

Ramezanianpour, A. and Hooton, R. (2010) 'Evaluation of two automated methods for air-void analysis of hardened concrete', in *Recent Advancement in Concrete Freezing-Thawing (FT) Durability*. ASTM International.

Reid, W.P. (1955) 'Distribution of sizes of spheres in a solid from a study of slices of the solid', *Journal of Mathematics and Physics*, 34(14), pp. 95–102.

Roberts, L. and Scheiner, P. (1981) 'Microprocessor-based linear traverse apparatus for air-void distribution analysis', *Proc. of the 3th ICMA, Texas*, pp. 211–227.

Rose, K., Hope, B. and Ip, A. (1989) 'Statistical analysis of strength and durability of concrete made with different cements', *Cement and Concrete Research*, 19(3), pp. 476–486.

Rønning, T. (1999) 'Moisture absorption during freeze-thaw and relation to deterioration, Frost resistance of building materials', in *Proceedings of the 3rd Nordic Research Seminar in Lund, Report TVBM3087*, pp. 113–118.

Rønning, Terje F (2001) 'Freeze-Thaw Resistance of Concrete: Effect of: Curing Conditions, Moisture Exchange and Materials'. Ph.D. thesis, Institute of Technology, Trondheim, Norway.

Sakai, K., Banthia, N. and Gjørv, Odd E (1995) *Concrete Under Severe Conditions:*

Environmental and Loading. Taylor & Francis US.

San and Mateo, (2012) 'The shapley value', *Multi Criteria Analysis in the Renewable Energy Industry*, pp. 95–101.

Sandström, T., Fridh, K., Emborg, M. and Hassanzadeh, M. (2012) 'The influence of temperature on water absorption in concrete during freezing', *Nordic Concrete Research*, 45(1), pp. 45–58.

Scrivener, K.L., Crumbie, A.K. and Laugesen, P. (2004) 'The interfacial transition zone (ITZ) between cement paste and aggregate in concrete', *Interface science*, 12, pp. 411–421.

Sellevold, E. J.(1990) 'Liquid permeability, capillary suction: PF-method', *Note*.

Sellevold, E.J. and Farstad, T. (1991) *Frost/salt-testing of concrete: Effect of test parameters and concrete moisture history*. Nordic Concrete Federation.

Setzer, M. (2001) 'Micro-ice-lens formation in porous solid', *Journal of colloid and interface science*, 243(1), pp. 193–201.

Setzer, M. (2009) 'Frost-attack on concrete—modeling by the micro-ice-lens model—evaluating by RILEM CIF test', *Creep, Shrinkage and Durability Mechanics of Concrete and Concrete Structures*, pp. 971–977.

Setzer, M. and Auberg, R. (1995) 'Freeze-thaw and deicing salt resistance of concrete testing by the CDF method CDF resistance limit and evaluation of precision', *Materials and Structures*, 28, pp. 16–31.

Setzer, M. and Liebrecht, A. (2004) 'Modeling and Testing the Freeze-Thaw Attack by MicroIceLens Model and CDF/CIF Test', in *Proceedings of the International Workshop on Microstructure and Durability to Predict Service Life of Concrete Structures*. Hokkaido University Sapporo, Japan, pp. 17–28.

Setzer, M., Fagerlund, G. and Janssen, D.J. (1996) 'CDF test—Test method for the freeze-thaw resistance of concrete tests with sodium chloride solution (CDF) Recommendation', *Materials and structures*, 29(9), pp. 523–528.

Setzer, M., Heine, P., Kasparek, S., Palecki, S., Auberg, R., Feldrappe, V. and Siebel, E. (2004) 'RILEM TC 176IDC: Internal damage of concrete due to frost action. Final recommendation: Test methods of frost resistance of concrete: CIF Test: Capillary suction, internal damage and freeze-thaw test–Reference method and alternative methods A and B', *Materials and structures*, 37, pp. 743–753.

Sharp, S.R. and Celik, O.H. (2007) *Influence of Hycrete DSS on Virginia Department of Transportation Class A4 concrete mix designs.* Virginia Transportation Research Council.

Shirtcliffe, N., McHale, G. and Newton, M. (2009) 'Learning from superhydrophobic plants: The use of hydrophilic areas on superhydrophobic surfaces for droplet control', *Langmuir*, 25(24), pp. 14121–14128.

Sjöstrand, N. G.(2002) ‘What is the average chord length?’, *Annals of Nuclear Energy*,29(13), pp. 1607–1608. doi: 10.1016/S0306-4549(02)00003-8.

Skidmore, M., Jungblut, A., Urschel, M. and Junge, K. (2011) ‘Cryospheric environments in polar regions (glaciers and ice sheets, sea ice, and ice shelves)’, *Polar microbiology: life in a deep freeze*, pp. 218–239.

Snyder, K.A. (1998) ‘A numerical test of air void spacing equations’, *Advanced cement based Materials*, 8(1), pp. 28–44.

Snyder, K.A., C, H.K. and Natesaiyer, K. (2001) ‘The Stereological and Statistical Properties of Entrained Voids in Concrete: A Mathematical Basis for Air Void System Characterization’. In: Mindess S, Skalny J (eds) Materials science of concrete VI. American Ceramic Society, Westerville, pp. 129–214.

Sommer, H. (1979) ‘The precision of the microscopical determination of the air-void system in hardened concrete’, *Cement, Concrete and Aggregates*, 1(2), pp. 49–55.

Sorensen, E.V. (1983) ‘Freezing and thawing resistance of condensed silica fume (Microsilica) concrete exposed to deicing chemicals’, *ACI Special Publication*, 79, pp. 709–718.

Streeter, D.A., Wolfe, W.H. and Vaughn, R.E. (2012) ‘Field performance of internally cured concrete bridge decks in New York State’, *ACI Special Publication*, 290, pp. 1–16.

Studer, W., (1993) ‘Internal comparative tests on frost-deicing salt resistance’, *International Workshop on the Resistance of Concrete to Scaling Due to Freezing in the Presence of Deicing Salts, Centre de Recherche Interuniversitaire sur le Beton, Université de Sherbrooke-Université* Laval, Quebec. pp. 175–187.

Swedish Institute for Standards (2019) *SS 137244:2019 Concrete testing – Hardened concrete – Scaling at freezing*. Swedish Institute for Standards.

Talbot, C., Pigeon, M. and Marchand, J. (2000) ‘Influence of fly ash and slag on deicer salt scaling resistance of concrete’, *ACI Special Publication*, 192, pp. 645–658.

Tanesi, J. and Meininger, R. (2007). ‘Freeze-thaw resistance of concrete with marginal air content’, *Transportation research record*, 2020(1), pp. 61-66.

Tasdemir, C. (2003) ‘Combined effects of mineral admixtures and curing conditions on the sorptivity coefficient of concrete’, *cement and concrete research*, 33(10), pp. 1637–1642.

Tavasoli, S., Nili, M. and Serpoush, B. (2018) ‘Effect of GGBS on the frost resistance of self-consolidating concrete’, *Construction and Building Materials*, 165, pp. 717–722.

Taylor, P., Sadati, S., Wang, K., Ling, Y., Wang, X., Sun, W., Kevern, J.T. and Ryazi, S. (2021) *Entrained air-void systems for durable highway concrete*, NCHRP 961 (80).

Thomas, M. (1997) ‘Laboratory and field studies of salt scaling in fly ash concrete’, in *RILEM*

Proceedings. Chapman & Hall, pp. 21–30.

Tibbetts, C.M., Riding, K.A. and Ferraro, C.C. (2021) 'A critical review of the testing and benefits of permeability reducing admixtures for use in concrete', *Cement*, 6, p. 100016.

Tittarelli, F. and Moriconi, G. (2008) 'The effect of silane-based hydrophobic admixture on corrosion of reinforcing steel in concrete', *Cement and Concrete Research*, 38(11), pp. 1354–1357.

Valenza, J. and Scherer, G.W. (2007) 'A review of salt scaling: II. Mechanisms', *Cement and Concrete Research*, 37(7), pp. 1022–1034.

Verbeck, G.J. and Klieger, P. (1957) 'Studies of "salt" scaling of concrete', *Highway Research Board Bulletin*, (150).

Walker, H. (1980) 'Formula for calculating spacing factor for entrained air voids', *Cement, Concrete and Aggregates*, 2(2), pp. 63–66.

Wan, X. (2019) 'The effect of regularization coefficient on polynomial regression', in *Journal of Physics: Conference Series*. IOP Publishing, p. 42054.

Washburn, E. W. (1921). 'The dynamics of capillary flow', *Physical review*, 17(3), pp. 273.

Wei, Y. (2008) *Modeling of autogenous deformation in cementitious materials, restraining effect from aggregate, and moisture warping in slabs on grade*. University of Michigan.

Wei, Y. and Hansen, W. (2008) 'Presoaked lightweight fine aggregates as additives for internal curing in concrete', *ACI Special Publication*, 256, pp. 35–44.

Whitaker, S. (1986) 'Flow in porous media I: A theoretical derivation of Darcy's law', *Transport in porous media*, 1, pp. 3–25.

Whiting, D. (1989) 'Deicer scaling resistance of lean concretes containing fly ash', *ACI Special Publication*, 114, pp. 349–372.

Whiting, D. and Stark, D. (1983) 'Control of air content in concrete', *NCHRP report*, (258).

Wilson, M., Carter, M. and Hoff, W. (1999) 'British Standard and RILEM water absorption tests: A critical evaluation', *Materials and Structures*, 32, pp. 571–578.

Yang, L., Liu, G., Gao, D. and Zhang, C. (2021) 'Experimental study on water absorption of unsaturated concrete: w/c ratio, coarse aggregate and saturation degree', *Construction and Building Materials*, 272, p. 121945.

Yong, R.N., Mohamed, A.O. and Warkentin, B.P. (1992) *Principles of contaminant transport in soils.* Amsterdam, The Netherlands: Elsevier Science Publishers.

Yu, H., Ma, H. and Yan, K. (2017) 'An equation for determining freeze-thaw fatigue damage in concrete and a model for predicting the service life', *Construction and building materials*, 137, pp. 104–116.

Zhang, C., Zhang, S., Yu, J. and Kong, X. (2022) 'Water absorption behavior of hydrophobized concrete using silane emulsion as admixture', *Cement and Concrete Research*, 154, p. 106738.

Zhou, T., Mirzadeh, M., Pellenq, R.J. and Bazant, M.Z. (2020) 'Freezing point depression and freeze-thaw damage by nanofluidic salt trapping', *Physical Review Fluids*, 5(12), p. 124201.

Zhu, Y., Kou, S., Poon, C., Dai, J. and Li, Q. (2013) 'Influence of silane based water repellent on the durability properties of recycled aggregate concrete', *Cement and Concrete Composites*, 35(1), pp. 32–38.